Mechanics dictate stromal cell-ECM dynamic interactions: studies using organ-derived ECM hydrogels

Fenghua Zhao

Propositions

1. Extracellular matrix (ECM) stiffness drives vascular network formation. (This thesis)

2. ECM remodeling provides mechanical feedback that drives vascularization processes in a reciprocal fashion. (This thesis)

3. Cells embedded in organ ECM-derived hydrogels with tunable stiffness respond in a physiological fashion while cells cultured in 2D on plastic do not. (This thesis)

4. Ruthenium-induced crosslinking of tissue-derived ECM modulates stiffness without altering its biochemical composition. (This thesis)

5. Dermal fibroblasts align at a 45° angle relative to the stiffness gradient. (This thesis)

6. Irrespective of high or low stiffness, mesenchymal cells remodel ECM to create a suitable microenvironment with intermediate stiffness. (This thesis)

7. Piezo1 and FAK but not YAP, serve as mechanosensors mediating stiffness-dependent ECM remodeling by umbilical cord mesenchymal stem cells in 3D hydrogels. (This thesis)

8. Learning (when) to say no is an important lesson. (Fenghua)

9. All things are difficult before they are easy. (Thomas Fuller)

10 Discipline equals Freedom. (Jocko Willink)

Mechanics dictate stromal cell – ECM dynamic interactions: studies using organ-derived ECM hydrogels

Fenghua Zhao

The studies presented in this thesis were performed at the Departments of "Pathology and Medical Biology" and "Biomaterials & Biomedical Technology", University Medical Center Groningen (UMCG), University of Groningen, the Netherlands. The PhD was funded by Chinese Scholarship Council, and Graduate School of Medical Sciences, University of Groningen.

The printing of this thesis was financially supported by the Graduate School of Medical Sciences, UMCG, and University of Groningen.

Cover design: Fenghua Zhao, Studio Shu | shu.artdesign@gmail.com
Printed by: Proefschriftmaken | www.proefschriftmaken.nl
Layout and design: Fenghua Zhao

university of groningen

Mechanics dictate stromal cell – ECM dynamic interactions: studies using organ-derived ECM hydrogels

PhD thesis

to obtain the degree of PhD at the
University of Groningen
on the authority of the
Rector Magnificus Prof. J.M.A. Scherpen
and in accordance with
the decision by the College of Deans.

This thesis will be defended in public on

Monday 8 September 2025 at 14:30 hours

by

Fenghua Zhao

born on 21 January 1996

in Henan, China

Supervisors

Prof. M.C. Harmsen

Dr. P.K. Sharma

Prof. J.K. Burgess

Assessment Committee

Prof. P. van Rijn

Prof. R. Gosens

Prof. L.F.P. Moreira

Table of contents

Chapter 1

General introduction

1. ECM Composition and Function in organs

Extracellular matrix (ECM) is a biologically active network of molecules, which are secreted by cells in all tissues and organs[1]. ECM provides structural support for cells and ensures the integrity of tissues. In addition, the ECM regulates cell fate and function through biochemical and biomechanical cues[2]. The ECM is composed of various proteins, proteoglycans and glycosaminoglycans (GAGs), including collagens, elastin, fibronectin, laminin, hyaluronan, and chondroitin sulfate[3].

Collagen is a major component of the ECM, with 28 different types playing distinct structural and functional roles. Fibrillar collagens (e.g., type I, II, and III) provide tensile strength and structural support, ensuring tissue integrity and stability, while non-fibrillar collagens (e.g., type IV) adopt sheet-like or mesh-like configurations, contributing to specialized functions such as basement membrane organization (a specialized, thin, and condensed ECM structure). **Elastin** imparts elasticity to tissues, allowing them to stretch and contract as needed[4]. This property is particularly vital in dynamic tissues such as the lungs, arteries, and skin. **Fibronectin and laminin are** glycoproteins that provide binding sites for cell adhesion receptors, such as integrins, facilitating processes like cell attachment, growth, migration, and differentiation. Laminin is also a major component of the basement membrane. **GAGs and Proteoglycans:** GAGs are long and linear strongly negatively charged polysaccharides composed of repeating disaccharide units. Their negative charge enables them to retain water, which is essential for their functions in shaping tissue volume, providing shock absorption, and, specifically in joints, serving as lubricants. In addition, GAGs may attach to core proteins to form proteoglycans (PGs). Proteoglycans consist of a protein core with covalently attached GAGs via a xylose-galactose-N-acetylgalactosamine-N-acetylglucosamine tetramer. While the core proteins anchor GAGs, the GAGs themselves can interact with other ECM proteins and cells. PGs bind large amounts of water, contributing to tissue lubrication and resistance to compressive forces[5]. Beyond their structural role, GAGs and proteoglycans reversibly bind soluble factors, such as chemokines, growth factors and biologically active ECM degradation products, thus serving as ‘on-demand’ release reservoirs. PGs like nidogen and perlecan, serve a specific role in the makeup of the basement membrane.

The specific composition of ECM varies across tissues and organs, reflecting the unique structural and functional requirements of each organ[2]. For example, skin and lungs have the same main ECM components: collagen types I, III and elastin which retain tensile strength and elasticity. However, the dermis of skin has more abundant GAGs (hyaluronic acid in particular) to maintain moisture and support wound healing[3]. The lungs on the other hand, have a higher concentration of elastin to support their repeated expansion and contraction during respiration. Elastin makes up approximately 30% of dry weight in lungs but only 2-4% of dry weight in skin dermis of adults[6-9]. These variations in ECM composition give rise to differences in matrix microstructure and mechanical properties, enabling each organ to meet its distinct physiological demands [10].

2. ECM modulates cellular functions

The ECM regulates cellular function through a combination of biochemical and mechanical cues.

2.1 Biochemical cues:

Integrins, are heterodimers composed of α and β subunits, that act as versatile receptors that mediate cell-ECM attachment. At least 19 α and 8 β subunits give rise to 24 distinct integrins. These function by indirectly linking the cytoskeleton to ECM components such as fibronectin, collagen, and laminin[11]. These interactions are specific because integrins recognize distinct short recognition sequences of three to ten amino acids in ECM molecules (Table 1)[11-14]. For instance, integrins α5β1 and αvβ3 bind to the RGD (arginine-glycine-aspartate) motif on fibronectin and laminin, whose accessibility and abundance make it particularly effective in promoting cellular adhesion. Similarly, integrin α2β1 interacts with the GFOGER (glycine-phenylalanine-hydroxyproline-glycine-glutamate-arginine) sequence in collagen, while laminins engage integrins such as α6β1 and α6β4 via specific LG (laminin globular) domains. Upon binding to their ligands, integrins transmit critical signals about the extracellular environment into the cell, initiating signal transduction pathways that regulate various cellular processes[15]. The integrin – ECM interaction has redundancy as cells have multiple integrins species and ECM molecules often have multiple integrins-binding motifs.

Beyond providing a scaffold for cell attachment, the ECM functions as a reservoir for growth factors and cytokines, which are stored and released in response to mechanical stress, enzymatic degradation, or environmental changes[1, 2]. This regulated release modulates cell behavior by establishing localized variations in factor availability and concentration. For example, during wound healing, transforming growth factor β (TGF-β), secreted by cells such as platelets, macrophages, and fibroblasts, is stored within the ECM. The localized release of TGF-β near fibroblasts induces their expression of alpha smooth muscle actin (α-SMA), differentiation into myofibroblasts, and production of ECM proteins, thereby facilitating tissue repair[16, 17]. Furthermore, ECM-mediated integrin binding synergizes with growth factor signaling to suppress apoptosis. In the absence of either integrin engagement or growth factors, cells quickly undergo apoptosis, highlighting the dual roles of ECM as a structural scaffold and a dynamic signaling regulator.

Table 1. the specific recognition sequences on ECM components and their corresponding integrin receptors

ECM Component	Specific Recognition Sequences	Integrin Receptors
Fibronectin	RGD motif	α5β1, αvβ3
Collagen	GFOGER sequence	α1β1, α2β1
Laminin	LG domains	α6β1, α6β4, α3β1
Vitronectin	RGD motif	αvβ3, αvβ5
Fibrinogen	RGD motif	αvβ3, αIIbβ3

2.2 Mechanical cues:

Mechanical cues from the ECM, both static (e.g., viscoelasticity, including stiffness and stress relaxation, and topography) and dynamic ((e.g., mechanical loading or tissue deformation), exert significant influence on cellular phenotype and tissue organization. Cells sense and respond to these cues through

mechanotransduction; converting mechanical forces into biochemical signals. For instance, aligned collagen fibers guide the direction of cell migration while influencing cell polarity and cytoskeletal organization[18]. ECM stiffness, dictates mesenchymal cell fate in conjunction with paracrine signals. For lineage-specific differentiation of mesenchymal stromal cells (MSCs), soft matrices (e.g., those that mimic brain tissue) promote neurogenic and adipogenic differentiation, while stiffer matrices favor myogenic, chondrogenic or osteogenic lineages i.e. cells of stiffer tissues[19]. Specific mesenchymal lineages like fibroblasts similarly sense and respond to ECM stiffness: a higher than normal physiological stiffness promotes their differentiation into myofibroblasts. In wound healing, myofibroblasts are essential for wound contraction and ECM deposition, facilitating tissue repair yet this is predominantly governed by biochemical cues such as TGFβ signaling. However, in dysregulated wound healing, their persistent activation contributes to fibrosis which is also driven by the chronically increased higher stiffness[20]. In neoplastic disease, cancer cells exploit ECM viscoelasticity to migrate through dense tissues, through secretion of proteases that remodel the ECM to literally generate tracks for metastatic invasion[21].

The dynamic interaction between the ECM and cells is bidirectional. Under normal physiological conditions, this interaction is finely balanced. The ECM regulates cellular behavior through biochemical and mechanical cues, while cells actively maintain and remodel the ECM by synthesizing, rearranging and degrading matrix components some of which harbor biochemical activity. This dynamic reciprocity ensures proper tissue homeostasis. However, when the balance between cells and the ECM is disrupted - due to factors such as tissue damage or mechanical stress – this may lead to altered cellular phenotypes and changes in ECM composition and mechanics. The knowledge of the influence of the ECM's mechanical properties on cellular phenotype and ECM remodeling is still in its infancy to date.

3. ECM remodeling

3.1 Matrix deposition

The deposition of ECM is primarily driven by mesenchymal cells such as fibroblasts, myofibroblasts, pericytes and smooth muscle cells in soft tissues. However, epithelial and endothelial cells also contribute to ECM production and

deposit their own basement membranes that warrant their polarized nature[22, 23].

Key regulators of ECM deposition are members of the transforming growth factor (TGF) family, in particular TGF-β. During tissue repair and wound healing, TGF-β signaling drives fibroblast activation and upregulates expression of collagen and other ECM genes, promoting matrix deposition[24]. Similarly, platelet-derived growth factor (PDGF) and fibroblast growth factors (FGF) promote proliferation of (myo)fibroblasts and smooth muscle cells and their secretion of fibronectin and laminin to re-establish the structural integrity of tissues[25]. These factors are relevant to tissue regeneration and pathological ECM remodeling because they drive the molecular processes underlying ECM dynamics.

As stated earlier, mechanical cues drive cellular plasticity, meaning that cells adjust and adapt their phenotype in response to their environment. Consequently, ECM production and deposition are also influenced by these mechanical signals from the surrounding microenvironment. Substrates that mimic the natural stiffness of a tissue promote normal ECM production, whereas excessively stiff environments, as seen in fibrosis, can lead to aberrant ECM deposition and crosslinking[26-28]. In response to pulsatile shear stress, arterial smooth muscle cells align concentrically and deposit ECM components such as elastin and other structural ECM components in a concentric fashion to support proper vessel elasticity and resilience[29].

3.2 Matrix degradation

The degradation of ECM is equally important for remodeling as deposition and is carried out by matrix metalloproteinases (MMPs) and a plethora of other proteases [30]. MMPs are a group of zinc-dependent endopeptidases that target and degrade a variety of ECM components. Table 2 provides an overview of the specific ECM components targeted by different MMPs. MMP1, MMP2 and MMP8, for instance, degrade collagens such as types I, II, and III, while MMP2 and MMP9 can also degrade type IV collagen, elastin, fibronectin and laminin[31]. MMP13, in particular, degrades type II collagen along with types I and III collagen, which is essential in cartilage degradation and osteoarthritis pathology. MMP3, MMP10, and MMP13 also degrade proteoglycans, laminin,

fibronectin, gelatin, type IV and type IX collagen[32, 33]. Additionally, MMP12, an elastase, is particularly important in degrading elastin. Unlike secreted MMPs, which require proteolytic activation, MMP14 is active at the cell surface and activates all other MMPs, with the help of TIMP2 (tissue inhibitor of metalloproteinases 2). This activation process underscores the intricate regulation of MMP activity within the ECM. To maintain ECM homeostasis and prevent excessive matrix degradation, the activity of MMPs is tightly regulated by TIMPs. In tissues, TIMP1, one of the four members of the TIMP family, is the prime MMP inhibitor next the TIMP2. TIMP 3 and 4 harbor slightly different functions. For instance, TIMP3 also regulates A Disintegrin and Metalloproteinases (ADAMs). Additionally, TIMP3 binds to other molecules, such as the angiotensin II type 2 receptor (AT2R) and GAGs, playing roles in signaling and matrix regulation[34]. Collectively, the TIMPs contribute to the fine-tuned balance between ECM synthesis and degradation.

Other protease families, such as ADAMs and ADAMs with Thrombospondin Motifs (ADAMTSs) are also involved in ECM degradation and thus in remodeling. ADAMs regulate cell communication and function by cleaving proteins on the cell surface, such as growth factors and receptors[35]. ADAMTSs mainly degrade proteoglycans, such as aggrecan and versican[36].

ECM degradation happens in both physiological and pathological contexts. During angiogenesis, endothelial cells express MMP2, MMP9, and MMP14 to degrade the basement membrane and surrounding ECM, facilitating endothelial sprouting and new blood vessel formation[37]. Similarly, macrophages secrete MMPs to clear damaged ECM components at sites of inflammation, preparing the tissue for repair and regeneration[38]. In fibrotic diseases, fibroblasts are activated to deposit excessive collagens. Concurrently, fibroblasts secrete MMPs like MMP2 and MMP9 to degrade existing ECM, facilitating the replacement with newly synthesized matrix[39, 40]. The non-protein components of the ECM such as GAGs are degraded by a series of specialized enzymes, including endoglycosidases, endosulfatases, hyaluronidases, and heparanases. These enzymes work in a coordinated manner to break down complex carbohydrate structures[41].

Table 2. Functions and targets of key matrix metalloproteinases (MMPs) in ECM remodeling.

MMP	Targets/Substrates	Functional Importance
MMP1	Collagen fibers (types I, II, III)	Essential for collagen degradation and remodeling
MMP2	Type IV collagen, elastin, fibronectin, laminin	Key role in basement membrane degradation and ECM remodeling
MMP3	Proteoglycans, laminin, fibronectin, gelatin, type IV and IX collagen	Degrades multiple ECM components; involved in tissue remodeling
MMP8	Types I, II, III collagen	Major role in collagen degradation
MMP9	Type IV collagen, elastin, fibronectin, laminin	Breakdown of basement membrane and other ECM components
MMP10	Proteoglycans, laminin, fibronectin, gelatin, type IV and IX collagen	Involved in ECM component degradation
MMP12	Elastin	Specialized for elastin degradation; important in elastic tissue remodeling
MMP13	Type II collagen; also types I and III collagen	Critical in cartilage breakdown and osteoarthritis pathology
MMP14	Activates other MMPs (e.g., MMP2 with TIMP2); active at cell surface	Facilitates activation of other MMPs; crucial for pericellular proteolysis

MMP: matrix metalloproteinase; TIMP: tissue inhibitor of metalloproteinases.

3.3 ECM remodeling during wound healing

Wound healing is a multi-staged process involving ECM remodeling and various cellular events (Fig.1)[42, 43]. The first stage is hemostasis, where the clotting cascade is activated to prevent blood loss and form a provisional matrix consisting of a fibrin network. This network traps activated platelets that release a host of growth factors that regulate subsequent phases. This is followed by the inflammatory phase, characterized by an influx of immune cells such as neutrophilic granulocytes, monocytes and macrophages to the wound site to clear bacteria and debris.

Overlapping with this phase is the proliferative phase, during which signaling paracrine molecules like cytokines and growth factors including TGF-β, PDGF, FGF, as well as vascular endothelial growth factor (VEGF) were released by captured platelets and also by macrophages that activate stromal cells, such as fibroblasts and drive angiogenesis too[44]. Activated fibroblasts serve as the 'workhorses' of repair and regeneration by producing ECM and differentiating to myofibroblasts to contract the wound, while angiogenesis starts from sprouting endothelial cells that form new vessels that act as transport conduits for subsequent waves of monocytes. These monocytes differentiate into M2 macrophages to support ongoing tissue repair and regeneration[45, 46].

During the proliferative phase, the ‘old’ ECM is partially degraded by proteases such as MMPs, secreted by macrophages and fibroblasts[47]. Concurrently, fibroblasts and myofibroblast deposit a new provisional ECM containing a high collagen type III content to support tissue reconstruction[45]. Additionally, these cells secrete collagen crosslinking enzymes, such as lysyl oxidases and transglutaminases, to reinforce the matrix structure. The largely hypoxic wound bed, together with VEGF-A and angiopoietin-2 derived from platelets and invading cells, triggers endothelial cells to engage in angiogenesis[48]. During angiogenesis, endothelial cells secrete PDGF -BB which attract pericytes that stabilize and facilitate maturation of the newly formed vascular tubes.

The remodeling phase, which is the next wound healing process, is characterized by wound contraction and closure. Myofibroblasts express αSMA, which renders them contractile and capable of migrating to wound edges, where they facilitate wound closure[49]. However, unresolved infections, the presence of foreign

bodies, chronic diseases such as diabetes, hypoxic conditions, continuous mechanical stress, or repeated injury can lead to prolonged activation of fibroblasts and macrophages e.g. through sustained TGF-β signaling. The result is excessive ECM accumulation, significant collagen crosslinking, and increased tissue stiffness, ultimately leading to scar formation[50]. Notably, in mature pathologic dermal scars, fibroblasts and myofibroblasts are largely absent, leaving behind dense, 'inert' collagen that contributes to scar rigidity.

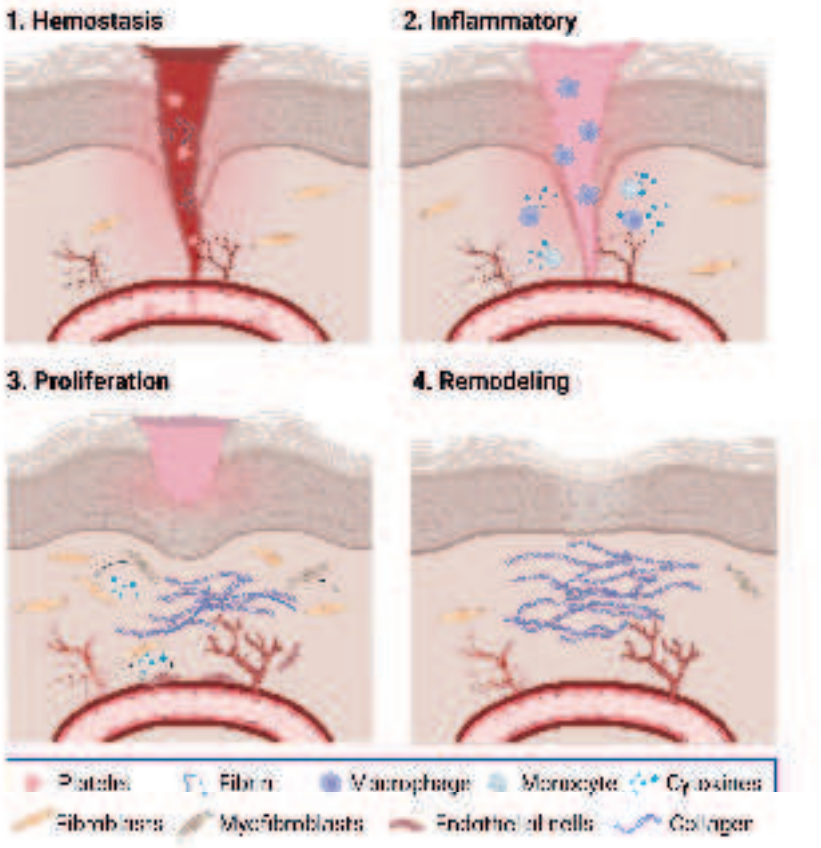

Figure 1. Stages of wound healing. The wound healing process comprises four phases: 1. Hemostasis: Platelets form a clot and establish a fibrin matrix to stop bleeding. 2. Inflammatory: Immune cells, such as macrophages, clear debris and secrete cytokines to initiate repair. 3. Proliferative: Fibroblasts and myofibroblasts deposit ECM while endothelial cells drive angiogenesis. 4. Remodeling: Myofibroblasts contract the wound.

ECM is remodeled and crosslinked to strengthen tissue. Chronic activation can lead to scar formation. ECM: extracellular matrix. Figure created with BioRender.

3.4 ECM remodeling in fibrosis

Not only skin, but other organs such as liver, lungs, heart and kidneys are also prone to develop fibrosis, including excessive ECM accumulation. During fibrosis, affected tissue becomes stiffer and accumulates within the tissue (called interstitial fibrosis) which compromises organ function[51-54]. Increased ECM density physically constrains resident cells and limits nutrient and gas diffusion, compromising cellular metabolism and survival. Additionally, the altered mechanical properties of fibrotic ECM, such as increased stiffness, disrupt normal cell-ECM signaling pathways. This stiff microenvironment hinders cell migration and promotes maladaptive cellular phenotypes, reinforcing a cycle of pathological ECM deposition[55-57].

In pulmonary fibrosis, the destruction of the alveolar wall and abnormal ECM accumulation replace the normal lung structure, impeding expansion and contraction, hindering gas exchange, and leading to respiratory dysfunction[53]. Increased ECM stiffness activates fibroblasts into myofibroblasts while inhibiting epithelial cell proliferation and migration. It also induces epithelial-mesenchymal transition (EMT), further perpetuating fibrosis and compromising lung function[58].

In the kidneys, ECM accumulation disrupts the filtration barrier in glomeruli, altering nephron structure and impeding effective blood filtration. Mechanical changes in the ECM create feedback signals that induce renal cells to further increase ECM production, perpetuating fibrotic scarring and reducing kidney function[59, 60]. Similarly, cardiac fibrosis results from excess ECM deposition that stiffens the myocardium, impairs contractility and compromises cardiac electrical conduction. These changes reduce pumping efficiency, alter electrical signaling, and increase the risk of arrhythmias and development of heart failure[61].

In summary, in each case of organ fibrosis, excessive ECM remodeling hampers essential cellular functions and the altered matrix properties further exacerbate the cycle of fibrosis and tissue dysfunction. Understanding the mechanisms

underlying ECM remodeling is essential for developing therapeutic strategies aimed at restoring normal ECM dynamics in various diseases.

4. The effect of ECM biomechanics on cellular behavior

ECM remodeling and changes in its mechanical properties, particularly increased stiffness, are observed in the formation of dermal scars and fibrosis in various tissues. The increased stiffness of the ECM not only affects the structure of the tissue but also regulates cellular behavior through mechanotransduction. Therefore, studying the biomechanical properties of the ECM and their impact on cells is essential for understanding the role of biomechanics in processes such as fibrosis and tissue repair.

4.1 Viscoelasticity of ECM

Living tissues and ECM exhibit viscoelastic properties, meaning they possess both viscous and elastic characteristics. Purely elastic materials follow Hooke's law, where stress (σ) is directly proportional to strain (ϵ): $\sigma=E\cdot\epsilon$, with E representing the elastic modulus (or stiffness). This linear relationship reflects the material's ability to store and release strain energy efficiently without time-dependent deformation, as observed in materials such as springs and covalently crosslinked polymers. In contrast, viscoelastic materials exhibit a more complex, non-linear stress-strain relationship. This non-linearity arises from molecular rearrangements and time-dependent relaxation mechanisms, particularly under slow mechanical deformation, as seen in materials like jelly and hydrogels (Fig.2).

When subjected to a rapid, mechanical deformation (e.g., within 1 second) followed by maintained constant deformation, viscoelastic materials initially display an elastic response characteristic of purely elastic solids. This immediate reaction is subsequently followed by rearrangement within the material, a hallmark of viscous liquid behavior and breakage and reestablishment of physical bonds between ECM molecules (Fig.2)[62]. Elasticity of the ECM is generally defined by its stiffness, which enables it to return to its original shape after deformation. Viscosity, on the other hand, reflects its capacity to dissipate energy over time under constant deformation, a process known as "stress relaxation." Another aspect of viscosity is "creep," where the ECM undergoes continuous deformation under a constant load. However, in this thesis, we focused on

characterizing ECM viscosity through stress relaxation measurements, which provided insights into its time-dependent mechanical behavior.

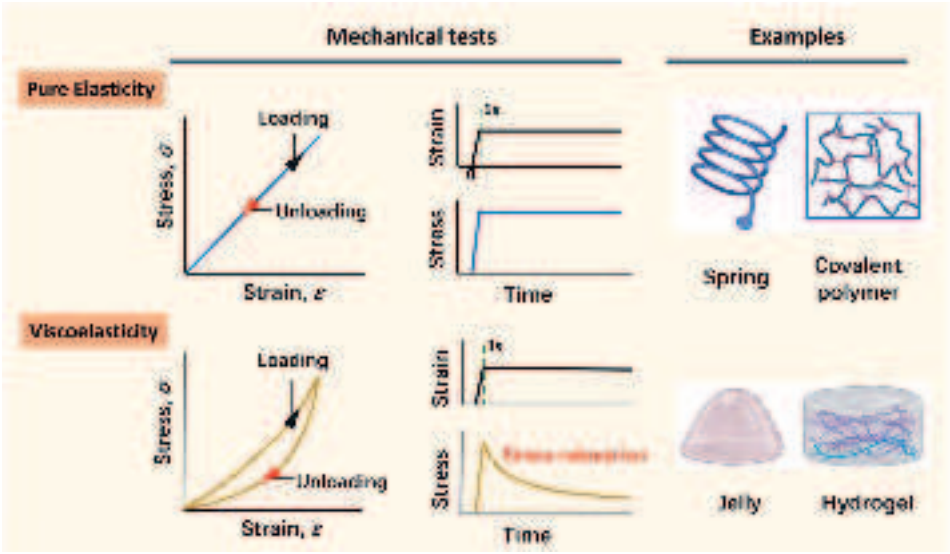

Figure 2. Distinct mechanical responses of purely elastic and viscoelastic materials. Purely elastic materials exhibit a linear stress-strain relationship and fully recover their original shape after deformation without time-dependent effects, as shown in the loading and unloading curves. Viscoelastic materials, however, demonstrate a non-linear stress-strain relationship, with characteristics such as energy dissipation during deformation and stress relaxation under constant strain. Examples of purely elastic materials include springs and covalently crosslinked polymers, while jelly and hydrogels are typical viscoelastic materials. Figure created with BioRender.

The stiffness of the ECM stems from the combined properties of the individual components and their structural organization. Collagen and elastin are the major structural proteins that impart stiffness and strength to the ECM. The hierarchical assembly of collagen fibers enables collagen to resist deformation under mechanical stress. The force-dissipating properties of the ECM involve several mechanisms. Water content and the flow of water within the ECM are major contributors to its viscosity. This viscosity also depends on the mesh size of the ECM structure, which regulates water movement, as well as the speed and extent to which the ECM absorbs and distributes water[63-66]. Another important factor of viscosity is the weak physical cross-linking, such as hydrogen bonds or ionic interactions of non-covalent interactions between collagen fiber networks and the

presence of highly hydrated flexible polysaccharides and other macromolecules tissues. However, the mechanical properties of the ECM are not static. They can be modulated by various physiological and pathological factors, including cellular activity and disease states.

4.2 Changes in viscoelasticity of ECM during fibrosis

Fibrosis is characterized by excessive ECM deposition and crosslinking, leading to significant changes in viscoelastic properties, most notably an increase in ECM stiffness[51, 52, 67, 68]. In dermal scars the stiffness increases up to 20-fold compared to healthy skin dermis[69, 70]. The stiffness of IPF (idiopathic pulmonary fibrosis) tissue is significantly elevated compared to normal lung tissue. In healthy lung tissue, the median stiffness is approximately 1.6 kPa, whereas in IPF tissue, the median stiffness increases to around 16 kPa, with localized stiffness reaching to 50–100 kPa[71, 72]. Comparison of intact and decellularized IPF matrices demonstrated minimal differences in mechanical properties, suggesting that the stiffness changes are predominantly accounted for by alterations in the ECM[72].

Changes in stress relaxation is another important aspect of ECM mechanics during fibrosis, although this aspect is less well-studied compared to stiffness. The accumulation of fibrotic ECM components alters the interaction dynamics between ECM molecules and water, leading to slower stress relaxation. In IPF, for example, while lung stiffness increases, the ability of the ECM to relax stress over time is significantly reduced[73]. Similarly, in ischemic heart failure (HF), the endocardium of the human left ventricle (LV) exhibits slower stress relaxation compared to non-failing tissue. This phenomenon has been associated with increased collagen deposition and elevated α-SMA stress fibers in myofibroblasts[74].

4.3 Mechanotransduction Pathways

Mechanotransduction is the process by which cells sense and relay mechanical stimuli from the ECM or adjacent cells and convert these into intracellular signals. These signals influence cellular behavior, including changes in gene expression, cytoskeletal organization, and cellular phenotype, thus regulating critical processes such as proliferation, migration, differentiation, and survival[23].

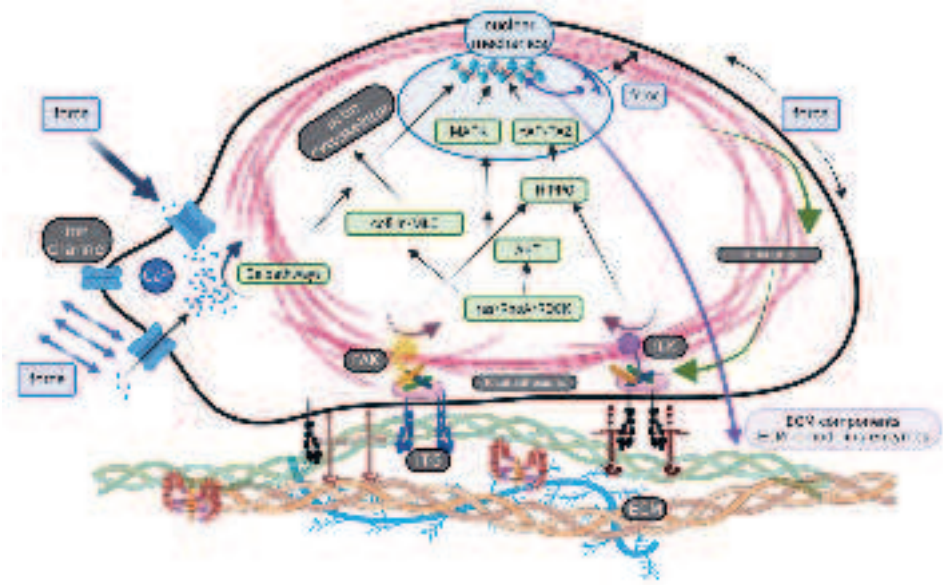

Figure 3. Mechanosensing and mechanosignaling. Cells anchored with integrins (ITG) to the ECM transduce mechanical stimulation (force) in focal adhesions by activation of the protein kinases FAK and ILK. Downstream these activate small GTPases (ras family) and the contractile machinery (cofilin/MLC) or affect the Hippo pathway and cause nuclear translocation of YAP/TAZ. In the nucleus, MAP kinases (MAPK) and mechanoresponsive transcription factors (YAP/TAZ) regulate mechanoresponsive genes. Mechanical distortion of cells may cause ions such as calcium transients that converge into the before-mentioned pathways. Alternatively, this distortion is conveyed via the cytoskeleton (tensegrity) to FAK/ILK stimulation. The actin cytoskeleton, via nesprins and lamins, also directly affects chromatin and with it, mechanoresponsive genes. The results of mechanosignaling vary between ECM remodeling, migration, proliferation, differentiation, and survival. YAP: Yes-associated protein ; TAZ: Transcriptional coactivator with PDZ-binding motif. Figure reproduced with permission from [75].

Key mediators of mechanotransduction include matrix-integrin-cytoskeleton-based interactions, mechanosensitive ion channels, and cell-cell adhesion complexes[23, 76]. **Integrins**, as principal ECM receptors, transmit mechanical signals by indirectly connecting to the cytoskeleton through focal adhesion complexes. This linkage enables cells to sense and respond to ECM properties such as stiffness, topography, and tension. In conjunction with growth factor signaling a main function of integrin-based signaling is suppression of apoptosis. **Mechanosensitive ion channels** respond to mechanical cues like membrane

tension, pressure, and stretch. When activated, these channels physically open to allow the influx of cations such as calcium (Ca^{2+}), sodium (Na^{+}), or potassium (K^{+}). This triggers intracellular signaling cascades that regulate cellular processes such as migration, differentiation, and proliferation. Examples include the Piezo1 and Piezo2 channels, which sense membrane deformation caused by external forces. Similarly, TRPV4 (transient receptor potential vanilloid 4) is another mechanosensitive ion channel that detects ECM stiffness and shear stress, influencing cytoskeletal dynamics and tissue remodeling. **Intercellular junctions**, including tight junctions and adherens junctions, mediate mechanical coupling between cells and facilitate force transmission across tissues. Tight junctions, composed of proteins such as claudins and occludins, maintain epithelial and endothelial barrier integrity while adapting to mechanical stress by modulating their assembly and signaling. Adherens junctions, anchored to the actin cytoskeleton, are formed by homotypically binding cadherins (e.g., E-cadherin) and cytoplasmic catenins. These junctions are critical in processes like epithelial-mesenchymal transition (EMT), which is associated with fibrosis and cancer progression.

Upon sensing mechanical stimuli, the ECM conveys forces to the cytoskeleton, triggering deformation of actin filaments, microtubules, and intermediate filaments. These deformations are converted into biochemical signals through the activation of key pathways such as focal adhesion kinase (FAK)-mediated and integrin-linked kinase focal adhesion signaling, as well as the Wnt, Hippo, and Piezo pathways[77, 78]. Among the diverse mechanotransduction pathways, the Yes-associated protein and Transcriptional coactivator with PDZ-binding motif (YAP/TAZ) and Piezo pathways have emerged as critical regulators in both normal tissue remodeling and pathological conditions like fibrosis, albeit that much of this knowledge was gathered from 2D culture models on tissue culture polystyrene which has a high stiffness.

In the following sections, 4.3.1 YAP/TAZ Pathway and 4.3.2 Piezo Pathway, the introduction primarily focuses on ECM stiffness—i.e., the elastic component of viscoelasticity—in relation to mechanosignaling and its consequences. However, the role of viscosity remains largely unexplored. This is because the primary aim of this thesis is to decouple the elasticity and viscosity of tissue ECM and specifically investigate how changes in ECM stiffness, while maintaining

constant viscosity, regulate cell phenotype and the associated mechanotransduction pathways.

4.3.1 YAP/TAZ pathway

YAP/TAZ are the key transcription factors of the Hippo signaling pathway[79]. YAP/TAZ regulates tissue and organ development, cell migration, tissue regeneration, and homeostasis[80]. In its activated state, the Hippo pathway inactivates both transcription factors through phosphorylation. Both YAP and TAZ are phosphorylated via a kinase cascade involving MST1/2 (Mammalian Sterile 20-like kinase 1/2) and LATS1/2 (Large Tumor Suppressor kinase 1/2). As illustrated in Fig. 4, MST1/2, the mammalian orthologs of the Drosophila Hippo kinase, serve as core components of the Hippo signaling pathway. They interact with SAV1 to form an enzymatically active complex, which phosphorylates and activates LATS1/2 kinases along with their regulatory subunits, MOB1. The activated LATS1/2-MOB1 complex subsequently phosphorylates YAP and TAZ, the key downstream effectors of the Hippo pathway. The degradation of phosphorylated YAP/TAZ is accomplished through its immediate ubiquitination and subsequent proteasomal degradation. Mechanical stimuli such as a high stiffness inactivate the Hippo pathway and render MST and LATS inactive, resulting in unphosphorylated YAP/TAZ. These unphosphorylated transcription factors translocate to the nucleus and bind to the transcriptional coactivator TEA Domain Transcription Factor (TEAD). This activates downstream mechanosensitive genes like collagens as well as genes pertaining to cell proliferation and apoptosis inhibition.

The YAP/TAZ transcription factors are activated in stiffened ECM microenvironments such as in fibrotic tissues[81]. YAP/TAZ signaling promotes pathological activation of fibroblasts and hepatic stellate cells during pulmonary fibrosis and liver fibrosis[82, 83]. Furthermore, YAP/TAZ is activated in fibroblasts during keloid formation, where it contributes to increased collagen production, fibroblast activation, and myofibroblast differentiation. Transcription factors YAP/TAZ also serve as coordinators in ECM matrix synthesis: nuclear YAP/TAZ activates transcription of genes encoding ECM such as collagen upon culturing of fibroblasts on (pathologically) stiff matrices, whereas this activation does not occur on physiologically soft matrices. As mentioned, often studies were done with 2D culture systems, and their translation to 3D systems is yet to be

explored. Interestingly, the behavior of YAP/TAZ signaling in human MSCs shows distinct differences between 2D and 3D cultures: MSCs cultured on stiffer hydrogels show increased spreading and YAP/TAZ nuclear localization, while encapsulation in 3D hydrogels downregulate nuclear YAP/TAZ and spreading[84]. In addition, YAP/TAZ interacts with other signaling pathways, such as Wnt and TGF-β, which are involved in fibrosis. This crosstalk amplifies the fibrotic response[85, 86].

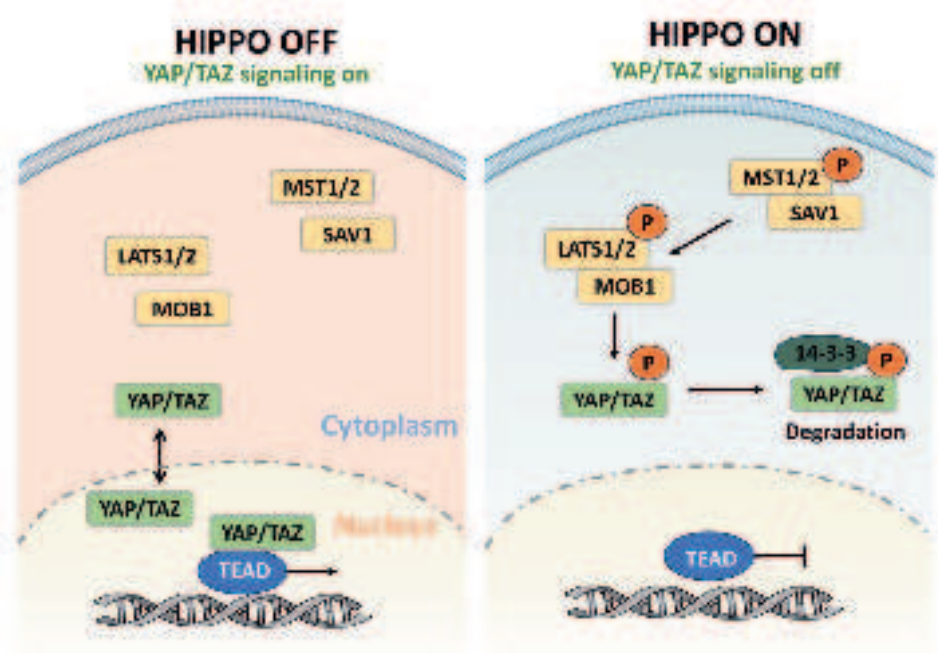

Figure 4. YAP/TAZ and Hippo signaling pathway. When the Hippo signaling pathway is activated, MST1/2 and its scaffold protein SAV1 could phosphorylate LATS1/2 and their regulatory subunits MOB1. Then the activated LATS1/2-MOB1 complex phosphorylates and inactivates YAP/TAZ. Phosphorylated YAP/TAZ associates with 14-3-3 proteins in the cytoplasm, leading to their ubiquitination and eventual degradation (right panel). Conversely, when the Hippo signaling pathway is inhibited, YAP/TAZ translocates to the nucleus to binds to TEAD transcription factors to regulate the expression of downstream genes (left panel). Figure created with BioRender.

4.3.2 Piezo pathway

Mechanically activated ion channels also are yet another type of mechanosensors[87-89]. In 2010, Piezo1 and its close homolog Piezo2 channels were first cloned as a mechanosensitive, non-selective cation channel that facilitates the influx of Ca^{2+} cations but also Na^{+}, K^{+} and Mg^{2+} [90].

The Piezo protein family comprises evolutionarily conserved, large membrane proteins. Piezo1 and Piezo2 share a triskelion-like structure, with three-bladed, propellerlike arms surrounding a central ion-conducting pore capped by an extracellular domain[91]. Mechanical stimuli cause the arms to bend, deforming the cell membrane locally and forming specific protein-lipid interactions. This leads to the formation of a channel that allows cations, such as Ca^{2+} to enter the cytoplasm, which triggers a cascade of downstream signaling pathways that regulate various cellular functions.

Piezo1 is highly expressed in tissues such as the skin, lungs, and bladder, while Piezo2 is predominantly found in sensory neurons[92, 93]. Piezo1 channels can be directly activated by membrane tension and deformation and exhibit voltage-dependent inactivation, indicating intrinsic mechanosensitivity[91, 94]. In contrast, the intrinsic mechanosensitivity of Piezo2 remains unconfirmed[95]. Despite this, both channels share structural and functional similarities, and Piezo2's involvement in mechanotransduction remains an area of growing interest. This discussion, however, will focus primarily on Piezo1.

The expression of PIEZO1 (human) and Piezo1 (mouse) is upregulated in fibrotic skin fibroblasts in both species. Knocking down *Piezo1* in mouse dermal fibroblasts suppresses their fibroproliferative phenotype, even under stiffer conditions. This suggests a role for Piezo1-based mechanosignaling in fibrotic disease. This is supported by mechanical stimulation of Piezo1 causing Wnt2/Wnt11 pathway activation and upregulating secretion of the pro-fibrotic C-C motif chemokine ligand 24 (CCL24). Briefly, Piezo1 activation triggers calcium influx, which indirectly modulates the expression of *Wnt2* and *Wnt11*, linking mechanical signals to Wnt pathway activation (*Piezo1* knockdown downregulated the gene expression of *Wnt2* and *Wnt11*). Overall, the increased matrix stiffness-induced activation along the Piezo1-Wnt2/Wnt11-CCL24 pathway promotes the progression of dermal scarring by enhancing the inflammatory response and pro-fibrotic ECM remodeling[96]. In a mechanically induced osteoarthritis cartilage model, the overexpression of Piezo1 promotes

cartilage matrix degradation by mediating the nuclear translocation of YAP and upregulating the expression of MMP13 and ADAMTS5. Piezo1 activation promotes nuclear translocation of YAP through downregulation of MOB1(Fig. 4)[97, 98]. Piezo channels are also vital for MSCs to sense mechanical stimuli[75]. PIEZO1 expression in human umbilical cord MSCs (UC-MSCs) is positively correlated with substrate stiffness. High stiffness matrices (62-68 kPa, mimicking fibrotic myocardium stiffness) induce high PIEZO1 expression and integrin β1 compared to the soft matrices (13-16 kPa, mimicking healthy heart tissue stiffness)[99]. In conclusion, while Piezo1 activation is crucial for normal mechanotransduction, its increased expression under pathological stiffness conditions contributes to adverse ECM remodeling, fibrosis, and tissue degeneration, and its role in MSC mechanosensing also suggests an environment-dependent function.

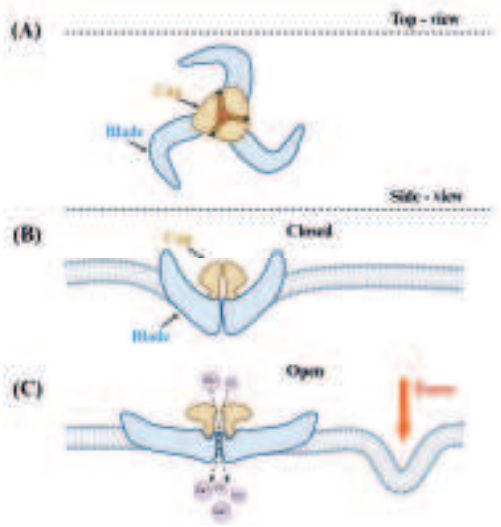

Figure 5. Structural and functional representation of Piezo1/2 channels. Piezo1/2 channels consist of a triskelion-like structure with three curved blades surrounding a central ion-conducting pore capped by an extracellular domain ("Cap"). The top view (Fig.5A) illustrates the triskelion structure, while the side view shows the channel in its closed (Fig.5B) and open states (Fig.5C). Upon mechanical force applied to the membrane, the curved blades bend and deform the surrounding lipid bilayer, inducing specific protein-lipid interactions. This mechanical deformation leads to the opening of the central pore, allowing cations, such as Ca^{2+}, to flow into the cytoplasm and initiate downstream signaling pathways. Figure created with BioRender.

Thus, understanding the ECM mechanics and their changes during fibrosis, as well as the exploration of mechanotransduction pathways involved, provides valuable insights into how cells interpret and respond to their mechanical environment. By targeting these pathways and modulating ECM properties, it may be possible to mitigate fibrosis and restore normal tissue function. This research has broad implications for regenerative medicine and the treatment of fibrotic diseases.

5. Organ-derived ECM hydrogel platform

Various materials are employed to replicate the mechanical properties of the ECM and provide a controlled environment for cellular studies. These materials range from 2D substrates to 3D scaffolds and hydrogels. 2D cell culture models, such as the polymer coatings and hydrogels, are easy to manipulate and provide a consistent environment for cells to explore cell behavior. However, they lack the complex structural, architectural, topographical, and mechanical characteristics of the 3D environment that cells experience *in vivo*, which limits the physiological relevance of the findings[100]. To address these limitations, various 3D hydrogel systems made from synthetic or natural materials have been developed, offering environments that more closely mimic the native conditions of cells in living tissues. Normal tissue can be considered as a hydrogel with embedded cells that offers structural support and participates in cell signaling. In other words, these hydrogels aim to replicate both (bio)mechanical and biochemical signaling components of native ECM.

Commonly used 3D hydrogels are often comprised of single-component natural polymers, such as collagen, methacrylated gelatin, fibrin, and hyaluronic acid, or they may include chemically modified polymers like polyethylene glycol (PEG) that can form hydrogels[101-105]. While chemically produced polymer hydrogels allow for tunable mechanical and chemical properties, they lack the variety of biological moieties present in natural polymers, which contribute to specific cell interactions and signaling. On the other hand, natural polymers, though biologically relevant, typically consist of a single component, which limits the replication of native ECM complexity.

To address the need for more complex ECM components and structures, decellularized tissues have become increasingly popular to replicate native

tissues. These decellularized scaffolds are particularly useful to study ECM-cell interactions in a biologically and clinically relevant context [106-109]. However, due to the limited ability of cells to penetrate and populate the structure of decellularized tissues, cellular interactions often remain confined to the surface. This limitation restricts the scaffolds' utility for studies requiring fully three-dimensional cell invasion and migration. Furthermore, the stiffness of decellularized scaffolds is generally fixed, which reduces their flexibility in studies that require tunable mechanical properties.

The process of preparing decellularized ECM typically involves a combination of chemical methods (using detergents), enzymatic methods (using enzymes like trypsin), and physical methods (such as grinding and freeze-thaw cycles) that disrupt ECM integrity and remove cell components[110]. After completion of the decellularization, the ECM is vacuum-dried and milled into a fine powder. This powder is reconstituted as a hydrogel by dissolving it in diluted hydrochloric acid and partially digesting it with pepsin. Digestion is terminated by neutralizing the pH with NaOH and the solution is adjusted to isotonic values by 10x PBS to generate a pre-gel solution that is storable long term at 4°C. Upon raising the temperature of a pregel to 37°C, an ECM hydrogel forms which retains relevant biochemical and mechanical cues of the corresponding native tissue ECM[111]. Such ECM hydrogels have been widely utilized to model mesenchymal cell interactions, angiogenesis, and other cellular behavior. Introducing covalent crosslinkers, such as Ruthenium ions which are often combined with visible light activation (Ruthenium (II) complexes with sodium persulfate) or enzymatic crosslinkers like transglutaminase, allows the stiffness to be modified[112, 113]. This adjustment provides an invaluable model to explore the role of matrix stiffness in cellular plasticity, phenotype, and function. Furthermore, the specific tissue-derived ECM hydrogels with tunable stiffness allow for studying disease processes and developing regenerative therapies. For example, by mimicking the biomechanical environment of fibrotic tissues, ECM hydrogels can be used to examine cell responses and associated mechanotransduction pathways. Embedding MSCs derived from umbilical cord or adipose tissue in scar-mimicking ECM hydrogels is but one specific example of how these hydrogels can provide insights into the role of stem cells in scar remodeling and repair.

6. Research aims and outline of this thesis

Despite significant progress in understanding the role of the ECM in regulating cellular behavior, substantial knowledge gaps remain. Too little is known about the influence of biochemical and biomechanical properties on (fibrotic) disease progression and tissue regeneration. Current 2D and even some 3D culture models fail to fully replicate the complex in vivo environment, limiting the physiological relevance and translatability of experimental outcomes. Organ-derived ECM hydrogels provide a promising solution, as they offer a more accurate simulation of native tissue environments by preserving both the biochemical complexity and the mechanical characteristics of the ECM.

However, a key limitation in existing research is the inability to separate the influence of biochemical and biomechanical properties of the ECM while maintaining its native composition. This flexibility is crucial for a deeper understanding of how mechanical signals specifically influences cellular responses. By leveraging organ-derived ECM hydrogels, this thesis aims to address this gap by regulating the mechanics of ECM hydrogels and exploring the dynamic interplay between ECM's mechanical properties and cell behavior.

Specifically, the research goals are to, firstly investigate how variations in biochemical and mechanical properties of ECM derived from different tissues affect cellular phenotype, focusing on processes such as vascularization, fibrosis, and matrix remodeling (Chapters 3, 4). And secondly to develop a versatile platform that allows for precise control over the mechanical properties of ECM hydrogels, facilitating the decoupling of biochemical and mechanical cues (Chapters 5, 6, 7). Finally, and thirdly, to use the developed platform to better understand how changes in ECM mechanics influence cell-ECM interactions, particularly in the context of disease mechanisms such as fibrosis and explore potential therapeutic strategies. (Chapters 6, 7)

Scope of the thesis:

In Chapter 1, we introduce the topic and background of this thesis.

In Chapter 2, we discuss the development and application of organ-derived ECM hydrogels, emphasizing their role in studying the biomechanical and biochemical impacts on cells and developing therapeutic strategies.

In Chapter 3, we investigate how ECM from specific tissues influences *in vitro* vascular network formation (VNF) by endothelial cells (ECs). We compare VNF and ECM remodeling in hydrogels derived from skin, lung, and their combination (hybrid), using microvascular ECs. We assess the remodeling of ECM over time measured as changes in viscoelasticity, fiber diameter, pore area, and fiber distribution. Principal Component Analysis (PCA) was used to gauge the influence of hydrogel mechanical properties and biochemical components on VNF.

In Chapter 4, we examine how fibroblasts modify the physical properties of skin-derived ECM hydrogels to enhance the angiogenesis of co-cultured ECs *in vitro*. We focus on how fibroblasts would remodel ECM through the aspects of altering ECM's fiber structure, density, and arrangement, regulating hydrogel stiffness and viscosity and promoting the expression of proteins associated with VNF.

In Chapter 5, we modulate the mechanical properties of lung-derived ECM hydrogels by artificially introducing fiber crosslinking induced by ruthenium to mimic the lung fibrosis tissue. We hypothesized that applying additional fiber crosslinking would result in increased stiffness, and in turn, would trigger cellular changes that are also observed during the fibrosis process. We test the mechanics and fiber organization changes after crosslinking and examine cellular responses concerning fibroblast activation.

In Chapter 6, we introduce the Ruthenium-induced ECM crosslinking technology in Chapter 5 into the skin ECM hydrogel, establishing a Ruthenium-ECM stiffness gradient hydrogel that models the physiology of the scarred skin. This chapter delves into the effects of stiffness gradients in skin-derived ECM hydrogels on 3D cultured fibroblast behavior. It describes how varying stiffness within the hydrogel can direct fibroblast alignment and remodeling activities, offering insights into tissue development and regeneration processes.

In Chapter 7, we embed umbilical cord stem cells (UC-MSCs) into skin-derived dECM hydrogel with different stiffnesses which mimics normal skin and scar tissue to explore the function of ECM remodeling from UC-MSCs. We assess the stiffness influences on cell viability, morphology, and matrix remodeling by cells. The mechanotransduction pathways involved in mediating UC-MSCs' responses to changed stiffness are also explored.

In Chapter 8, the findings of this thesis are synthesized, discussed and compared with existing literature to provide a comprehensive understanding of the role of ECM in regulating cellular behavior. We highlight organ-derived ECM hydrogels as a powerful model for studying mechanical cues while also addressing areas that require further optimization. Additionally, this chapter connects the findings & insights gained from cell-ECM interplay within the 3D ECM hydrogel model to tissue regeneration and disease progression. Furthermore, we explore how to diverse fibrosis by tuning ECM mechanics and provide the potential therapeutic strategies.

References:

1 Karamanos, N. K. *et al.* A guide to the composition and functions of the extracellular matrix. *FEBS J* 288, 6850-6912, doi:10.1111/febs.15776 (2021).

2 Frantz, C., Stewart, K. M. & Weaver, V. M. The extracellular matrix at a glance. *J Cell Sci* 123, 4195-4200, doi:10.1242/jcs.023820 (2010).

3 Theocharis, A. D., Skandalis, S. S., Gialeli, C. & Karamanos, N. K. Extracellular matrix structure. *Adv Drug Deliv Rev* 97, 4-27, doi:10.1016/j.addr.2015.11.001 (2016).

4 Shoulders, M. D. & Raines, R. T. Collagen structure and stability. *Annu Rev Biochem* 78, 929-958, doi:10.1146/annurev.biochem.77.032207.120833 (2009).

5 Iozzo, R. V. & Schaefer, L. Proteoglycan form and function: A comprehensive nomenclature of proteoglycans. *Matrix Biol* 42, 11-55, doi:10.1016/j.matbio.2015.02.003 (2015).

6 Chrzanowski, P. K., P.S. Cerreta,J. Mandl,I. Turino,G.M. . Elastin content of normal and emphysematous lung parenchym. *The American Journal of Medicine* 69, 351-369, doi:10.1016/0002-9343(80)90004-2 (1990).

7 Baumann, L. *et al.* Clinical relevance of elastin in the structure and function of skin. *Aesthet Surg J Open Forum* 3, ojab019, doi:10.1093/asjof/ojab019 (2021).

8 Pasquali-Ronchetti, I. B.-C., M. Elastic fiber during development and aging. *Microscopy Research and Technique* 38, 428-435, doi:10.1002/(sici)1097-0029(19970815)38:4<428::Aid-jemt10>3.0.Co;2-l (1997).

9 Uitto, J., Li, Q. & Urban, Z. The complexity of elastic fibre biogenesis in the skin--a perspective to the clinical heterogeneity of cutis laxa. *Exp Dermatol* 22, 88-92, doi:10.1111/exd.12025 (2013).

10 Zhang, M. *et al.* Physical properties and biochemical composition of extracellular matrix-derived hydrogels dictate vascularization potential in an organ-dependent fashion. *ACS Appl Mater Interfaces* 16, 29930-29945, doi:10.1021/acsami.4c05864 (2024).

11 Barczyk, M. C., S. Gullberg, D. Integrins. *Cell Tissue Res* 339, 269-280, doi:10.1007/s00441-009-0834-6 (2010).

12 Hynes, R. O. Integrins: a family of cell surface receptors. *Cell* 48, 549-554, doi:10.1016/0092-8674(87)90233-9 (1987).

13 Hansen, U. Analysis of collagen-binding integrin interactions with supramolecular aggregates of the extracellular matrix. *Methods in molecular biology (Clifton, N.J.)* 1944, 157-166, doi:10.1007/978-1-4939-9095-5_12 (2019).

14 Kanchanawong, P. & Calderwood, D. A. Organization, dynamics and mechanoregulation of integrin-mediated cell-ECM adhesions. *Nat Rev Mol Cell Biol* 24, 142-161, doi:10.1038/s41580-022-00531-5 (2023).

15 Davis, G. E. & Senger, D. R. Endothelial extracellular matrix: biosynthesis, remodeling, and functions during vascular morphogenesis and neovessel

stabilization. *Circ Res* 97, 1093-1107, doi:10.1161/01.RES.0000191547.64391.e3 (2005).

16 Leask, A. & Abraham, D. J. TGF-beta signaling and the fibrotic response. *FASEB J* 18, 816-827, doi:10.1096/fj.03-1273rev (2004).

17 Shibuya, M. Vascular endothelial growth factor (VEGF) and its receptor (VEGFR) signaling in angiogenesis: A crucial target for anti- and pro-angiogenic therapies. *Genes Cancer* 2, 1097-1105, doi:10.1177/1947601911423031 (2011).

18 Ramirez-San Juan, G. R. O., P. W. Gardel, M. L. Contact guidance requires spatial control of leading-edge protrusion. *Mol Biol Cell* 28, 1043-1053, doi:10.1091/mbc.E16-11-0769 (2017).

19 A.J. Engler, H. L. S., D.E. Discher, J.E. Schwarzbauer. Extracellular matrix elasticity directs stem cell differentiation. *J Musculoskelet Neuronal Interact* 7, 4, doi:10.1016/j.cell.2006.06.044 (2007).

20 D'Urso, M. & Kurniawan, N. A. Mechanical and Physical Regulation of Fibroblast-Myofibroblast Transition: From Cellular Mechanoresponse to Tissue Pathology. *Front Bioeng Biotechnol* 8, 609653, doi:10.3389/fbioe.2020.609653 (2020).

21 Fischer, R. S. *et al.* Contractility, focal adhesion orientation, and stress fiber orientation drive cancer cell polarity and migration along wavy ECM substrates. *Proc Natl Acad Sci U S A* 118, doi:10.1073/pnas.2021135118 (2021).

22 Rozario, T. & DeSimone, D. W. The extracellular matrix in development and morphogenesis: a dynamic view. *Dev Biol* 341, 126-140, doi:10.1016/j.ydbio.2009.10.026 (2010).

23 Humphrey, J. D., Dufresne, E. R. & Schwartz, M. A. Mechanotransduction and extracellular matrix homeostasis. *Nat Rev Mol Cell Biol* 15, 802-812, doi:10.1038/nrm3896 (2014).

24 Tracy, L. E., Minasian, R. A. & Caterson, E. J. Extracellular matrix and dermal fibroblast function in the healing wound. *Adv Wound Care (New Rochelle)* 5, 119-136, doi:10.1089/wound.2014.0561 (2016).

25 Nelson, P. R. Y., S. Kent, K.C. Platelet-derived growth factor and extracellular matrix proteins provide a synergistic stimulus for human vascular smooth muscle cell migration. *JOURNAL OF VASCULAR SURGERY* 26, 12, doi:10.1016/s0741-5214(97)70153-8 (1997).

26 Solon, J., Levental, I., Sengupta, K., Georges, P. C. & Janmey, P. A. Fibroblast adaptation and stiffness matching to soft elastic substrates. *Biophys J* 93, 4453-4461, doi:10.1529/biophysj.106.101386 (2007).

27 Engler, A. J., Sen, S., Sweeney, H. L. & Discher, D. E. Matrix elasticity directs stem cell lineage specification. *Cell* 126, 677-689, doi:10.1016/j.cell.2006.06.044 (2006).

28 Nho, R. S., Ballinger, M. N., Rojas, M. M., Ghadiali, S. N. & Horowitz, J. C. Biomechanical force and cellular stiffness in lung fibrosis. *Am J Pathol* 192, 750-761, doi:10.1016/j.ajpath.2022.02.001 (2022).

29 Wagenseil, J. E. & Mecham, R. P. Vascular extracellular matrix and arterial mechanics. *Physiol Rev* 89, 957-989, doi:10.1152/physrev.00041.2008 (2009).

30 Lu, P., Takai, K., Weaver, V. M. & Werb, Z. Extracellular matrix degradation and remodeling in development and disease. *Cold Spring Harb Perspect Biol* 3, doi:10.1101/cshperspect.a005058 (2011).

31 de Almeida, L. G. N. T., H. Eslambolchi, Y. Chopra, S. Young, D. Gill, S. Devel, L. Dufour, A. Matrix metalloproteinases: from molecular mechanisms to physiology, pathophysiology, and pharmacology. *Pharmacol Rev* 74, 712-768, doi:10.1124/pharmrev.121.000349 (2022).

32 Zhao, P., Sun, T., Lyu, C., Liang, K. & Du, Y. Cell mediated ECM-degradation as an emerging tool for anti-fibrotic strategy. *Cell Regen* 12, 29, doi:10.1186/s13619-023-00172-9 (2023).

33 Nagase, H., Visse, R. & Murphy, G. Structure and function of matrix metalloproteinases and TIMPs. *Cardiovasc Res* 69, 562-573, doi:10.1016/j.cardiores.2005.12.002 (2006).

34 Fan, D. & Kassiri, Z. Biology of tissue inhibitor of metalloproteinase 3 (TIMP3), and its therapeutic implications in cardiovascular pathology. *Front Physiol* 11, 661, doi:10.3389/fphys.2020.00661 (2020).

35 Edwards, D. R., Handsley, M. M. & Pennington, C. J. The ADAM metalloproteinases. *Mol Aspects Med* 29, 258-289, doi:10.1016/j.mam.2008.08.001 (2008).

36 Bonnans, C., Chou, J. & Werb, Z. Remodelling the extracellular matrix in development and disease. *Nat Rev Mol Cell Biol* 15, 786-801, doi:10.1038/nrm3904 (2014).

37 van Hinsbergh, V. W. & Koolwijk, P. Endothelial sprouting and angiogenesis: matrix metalloproteinases in the lead. *Cardiovasc Res* 78, 203-212, doi:10.1093/cvr/cvm102 (2008).

38 Wynn, T. A. & Ramalingam, T. R. Mechanisms of fibrosis: therapeutic translation for fibrotic disease. *Nat Med* 18, 1028-1040, doi:10.1038/nm.2807 (2012).

39 Hinz, B. Formation and function of the myofibroblast during tissue repair. *J Invest Dermatol* 127, 526-537, doi:10.1038/sj.jid.5700613 (2007).

40 Lindner, D. *et al.* Differential expression of matrix metalloproteases in human fibroblasts with different origins. *Biochem Res Int* 2012, 875742, doi:10.1155/2012/875742 (2012).

41 Ernst, S., Langer, R., Cooney, C. L. & Sasisekharan, R. Enzymatic degradation of glycosaminogIycans. *Critical Reviews in Biochemistry and Molecular Biology* 30, 387-444, doi:10.3109/10409239509083490 (1995).

42 Sorg, H., Tilkorn, D. J., Hager, S., Hauser, J. & Mirastschijski, U. Skin wound healing: An update on the current knowledge and concepts. *Eur Surg Res* 58, 81-94, doi:10.1159/000454919 (2017).

43 Spielman, A. F. *et al.* Beyond the scar: A basic science review of wound remodeling. *Adv Wound Care (New Rochelle)* 12, 57-67, doi:10.1089/wound.2022.0049 (2023).

44 Broughton, G. I., Janis, J. E. & Attinger, C. E. The basic science of wound healing. 117, 12S-34S, doi:10.1097/01.prs.0000225430.42531.c2 (2006).

45 Li, B. & Wang, J. H. Fibroblasts and myofibroblasts in wound healing: force generation and measurement. *J Tissue Viability* 20, 108-120, doi:10.1016/j.jtv.2009.11.004 (2011).

46 Demidova-Rice, T. N., Durham, J. T. & Herman, I. M. Wound healing angiogenesis: innovations and challenges in acute and chronic wound healing. *Adv Wound Care (New Rochelle)* 1, 17-22, doi:10.1089/wound.2011.0308 (2012).

47 Sorokin, L. The impact of the extracellular matrix on inflammation. *Nat Rev Immunol* 10, 712-723, doi:10.1038/nri2852 (2010).

48 Wynn, T. A. & Vannella, K. M. Macrophages in tissue repair, regeneration, and fibrosis. *Immunity* 44, 450-462, doi:10.1016/j.immuni.2016.02.015 (2016).

49 Janson, D. G., Saintigny, G., van Adrichem, A., Mahe, C. & El Ghalbzouri, A. Different gene expression patterns in human papillary and reticular fibroblasts. *J Invest Dermatol* 132, 2565-2572, doi:10.1038/jid.2012.192 (2012).

50 Rippa, A. L., Kalabusheva, E. P. & Vorotelyak, E. A. Regeneration of dermis: scarring and cells involved. *Cells* 8, doi:10.3390/cells8060607 (2019).

51 Graham, C. S., P. in *Cardiovascular Signaling in Health and Disease* (ed N. L. Hund Parinandi, T. J.) 287-321 (2022).

52 Rayego-Mateos, S. *et al.* Interplay between extracellular matrix components and cellular and molecular mechanisms in kidney fibrosis. *Clin Sci (Lond)* 135, 1999-2029, doi:10.1042/CS20201016 (2021).

53 Richeldi, L., Collard, H. R. & Jones, M. G. Idiopathic pulmonary fibrosis. *Lancet* 389, 1941-1952, doi:10.1016/S0140-6736(17)30866-8 (2017).

54 Kisseleva, T. & Brenner, D. Molecular and cellular mechanisms of liver fibrosis and its regression. *Nat Rev Gastroenterol Hepatol* 18, 151-166, doi:10.1038/s41575-020-00372-7 (2021).

55 Yeung, T. *et al.* Effects of substrate stiffness on cell morphology, cytoskeletal structure, and adhesion. *Cell Motil Cytoskeleton* 60, 24-34, doi:10.1002/cm.20041 (2005).

56 Jagiello, A., Castillo, U. & Botvinick, E. Cell mediated remodeling of stiffness matched collagen and fibrin scaffolds. *Sci Rep* 12, 11736, doi:10.1038/s41598-022-14953-w (2022).

57 Wahlsten, A. *et al.* Mechanical stimulation induces rapid fibroblast proliferation and accelerates the early maturation of human skin substitutes. *Biomaterials* 273, 120779, doi:10.1016/j.biomaterials.2021.120779 (2021).

58 Kalluri, R. & Weinberg, R. A. The basics of epithelial-mesenchymal transition. *J Clin Invest* 119, 1420-1428, doi:10.1172/JCI39104 (2009).

59 Duffield, J. S. Cellular and molecular mechanisms in kidney fibrosis. *J Clin Invest* 124, 2299-2306, doi:10.1172/JCI72267 (2014).

60 Liu, Y. Cellular and molecular mechanisms of renal fibrosis. *Nat Rev Nephrol* 7, 684-696, doi:10.1038/nrneph.2011.149 (2011).

61 Weber, K. T., Sun, Y., Bhattacharya, S. K., Ahokas, R. A. & Gerling, I. C. Myofibroblast-mediated mechanisms of pathological remodelling of the heart. *Nat Rev Cardiol* 10, 15-26, doi:10.1038/nrcardio.2012.158 (2013).

62 Chaudhuri, O., Cooper-White, J., Janmey, P. A., Mooney, D. J. & Shenoy, V. B. Effects of extracellular matrix viscoelasticity on cellular behaviour. *Nature* 584, 535-546, doi:10.1038/s41586-020-2612-2 (2020).

63 Dzobo, K. & Dandara, C. The extracellular matrix: Its composition, function, remodeling, and role in tumorigenesis. *Biomimetics (Basel)* 8, doi:10.3390/biomimetics8020146 (2023).

64 Nam, S., Hu, K. H., Butte, M. J. & Chaudhuri, O. Strain-enhanced stress relaxation impacts nonlinear elasticity in collagen gels. *Proc Natl Acad Sci U S A* 113, 5492-5497, doi:10.1073/pnas.1523906113 (2016).

65 Connizzo, B. K. & Grodzinsky, A. J. Multiscale poroviscoelastic compressive properties of mouse supraspinatus tendons are altered in young and aged mice. *J Biomech Eng* 140, 0510021-0510028, doi:10.1115/1.4038745 (2018).

66 Sauer, F. *et al.* Collagen networks determine viscoelastic properties of connective tissues yet do not hinder diffusion of the aqueous solvent. *Soft Matter* 15, 3055-3064, doi:10.1039/c8sm02264j (2019).

67 Mueller, S. *et al.* Increased liver stiffness in alcoholic liver disease: differentiating fibrosis from steatohepatitis. *World J Gastroenterol* 16, 966-972, doi:10.3748/wjg.v16.i8.966 (2010).

68 Burgess, J. K. & Harmsen, M. C. Chronic lung diseases: entangled in extracellular matrix. *Eur Respir Rev* 31, doi:10.1183/16000617.0202-2021 (2022).

69 Huang, C. *et al.* Keloid progression: a stiffness gap hypothesis. *Int Wound J* 14, 764-771, doi:10.1111/iwj.12693 (2017).

70 J. A. Clark, J. C. Y. C., K. S. Leung. Mechanical properties of normal skin and hypertrophic scars. *Burns* 22, 443-446, doi:10.1016/0305-4179(96)00038-1 (1996).

71 Liu, F. *et al.* Mechanosignaling through YAP and TAZ drives fibroblast activation and fibrosis. *Am J Physiol Lung Cell Mol Physiol* 308, L344-357, doi:10.1152/ajplung.00300.2014 (2015).

72 Booth, A. J. *et al.* Acellular normal and fibrotic human lung matrices as a culture system for in vitro investigation. *Am J Respir Crit Care Med* 186, 866-876, doi:10.1164/rccm.201204-0754OC (2012).

73 de Hilster, R. H. J. *et al.* Human lung extracellular matrix hydrogels resemble the stiffness and viscoelasticity of native lung tissue. *Am J Physiol Lung Cell Mol Physiol* 318, L698-L704, doi:10.1152/ajplung.00451.2019 (2020).

74 Gionet-Gonzales, M. *et al.* Stress relaxation rates of myocardium from failing and non-failing hearts. doi:10.1101/2024.07.24.604845 (2024).

75 Harmsen, M. C. *et al.* in *Handbook of the extracellular matrix* Ch. Chapter 43-1, 1-27 (2023).

76 Saraswathibhatla, A., Indana, D. & Chaudhuri, O. Cell-extracellular matrix mechanotransduction in 3D. *Nat Rev Mol Cell Biol* 24, 495-516, doi:10.1038/s41580-023-00583-1 (2023).

77 Sun, Z., Guo, S. S. & Fassler, R. Integrin-mediated mechanotransduction. *J Cell Biol* 215, 445-456, doi:10.1083/jcb.201609037 (2016).

78 Owsianik, B. N. G. The transient receptor potential family of ion channels. *Genome Biology* 12, doi:10.1186/gb-2011-12-3-218 (2011).

79 Kaan, H. Y. K., Sim, A. Y. L., Tan, S. K. J., Verma, C. & Song, H. Targeting YAP/TAZ-TEAD protein-protein interactions using fragment-based and computational modeling approaches. *PLoS One* 12, e0178381, doi:10.1371/journal.pone.0178381 (2017).

80 Koo, J. H. & Guan, K. L. Interplay between YAP/TAZ and Metabolism. *Cell Metab* 28, 196-206, doi:10.1016/j.cmet.2018.07.010 (2018).

81 Yeh, C. F., Chou, C. & Yang, K. C. Mechanotransduction in fibrosis: Mechanisms and treatment targets. *Curr Top Membr* 87, 279-314, doi:10.1016/bs.ctm.2021.07.004 (2021).

82 Chu, C. Q. & Quan, T. Fibroblast Yap/Taz signaling in extracellular matrix homeostasis and tissue fibrosis. *J Clin Med* 13, doi:10.3390/jcm13123358 (2024).

83 Noguchi, S., Saito, A. & Nagase, T. YAP/TAZ signaling as a molecular link between fibrosis and cancer. *Int J Mol Sci* 19, doi:10.3390/ijms19113674 (2018).

84 Caliari, S. R., Vega, S. L., Kwon, M., Soulas, E. M. & Burdick, J. A. Dimensionality and spreading influence MSC YAP/TAZ signaling in hydrogel environments. *Biomaterials* 103, 314-323, doi:10.1016/j.biomaterials.2016.06.061 (2016).

85 Piersma, B., Bank, R. A. & Boersema, M. Signaling in fibrosis: TGF-beta, WNT, and YAP/TAZ converge. *Front Med (Lausanne)* 2, 59, doi:10.3389/fmed.2015.00059 (2015).

86 Papavassiliou, K. A. *et al.* YAP/TAZ signaling in the pathobiology of pulmonary fibrosis. *Cells* 13, doi:10.3390/cells13181519 (2024).

87 Ranade, S. S., Syeda, R. & Patapoutian, A. Mechanically activated ion channels. *Neuron* 87, 1162-1179, doi:10.1016/j.neuron.2015.08.032 (2015).

88 Martinac, B. & Poole, K. Mechanically activated ion channels. *Int J Biochem Cell Biol* 97, 104-107, doi:10.1016/j.biocel.2018.02.011 (2018).

89 Kefauver, J. M., Ward, A. B. & Patapoutian, A. Discoveries in structure and physiology of mechanically activated ion channels. *Nature* 587, 567-576, doi:10.1038/s41586-020-2933-1 (2020).

90 Tadge, T. *et al.* The role of Piezo1 and Piezo2 proteins in tissue engineering: A Comprehensive review. *Engineered Regeneration* 5, 170-185, doi:10.1016/j.engreg.2024.03.001 (2024).

91 Syeda, R. *et al.* Piezo1 channels are inherently mechanosensitive. *Cell Rep* 17, 1739-1746, doi:10.1016/j.celrep.2016.10.033 (2016).

92 Douguet, D. & Honore, E. Mammalian mechanoelectrical transduction: structure and function of force-gated ion channels. *Cell* 179, 340-354, doi:10.1016/j.cell.2019.08.049 (2019).

93 Gottlieb, P. A. A tour de force: the siscovery, properties, and function of Piezo channels. *Curr Top Membr* 79, 1-36, doi:10.1016/bs.ctm.2016.11.007 (2017).

94 Cox, C. D. *et al.* Removal of the mechanoprotective influence of the cytoskeleton reveals PIEZO1 is gated by bilayer tension. *Nat Commun* 7, 10366, doi:10.1038/ncomms10366 (2016).

95 Szczot, M., Nickolls, A. R., Lam, R. M. & Chesler, A. T. The form and function of PIEZO2. *Annu Rev Biochem* 90, 507-534, doi:10.1146/annurev-biochem-081720-023244 (2021).

96 He, J., Cheng, X., Fang, B., Shan, S. & Li, Q. Mechanical stiffness promotes skin fibrosis via Piezo1-Wnt2/Wnt11-CCL24 positive feedback loop. *Cell Death Dis* 15, 84, doi:10.1038/s41419-024-06466-3 (2024).

97 Feng, X. *et al.* Piezo1 mediates the degradation of cartilage extracellular matrix in malocclusion-induced TMJOA. *Oral Dis* 30, 2425-2438, doi:10.1111/odi.14615 (2024).

98 Ma, S., Meng, Z., Chen, R. & Guan, K. L. The Hippo Pathway: Biology and Pathophysiology. *Annu Rev Biochem* 88, 577-604, doi:10.1146/annurev-biochem-013118-111829 (2019).

99 Pei, F. *et al.* The functions of mechanosensitive ion channels in tooth and bone tissues. *Cell Signal* 78, 109877, doi:10.1016/j.cellsig.2020.109877 (2021).

100 Sun, Y. L., Jingwei Xu,Ziran Lin,Xiaoxuan Zhang,Xiaoling Li,Lisha Li,Yulin Matrix stiffness regulates myocardial differentiation of human umbilical cord mesenchymal stem cells. *Aging* 13, doi:10.18632/aging.202244 (2021).

101 Baker, B. M. & Chen, C. S. Deconstructing the third dimension: how 3D culture microenvironments alter cellular cues. *J Cell Sci* 125, 3015-3024, doi:10.1242/jcs.079509 (2012).

102 Ishihara, S., Kurosawa, H. & Haga, H. Stiffness modulation of collagen gels by genipin-crosslinking for cell culture. *Gels* 9, doi:10.3390/gels9020148 (2023).

103 Ren, Y. *et al.* Hyaluronic acid hydrogel with adjustable stiffness for mesenchymal stem cell 3D culture via related molecular mechanisms to maintain stemness and induce cartilage differentiation. *ACS Appl Bio Mater* 4, 2601-2613, doi:10.1021/acsabm.0c01591 (2021).

104 Shariatinia, Z. & Jalali, A. M. Chitosan-based hydrogels: Preparation, properties and applications. *Int J Biol Macromol* 115, 194-220, doi:10.1016/j.ijbiomac.2018.04.034 (2018).

105 Liu, Y., Mao, J., Guo, Z., Hu, Y. & Wang, S. Polyvinyl alcohol/carboxymethyl chitosan hydrogel loaded with silver nanoparticles exhibited antibacterial and self-healing properties. *Int J Biol Macromol* 220, 211-222, doi:10.1016/j.ijbiomac.2022.08.061 (2022).

106 Liang, Y., Shen, Y., Sun, X. & Liang, H. Preparation of stretchable and self-healable dual ionically cross-linked hydrogel based on chitosan/polyacrylic acid with anti-freezing property for multi-model flexible sensing and detection. *Int J Biol Macromol* 193, 629-637, doi:10.1016/j.ijbiomac.2021.10.060 (2021).

107 Wainwright, J. M. C., C.A. Patel, U.B. Freytes, D.O. Tobita, K. Gilbert, T.W. Badylak,S.F. . Preparation of Cardiac Extracellular Matrix from an Intact Porcine Heart. *TISSUE ENGINEERING: Part C* 16, doi:10.1089/ten.TEC.2009.0392 (2010).

108 Ott, H. C. *et al.* Perfusion-decellularized matrix: using nature's platform to engineer a bioartificial heart. *Nat Med* 14, 213-221, doi:10.1038/nm1684 (2008).

109 Uygun, B. E. *et al.* Organ reengineering through development of a transplantable recellularized liver graft using decellularized liver matrix. *Nat Med* 16, 814-820, doi:10.1038/nm.2170 (2010).

110 Crapo, P. M., Gilbert, T. W. & Badylak, S. F. An overview of tissue and whole organ decellularization processes. *Biomaterials* 32, 3233-3243, doi:10.1016/j.biomaterials.2011.01.057 (2011).

111 Gilbert, T. W., Sellaro, T. L. & Badylak, S. F. Decellularization of tissues and organs. *Biomaterials* 27, 3675-3683, doi:10.1016/j.biomaterials.2006.02.014 (2006).

112 Getova, V. E., van Dongen, J. A., Brouwer, L. A. & Harmsen, M. C. Adipose tissue-derived ECM hydrogels and their use as 3D culture scaffold. *Artif Cells Nanomed Biotechnol* 47, 1693-1701, doi:10.1080/21691401.2019.1608215 (2019).

113 Nizamoglu, M. *et al.* An in vitro model of fibrosis using crosslinked native extracellular matrix-derived hydrogels to modulate biomechanics without changing composition. *Acta Biomater* 147, 50-62, doi:10.1016/j.actbio.2022.05.031 (2022).

114 Zhao, F. *et al.* Fibroblast alignment and matrix remodeling induced by a stiffness gradient in a skin-derived extracellular matrix hydrogel. *Acta Biomater* 182, 67-80, doi:10.1016/j.actbio.2024.05.018 (2024).

Chapter 2

Organ-derived extracellular matrix (ECM) hydrogels: versatile systems to investigate the impact of biomechanics and biochemistry on cells in disease pathology

Martin C. Harmsen[1,2,3 *], Vasilena Getova[1,2], Meng Zhang[1,2], **Fenghua Zhao[1,2],** Joris van Dongen[4], Francisco D. Martinez Garcia[1,2], Mehmet Nizamoglu[1,3] and Janette K. Burgess[1,2,3]

1 University of Groningen, University Medical Center Groningen, Department of Pathology and Medical Biology, 9713 GZ Groningen, the Netherlands

2 W.J. Kolff Research Institute, University Medical Center Groningen, University of Groningen, 9713 AV Groningen, the Netherlands

3 Groningen Research Institute for Asthma and COPD (GRIAC), University Medical Center

Groningen, University of Groningen, 9713 GZ Groningen, the Netherlands

4 University of Utrecht, University Medical Center Utrecht, Department of Plastic Surgery, Utrecht, the Netherlands

Springer Nature Switzerland AG 2023, Handbook of the Extracellular Matrix

https://doi.org/10.1007/978-3-030-92090-6_43-1

Chapter 2

Abstract: The extracellular matrix (ECM) provides instructive and constructive support to cells in all organs. The ECM's composition and structure is organ-dependent. The adhesion of cells to ECM with e.g. integrins triggers cellular mechanosignaling. The role of mechanical properties of ECM hydrogels *in vivo* remains scarce. To replicate the ECM-cell interactions requires organ and tissue-specific ECM hydrogels. Such 3D culture systems allow the monitoring of ECM dynamics i.e. turnover and mechanical changes (stiffness and stress relaxation). Compression testing allows to determine stiffness and stress relaxation. Hydrogels' stress relaxation is governed by displacement of water, large macromolecules and cells in a time- and organ origin-dependent fashion. The ECM biochemistry also regulates cell fate and function e.g., through integrin signalling and via small molecules like growth factors that bind to specific ECM components. Organ-derived ECM hydrogels gain increasing interest due to their promising prospects for clinical use to augment tissue regeneration.

Keywords: Stiffness, viscoelasticity, hydrogel, 3D, mechanical properties, mechanosignalling, extracellular matrix

1. Introduction

The earth is not flat, and neither are our tissues and organs. Why then do we culture cells on stiff tissue culture polystyrene plates to model their *in vivo* fate and function? Obviously, genuine replication of (patho-) physiological processes in tissues and organs demands culturing of cells with orientation in all three dimensions (3D). In its simplified view, a tissue comprises cells surrounded by an extracellular matrix (ECM). The ECM consists of force-conducting and force-dissipating fibrous proteins such as collagens and elastin that are embedded in a gel-like substance containing highly negatively charged, water-retaining, glycosaminoglycans (GAGs) i.e. polysaccharides. Intrinsically, the ECM acts as a reservoir for small soluble signalling factors like growth factors, chemo/cytokines and biologically active ECM degradation products such as matrikines and matricryptins (Ricard- Blum and Salza, 2014, Ricard-Blum and Vallet, 2016). The dissection of the specific molecular makeup of the ECM is still in its infancy, if only because a high throughput methodology for polysaccharides does not exist as yet to mention one of the limitations. In concert, the detail of the proteome, aka matrisome, of the ECM is currently emerging (Hynes and Naba, 2012, Karamanos et al., 2021).

Regulation of cellular fate and function by the ECM's biochemical features is well-established. In contrast, the influence of mechanical properties of ECM on cells in health and disease and the influence of cells on ECM have gained increasing interest over the past decade. Much of this research employed ECM mimics such as chemical polymers or single ECM components such as hyaluronic acid or gelatine. With improved decellularization methods, came the possibility to assess cell-matrix interactions in native ECM from healthy or disease-affected organs and tissues.

2. Mechanosensing and mechanotransduction

Any organ or tissue consists essentially of cells embedded in an extracellular matrix (ECM). Cell density varies from scarce, such as in cartilage, to dense, such as in the heart. The ECM of musculoskeletal tissue like bone, cartilage and tendon serves to bear load and strain. Thus, cells in these tissues are not only exposed to compression and tensile forces but also respond to these via mechanisms that involve mechanosensing and its consequence, mechanosignaling. Besides the

musculoskeletal system, virtually all tissues in the body perceive mechanical stimuli that range from the shear stress of vascular endothelial cells, a cyclic strain of the beating heart and breathing cycles of lungs to stretching of the skin. Except for circulating blood cells, all cells in the body are attached to ECM. Thus, forces exerted on tissues will result in the physical movement of ECM and simultaneously cells are pulled, strained, or compressed.

A dominant group of receptors with which cells attach to ECM molecules are the integrins. These heterodimers recognize short amino acid stretches within ECM molecules e.g., collagens, laminins, and fibronectin, to which the integrins bind. Most well-known is probably the RGD motif in fibronectin to which e.g. $\alpha_v\beta_3$ integrin binds, but also dozens more (Ruoslahti, 1996). Integrins aggregate in the cell membrane to form focal adhesions. The short intracytoplasmic tails of integrins connect via a series of adaptor proteins such as vinculin, paxillin, talin, tensin and α-actinin, to the cortical actin cytoskeleton of a cell. A focal adhesion is a mechanotransduction protein complex by virtue of two kinases i.e. focal adhesion kinase (FAK) and integrin-linked kinase (ILK). These kinases may activate small GTPases such as RhoA and ROCK to stimulate cell movements including contraction and migration but also affect cell survival via the phosphorylation of PI3K and AKT-1.

The stretching and straining of cells physically opens calcium channels, triggering downstream signalling by the influx of calcium ions (Ca^{2+}). The piezo (calcium) channel is a well-known mechanosensor that responds to ECM stiffness and influences physiological processes like angiogenesis (Li et al., 2022). Calcium is retained as free-floating ions in the ECM but is also bound to ECM components such as laminin (Gopal et al., 2020). Intercellular adhesion molecules as well as ECM receptors such as integrins also rely on the binding of multiple Ca^{2+} ions for their activity (Alberts et al., 2017). Calcium is a second messenger that binds to calmodulin (CaM, calcium-modulated protein), which directly and indirectly, activates small GTPases including ROCK and RhoA regulating contraction and migration (Fig. 1). Much of the calcium/CaM actions are mediated by CaM kinases (Gopal et al., 2020, Racioppi and Means, 2012) e.g., CaM influences PI3kinase – AKT1 signalling and MAPkinase (MAPK) signalling which influences cell survival and proliferation.

The cell's cytoskeleton is connected to the ECM via various surface receptors of

which the integrins are the most important. The integrins cluster in downstream signalling focal complexes in which the FAK and ILK phosphorylate targets. Forces exerted at the cell surface are forwarded by the cortical actin cytoskeleton and thus received by the focal adhesions at the basal site of cells. This concept of integration of tension into integrin signalling was coined tensegrity over almost three decades ago (Wang et al., 1993).

Intriguingly, via integrins, the actin cytoskeleton and the microtubules the ECM can directly exert mechanical stimulation in the nucleus (Jaalouk and Lammerding, 2009, Martino et al., 2018). Nesprins, bound to nuclear lamins transduce forces directly to chromatin and alter the expression of mechanoresponsive genes.

All of the above warrant the development of appropriate physiologically relevant cell culture systems with tunable mechanical properties. This is discussed in the following sections.

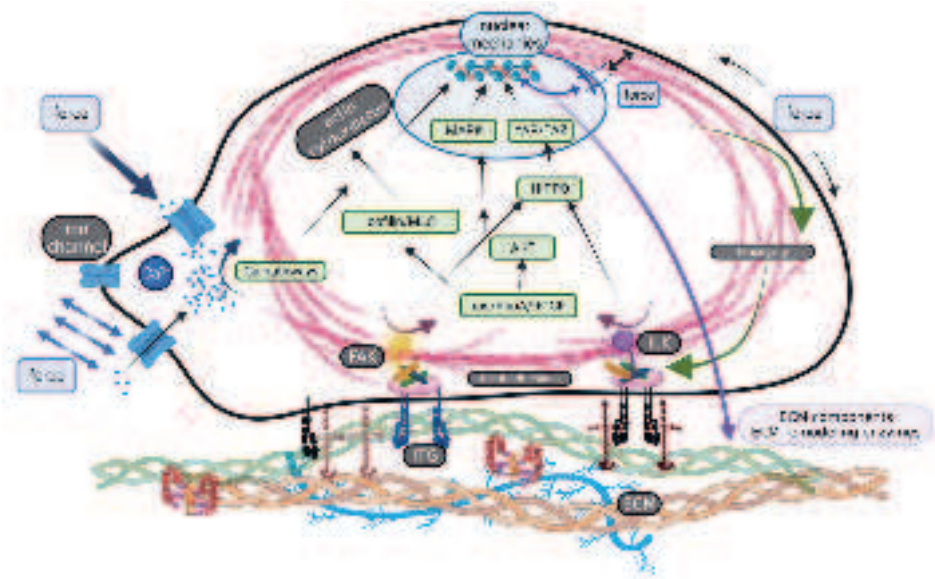

Fig. 1 Mechanosensing and mechanosignalling. Cells anchored with integrins (ITG) to the ECM transduce mechanical stimulation (force) in focal adhesions by activation of the protein kinases FAK and ILK. Downstream these activate small GTPases (ras family) and the contractile machinery (cofilin/MLC) or affect the Hippo pathway and cause nuclear translocation of YAP/TAZ. In the nucleus, MAPkinases (MAPK) and mechanoresponsive transcription factors (YAP/TAZ) regulate mechanoresponsive genes.

Mechanical distortion of cells may cause ions such as calcium transients that converge into the before-mentioned pathways. Alternatively, this distortion is conveyed via the cytoskeleton (tensegrity) to FAK/ILK stimulation. The actin cytoskeleton, via nesprins and lamins, also directly affects chromatin and with it, mechanoresponsive genes. The results of mechanosignalling vary between ECM remodelling, migration, proliferation, differentiation, and survival. Figure created with BioRender.

3. From 2D to 3D

In 1907, Ross G. Harrison was among the first to describe a successful procedure to grow live tissue outside of the parent organism (reviewed in (Yao and Asayama, 2017)). Harrison's efforts were the first step toward sustaining living cells in sterile, *in vitro* conditions, namely cell culture (Antoni et al., 2015). Most of our current knowledge in cell biology, physiology and pathophysiology derives from cell culture models (Caliari and Burdick, 2016, Edmondson et al., 2014). Early modifications to standard cell culture systems included using hydrogels as 2D platforms. These experiments with hydrogels demonstrate that cell morphology varies depending on the available substrate ligand (Rowlands et al., 2008). Moreover, said 2D systems also showed the relevance of mechanics guiding gene expression. In a synthetic hydrogel (i.e. polyethylene glycol; PEG) model of variable stiffness, mesenchymal stem cells (MSCs) differentiated towards neuronal (0.1-1 kPa), myoblastic (8-17 kPa) or osteoblastic (> 100 kPa) phenotypes as shown by Discher and colleagues in their hallmark paper (Engler et al., 2006). Variable stiffnesses are commonly achieved by increasing the polymer concentration used in a hydrogel formulation. Increasing said concentration results in macromolecular crowding and tighter crosslinks within the substrate. In the case of organ-derived ECM hydrogels, recent efforts demonstrated that it is possible to increase hydrogel stiffness without altering its composition using photo crosslinkers (Nizamoglu et al., 2022). Thus, it was possible to reduce experimental variables within already heterogeneous systems. The morphology and survival of hydrogel-embedded MSCs correlate with concentration i.e. stiffness (Martinez-Garcia et al., 2021b). Limitations of standard 2D cell culture models are also present in 2D hydrogel systems where cells are cultured on top of the hydrogels. These include restricted cell adherence to a single plane, forced apical-basal polarity, and the absence of gradients of growth factors. Although it should be acknowledged, the last point could be

debated due to the innate hydrophilicity of any hydrogel. Also, in conventional 2D cultures, the high stiffness of surface of the culture plastic leads to unconstrained cell spreading and proliferation, which is only halted by contact inhibition. However, most cells live in a 3D ECM-based environment (Jensen and Teng, 2020). For this reason and as a more physiological model, cells can also be embedded inside hydrogels. Within the hydrogels, cells will initially perceive the mechanics of their surroundings, and express cell surface receptors that will transduce the biomechanical and biochemical cues from their environment (Fig. 1). Of note, this chapter only discusses the use of cast 3D ECM hydrogels for cell culture. Chapters on 3D bioprinting of hydrogels and organ-on-chip-like approaches that also employ hydrogels are found elsewhere in this handbook.

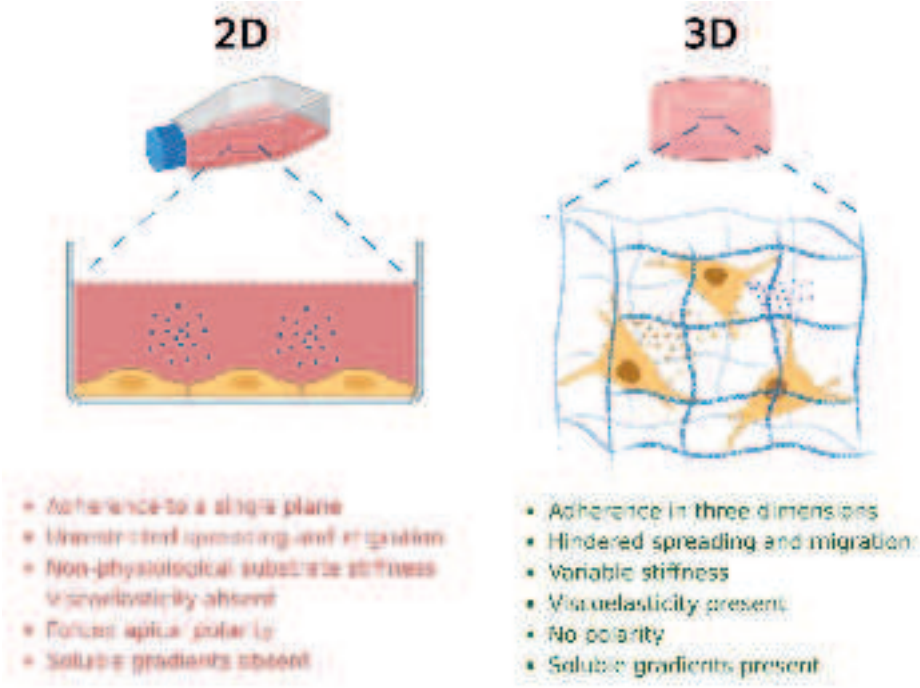

Fig. 2 Limitations of 2D cell cultures compared with 3D cultures. Adapted from (Martinez-Garcia, 2022) with permission. Figure created with BioRender.

4. Recapitulation of physiological extracellular matrix in vitro

4.1 Decellularisation and sol-gel transition of organ-derived ECM

Decellularisation is the procedure which yields purified ECM by removing all cellular material from a tissue. Of note, many of the published procedures focus on the decellularisation of whole organs with the purpose of maintaining architecture and structure for reseeding cells. More recently, protocols have been developed to also generate hydrogels from these decellularised tissues. ECM can be isolated from any human or animal organ. To date, literature describes isolation of ECM from soft and hard organs including adipose tissue, blood vessels, bone, brain, cartilage, colon, cornea, oesophagus, heart, heart valves, kidney, liver, lungs, pancreas, skeletal muscle, skin, small intestine, tendon, tooth, umbilical cord, urinary bladder (Porzionato et al., 2018, Saldin et al., 2017). Progress in decellularisation procedures and preparation of natural-derived ECM hydrogels have been made (extensively reviewed in (Xia and Chen, 2022, Brown et al., 2022) enabling the generation of biomimetic model systems. For the generation of organ-derived ECM hydrogels, every organ requires a specific protocol to achieve optimal removal of cells but retention of ECM components, but the main steps (Fig. 3) comprise of firstly mechanical dissociation, by simply cutting or blending the tissue. This step is followed by mild enzymatic tissue digestion, usually with trypsin. Then, the lipid membranes and any remaining cellular proteins are removed by sequential incubations with detergents such as sodium dodecyl sulphate (SDS) or TritonX100 and repeated washings. While nuclear DNA is a negatively charged polysaccharide akin to GAGs, it adheres to ECM and requires removal by digestion with DNAse. Completion of these steps yields a near-pure ECM devoid of cellular constituents, which can be sterilised by incubation in 70% (v/v) ethanol. This decellularised ECM is freeze-dried and ground into a fine powder (Fig. 3). Longterm storage is possible at -20˚C or -80˚C. The ECM powder should not contain any clumps of material or fragments visible to the naked eye. Decellularisation protocols differ per organ due to differences in cellular constituents and density, as well as matrix composition. Certain short procedures claim to yield decellularised ECM in hours, other procedures, in more complex organs, may take several weeks (Badylak et al., 2011). For example, the adequate removal of triglycerides and fat during the decellularisation of adipose tissue remains a challenge (van Dongen et al., 2019b). Uniform, standardised protocols to decellularise tissues have yet to be defined in the field, hampering potential approval for future clinical applications (Vriend et al., 2021).

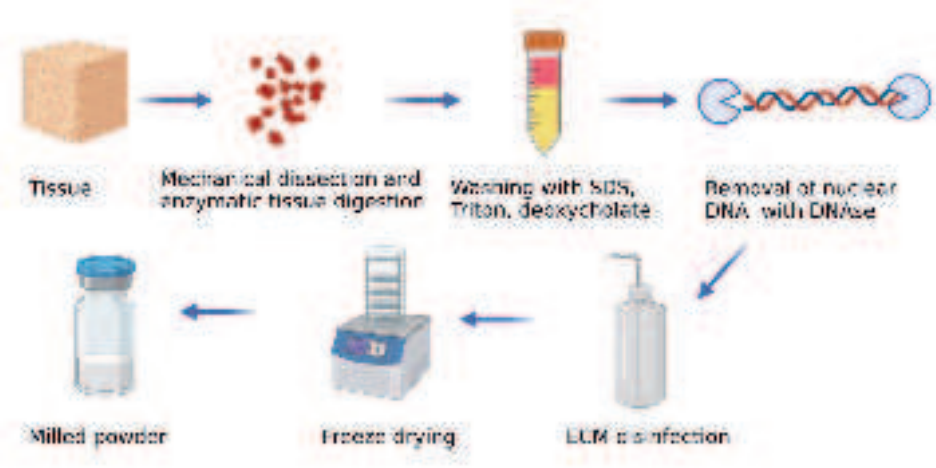

Fig. 3 General scheme for tissue decellularisation and ECM purification. Figure created with BioRender.

Hydrogels are generated from the milled ECM powder by mild pepsin degradation in HCl at pH 1 at room temperature followed by pH neutralisation and adjustment to isotonic conditions with PBS (Fig. 4). The digestion time varies per organ from 6 hours for the heart to 96 hours for bone ECM and requires optimisation per batch (Liguori et al., 2020, Paduano et al., 2016). These resultant pre-gels remain stable for months at 4˚C. At the time of casting, the pre-gel can be mixed with cells and incubated at 37˚C for a half hour to form a mature relatively homogeneous hydrogel after which a culture medium is added. Hydrogels can be generated to seed cells on top in order to study cellular migration into ECM or to force basal-apical polarisation by the ECM – liquid transition (Fig. 4).

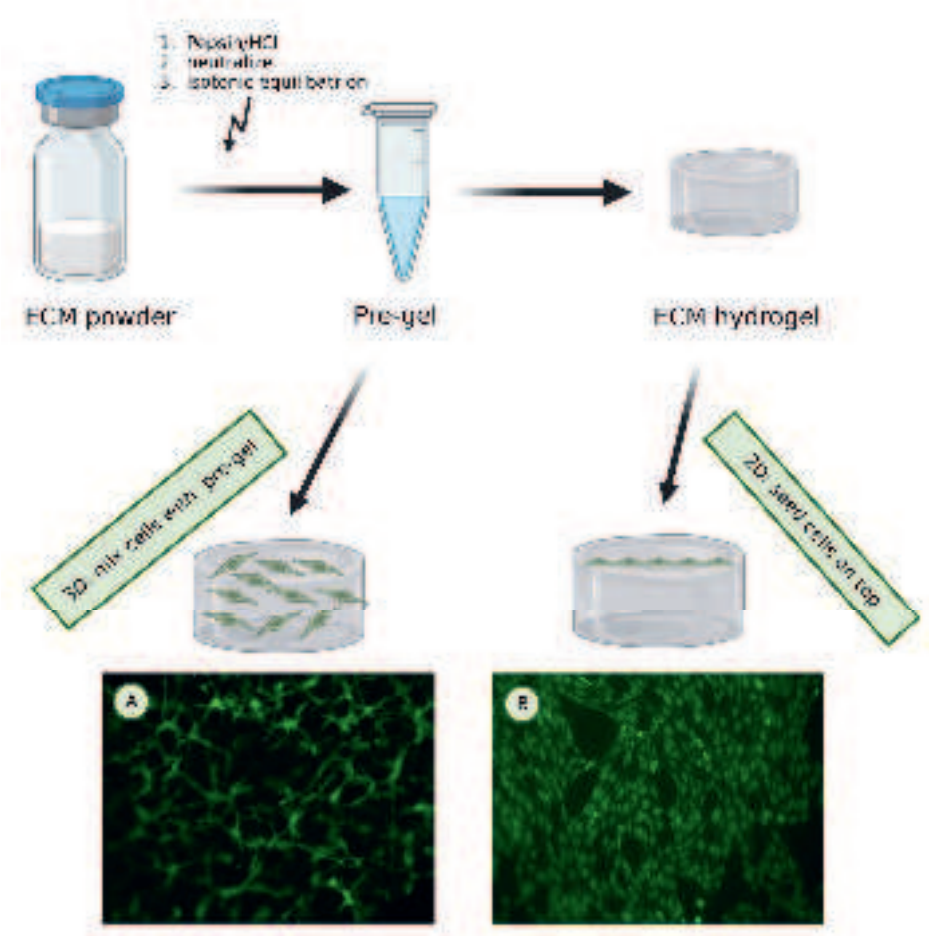

Fig. 4 Schematic of the process to generate ECM hydrogels and seeding these with (endothelial) cells inside (A) prior to sol-gel transition or seeding (endothelial) cells on top of a pre-cast hydrogel (B). Note the impact of 3D culturing i.e. vascular-like network formation while in 2D, cells proliferated. Endothelial cells were incubated for 14 days and visualized by inverted fluorescence microscopy after vital staining with calcein-AM. ECM was isolated from the porcine myocardial left ventricular wall (Liguori et al., 2020). Figure partly generated with BioRender, micrographs: Harmsen/Burgess lab.

4.2 Chemical characterisation of ECM hydrogels

Purified ECM should comprise only proteins and GAGs the quantity of which should be determined with appropriate assays. Yet, contaminants such as LPS and DNA should be minimal (DNA) if not virtually absent (LPS). LPS is

introduced into any biological system by less than careful handling. It is a constituent of Gram-negative bacteria which strongly activates the immune system. Most hospital pharmacies routinely test equipment and compounds for LPS but a plethora of readily available commercial tests exist. The presence of detectable LPS precludes the use of ECM in cell experiments as it cannot be eliminated. The use of pyrolyzed glassware and sterile plastic tubes and avoidance of skin contact is prime to prevent LPS contamination. Gloves are of limited use because researchers may unknowingly touch (facial) skin or hair. Being a polysaccharide, DNA interferes with the sol-gel transition of pre-gels. DNA determination requires a standard isolation procedure in which the ECM is treated at 56˚C in an SDS solution with proteinase K, and chloroform extracted. Purified DNA is readily quantified by microvolume UV spectroscopy e.g., using Nanodrop equipment (such as Implen™ NanoPhotometer™ N60 [Westburg, Leusden, the Netherlands]).

Commercially available scaffolds contain minimal DNA (Gilbert et al., 2009). Current consensus dictates that purified ECM may have no more than 50ng/mg DNA which is several tenfold to hundredfold less than native tissue (Liguori et al., 2020). Where higher DNA levels are detected, the DNAse treatment of the decellularised ECM should be repeated.

The purification of ECM invariably leads to the loss of GAGs, yet the degree of loss differs per organ and procedure (Tsuchiya et al., 2014). The GAGs serve to bind and release on-demand signalling factors such as growth factors (Uhl et al., 2020, van Dongen et al., 2019a). Organ-derived ECM hydrogels efficiently bind and release secretome factors of adipose tissue-derived stromal cells (van Dongen et al., 2019a, Liguori et al., 2021). Similarly as for LPS, there are commercially available kits to determine the contents of sulphated and non-sulphated GAGs (sGAGs) in ECM in 96 wells format suitable for spectrophotometric readouts. Most of these rely on the binding of Alcian Blue or Dimethylmethylene Blue (DMMB) to sGAGs.

For a more detailed analysis of the ECM, single proteins can be identified by different means such as a global approach by proteomics analysis or a more specific approach by antibody staining or western blot. Each of those techniques requires a certain knowledge and technical expertise. Proteomics analysis gives a complete list of the detectable proteins inside the hydrogel, cons are that it is time-

consuming, and can be up to months before results are finalised. Antibody staining requires a period of optimisation, to find the right antibody that is suitable and proves to work with the given project, and one or few proteins can be detected at a time. Western blots again analyse proteins individually via the binding of an antibody to identify the presence of a size discriminated protein.

5. Physical characterisation

Extracellular matrix is more liquid than solid, in other words: ECM is a gel. This means that ECM responds to compression in a viscoelastic fashion: the water content dictates a part of gel's viscosity while the proteins primarily dictate the elasticity i.e., the propensity to return to its original shape after compression. To date, in general material scientists assess the stiffness of biomaterials yet ignore viscoelasticity. In conjunction with biochemical signalling, the viscoelasticity of ECM via mechanosignalling (Fig. 1), regulates pivotal processes including proliferation, magnification, differentiation, and survival (Chaudhuri et al., 2020). It is long established that pathophysiological processes like fibrosis correlate with increased matrix stiffness and crosslinking yet altered viscoelastic properties also correlate with various other pathologies (Handorf et al., 2015), albeit that is remains challenging to show cause or consequence (Handorf et al., 2015).

Below, typical physical features are explained that together determine the mechanical properties of biomaterials including ECM hydrogels.

5.1 Stiffness

Stiffness is the resistance of a biomaterial to deformation under a specified stress. It represents the elastic property of viscoelasticity. When a hydrogel is exposed to an instant tensile force or compressive force, it will respond with a linear stress-stain curve immediately after the release of the force. The slope of this line is defined as stiffness or Young's modulus/ storage modulus denoted as E. If the force applied is a shear force, the slope of this line is called storage modulus denoted as G. The low elasticity of organ-derived ECM hydrogels renders these unsuitable for mechanical tension testing using tension, which is the reason these measurements are made after compression or shear. Young's modulus is expressed in (k)Pascal.

5.2 Stress relaxation

The stress relaxation test is performed in shear mode or compression mode. A constant strain (ε0) is applied to the sample, the stress reaches a peak after the rapid application of deformation, which point is called the initial stress (σ(0)) of the stress relaxation period. and then the corresponding stress (σ(t)) in it will be recorded over time. The viscoelastic material will dissipate the initial storage stress accompanied by stress relaxation. Typically, the degree of relaxation compared to the initial stress in a certain time or the time it takes to relax to half of the initial stress (σ(0)) are the reported parameters to characterize the speed of relaxation of a material which is a measure of viscosity. Stress relaxation is non-linear, and Maxwell developed algorithms to identify elements within the relaxation profile. These algorithms are often applied to understand the viscoelasticity of biomaterial hydrogels (Babaei et al., 2015, Martinez-Garcia et al., 2021a, Nizamoglu et al., 2022). Detailed information on mathematical modelling follows in the next section.

5.3 Creep

While elasticity is the propensity of a (bio)material to return to its original shape after strain, creep is the permanent deformation that occurs either spontaneously or after strain. Like stiffness, creep is assessed using strain tests. Constant stress(σ0) is applied to the sample under shear, compression or tension, and creep is expressed as a measure of the (permanent) deformation of the sample (ε(t)) over time. Similar to stress relaxation characterisation, creep is usually represented as the percentage of deformation in a certain time or time required to reach 150% deformation of the initial value (Chaudhuri, 2017).

5.4 Methods to measure viscoelastic properties of ECM hydrogels

Measurement of the viscoelastic properties of ECM hydrogels always relies on equipment that applies stress or strain. This may vary from compression of hydrogels with plungers in which the size of the force-applying plunger is in the range of nm to mm, to other modes of force application (axial tension/compression, shear). Alternatively, atomic force microscopy (AFM) and rheometer are frequently used as introduced below. A recent review describes multiple assays to assess mechanical properties and visualisation techniques in ECM hydrogels in detail (Martinez-Garcia et al., 2022a).

The low load compression tester (LLCT) measures the stiffness and stress

relaxation of ECM hydrogels using a compression mode. With its plunger scale being in the millimetre range (minimum is 0.5mm), LLCT is predominantly suited for use on at least equivalently sized or larger hydrogels. During testing, the plunger contacts the surface of the hydrogel, and force is applied to reach approx. 20% deformation within one second. Next, stress relaxation is recorded over time, often 100s, while maintaining a constant strain. The stiffness is calculated according to the linear part of the stress-strain curve during the first second after applying strain. The recorded stress relaxation is processed using Maxwell model fitting (see next section). For smaller samples and for higher resolution local measurements micro LLCT (μLLCT) is used in which the sensing probe is about ten fold smaller; 50 μm compared to ≥ 0.5 mm for LLCT. In general, μLLCT is suitable for precise tests, for example using it for lung airway wall measurements (Migulina et al., 2022).

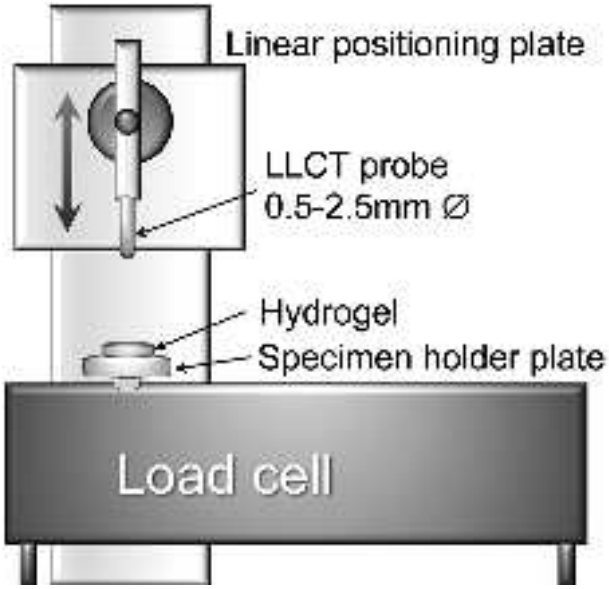

Fig. 5 Low load compression tester (LLCT) schematic. The hydrogel specimen is placed on a heated specimen holder plate. The linear positioning plate moves on a vertical axis (blue arrow) and is lowered to make contact with the surface of the hydrogel. The probe is moved downwards to achieve 20% strain, the amount of force required is dependent on the biomaterial used. In the follow-up phase of approx. 100 s, the stress-strain relief is recorded by the equipment. (Figure made with Adobe Illustrator)

AFM scans surfaces, including hydrogels, with a fine needle tip that connects to a microcantilever. The small distortions (μN) of the surface the needle passes over, are recorded and converted to either topographical maps or to reflect mechanical properties such as stiffness and stress-relaxation (Martinez-Garcia et al., 2022a). This method allows recording of surface measurements at high resolution more than the generation of a mechanical view of an entire hydrogel. An advantage of AFM is that interaction forces between hydrogel molecules and adhered cells can be measured.

The rheometer is a classic instrument based on the liquid flow that is used to determine the viscoelasticity of materials. It employs the stress-strain response of materials in shear mode, mainly to study the time-dependent flow and deformation of hydrogels under external forces. The rheological parameters of hydrogels that can be measured are the storage modulus (G') and the viscous modulus (G"), the latter also known as the loss modulus. The storage modulus represents the solid-like behaviour of hydrogels, while the viscous modulus refers to the heat dissipation of the material after the application of force or deformation and characterizes the liquid behaviour similar to water (Sathaye et al., 2015, Stojkov et al., 2021). Besides the requirement of usually millilitre volumes, a challenge for the use of rheometry on ECM hydrogels is that these are 'more liquid than solid' i.e. their stiffness is often in the low ten kPa range. These soft gels are readily damaged prior to and during the measurement which compromises adequate measurements. While the procedure is inherently destructive and non-sterile it is of lower value to measure hydrogel embedded with cells.

6. Mathematical modelling of hydrogel viscoelasticity

The use of mathematical viscoelasticity models in hydrogels allows for the identification of material properties and correlates with biological responses. Diverse models of viscoelasticity (Fig. 6) are reported in the literature concerning hydrogels (Mierke, 2021). The Maxwell model is among the earliest descriptions of viscoelasticity, represented by a string and a dashpot (Fig. 6a). The Kelvin-Voight model (Fig. 6b) shows the spring and dashpot connected in parallel (Zhang et al., 2021, Yang et al., 2022). The Burgers model (Fig. 6c) is a combination of both the Kelvin-Voigt and Maxwell models and has been applied to natural (e.g.

gelatine, alginate, and fibrinogen) and synthetic (polyethylene glycol) hydrogels (Hong et al., 2016, Rial et al., 2020, Toledo et al., 2020). Further modifications to the Maxwell model include the Maxwell-Wiechert model, also known as the generalised Maxwell model**,** represented by a series of springs and dashpots connected in series (Fig. 8a).

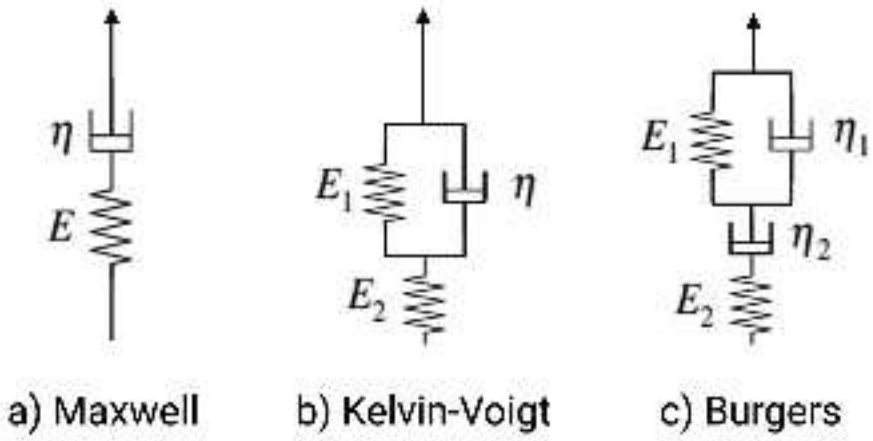

Fig. 6 Mathematical models of viscoelasticity The Maxwell model is shown as a connected spring and dashpot. The Kelvin Voight shows both spring and dashpot working in parallel. The Burgers model consists of a Maxwell element and a Voigt element in a series. E represents the general elastic modulus and η indicates the viscosity. Figure created with BioRender.

It is possible to apply multiple models during the characterisation of hydrogel viscoelasticity, albeit recognising that each comes with limitations. For example, the generalised Maxwell model does not describe material creep, being more representative of stress relaxation when modelling small strains and the viscous response. In contrast, the Kelvin-Voight model describes material creep but is limited in predicting stress relaxation, as shown in crosslinked alginate hydrogels (Chejara et al., 2013, Mitchell and Blanshard, 1976). Thus, this model is deemed suitable for modelling viscoelastic solid materials (Jachowicz et al., 2007). Similarly, the Burgers model describes material creep and its (elastic) recovery. Thus, these models describe viscoelasticity distinctively and should be applied accordingly to the mechanical test employed. Overall, mathematical modelling has demonstrated that hydrogels stiffen as strained, but this phenomenon

diminishes with time due to strain-enhanced stress relaxation (Nam et al., 2016). Such viscoelasticity models have already been applied in the food industry to predict fruit and grain firmness, ripeness and palatability (Blahovec, 1996, Hassan et al., 2005). To a similar extent, modelling hydrogel viscoelasticity could predict their mechanical and biological behaviour *in vitro*, before biomedical applications.

6.1 The generalised Maxwell model

This model of viscoelasticity is the most commonly used in the characterisation of hydrogel's viscoelasticity and it will be the focus of this section. Of the three available mathematical models for viscoelasticity, Maxwell's model is increasing used (Fig. 7).

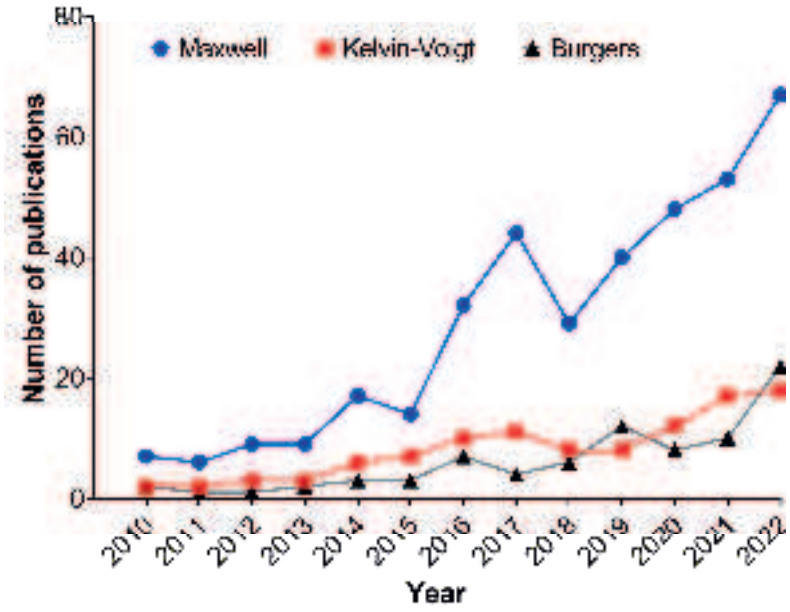

Fig. 7 Research articles published per year from 2010 to August 2022 according to the ScienceDirect database (accessed on 25 August 2022), using the keywords "hydrogel + viscoelasticity + Maxwell" (n = 375); "hydrogel + viscoelasticity + Kelvin-Voigt" (n = 107) and "hydrogel + viscoelasticity + Burgers" (n = 81).

The generalised Maxwell model (Fig. 8a) considers the heterogeneity of the system, in that diverse components will dissipate stress at shorter or longer time scales based on their chemical and physical composition. The model assumes the existence of a series of spring elements in which the spring constant (Ei) represents stiffness, and a dashpot (ηi) represents the damping of viscous resistance. Mathematically, the analysis fits 3 or 4 maxwell elements according to the formula: $E(t) = E_1 e^{\frac{-t}{\tau_1}} + E_2 e^{\frac{-t}{\tau_2}} + \cdots + E_i e^{\frac{-t}{\tau_i}}$ Here, E(t) is the relation between stress and strain with time, and results from the combination of i Maxwell elements, while τ_i represents η_i / E_i. Thus, said components will actively dissipate stress at distinct time(s) (tau; τ). For this reason, the diverse components can be theoretically allocated into Maxwell elements, numerical, although arbitrary, representations of their participation in the stress relaxation process (Fig. 8b). From a mathematical perspective, hydrogels may have an infinite number of Maxwell elements practice, the number of elements reported does not exceed four (Liguori et al., 2020, Martinez-Garcia et al., 2021b). Because the amount of stress dissipated by each Maxwell element is variable and hydrogel-dependent, each element has its relative importance (R_i) proportionally expressed (Fig. 8b). The application of the Maxwell model to diverse hydrogel biosystems has consistently identified that the number of Maxwell elements increases in a stiffness-related fashion (de Hilster et al., 2020, van Dongen et al., 2019a). Increasing the agarose concentration of platelet-poor plasma/agarose (PA) copolymer hydrogels not only incremented their stiffness but also the τ_1 and τ_2, corresponding to the fast and intermediate Maxwell elements in a three-element model (Patino Vargas et al., 2022). In cell-loaded PA hydrogels, Maxwell analysis showed a correlation between cell viability and metabolism to τ_1 and τ_2 during the early stages of cell culturing (Patino Vargas et al., 2022). Overall, loading cells into hydrogels do not increase or decrease the number of Maxwell elements detected (de Hilster et al., 2020, Patino Vargas et al., 2022). While the lack of effect of cells on the number of Maxwell elements might be number dependent, a comparison between native tissue (i.e. lung) and its decellularised hydrogel counterpart showed the same number of Maxwell elements; although their respective R_i and τ differed (de Hilster et al., 2020). This evidence is indicative of cells actively participating in the stress relaxation process. Moreover, cells such as adipose tissue-derived stromal cells (ASCs) can modify the Maxwell elements' R_i depending on the polymer concentration (i.e GelMA) and the mechanics of their environment

(Martinez-Garcia et al., 2021b). It is suggested these changes occur through elusive spatiotemporally regulated mechanisms that might stem from a balance between matrix turnover and/or hydrogel degradation (Martinez-Garcia et al., 2022b, Wan et al., 2011). Said viscoelastic changes might be traceable in organ-derived hydrogels, but the literature evaluating long-term 3D cell culture mechanics is, as yet, scarce.

Non-covalently bound hydrogels (e.g. skin, lung, cardiac left ventricle) demonstrate a consistent predominance in the R_i of the first (i.e. fastest) Maxwell elements (Martinez-Garcia et al., 2021a). In contrast, covalently bound hydrogels (e.g. GelMA) have greater R_i in the last (i.e. slowest) elements (Martinez-Garcia et al., 2021b).

Hypothetically, the first Maxwell elements would correspond to the fastest stress-dissipating components found within the polymer network, namely unbound water molecules and small molecules such as growth factors. Additional Maxwell elements required to fit the model thus correspond to hydrogel components that do not dissipate mechanical stress with the same ease. Such components could be bound to water and crosslinked proteins, including those forming the polymer network and possibly cells (Fig. 8c). However, a clear association between the diverse Maxwell elements and hydrogel components remains a purely hypothetical exercise due to the lack of a systematic study (Nizamoglu et al., 2022), unlike in other biological systems such as bacterial biofilms (Peterson et al., 2013, Rozenbaum et al., 2019).

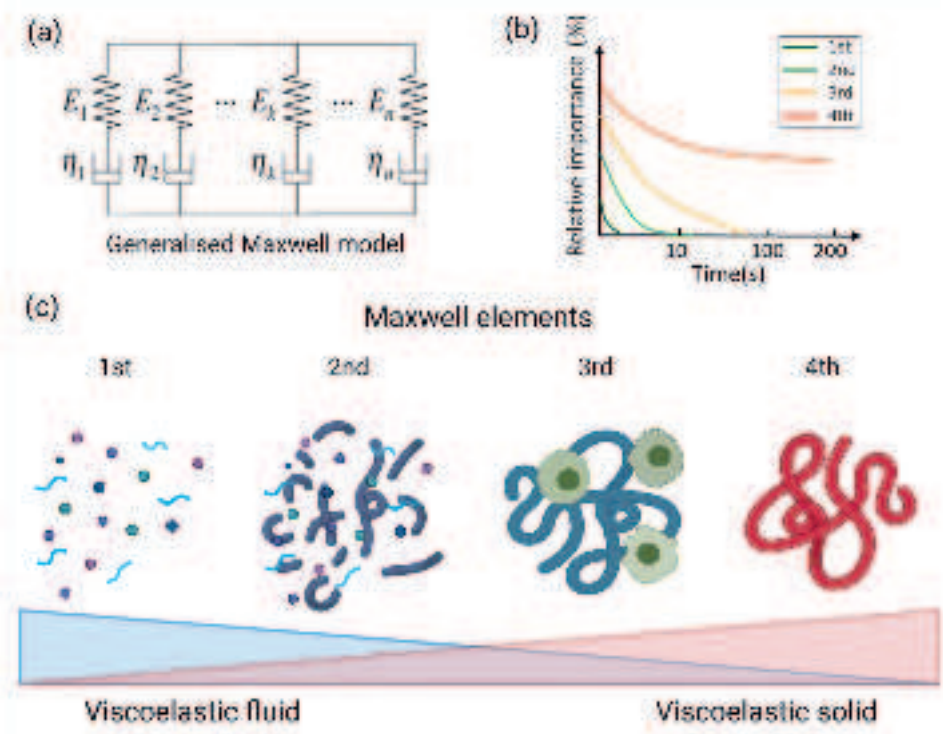

Fig. 8 Mathematical modelling hydrogel viscoelasticity where a) shows the generalised Maxwell model in a series of springs and dashpots, each corresponding to an individual Maxwell element. b) Indicates the relative importance of each Maxwell element over time. c) Hypothetical interpretation of the Maxwell model in cell-loaded hydrogels, where viscoelastic fluids have predominant water and small molecules components. In contrast, a viscoelastic fluid has heavy proteins. Thus, hydrogels that act as viscoelastic fluids show faster stress relaxation than viscoelastic solids, whose stress relaxation is slower. Adapted from (Martinez-Garcia, 2022) with permission. Figure partially created with BioRender.

7. Methods to Adjust Mechanical Properties of ECM Hydrogels

Opportunities for altering the mechanical properties of the decellularised ECM-derived hydrogels have also been focused on over the last decade. Even though these hydrogels can demonstrate similar trends with respect to mechanical properties in health and disease as the native tissue samples would do (de Hilster et al., 2020), the mechanical properties can be further tailored. The need to alter

such properties can arise for different reasons such as increasing stability for bioprinting purposes or replicating the mechanical environment of diseased ECM. As these hydrogels are a dynamic network of several different proteins found in the native tissue, one of the initial attempts to alter the mechanical properties was to crosslink these proteins to each other to reinforce the network. Crosslinking of proteins can be achieved simply through the use of chemical agents like glutaraldehyde or genipin, shown as increased G' and G'' values of treated porcine ventricular myocardium ECM-derived hydrogels. A similar approach used EDC on umbilical cord ECM-derived hydrogels: EDC-crosslinked hydrogels had reinforced storage modulus compared with unmodified hydrogels (Výborný et al., 2019). An alternative to systems that rely on genipin alone was later presented as a pH-driven reaction using a PEG-genipin conjugate (Nishiguchi and Taguchi, 2021), resulting in increased tensile strength and shear modulus in crosslinked hydrogels compared with native hydrogels. Adding methacrylate to free amine groups in proteins has been previously used for single ECM protein-based hydrogels such as gelatine (Loessner et al., 2016) to fine-tune mechanical properties. The same method was later applied to several different tissue ECM-derived hydrogels such as bone (Parthiban et al., 2021), cartilage (Behan et al., 2022), liver (Ravichandran et al., 2021) and kidney (Ali et al., 2019) to increase the stiffness of these ECM hydrogels. Adding thiol groups to the ECM-derived hydrogels was also demonstrated: thiol-functionalized lung ECM-derived hydrogels in combination with additional PEG-MA (Petrou et al., 2020, Saleh et al., 2022) altered the mechanical properties. Light-triggered methods that do not rely on additional functionalisation of the starting material have also been recently described. Using a ruthenium complex as the catalyst and sodium persulfate as the substrate, increased stiffness on the cornea (Kim et al., 2021) and lung (Nizamoglu et al., 2022) ECM-derived hydrogels without further modifications have been demonstrated. The latter study describing the ruthenium-crosslinking on lung ECM hydrogels showed that fibre crosslinking alters the viscoelastic stress relaxation property of the hydrogels as well.

Modifying the mechanical properties of ECM-derived hydrogels emerges as a potent method to increase hydrogel potential for diverse applications such as bioprinting or 3D *in vitro* modelling. The initial efforts have focused on increasing the stiffness and other mechanical properties such as viscoelastic stress relaxation or creep now also need to be included in characterising the influence

of fibre crosslinking. Ideally, finding tailored methods for modifying individual mechanical properties without changing any other properties of the hydrogels should be the goal.

8. Applications and translational aspects

8.1 3D ECM hydrogels to investigate vascularisation

In physiological wound repair, remodelling of the ECM and angiogenesis (formation of new blood vessels) is essential. Connective tissue mesenchymal cells such as fibroblasts, smooth muscle cells and pericytes are professional ECM remodellers that simultaneously drive angiogenesis during tissue regeneration (Nehls et al., 1994). Obviously, surrogate hydrogels like fibrin (Nam et al., 2016), Matrigel™ (Nicosia and Ottinetti, 1990), and purified collagen (Andree et al., 2019, Montesano and Orci, 1985) have served to generate understanding of the governing principles of angiogenesis. Endothelial cells also remodel ECM hydrogels and deposit their own cell-derived ECM molecules during vascular tube formation (Davis and Senger, 2005). In traditional hydrogel systems, the stiffness, architecture and dynamics influence angiogenesis (Wei et al., 2020) in a mechanosignalling-dependent fashion (Guo et al., 2022). While the dependence of endothelial phenotype and physiology on mechanical forces is undisputed (Gordon et al., 2020), the influence of biochemical composition and mechanical properties of ECM hydrogels on angiogenesis is virtually unknown.

In Matrigel™, ASCs drive vascular tube formation by human umbilical vein endothelial cells (HUVEC) in a NOTCH2-dependent fashion (Terlizzi et al., 2018). Yet, this is an artificial system with macrovascular embryonic ECs in a tumour-derived matrix. Tissue regeneration depends on capillarisation i.e., the formation of small vessels by microvascular ECs. Organ ECM-derived hydrogels support the formation of vascular tubes by ECs such as human microvascular ECs (HMECs) and human pulmonary microvascular ECs (HPMECs) (Fig. 9). Even without the support of mural cells such as ASCs, these networks are formed while macrovascular ECs such as HUVEC require ASC to form networks (Liguori et al., 2020). While surrogate hydrogels may teach much about molecular mechanisms, the use of organ-derived ECM hydrogels appears closer to nature. This is important in a translational setting e.g., if ECM hydrogels are to be used

to promote (dermal) wound healing (Vriend et al., 2021, Vriend et al., 2022).

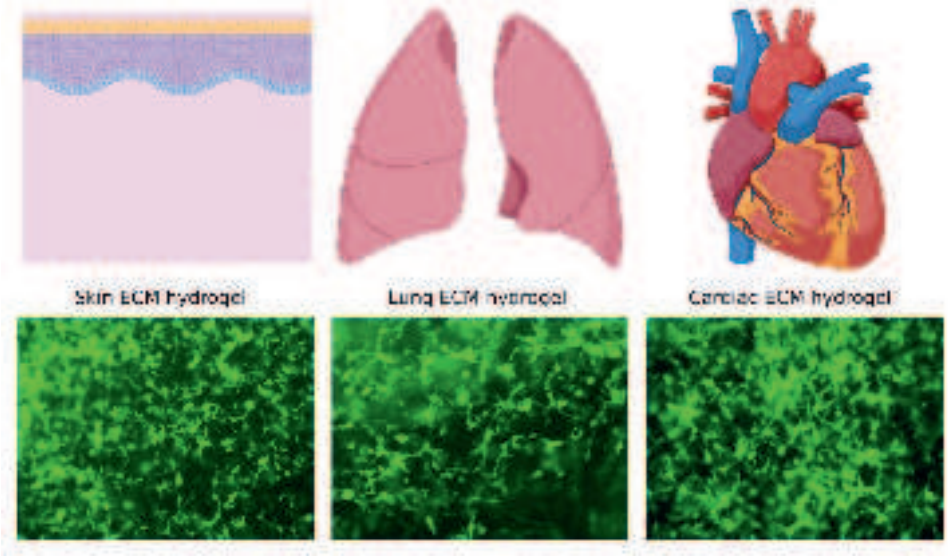

Fig. 9 Use of skin (left), lung (middle) and cardiac left ventricular-derived (right) porcine ECM hydrogels to study vascularization. HPMEC were cultured inside 2% w/v ECM hydrogels and stained for vitality using calcein-AM (green) after three days. Images were taken at tenfold original magnification with an inverted fluorescent microscope. Tubes are readily seen as elongated structures at various depths in the gels. Imaging is challenged by the limited depth of field of inverted microscopes. Figure partially created with BioRender. Micrographs: Harmsen/Burgess lab.

The organ source ,i.e. the biochemical composition, of the ECM may influence the formation of networks and long-term stability of vascular tubes formation by HPMEC. In general, vascular networks form within three days in organ-derived ECM hydrogels (Fig. 8). These 2% w/v hydrogels vary in stiffness from less than 1 kPa for skin to approximately 10 kPa for lung and cardiac while stress relaxation was faster in the skin than lung or cardiac hydrogels as measured by low-load compression test (Martinez-Garcia et al., 2021a). Interestingly, tubes remained stable for more than 1 week in cardiac hydrogels while these had collapsed in skin or lung gels by then (data not shown).

To date, interactions of endothelial mechanosensors such as integrins (Mrugacz et al., 2021) with molecules in hydrogels of normal and pathophysiological ECM

are *terra incognita*. Also, the influence of the mechanical properties of ECM hydrogels on angiogenesis is not studied. As before-mentioned, it is possible to tweak the mechanical properties of hydrogels without affecting their biochemical composition - two tightly-linked properties regarded as inseparable. Yet, now that cell culture-compatible crosslinking methods are available (previous sections) and ECM hydrogels are readily generated and their properties known (Saldin et al., 2017), it becomes possible to optimise vascularisation *in vitro*. This is relevant for (pre)clinical application to treat, among other indications, cardiovascular disease, promising as reported here (Mewhort et al., 2017, Seif-Naraghi et al., 2012, Singelyn et al., 2009).

8.2 Translation to the clinic

In vitro culture systems, be it 2D or 3D, can never replicate normal physiology like wound healing and tissue regeneration, or for that matter pathophysiology like fibrosis or diabetic ulcers. Yet, it is plausible to postulate that the regeneration of damaged tissues and organs is augmented by introducing native ECM for that tissue because these contain the matrix-governed cues and clues to instruct the surrounding cells. This reasoning falls short of substantial experimental evidence, while additions of therapeutic cells or their products might be required to enhance repair and regeneration or to reverse adverse processes. To date, several clinical trials have been listed (ClinicalTrials.Gov) that use ECM from various organ sources to treat diseases ranging from osteoarthritis, through muscular and cardiac disease to non-healing diabetic ulcers. Occasionally, homologous ECM is used (from the same organ), sometimes even formulated as hydrogels. Most studies are Phase 1 (safety only) and recruit but few patients. Yet e.g., with Ventrigel, a left ventricular-derived ECM hydrogel, promising results were obtained in patients after myocardial infarction (Traverse et al., 2019). Clinical translation of ECM hydrogels to treat soft tissue disease is in its infancy, particularly with respect to knowledge of required mechanical properties. The first question asked by clinicians often is: ‘Is the hydrogel easily injectable and will it pass through a catheter?’ For engineers and biomedical scientists, these logical questions pose a large challenge: high viscosity is incompatible with small diameter needles and catheters while shear-thinning might compromise application as well. These demands adjustments be made possible of mechanical properties *in situ* after injection e.g., by means of UV photocrosslinking (Fig. 10).

This hurdle can be overcome with sophisticated engineering and miniaturization of UV light sources. This also induces the risk that hydrogels, fortunately, spread throughout lesions to sites outside of the UV light. Therefore, current applications rely on the self-gelling capacity of ECM hydrogels at body temperature. The entire clinical pipeline from organ-derived ECM hydrogel to treatment of damaged and diseased organs is depicted in Fig. 10. The regenerative properties of ECM-derived hydrogels can be enhanced by using additives such as cultured therapeutic cells like MSCs and their secretome (Fig. 10) or antimicrobials (Fig. 10). These additives can be bound by specific organ-derived ECM hydrogels and released in a sustained fashion (Liguori et al., 2021, van Dongen et al., 2019a). The cited studies did not assess which components of the ECM bound the growth factors but these likely include GAGs and to some extent proteins such as fibronectin. Paracrine factors such as interleukin-6 and 10 inhibit inflammation, while vascular endothelial growth factor (VEGF) and fibroblast growth factor (FGF) are pro-angiogenic. The addition of these paracrine factors to ECM hydrogels is expected to augment wound healing. Unfortunately, no evidence exists of how the mechanical properties of ECM hydrogels influence the release of paracrine factors. To augment all phases of wound healing and regeneration administration of the secretome of MSCs is well-accepted. A major advantage of ECM hydrogels as a delivery vehicle is the lack of an adverse immune response while macrophages appear to be directed toward a regenerative (M2) phenotype by MSCs and their secretome (Stevens et al., 2020). This creates the opportunity for allogenic injection with an off-the-shelf product without the need for invasive surgery. While secretome-loaded and ‘mechanically tweaked’ ECM hydrogels are not common pharmaceutical drugs nor stem cell therapy, legislators, and government organisations such as the FDA and EMA need to be closely involved. University hospitals need to build GMP/GLP facilities to facilitate the preparation of hydrogels and secretomes. The future clinical application therefore not only depends on understanding the mechanical properties of ECM hydrogels. However, several challenges and opportunities remain in that respect.

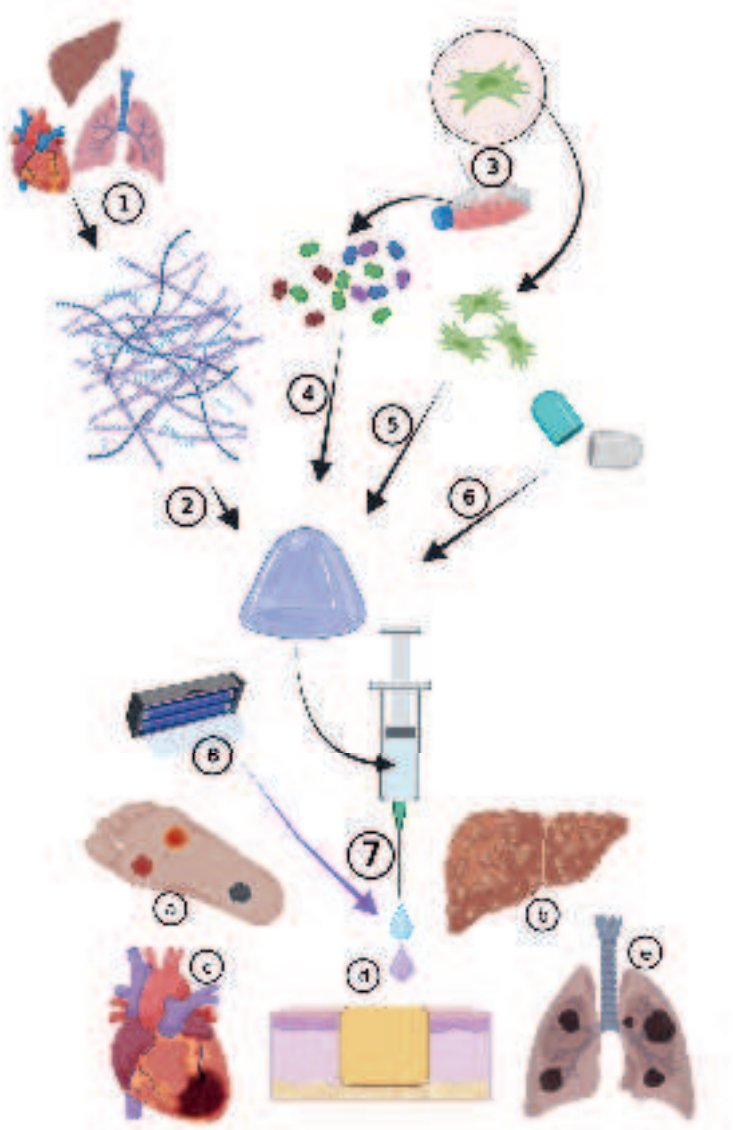

Fig. 10 Hydrogel clinical pipeline. From source organs (1), ECM is isolated and processed to a (pre)gel (2). Therapeutic additives are generated by culture of e.g. stem cells (3) from which either the secretome (secreted factors) or/and the cells are isolated and mixed with the pre-gel. Alternatively, single (growth) factors can be added. To dampen infection risk in superficial wounds (7a), antimicrobials are added (6). Pre-gel is administered topically or by injection to treat pathologies that may range from diabetic foot ulcers (a), liver fibrosis (b), myocardial infarction (c), and dermal scars (d) to COPD and lung fibrosis (e) to give a few examples. Finally, mechanical properties are controlled by UV photocrosslinking in situ (8). Figure created with BioRender.

9. Opportunities and Challenges:

Organ-derived ECM hydrogels provide a valuable opportunity due to their wide versatility in mimicking the native biochemical and mechanical properties of the tissue microenvironment. While the advantages of using such hydrogels over synthetic or single ECM protein-based hydrogels are being established, there are several challenges that need to be overcome before using organ-derived ECM hydrogels can be considered as a gold standard. One of the initial challenges arises from the organ decellularisation procedure: preserving the native composition remains a hurdle (Ebrahimi Sadrabadi et al., 2021). Some ECM components, such as specific GAGs and most of theECM- bound growth factors, are partially lost during the decellularisation process in an organ-dependent fashion (Moura et al., 2022). Improved protocols are warranted where GAGs and growth factors retention are secured. New methodologies such as supercritical CO_2-assisted (Duarte et al., 2022) or apoptosis-assisted (Song et al., 2021) decellularisation techniques could pave the way towards achieving this goal. A distinct challenge regarding the reinforcement of mechanical properties of ECM-derived hydrogels has recently surfaced. Although initial studies have shown that diverse strategies can modify hydrogel stiffness, the potential influences of the applied methods on other properties (such as viscoelastic stress relaxation, fibre alignment, and pore size) have yet to be investigated. With advancing technology, innovative techniques will be developed to solve the challenge of fine-tuning of hydrogel mechanics. Imaging is another important challenge for the characterisation of ECM-derived hydrogels. The limited depth of field of any type of optical microscopy and the low translucence i.e., high turbidity of hydrogels disqualifies high-resolution imaging throughout hydrogels with current microscopy approaches. Fortunately, microscopy methodology is rapidly developing and will open new avenues for ECM researchers in the future. The autofluorescence of matrix fibres allows for visualisation by second and third harmonics generation (SHG and THG) while intriguing microscopy methods like CARS, FLIM, SIM, STED, GSD and PALM offer opportunities too (reviewed in (Poole and Mostaço-Guidolin, 2021)). Mechanical property measurements are not possible with a high spatial resolution throughout ECM hydrogels yet. As cells alter ECM and with it, the mechanical properties, 3D mapping at a high (cellular) resolution of stiffness and stress relaxation is warranted preferably in real-time allowing multiple measurements to study microscale cell-ECM

dynamics.

In late December 2022, new legislation passed in the USA, eliminating the FDA requirement for new drugs to undergo animal testing in the development pipeline (Wadman, 2023). In vitro 3D (organ) models, such as ECM hydrogels, will play an important role in the advancement of the drug-development pipeline as this new legislation enables the exploration of biomimicking model systems.

In summary, numerous challenges revolving around the utilisation of ECM-derived hydrogels exist. Solving these challenges by providing alternative methodologies represents an invaluable opportunity to advance our knowledge in cell-matrix biology, tissue engineering and regenerative medicine and to create innovative setups using ECM-derived hydrogels.

Conclusion

Organ-derived ECM hydrogels are versatile 3D systems that allow us to investigate the impact of biomechanics and biochemistry on cells in disease pathology. The extracellular matrix can be isolated from any human or animal organ while retaining the organ-specific matrix characteristics. Various techniques are available to determine the physical features of an ECM hydrogel, which together determine its mechanical properties, such as viscoelasticity. As an in vitro 3D model, ECM hydrogels provide a new opportunity for providing a bridge towards clinical application, reducing the need for animal studies in the future.

Acknowledgements

FDMG was supported by the Mexican National Council of Science and Technology (CONACyT; CVU 695528) and by the De Cock-Hadders Foundation (2021-16). JKB was supported by a Rosalind Franklin Fellowship co-funded by the University of Groningen and the European Union. MZ and FZ received a China scholarship council. FDMG and VG received funding from the Stichting De Cock-Hadders foundation.

References

ALBERTS, B., JOHNSON, A., LEWIS, J., MORGAN, D., RAFF, M., ROBERTS, K., WALTER, P., WILSON, J. & HUNT, T. 2017. *Molecular Biology of the Cell*, W.W. Norton & Company.

ALI, M., PR, A. K., YOO, J. J., ZAHRAN, F., ATALA, A. & LEE, S. J. 2019. A Photo-Crosslinkable Kidney ECM-Derived Bioink Accelerates Renal Tissue Formation. *Adv Healthc Mater,* 8**,** e1800992.

ANDREE, B., ICHANTI, H., KALIES, S., HEISTERKAMP, A., STRAUSS, S., VOGT, P. M., HAVERICH, A. & HILFIKER, A. 2019. Formation of three-dimensional tubular endothelial cell networks under defined serum-free cell culture conditions in human collagen hydrogels. *Sci Rep,* 9**,** 5437.

ANTONI, D., BURCKEL, H., JOSSET, E. & NOEL, G. 2015. Three-dimensional cell culture: a breakthrough in vivo. *Int J Mol Sci,* 16**,** 5517-27.

BABAEI, B., DAVARIAN, A., PRYSE, K. M., ELSON, E. L. & GENIN, G. M. 2015. Efficient and optimized identification of generalized Maxwell viscoelastic relaxation spectra. *J Mech Behav Biomed Mater,* 55**,** 32-41.

BADYLAK, S. F., TAYLOR, D. & UYGUN, K. 2011. Whole-organ tissue engineering: decellularization and recellularization of three-dimensional matrix scaffolds. *Annu Rev Biomed Eng,* 13**,** 27-53.

BEHAN, K., DUFOUR, A., GARCIA, O. & KELLY, D. 2022. Methacrylated Cartilage ECM-Based Hydrogels as Injectables and Bioinks for Cartilage Tissue Engineering. *Biomolecules,* 12.

BLAHOVEC, J. 1996. Stress relaxation in cherry fruit. *Biorheology,* 33**,** 451-62.

BROWN, M., LI, J., MORAES, C., TABRIZIAN, M. & LI-JESSEN, N. Y. K. 2022. Decellularized extracellular matrix: New promising and challenging biomaterials for regenerative medicine. *Biomaterials,* 289**,** 121786.

CALIARI, S. R. & BURDICK, J. A. 2016. A practical guide to hydrogels for cell culture. *Nat Methods,* 13**,** 405-14.

CHAUDHURI, O. 2017. Viscoelastic hydrogels for 3D cell culture. *Biomater Sci,* 5**,** 1480-1490.

CHAUDHURI, O., COOPER-WHITE, J., JANMEY, P. A., MOONEY, D. J. & SHENOY, V. B. 2020. Effects of extracellular matrix viscoelasticity on cellular behaviour. *Nature,* 584**,** 535-546.

CHEJARA, D. R., KONDAVEETI, S., PRASAD, K. & SIDDHANTA, A. K. 2013. Studies on the structure–property relationship of sodium alginate based thixotropic hydrogels. *RSC Advances,* 3.

DAVIS, G. E. & SENGER, D. R. 2005. Endothelial extracellular matrix: biosynthesis, remodeling, and functions during vascular morphogenesis and neovessel stabilization. *Circulation research,* 97**,** 1093-107.

DE HILSTER, R. H. J., SHARMA, P. K., JONKER, M. R., WHITE, E. S., GERCAMA, E. A., ROOBEEK, M., TIMENS, W., HARMSEN, M. C., HYLKEMA, M. N. & BURGESS, J. K. 2020. Human lung extracellular matrix hydrogels resemble the stiffness and viscoelasticity of native lung tissue. *Am J Physiol Lung Cell Mol Physiol,* 318**,** L698-L704.

DUARTE, M. M., SILVA, I. V., EISENHUT, A. R., BIONDA, N., DUARTE, A. R. C. & OLIVEIRA, A. L. 2022. Contributions of supercritical fluid technology for advancing decellularization and postprocessing of viable biological materials. *Mater Horiz,* 9**,** 864-891.

EBRAHIMI SADRABADI, A., BAEI, P., HOSSEINI, S. & BAGHABAN ESLAMINEJAD, M. 2021. Decellularized Extracellular Matrix as a Potent Natural Biomaterial for Regenerative Medicine. *Adv Exp Med Biol,* 1341**,** 27-43.

EDMONDSON, R., BROGLIE, J. J., ADCOCK, A. F. & YANG, L. 2014. Three-dimensional cell culture systems and their applications in drug discovery and cell-based biosensors. *Assay Drug Dev Technol,* 12**,** 207-18.

ENGLER, A. J., SEN, S., SWEENEY, H. L. & DISCHER, D. E. 2006. Matrix elasticity directs stem cell lineage specification. *Cell,* 126**,** 677-89.

GILBERT, T. W., FREUND, J. M. & BADYLAK, S. F. 2009. Quantification of DNA in biologic scaffold materials. *J Surg Res,* 152**,** 135-9.

GOPAL, S., MULTHAUPT, H. A. B. & COUCHMAN, J. R. 2020. Calcium in Cell-Extracellular Matrix Interactions. *Adv Exp Med Biol,* 1131**,** 1079-1102.

GORDON, E., SCHIMMEL, L. & FRYE, M. 2020. The Importance of Mechanical Forces for in vitro Endothelial Cell Biology. *Front Physiol,* 11**,** 684.

GUO, Y., MEI, F., HUANG, Y., MA, S., WEI, Y., ZHANG, X., XU, M., HE, Y., HENG, B. C., CHEN, L. & DENG, X. 2022. Matrix stiffness modulates tip cell formation through the p-PXN-Rac1-YAP signaling axis. *Bioact Mater,* 7**,** 364-376.

HANDORF, A. M., ZHOU, Y., HALANSKI, M. A. & LI, W. J. 2015. Tissue stiffness dictates development, homeostasis, and disease progression. *Organogenesis,* 11**,** 1-15.

HASSAN, B. H., ALHAMDAN, A. M. & ELANSARI, A. M. 2005. Stress relaxation of dates at khalal and rutab stages of maturity. *Journal of Food Engineering,* 66**,** 439-445.

HONG, X., STEGEMANN, J. P. & DENG, C. X. 2016. Microscale characterization of the viscoelastic properties of hydrogel biomaterials using dual-mode ultrasound elastography. *Biomaterials,* 88**,** 12-24.

HYNES, R. O. & NABA, A. 2012. Overview of the matrisome--an inventory of extracellular matrix constituents and functions. *Cold Spring Harb Perspect Biol,* 4**,** a004903.

JAALOUK, D. E. & LAMMERDING, J. 2009. Mechanotransduction gone awry. *Nat Rev Mol Cell Biol,* 10**,** 63-73.

JACHOWICZ, J., MCMULLEN, R. & PRETTYPAUL, D. 2007. Indentometric analysis of in vivo skin and comparison with artificial skin models. *Skin Res Technol,* 13**,** 299-309.

JENSEN, C. & TENG, Y. 2020. Is It Time to Start Transitioning From 2D to 3D Cell Culture? *Front Mol Biosci,* 7**,** 33.

KARAMANOS, N. K., THEOCHARIS, A. D., PIPERIGKOU, Z., MANOU, D., PASSI, A., SKANDALIS, S. S., VYNIOS, D. H., ORIAN-ROUSSEAU, V., RICARD-BLUM, S., SCHMELZER, C. E. H., DUCA, L., DURBEEJ, M., AFRATIS, N. A., TROEBERG, L., FRANCHI, M., MASOLA, V. & ONISTO, M. 2021. A guide to the composition and functions of the extracellular matrix. *Febs j,* 288**,** 6850-6912.

KIM, H., KANG, B., CUI, X., LEE, S. H., LEE, K., CHO, D. W., HWANG, W., WOODFIELD, T. B. F., LIM, K. S. & JANG, J. 2021. Light-Activated Decellularized

Extracellular Matrix-Based Bioinks for Volumetric Tissue Analogs at the Centimeter Scale. *Advanced Functional Materials,* 31.

LI, M., ZHANG, X., WANG, M., WANG, Y., QIAN, J., XING, X., WANG, Z., YOU, Y., GUO, K., CHEN, J., GAO, D., ZHAO, Y., ZHANG, L., CHEN, R., CUI, J. & REN, Z. 2022. Activation of Piezo1 contributes to matrix stiffness-induced angiogenesis in hepatocellular carcinoma. *Cancer Commun (Lond)*.

LIGUORI, G. R., LIGUORI, T. T. A., DE MORAES, S. R., SINKUNAS, V., TERLIZZI, V., VAN DONGEN, J. A., SHARMA, P. K., MOREIRA, L. F. P. & HARMSEN, M. C. 2020. Molecular and Biomechanical Clues From Cardiac Tissue Decellularized Extracellular Matrix Drive Stromal Cell Plasticity. *Front Bioeng Biotechnol,* 8**,** 520.

LIGUORI, T. T. A., LIGUORI, G. R., VAN DONGEN, J. A., MOREIRA, L. F. P. & HARMSEN, M. C. 2021. Bioactive decellularized cardiac extracellular matrix-based hydrogel as a sustained-release platform for human adipose tissue-derived stromal cell-secreted factors. *Biomed Mater,* 16**,** 025022.

LOESSNER, D., MEINERT, C., KAEMMERER, E., MARTINE, L. C., YUE, K., LEVETT, P. A., KLEIN, T. J., MELCHELS, F. P. W., KHADEMHOSSEINI, A. & HUTMACHER, D. W. 2016. Functionalization, preparation and use of cell-laden gelatin methacryloyl–based hydrogels as modular tissue culture platforms. *Nature Protocols,* 11**,** 727-746.

MARTINEZ-GARCIA, F. D. 2022. *Characterising the elastic and viscoelastic interaction between the cell and its matrix in 3D: because it takes two to salsa dance.* PhD PhD, Groningen.

MARTINEZ-GARCIA, F. D., DE HILSTER, R. H. J., SHARMA, P. K., BORGHUIS, T., HYLKEMA, M. N., BURGESS, J. K. & HARMSEN, M. C. 2021a. Architecture and Composition Dictate Viscoelastic Properties of Organ-Derived Extracellular Matrix Hydrogels. *Polymers,* 13.

MARTINEZ-GARCIA, F. D., FISCHER, T., HAYN, A., MIERKE, C. T., BURGESS, J. K. & HARMSEN, M. C. 2022a. A Beginner's Guide to the Characterization of Hydrogel Microarchitecture for Cellular Applications. *Gels,* 8.

MARTINEZ-GARCIA, F. D., VALK, M. M., SHARMA, P. K., BURGESS, J. K. & HARMSEN, M. C. 2021b. Adipose Tissue-Derived Stromal Cells Alter the Mechanical

Stability and Viscoelastic Properties of Gelatine Methacryloyl Hydrogels. *International Journal of Molecular Sciences,* 22.

MARTINEZ-GARCIA, F. D., VAN DONGEN, J. A., BURGESS, J. K. & HARMSEN, M. C. 2022b. Matrix Metalloproteases from Adipose Tissue-Derived Stromal Cells Are Spatiotemporally Regulated by Hydrogel Mechanics in a 3D Microenvironment. *Bioengineering (Basel),* 9.

MARTINO, F., PERESTRELO, A. R., VINARSKY, V., PAGLIARI, S. & FORTE, G. 2018. Cellular Mechanotransduction: From Tension to Function. *Front Physiol,* 9**,** 824.

MEWHORT, H. E. M., SVYSTONYUK, D. A., TURNBULL, J. D., TENG, G., BELKE, D. D., GUZZARDI, D. G., PARK, D. S., KANG, S., HOLLENBERG, M. D. & FEDAK, P. W. M. 2017. Bioactive Extracellular Matrix Scaffold Promotes Adaptive Cardiac Remodeling and Repair. *JACC Basic Transl Sci,* 2**,** 450-464.

MIERKE, C. T. 2021. Viscoelasticity Acts as a Marker for Tumor Extracellular Matrix Characteristics. *Front Cell Dev Biol,* 9**,** 785138.

MIGULINA, N., TJIN, G., FAIZ, A., BORGHUIS, T., ZHAO, F., KAPER, H. J., METZLAR, M., VAN DIJK, E., SHARMA, P. K., TIMENS, W., GOSENS, R., BRANDSMA, C. A. & BURGESS, J. K. 2022. Differential roles for lysyl oxidase (like), family members in chronic obstructive pulmonary disease; from gene and protein expression to function. *Faseb j,* 36**,** e22374.

MITCHELL, J. R. & BLANSHARD, J. M. V. 1976. Rheological Properties of Alginate Gels. *Journal of Texture Studies,* 7**,** 219-234.

MONTESANO, R. & ORCI, L. 1985. Tumor-promoting phorbol esters induce angiogenesis in vitro. *Cell,* 42**,** 469-77.

MOURA, B. S., MONTEIRO, M. V., FERREIRA, L. P., LAVRADOR, P., GASPAR, V. M. & MANO, J. F. 2022. Advancing Tissue Decellularized Hydrogels for Engineering Human Organoids. *Advanced Functional Materials,* 32.

MRUGACZ, M., BRYL, A., FALKOWSKI, M. & ZORENA, K. 2021. Integrins: An Important Link between Angiogenesis, Inflammation and Eye Diseases. *Cells,* 10.

NAM, S., HU, K. H., BUTTE, M. J. & CHAUDHURI, O. 2016. Strain-enhanced stress relaxation impacts nonlinear elasticity in collagen gels. *Proceedings of the National Academy of Sciences,* 113**,** 5492-5497.

NEHLS, V., SCHUCHARDT, E. & DRENCKHAHN, D. 1994. The effect of fibroblasts, vascular smooth muscle cells, and pericytes on sprout formation of endothelial cells in a fibrin gel angiogenesis system. *Microvasc Res,* 48**,** 349-63.

NICOSIA, R. F. & OTTINETTI, A. 1990. Modulation of microvascular growth and morphogenesis by reconstituted basement membrane gel in three-dimensional cultures of rat aorta: a comparative study of angiogenesis in matrigel, collagen, fibrin, and plasma clot. *In Vitro Cell Dev Biol,* 26**,** 119-28.

NISHIGUCHI, A. & TAGUCHI, T. 2021. A pH-driven genipin gelator to engineer decellularized extracellular matrix-based tissue adhesives. *Acta Biomater,* 131**,** 211-221.

NIZAMOGLU, M., DE HILSTER, R. H. J., ZHAO, F., SHARMA, P. K., BORGHUIS, T., HARMSEN, M. C. & BURGESS, J. K. 2022. An in vitro model of fibrosis using crosslinked native extracellular matrix-derived hydrogels to modulate biomechanics without changing composition. *Acta Biomater*.

PADUANO, F., MARRELLI, M., WHITE, L. J., SHAKESHEFF, K. M. & TATULLO, M. 2016. Odontogenic Differentiation of Human Dental Pulp Stem Cells on Hydrogel Scaffolds Derived from Decellularized Bone Extracellular Matrix and Collagen Type I. *PLoS One,* 11**,** e0148225.

PARTHIBAN, S. P., ATHIRASALA, A., TAHAYERI, A., ABDELMONIEM, R., GEORGE, A. & BERTASSONI, L. E. 2021. BoneMA-synthesis and characterization of a methacrylated bone-derived hydrogel for bioprinting ofin-vitrovascularized tissue constructs. *Biofabrication,* 13.

PATINO VARGAS, M. I., MARTINEZ-GARCIA, F. D., OFFENS, F., BECERRA, N. Y., RESTREPO, L. M., VAN DER MEI, H. C., HARMSEN, M. C., VAN KOOTEN, T. G. & SHARMA, P. K. 2022. Viscoelastic properties of plasma-agarose hydrogels dictate favorable fibroblast responses for skin tissue engineering applications. *Biomater Adv,* 139**,** 212967.

PETERSON, B. W., VAN DER MEI, H. C., SJOLLEMA, J., BUSSCHER, H. J. & SHARMA, P. K. 2013. A distinguishable role of eDNA in the viscoelastic relaxation of biofilms. *mBio,* 4**,** e00497-13.

PETROU, C. L., D'OVIDIO, T. J., BÖLÜKBAS, D. A., TAS, S., BROWN, R. D., ALLAWZI, A., LINDSTEDT, S., NOZIK-GRAYCK, E., STENMARK, K. R., WAGNER, D. E. & MAGIN, C. M. 2020. Clickable decellularized extracellular matrix as a new tool for building hybrid-hydrogels to model chronic fibrotic diseases in vitro. *J Mater Chem B,* 8**,** 6814-6826.

POOLE, J. J. A. & MOSTAÇO-GUIDOLIN, L. B. 2021. Optical Microscopy and the Extracellular Matrix Structure: A Review. *Cells,* 10.

PORZIONATO, A., STOCCO, E., BARBON, S., GRANDI, F., MACCHI, V. & DE CARO, R. 2018. Tissue-Engineered Grafts from Human Decellularized Extracellular Matrices: A Systematic Review and Future Perspectives. *Int J Mol Sci,* 19.

RACIOPPI, L. & MEANS, A. R. 2012. Calcium/calmodulin-dependent protein kinase kinase 2: roles in signaling and pathophysiology. *J Biol Chem,* 287**,** 31658-65.

RAVICHANDRAN, A., MUREKATETE, B., MOEDDER, D., MEINERT, C. & BRAY, L. J. 2021. Photocrosslinkable liver extracellular matrix hydrogels for the generation of 3D liver microenvironment models. *Sci Rep,* 11**,** 15566.

RIAL, R., LIU, Z. & RUSO, J. M. 2020. Soft Actuated Hybrid Hydrogel with Bioinspired Complexity to Control Mechanical Flexure Behavior for Tissue Engineering. *Nanomaterials (Basel),* 10.

RICARD-BLUM, S. & SALZA, R. 2014. Matricryptins and matrikines: biologically active fragments of the extracellular matrix. *Exp Dermatol,* 23**,** 457-63.

RICARD-BLUM, S. & VALLET, S. D. 2016. Matricryptins Network with Matricellular Receptors at the Surface of Endothelial and Tumor Cells. *Front Pharmacol,* 7**,** 11.

ROWLANDS, A. S., GEORGE, P. A. & COOPER-WHITE, J. J. 2008. Directing osteogenic and myogenic differentiation of MSCs: interplay of stiffness and adhesive ligand presentation. *Am J Physiol Cell Physiol,* 295**,** C1037-44.

ROZENBAUM, R. T., VAN DER MEI, H. C., WOUDSTRA, W., DE JONG, E. D., BUSSCHER, H. J. & SHARMA, P. K. 2019. Role of Viscoelasticity in Bacterial Killing

by Antimicrobials in Differently Grown Pseudomonas aeruginosa Biofilms. *Antimicrob Agents Chemother,* 63.

RUOSLAHTI, E. 1996. RGD and other recognition sequences for integrins. *Annu Rev Cell Dev Biol,* 12**,** 697-715.

SALDIN, L. T., CRAMER, M. C., VELANKAR, S. S., WHITE, L. J. & BADYLAK, S. F. 2017. Extracellular matrix hydrogels from decellularized tissues: Structure and function. *Acta Biomater,* 49**,** 1-15.

SALEH, K. S., HEWAWASAM, R., ŠERBEDŽIJA, P., BLOMBERG, R., NORELDEEN, S. E., EDELMAN, B., SMITH, B. J., RICHES, D. W. H. & MAGIN, C. M. 2022. Engineering Hybrid-Hydrogels Comprised of Healthy or Diseased Decellularized Extracellular Matrix to Study Pulmonary Fibrosis. *Cellular and Molecular Bioengineering*.

SATHAYE, S., MBI, A., SONMEZ, C., CHEN, Y., BLAIR, D. L., SCHNEIDER, J. P. & POCHAN, D. J. 2015. Rheology of peptide- and protein-based physical hydrogels: are everyday measurements just scratching the surface? *Wiley Interdiscip Rev Nanomed Nanobiotechnol,* 7**,** 34-68.

SEIF-NARAGHI, S. B., HORN, D., SCHUP-MAGOFFIN, P. J. & CHRISTMAN, K. L. 2012. Injectable extracellular matrix derived hydrogel provides a platform for enhanced retention and delivery of a heparin-binding growth factor. *Acta Biomater,* 8**,** 3695-703.

SINGELYN, J. M., DEQUACH, J. A., SEIF-NARAGHI, S. B., LITTLEFIELD, R. B., SCHUP-MAGOFFIN, P. J. & CHRISTMAN, K. L. 2009. Naturally derived myocardial matrix as an injectable scaffold for cardiac tissue engineering. *Biomaterials,* 30**,** 5409-16.

SONG, Y. H., MAYNES, M. A., HLAVAC, N., VISOSEVIC, D., DARAMOLA, K. O., PORVASNIK, S. L. & SCHMIDT, C. E. 2021. Development of novel apoptosis-assisted lung tissue decellularization methods. *Biomater Sci,* 9**,** 3485-3498.

STEVENS, H. Y., BOWLES, A. C., YEAGO, C. & ROY, K. 2020. Molecular Crosstalk Between Macrophages and Mesenchymal Stromal Cells. *Front Cell Dev Biol,* 8**,** 600160.

STOJKOV, G., NIYAZOV, Z., PICCHIONI, F. & BOSE, R. K. 2021. Relationship between Structure and Rheology of Hydrogels for Various Applications. *Gels,* 7.

TERLIZZI, V., KOLIBABKA, M., BURGESS, J. K., HAMMES, H. P. & HARMSEN, M. C. 2018. The Pericytic Phenotype of Adipose Tissue-Derived Stromal Cells Is Promoted by NOTCH2. *Stem Cells,* 36**,** 240-251.

TOLEDO, L., PALACIO, D. A. & URBANO, B. F. 2020. Tuning the softness of poly(2-hydroxyethyl methacrylate) nanocomposite hydrogels through the addition of PEG coated nanoparticles. *J Colloid Interface Sci,* 578**,** 749-757.

TRAVERSE, J. H., HENRY, T. D., DIB, N., PATEL, A. N., PEPINE, C., SCHAER, G. L., DEQUACH, J. A., KINSEY, A. M., CHAMBERLIN, P. & CHRISTMAN, K. L. 2019. First-in-Man Study of a Cardiac Extracellular Matrix Hydrogel in Early and Late Myocardial Infarction Patients. *JACC Basic Transl Sci,* 4**,** 659-669.

TSUCHIYA, T., BALESTRINI, J. L., MENDEZ, J., CALLE, E. A., ZHAO, L. & NIKLASON, L. E. 2014. Influence of pH on extracellular matrix preservation during lung decellularization. *Tissue Eng Part C Methods,* 20**,** 1028-36.

UHL, F. E., ZHANG, F., POULIOT, R. A., URIARTE, J. J., ROLANDSSON ENES, S., HAN, X., OUYANG, Y., XIA, K., WESTERGREN-THORSSON, G., MALMSTRÖM, A., HALLGREN, O., LINHARDT, R. J. & WEISS, D. J. 2020. Functional role of glycosaminoglycans in decellularized lung extracellular matrix. *Acta Biomater,* 102**,** 231-246.

VAN DONGEN, J. A., GETOVA, V., BROUWER, L. A., LIGUORI, G. R., SHARMA, P., STEVENS, H. P., VAN DER LEI, B. & HARMSEN, M. C. 2019a. Adipose tissue-derived extracellular matrix hydrogels as a release platform for secreted paracrine factors. *J Tissue Eng Regen Med*.

VAN DONGEN, J. A., GETOVA, V., BROUWER, L. A., LIGUORI, G. R., SHARMA, P. K., STEVENS, H. P., VAN DER LEI, B. & HARMSEN, M. C. 2019b. Adipose tissue-derived extracellular matrix hydrogels as a release platform for secreted paracrine factors. *J Tissue Eng Regen Med,* 13**,** 973-985.

VRIEND, L., SINKUNAS, V., CAMARGO, C. P., VAN DER LEI, B., HARMSEN, M. C. & VAN DONGEN, J. A. 2021. Extracellular matrix-derived hydrogels to augment dermal wound healing: a systematic review. *Tissue Eng Part B Rev*.

VRIEND, L., VAN DONGEN, J., SINKUNAS, V., BROUWER, L., BUIKEMA, H., MOREIRA, L., GEMPERLI, R., BONGIOVANNI, L., DE BRUIN, A., VAN DER LEI,

B., CAMARGO, C. & HARMSEN, M. C. 2022. Limited efficacy of adipose stromal cell secretome-loaded skin-derived hydrogels to augment skin flap regeneration in rats. *Stem Cells Dev*.

VÝBORNÝ, K., VALLOVÁ, J., KOČÍ, Z., KEKULOVÁ, K., JIRÁKOVÁ, K., JENDELOVÁ, P., HODAN, J. & KUBINOVÁ, Š. 2019. Genipin and EDC crosslinking of extracellular matrix hydrogel derived from human umbilical cord for neural tissue repair. *Sci Rep,* 9**,** 10674.

WADMAN, M. 2023. FDA no longer has to require animal testing for new drugs. *Science,* 379**,** 127-128.

WAN, L. Q., JIANG, J., MILLER, D. E., GUO, X. E., MOW, V. C. & LU, H. H. 2011. Matrix deposition modulates the viscoelastic shear properties of hydrogel-based cartilage grafts. *Tissue Eng Part A,* 17**,** 1111-22.

WANG, N., BUTLER, J. P. & INGBER, D. E. 1993. Mechanotransduction across the cell surface and through the cytoskeleton. *Science,* 260**,** 1124-7.

WEI, Z., SCHNELLMANN, R., PRUITT, H. C. & GERECHT, S. 2020. Hydrogel Network Dynamics Regulate Vascular Morphogenesis. *Cell Stem Cell,* 27**,** 798-812.e6.

XIA, B. & CHEN, G. 2022. Research progress of natural tissue-derived hydrogels for tissue repair and reconstruction. *Int J Biol Macromol,* 214**,** 480-491.

YANG, J., CRAMER, H. C., BREMER, E. C., BUYUKOZTURK, S., YIN, Y. & FRANCK, C. 2022. Mechanical characterization of agarose hydrogels and their inherent dynamic instabilities at ballistic to ultra-high strain-rates via inertial microcavitation. *Extreme Mechanics Letters,* 51.

YAO, T. & ASAYAMA, Y. 2017. Animal-cell culture media: History, characteristics, and current issues. *Reprod Med Biol,* 16**,** 99-117.

ZHANG, R., XU, Q., TAO, Y. & WANG, X. 2021. Rheological and pH dependent properties of injectable and controlled release hydrogels based on mushroom hyperbranched polysaccharide and xanthan gum. *Carbohydrate Polymer Technologies and Applications,* 2.

Chapter 3

Fibroblasts alter the physical properties of dermal ECM-derived hydrogels to create a pro-angiogenic microenvironment

Meng Zhang [1,2], **Fenghua Zhao [2,3]**, Xue Zhang[1,2], Linda A. Brouwer [1], Janette K. Burgess [1,2,4] and Martin C. Harmsen [1,2,4]

1 University of Groningen, University Medical Centre Groningen, Department of Pathology and Medical Biology, Hanzeplein 1 (EA11), 9713 GZ Groningen, The Netherlands

2 University of Groningen, University Medical Centre Groningen, W.J. Kolff Institute for Biomedical Engineering and Materials Science-FB41, A. Deusinglaan 1, 9713 AV Groningen, The Netherlands

3 University of Groningen, University Medical Centre Groningen, Department of Biomedical Engineering-FB40, A. Deusinglaan 1, 9713 AV Groningen, The Netherlands

4 University of Groningen, University Medical Centre Groningen, Groningen Research Institute for Asthma and COPD (GRIAC), Hanzeplein 1 (EA11), 9713 AV Groningen, The Netherlands

Materials Today Bio

https://doi.org/10.1016/j.mtbio.2023.100842

Chapter 3

Abstract: This study aimed to investigate the impact of fibroblasts (MRC-5) on the extracellular matrix (ECM) microenvironment of endothelial cells (ECs) during the vascularization of skin-derived ECM hydrogel in vitro. Two types of ECs were studied: human dermal microvascular endothelial cells (HMEC) and human pulmonary microvascular endothelial cells (HPMEC). Results showed that the presence of MRC-5 fibroblasts increased the stiffness of the hydrogel and led to larger fiber diameters and increased porosity. Extensive collagen fiber remodeling occurred in the ECM hydrogel with MRC-5 fibroblasts. Additionally, higher levels of fibulin-1 and fibronectin were deposited in the hydrogel when co-cultured with MRC-5 fibroblasts. These findings suggest that MRC-5 fibroblasts play a role in modifying the ECM microenvironment, promoting vascularization through dynamic ECM remodeling.

Keywords: Vascularization, Extracellular matrix, ECM hydrogel, Endothelial cells, fibronectin, collagen, biomechanics.

1. Introduction

The skin, the largest organ of the human body, is constantly exposed to external injuries. As a result, the importance of wound healing therapy becomes particularly relevant, especially in the case of patients with persistent chronic dermal wounds, such as those suffering from diabetes [1, 2]. The process of dermal wound healing is intricate and involves four overlapping phases: hemostasis, inflammation, proliferation, and tissue remodeling or resolution [3, 4]. The inflammatory and subsequent phases rely on adequate neo-vascularization (referred to as vascularization hereafter), which is the formation of new blood vessels [5] [6]. These blood vessels facilitate the delivery of oxygen and nutrients and the disposal of waste products while also providing the gateway for the trafficking of regulatory immune cells [7].

The extracellular matrix (ECM) supports vascularization both biochemically and structurally [8, 9]. The ECM acts as a reservoir for angiogenic factors, such as vascular endothelial growth factor (VEGF), angiopoietin 2, and fibroblast growth factors (FGF) [10]. These factors are bound to glycosaminoglycans (GAGs) in the ECM and are released in response to specific signals to stimulate the proliferation, migration [11, 12], and differentiation of endothelial cells (ECs) [13]. Moreover, through adhesive interactions with integrins on the surface of ECs [14], ECM provides a scaffold that supports the growth and organization of ECs [10]. In addition to serving as a scaffold and supporting interaction with other cells, mechanical features of the ECM, such as stiffness, are sensed by virtually all cell types. They (mechano) transduce externally exerted forces to downstream pathways that regulate cell phenotype and function [15].

Mesenchymal cells like fibroblasts are activated during the reparative phase of wound healing and are pivotal in angiogenesis [16, 17]. They secrete angiogenic growth factors, such as VEGF and FGF, which promote vascularization [18, 19]. Previously, we showed that mesenchymal stromal cells from adipose tissue (ASC) co-cultured with large vessel endothelial cells, (Human umbilical vein endothelial cells，HUVECs) act as pro-angiogenic pericytes and promote vascular network formation (VNF) through paracrine and juxtracrine signaling both on culture plates [20] and in the three-dimensional (3D) environment of Matrigel® [21]. In vitro, ASC not only deposit ECM components [22] but also degrade ECM through action of their secreted enzymes, including matrix metalloproteinases

(MMPs) [23]. In skin, the main mesenchymal cell type is the fibroblast which is a 'professional' matrix remodeler. Fibroblasts newly deposit ECM components, including collagen I, collagen III, proteoglycans, fibulins and fibronectin [24, 25]. The latter two are instrumental in vascularization processes. During ECM remodeling, fibroblasts also degrade ECM through secretion of MMPs [25], creating spaces and pathways for new blood vessels to grow and develop. This remodeling of ECM by fibroblasts regulates proliferation of ECs and stabilizes vessels. Matrigel® offers a 3D environment yet is basement-membrane-derived. Pure collagen type I hydrogels replicate the major ECM component of organs. Yet in our hands, collagen I hydrogels did not support vascularization by ECs irrespective of the presence of mesenchymal cells (unpublished data). Interestingly, human pulmonary microvascular endothelial cells (HPMEC) show vascularization in cardiac left ventricle ECM hydrogels irrespective of the presence of mesenchymal support cells [26], which raises the question what the role of mesenchymal cells is in vascularization by ECs in organ- derived ECM hydrogels. We hypothesized that mesenchymal cells remodel the ECM, altering the mechanical properties which augments vascularization. In the present study, we examined the impact of matrix remodeling by MRC- 5 fibroblasts on VNF by skin-derived microvascular endothelial cells (HMEC) and HPMEC (lung) in a skin-derived ECM hydrogel.

2. Materials and methods

2.1 Hydrogel Synthesis

Porcine skin was purchased from a slaughterhouse (Kroon Vlees, Groningen, The Netherlands). The skin was cut into small pieces (1 cm^3) and mixed with ice-cold Dulbecco's phosphate-buffered saline (DPBS) (Lonza Walkersville, Inc., Walkersville, MD, USA). The mixture was minced in a kitchen blender (Bourgini,The Netherlands) with DPBS until it formed a homogeneous paste. The tissue homogenate was sonicated using an Ultrasonic homogenizer (Sigma Aldrich, Amsterdam, the Netherlands) at 100% power for 1 min, collected by centrifugation, washed using DPBS twice, and incubated with 0.05% trypsin in DPBS (Thermo Fisher Scientific, Waltham, MA, USA) at 37 °C with constant shaking for 4 hours (h). After washing twice with PBS, the slurry was incubated in Milli-Q® water with constant shaking at 37°C overnight. Next, the tissue

homogenate was treated with excess saturated NaCl (6M) for 3 h. Subsequently, the homogenate was incubated in 1% SDS (Sigma-Aldrich, St. Louis, MO, USA) and 1% Triton X- 100 (Sigma-Aldrich), followed by 1% sodium deoxycholate (Sigma-Aldrich) and 30 µg/mL DNase (Roche Diagnostics GmbH, Mannheim, Germany) in 1.3 mM $MgSO_4$ and 2 mM $CaCl_2$, Milli-Q® water was used as the base solution. All incubations were under shaking at 37°C overnight. The crude ECM was washed three times with MilliQ® water between all incubations. Lastly, the homogenate was washed for an hour with DPBS under constant shaking, this process repeated six times, collected after centrifugation at 3000g, and 70% ethanol was added for overnight sterilization at room temperature. The skin ECM samples were frozen in liquid nitrogen and lyophilized with a freeze dryer (Labconco, Kansas City, MO, USA) before being ground to a fine powder with an Ultra-Turrax homogenizer (IKA, Staufen, Germany). To generate hydrogels, 20 mg/mL of ECM powder was digested with 2 mg/mL of porcine pepsin (Sigma-Aldrich, St. Louis, MO, USA) in 0.01M HCl with constant stirring at room temperature for 24h. After digestion, the ECM was neutralized by adding 1/10th volume 0.1M NaOH and subsequently 1/10th volume 10xDPBS to generate an isotonic and neutral pH ECM pregel which was stored at 4°C until use.

2.2 3D Cell Culture

Both human microvascular endothelial cells (HMEC-1[27], HMEC in the text) and human pulmonary microvascular endothelial cells (HPMEC-ST1.6R [28] HPMEC in the text, kind gift from Dr. Kirkpatrick, Johannes Gutenberg University, Mainz, Germany) were tagged with EGFP (green fluorescence) by third generation VSV-pseudotyped replication-deficient lentiviruses [29]. HPMEC were maintained in endothelial culture medium, consisting of RPMI-1640 (Lonza, Basel, Switzerland) with 20% heat-inactivated fetal bovine serum (FBS, Sigma-Aldrich, MO, United States), 1% penicillin/streptomycin (#15140122, Gibco Invitrogen, Carlsbad, CA, USA), 1% L-glutamine (#17- 605E, Lonza BioWhittaker, Verviers, Belgium), 5 U/mL heparin (LEO Laboratories Limited, Ballerup, Denmark), and 20 µg/mL of endothelial growth factors (EGF, home-made bovine brain extract[30]). HMEC were maintained in MCDB 131 (Gibco, Carlsbad, CA, USA) with 10% FBS, 10 mM L-glutamine, 10 ng/ml EGF + 1 µg/ml hydrocortisone (Sigma, MO, United States). Primary lung fibroblast, MRC-5[31], was lentiviral tagged with dTomato (red fluorescent) using third

generation VSV-pseudotyped replication-deficient lentiviruses as describe above. The fibroblasts were maintained in Ham's F-12K (#BE12-615F, Lonza BioWhittaker, Verviers, Belgium) with 10% fetal bovine serum and 1% penicillin/streptomycin. For co-culture experiments, 0.5x106 ECs and $0.5x10^6$ MRC-5 cells were suspended in 20 µL of RPMI-1640 (Lonza, Basel, Switzerland) which was carefully and homogeneously mixed with 200 µL of skin ECM pregel taking care to avoid trapping air bubbles. The resulting cell-gel mixtures were cast into individual wells of 48-well plates and incubated at 37°C for 1 hour to solidify the gel. Subsequently, 500 µL of endothelial culture medium was added to each well. As controls, hydrogels without cells were used, or hydrogels seeded with 0.5x106 of each individual cell type.

2.3 Fluorescence cell imaging

After 5 days of culturing at 37°C with 5% CO_2, inverted fluorescence microscopy (EVOS model M5000, Thermo Fisher) was used to acquire fluorescence micrographs to visualize the cells. ECs were visualized using GPF 'light cubes' (λex 470/522 nm/λem 525/550 nm), and MRC-5 using Texas Red 'light cubes' (λex 585/629 nm/λem 628/632 nm). VNF was further analyzed using densitometry, through processing the fluorescence micrographs with the Endothelial Tube Formation Assay—angiogenesis analyzer in Fiji [32]. It should be noted that the depth of field with the inverted microscope was restricted and only enabled assessment of the lower part of the hydrogels. The captured digital micrographs compressed the originally 3D situation onto a 2D plane which comprised the ability to distinguish between genuine branched tubes and tubes that crossed each other at different planes in the gel. While this caused a systemic error, and because no suitable 3D imaging and quantification software exists to date, we decided to process all images this way.

Live 3D scans of cell-seeded hydrogels were captured using a confocal laser scanning microscope Zeiss Cell Discoverer 7 imaging system (Zeiss, Jena, Germany). Optical settings were an objective lens magnification of 5× and an Optovar magnification of 1×. The interval of the scanning was 2.5 µm. Detection wavelengths (excitation–emission) were 450–550 nm for GFP and 550–700 nm for dTomato. Image stacks and videos were generated using Zeiss Zen 3.3 software.

2.4 Characterization of the mechanical properties

The gels loaded with cells were subjected to uniaxial compression with a 2.5 mm plunger at three locations [33, 34], at least 2 mm away from the edge of the gel and ensuring 2 mm or more between each compression site. The stress relaxation test was performed with a low-load compression tester (LLCT) in 'wet' mode and at room temperature. The LLCT load cell and linear positioning for control and data were acquired using LabVIEW 7.1 software [35]. During compression, the increase in stress was continuously measured and the slope between the stress and strain curve was taken as the elastic modulus. Once the strain reached 0.2, it was maintained at this level for 100 s and the stress was continuously monitored. Percentage stress relaxation was calculated by comparing the stress at t = 0 s and t = 100 s.

2.5 Second harmonic generation (SHG) microscopy

Hydrogels were fixed with 2% formalin for 24 h at 4 °C. Samples were embedded in 2% agarose (Roche diagnostics, Indianapolis, USA) in PBS to prevent the hydrogel shrinkage during the dehydration process and dehydrated in a graded series of 50%, 70%, 80%, 90%, and 100% ethanol, and incubated in xylol. The samples were paraffin-embedded and thin sections cut (4μm) and mounted on glass slides. Subsequently, the slides underwent deparaffinized with xylene and a graded ethanol series to rehydrate. Microscopy Aquatex (Merck KGaA, Darmstadt, Germany) was used as mounting medium. Second harmonics generation (SHG) imaging was performed using a multiphoton laser confocal scanning microscope (model Zeiss 780, Zeiss, Jena, Germany). Generally, non-centrosymmetric molecules such as collagen will cause harmonics at half (425 nm) the wavelength of the incident light (850 nm) from which both forward and backward signals can be acquired. For this study backward SHG signals were acquired, and image analysis was performed using Fiji with Macro TWOMBLI [36].

2.6 Hydrogel Ultrastructure

Hydrogel ultrastructure was investigated with scanning electron microscopy (SEM). Upon conclusion of culturing, hydrogels were fixed with 2.5% glutaraldehyde (111-30-8, Sigma, Darmstadt, Germany) and 2% paraformaldehyde in PBS at 4°C for 24 h. Then, the hydrogel was prepared

following the procedures outlined in previously published literature [37]. Hydrogels were washed three times with DPBS and once with Milli-Q® water to remove any remaining fixatives and salts. Samples were dehydrated in the same way and embedded in paraffin as described above for the SHG samples. Then, 50 µm thick sections were cut and mounted onto glass coverslips (size 18x18 mm). After drying, the sections were deparaffinized in xylene and rehydrated in a series of 100%, 96%, and 70% ethanol. Dry slides were glued on top of 6mm SEM pin stubs (Agar Scientific, Stansted, UK) and Carbon coated with Leica EM ACE600 sputter coater device (Leica Microsystems B.V., Amsterdam, Netherlands). Hydrogels were visualized at 5,000×, 10,000×, and 25,000× magnification, at 3 kV with Zeiss Supra 55 STEM (Carl Zeiss NTS GmbH). Image analysis was performed using Fiji with plugin diameter [38].

2.7 Immunofluorescence staining

Thin paraffin sections (4 µm) were deparaffinized and rehydrated. For antigen retrieval, slides were incubated in 10 mM citric acid (pH 6) at 85°C overnight. Slides were washed with demi water and PBS and subsequently blocked in 4% BSA for 15 min at room temperature. Afterwards, the slides were incubated 1.5 h with a rabbit anti-human fibronectin antibody (ab6584, Abcam, 1:100) or mouse anti-human a fibulin-1 antibody (ab211536, Abcam, 1:100) at room temperature. After that, the slides were washed in PBS 3 times and incubated with a secondary antibody; for fibronectin: goat anti- rabbit HRP (P0448, Dako, 1:200) and for fibulin-1: rabbit anti mouse (F0313, Dako, 1:200) for 1h. Opal 650 (Akoya Biosciences, 1:200) diluted in 0.1M borate buffer with 0.003% hydrogen peroxide (Merck, Darmstadt, Germany) was added and the slides incubated for 15 mins. The slides were washed with demi water 3 times and incubated with DAPI (4′,6-diamidino-2- phenylindole, Merck 1:5,000) for 10 mins. Images were generated using a SP8 confocal microscope (Leica, Wetzlar, Germany). The acquired staining images were subject to analysis using Fiji. Three lines were drawn at predetermined positions (top, middle, and bottom) across each image (Fig. S1A). Importantly, the positioning of these lines in the field of view remained constant across all images analyzed. The corresponding plot profiles for the fluorescence signals along these three lines were extracted by Fiji built-in function: plot profile. Each group included three images. All plot profiles were calculated with total area under the curve (TAUC) and peak area under the curve

(TPAUC).

2.8 Statistical analysis

All statistical analyzes were performed using GraphPad Prism v9.2.0 (San Diego, CA, USA). All data were scrutinized for outliers using the robust regression and outlier removal (ROUT) test. All data except LLCT data were analyzed with one-way ANOVA. LLCT data were analyzed with two-way ANOVA. Differences were considered significant at $p< 0.05$ in the corresponding statistical tests.

3. Results

3.1 Fibroblasts promote endothelial vascular network formation in skin- derived ECM hydrogels

Formation of branched and extensive VNF by HMEC and HPMEC had occurred in skin-derived ECM hydrogels after 5 days of culturing (Fig.1A). The VNF (Fig.1A, green) also occurred in the presence of fibroblasts (MRC5, Fig.1A, red) where the fibroblasts often aligned closely to the endothelial branches (Suppl. Fig. S2A and B).

The extent of the VNF was quantified to determine the number of master junctions (cells linking at least three branches), the number of branches, and the total branching length (resp. Fig.1B, C and D). The analysis of VNF formed by ECs were delineated as illustrated in Suppl. Fig. S2C. Fibroblasts increased the number of master junctions in HMEC networks compared to HMEC alone (resp 45.9 ± 38.2 vs 21.2 ± 15.9, $p<0.05$), and increased the number of master junctions produced by compared to HPMEC alone (resp 58.9 ± 56.9 vs 31.7 ± 24.4, $p < 0.05$) (Fig. 1B). In addition, fibroblasts enhanced the number of branches generated by the ECs. Specifically, fibroblasts augmented branching by HMEC (80.2 ± 21.9), compared to HMEC alone (62.1 ± 29.3, $p < 0.05$). Similarly, fibroblast boosted branching by HPMEC, 82.9 ± 24.4 branches vs 57.7 ± 31.3 branches by HPMEC alone ($p < 0.05$, Fig.1C). Fibroblasts augmented the total branching length within the VNF (Fig. 1D) by HMEC (9703 ± 5125 μm vs 5217 ± 3001 μm in controls, $p < 0.01$) and HPMEC (13551 ± 6102 vs 5670 ± 3965 μm in controls, $p < 0.0001$) compared to the ECs alone.

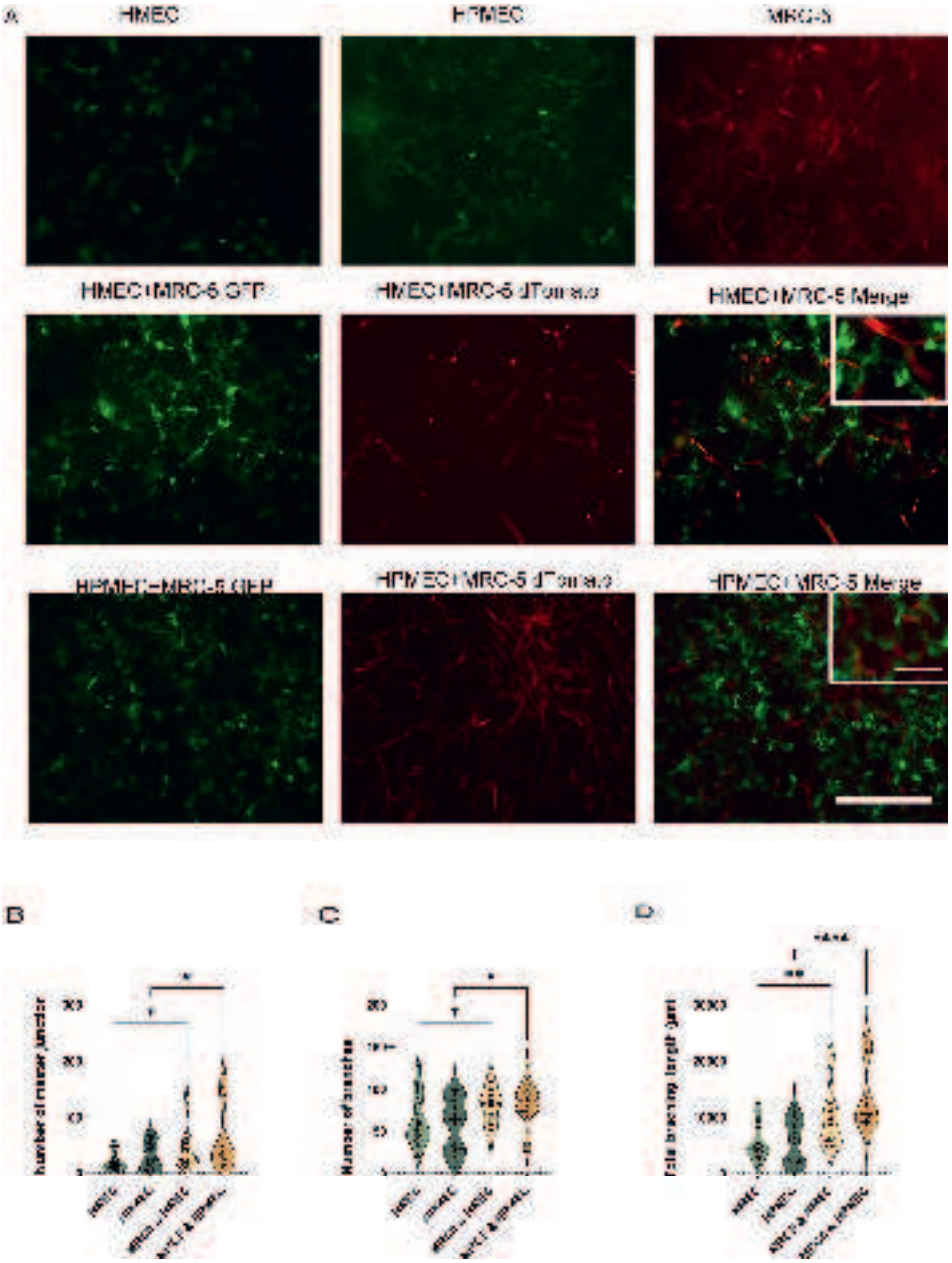

Figure 1. Vascular network formation (VNF) by endothelial cells (ECs) in a 3D culture system either alone or in co-culture with MRC-5 cells. (A) The EGFP- expressing human dermal microvascular endothelial cells (HMECs) or human pulmonary microvascular endothelial cells (HPMEC) (green) and dTomato- expressing MRC-5 fibroblasts (red) were cultured in 48-well plates for five days. Scale bar - 400 µm. (B) Comparison of the number of master junctions based on FIJI quantification of VNF by ECs either alone or

in co-culture with MRC-5 in skin extracellular matrix (ECM) hydrogels. (C) Comparison of the number of branches of VNF by ECs either alone or in co-culture in skin ECM hydrogels. (D) Comparison of total branching length based on FIJI quantification of VNF by ECs either alone or in co-culture with MRC-5 in skin ECM hydrogels. The data are from 7 independent experiments, while 3 different randomized regions were measured for every sample, each dot represents a measurement of a randomized region. Statistical testing by one-way ANOVA, * $p < 0.05$.

3.2 Fibroblasts acquire a pericytic position on endothelial branches in skin-ECM hydrogels

To further dissect the observed alignments and interactions of fibroblasts with endothelial tubes, real time 3D confocal laser scanning fluorescent microscopy (Zeiss Cell Discoverer 7) was used. The green channel was used to visualize the EGFP-tagged ECs, while the red channel was used to visualize the dTomato-tagged MRC-5 fibroblasts (Suppl. Video. S1). The video shows that branches of the tubes extended in all three dimensions and throughout the hydrogel. The meshes created by ECs had expanded to form a reticulated vascular-like network, to which the fibroblasts had aligned. Additionally, the fibroblasts had stretched into the ECM, indicating that these were in the process of remodeling the ECM that surrounded ECs and their network.

3.3 The changes of physical properties of skin ECM hydrogels by VNF is affected by fibroblasts

The stiffness of cell-loaded hydrogels was measured using a low-load compression tester (LLCT). After five days of culture, the stiffness of hydrogels containing ECs co-seeded with MRC-5 increased (Fig. 2A). In contrast, the stiffness of control gels i.e. seeded with only fibroblasts or ECs alone did not differ compared to day 1. Hydrogels containing co-cultures of fibroblasts and ECs had an almost twofold higher stiffness (resp. HMEC & MRC-5 and HPMEC & MRC-5: 651.7 ± 403.1 Pa and 661.9 ± 180.7 Pa) compared to controls (resp. HMEC and HPMEC: 386.9 ± 115.5 Pa, $p=0.0055$, and 383.7 ± 155.3 Pa, $p=0.0111$).

Besides the resistance to deformation i.e. stiffness (E), hydrogels comprise of a viscous component that dictates stress relaxation (σ). This is the time- dependent

decrease in stress under a constant strain. Both stiffness and stress relaxation of hydrogels were determined by compression testing after 20% strain and relaxation for 100s. After one day of culture, stress relaxation for all cell-loaded hydrogels was similar and reached close to 100% stress relaxation (Fig. 2B). Prolonged culturing (5 days) resulted in decreased stress relaxation in HMEC & fibroblast-seeded hydrogels compared to day 1 (Fig. 2B, resp. 66.8 ± 10.8 vs 86.7 ± 10.7, p= 0.0024). At day 5, hydrogels with fibroblasts co-cultured with HMEC or HPMEC had the largest reduction in stress relaxation compared to MRC-5 group (Fig. 2B, resp. 66.8 ± 10.8 vs 87.3 ± 8.4, p=0.0218 and 69.6 ± 16.3 vs 87.3 ± 8.4, p=0.0347). Stress relaxation of hydrogels with fibroblasts co-cultured with HMEC decreased compared to that in hydrogels with HMEC on day 5 (66.8 ± 10.8 vs 82.8 ± 15.78, p=0.0218).

Time to 50% stress relaxation is a surrogate measure for hydrogel strain release dynamics. After one day of culture, time to 50% relaxation did not differ between the different cell-seeded hydrogels yet the variation was large. The presence of fibroblasts and HMEC in the hydrogel increased time to 50% relaxation on day 5 compared to day 1 (Fig. 2C, 4.1 ± 2.7 vs 1.1± 0.6, P=0.0012). Hydrogels of fibroblasts co-seeded with HMEC tended to relax slower than HMEC only seeded hydrogels (4.1 ± 2.7 vs 1.3 ± 0.8, p<0.001) after 5 days of coculture, also hydrogel containing fibroblasts with HMEC increased time to 50% relaxation compared to MRC5 alone hydrogels (Fig. 2C, 4.1 ± 2.7 vs 1.2 ± 0.6, p<0.001).

Figure 2. Comparison of physical characteristics of skin ECM hydrogel loaded with ECs either alone or in co-culture with MRC-5 cells after one- and five-days culture. (A) Stiffness of skin ECM hydrogel loaded with ECs either alone or in co-culture with MRC-5 cells on days one and five. Skin ECM hydrogels were tested using low-load compression tester (LLCT) with a fixed 20% strain ratio. (B) Total stress relaxation of skin ECM hydrogel loaded with ECs either alone or in co-culture with MRC-5 cells on days one and five. After compressing the skin ECM hydrogel using LLCT with a fixed 20% strain ratio, the stress relaxation was recorded in 100s. (C) Time to 50% relaxation of skin ECM hydrogel loaded with ECs either alone or in co-culture with MRC-5 cells on day 1 and day 5. The data are from resp. three and five independent experiments for days one and five while three randomly selected spots on the hydrogel were measured for every single sample, and each dot represents a measurement. Statistical testing by two-way ANOVA, *$p < 0.05$, **$p < 0.0$, *** $p < 0.00$, **** $p < 0.0001$.

3.4 Remodeling of skin ECM hydrogels during VNF is augmented by fibroblasts

Second harmonic generation by 2-photon scattering confocal microscopy is an established method to visualize changes of collagen fiber architecture [39, 40]. Compared to blank skin-derived ECM hydrogels, the presence of cells altered the collagen architecture and increased the fiber density (Fig. 3A). In a bird's eye view the micrographs showed that after five days of culture fibroblast-seeded hydrogels did not differ from cell-free hydrogel controls (Fig. 3A). In contrast, five days of VNF led to a condensation of collagen fibers which appeared to be stimulated by fibroblasts (Fig. 3A), irrespective of the endothelial source. Hydrogels co-seeded with fibroblasts and ECs showed shorter and denser

collagen fibers compared to the ECs only control hydrogels. In contrast, the ECs only hydrogels displayed longer and thicker bundles of collagen fibers, with distinct intersecting gaps compared to the co- seeded groups. The collagen architecture was assessed by densitometry (Fig. 3B-J) using the TWOMBLI plugin in FIJI which generates several surrogate parameters as presented in the following. In general, these analyses confirmed the gross observations of the micrographs and showed that collagen architecture (endpoints, branching points, high density matrix (HDM) and fiber alignment) of cell-free gel was altered in ECs seeded gel during VNF. While collagen rearrangement was augmented by fibroblasts during VNF (Fig. 3B-E). Fibroblasts increased the density of the fibers in the co-cultured groups. While the number of branching points increased when fibroblasts were together with HMEC or HPMEC compared to ECs controls (HMEC & MRC5 vs HMEC: 76.6 ± 6.5 vs 63.9 ± 3.634, p=0.0063; HPMEC & MRC5 vs HPMEC: 76.85 ± 4.894 vs 59.50 ± 3.480 p=3.480, Fig.3C).

Moreover, fibroblasts increased the percentage of areas of high density of fibers in HPEMC-seeded hydrogels compared to HPMEC alone (10.0 ± 4.8 vs 1.8 ± 0.8, p=0.0021, Fig.3D). Fibroblasts also changed the patterns of the fiber arrangement. Fibroblasts decreased the alignment of the fibers in HPEMC-seeded hydrogels compared to HPMEC gels (0.07 ± 0.02 vs 0.12 ± 0.03, p=0.0185, Fig. 3E). The curvature of the collagen fibers, finally, is a parameter to reveal architectural remodeling and determines wave-like shapes. In other words, if fibers have a high frequency of bends and curves, this reflects as a high number below the arbitrary cutoff of 40 units. While above this threshold, this number is indicative of the wave amplitude, particularly for less ‘wavy’ fibers. Below 40 the curvature of the collagen fibers did not differ irrespective of the presence of cells. However, above the threshold, the curvature was higher in hydrogels loaded with HMEC alone compared to those co-cultured with fibroblasts and HMEC. This observation indicates that the fibers architecture was altered by cells (Fig. 3F – I).

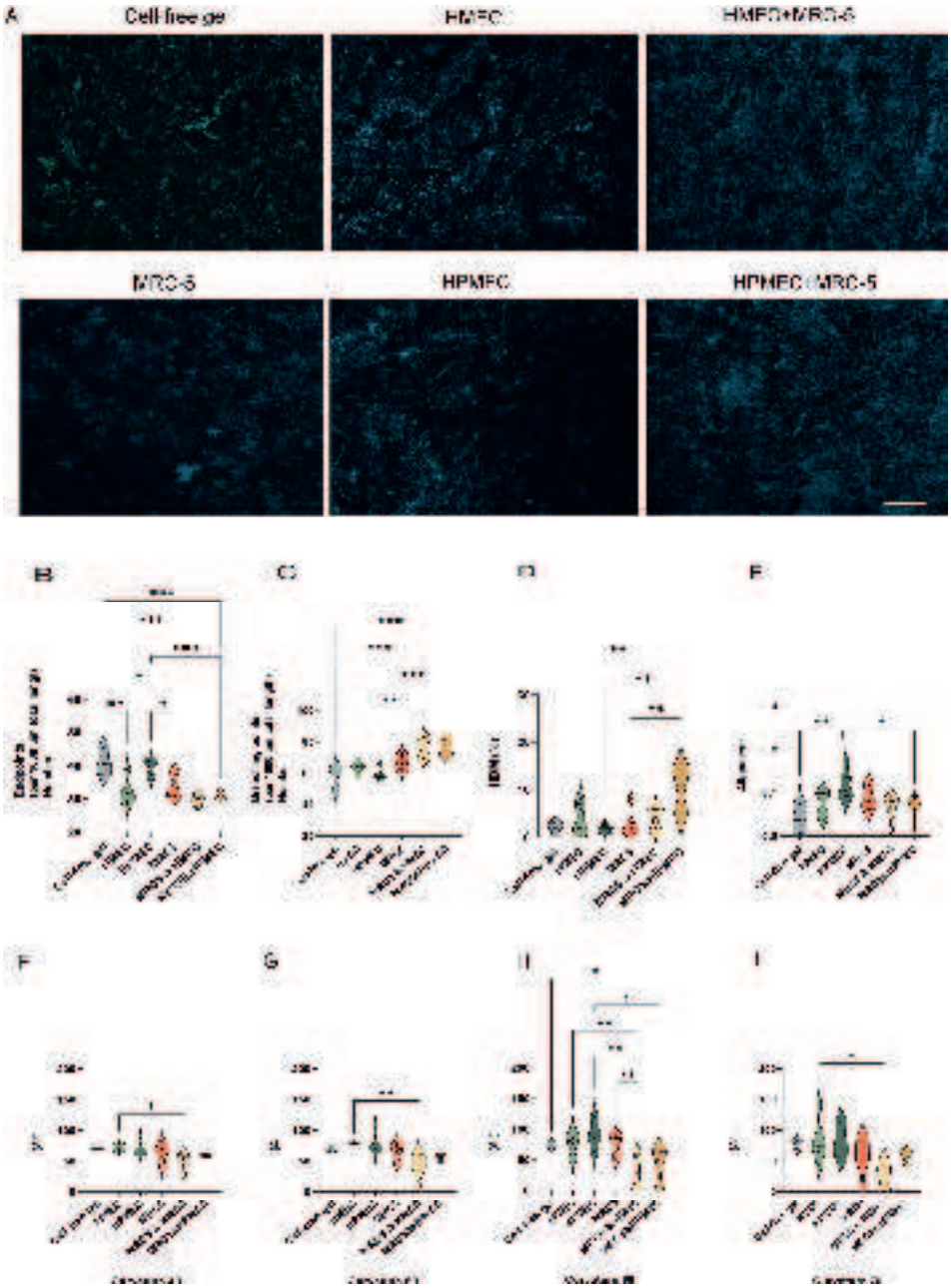

Figure 3. Remodeling of skin ECM hydrogels during VNF is augmented by fibroblasts. (A) Collagen fibers were detected by second harmonic generation (SHG) microscopy (scale bar - 50 µm). (B) Endpoints per 1,000 µm total length. (C) Branching points per 1,000 µm total length. (D) Percentage High-Density Matrix (HDM). (E) Fiber alignment. (F – I) Curvatures of resp. 40, 50, 60 and 70 arbitrary units. The data are generated from

five independent experiments while each dot represents a measurement on one SHG micrograph. Statistical testing by one-way ANOVA, * $p < 0.05$, ** $p < 0.01$.*** $p < 0.001$.

3.5 Fibroblasts promote pericellular matrix porosity through fiber condensation

The ultrastructure of the hydrogel was visualized by SEM (Fig. 4A). Irrespective of the presence of cells, the skin-derived ECM hydrogels comprised a network of more or less randomly organized fibers that were visible already at low magnifications (Fig. 4A, left columns). At higher magnifications, the fibers had variable thickness (Fig. 4A, right columns). The fibers showed the typical striped repeat pattern typical for collagen fibers (Suppl. Fig. S3). The matrix in the immediate surroundings of fibroblasts or endothelial tubes was reorganized by apparent thickening of the fibers creating pores (Fig. 4A, right columns). Fibers surrounding the cells, were assessed in 25,000-fold (25k) micrographs. The 'percentage of pores' corresponds to the proportion of pore area relative to the entire image. ECs had reduced the fraction of mesh holes compared to hydrogels without cells (HMEC 0.52 ± 0.006 vs 0.51 ± 0.005, $p= 0.0216$, and HPMEC 0.52 ± 0.006 vs 0.50 ± 0.005, $p= 0.0004$. Fig. 4B). While the mesh holes around fibroblasts did not differ from control hydrogels without cells, their co-culture with ECs increased the fraction of mesh holes compared to cell-free or EC-seeded hydrogels. The intersection density (the number of fiber overlaps divided by the total number of pixels in the assessed area) was affected by fibroblasts. The intersection density of fibers within hydrogels co-seeded with fibroblasts and HMEC was lower compared to hydrogels containing HMEC alone. (Lower than hydrogel without cells, Fig. 4C). ECs or fibroblasts alone, had no influence on the average collagen fiber diameter compared to cell- free hydrogels (Fig. 4D). Yet, fibroblasts co-seeded with the different types of ECs had opposite influences: fibroblast-HMEC co-cultures had increased collagen fiber diameters compared to HMEC-seeded or cell-free hydrogels. In contrast, HPMEC-fibroblast co-cultures had reduced collagen fiber diameters compared to fibroblasts alone, but these were similar to those seen with HPMEC alone (Fig. 4D).

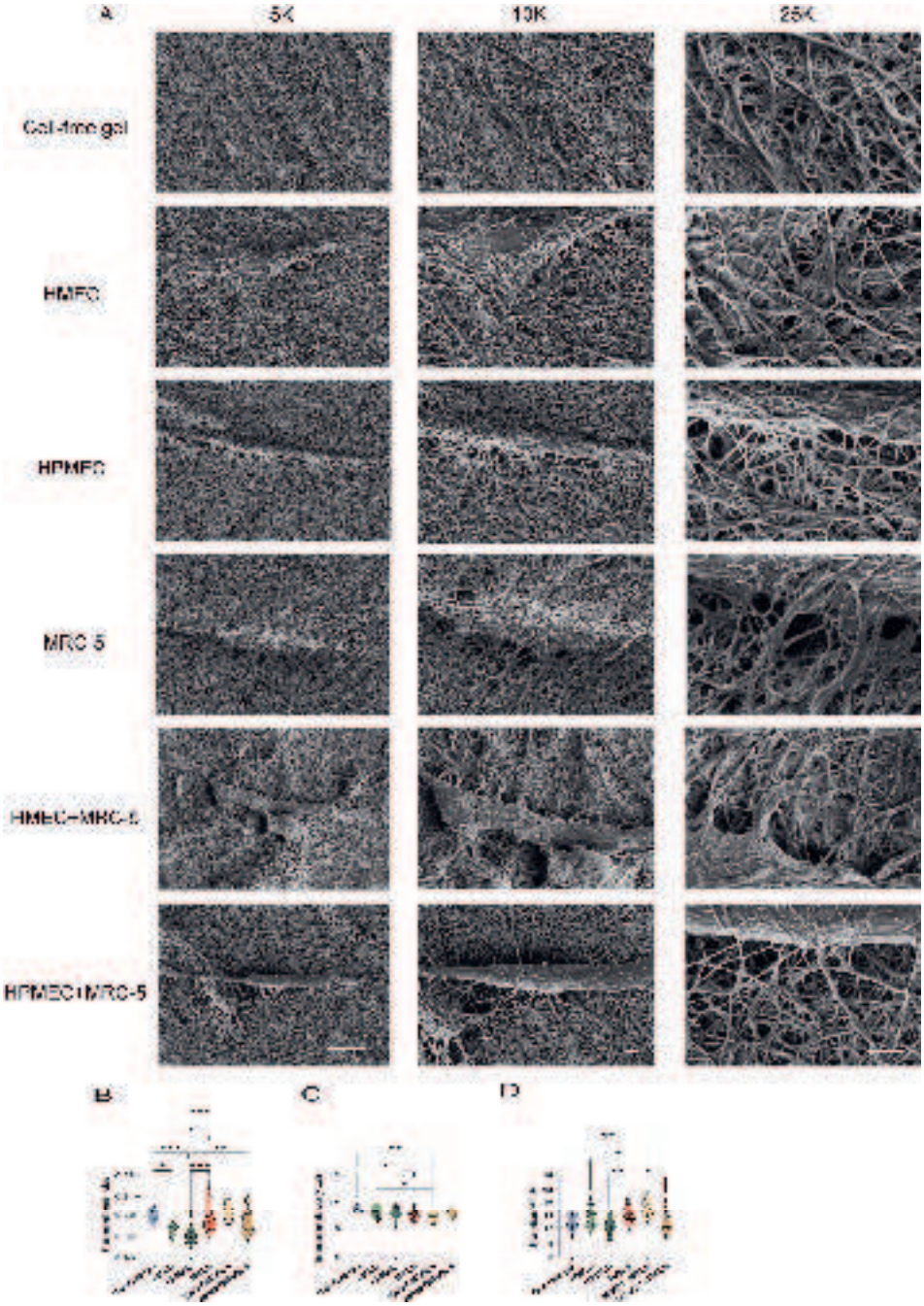

Figure 4. Ultrastructure of the extracellular matrix and analyses of the microstructure of the fibers and pores. (A) Fibers of the matrix were visualized by scanning electron microscopy (SEM) at three different magnifications: 5,000 (5k), 10,000 (10k), and 25,000 (25k). Scale bars represent 10 µm in 5k micrographs and 2 µm in both 10k and 25k

micrographs. (B) Mesh hole analysis of the fibers at 25k magnification. Percentage of porosity is the total number of holes pixels divided by the total image resolution. (C) Intersection density of the fibers at 25k magnification defined as [10,000 x (number of fiber overlaps) / (Total number of pixels in the micrograph)]. (D) Mean fiber diameter (μm). The data were generated from three independent experiments while three randomly selected regions were measured for every single sample, each dot represents a measurement of a randomized region. Statistical testing by one-way ANOVA comparing gel, * $p < 0.05$, ** $p < 0.01$.*** $p < 0.001$.

3.6 Fibroblasts promote deposition fibronectin and fibulin-1 during VNF

Cell-free skin-derived ECM hydrogels contained no detectable fibronectin, and during VNF by HMEC or HPMEC fibronectin deposition was minimal (Fig. 5). In contrast, fibroblasts deposited large amounts of fibronectin after five days of culture in the hydrogel (Fig. 5). Fibroblasts appeared to promote fibronectin deposition during VNF by either EC type compared to during EC VNF alone, yet this did not differ from the amount of fibronectin deposition by fibroblasts alone (Fig. 5). The cross-sectional fluorescence intensity plot profiles (Suppl. Fig. S4A) showed that the peaks of the curves, representing a high density of fibronectin deposition, coincided with the presence of cells. The curves obtained from the histograms representing the co-cultures and fibroblasts seeded alone showed more peaks and higher peak values compared to those from the ECs-seeded hydrogels and the cell-free hydrogel groups (Suppl. Fig. S4A). To quantify and compare the influence of fibroblasts on the deposition of fibronectin, the area under the curve were determined (Suppl. Fig. S4B and C). The TAUC (this sums positive peaks, negative peaks, peaks that are not high enough to count, and peaks that are too narrow to count, Suppl. Fig. S4B) and the TPAUC (the area under every peak, Suppl. Fig. S4C) were calculated, and both areas were larger in the co-culturing groups than in the ECs cultured alone group, suggesting a greater deposition of fibronectin surrounding the ECs in the presence of fibroblasts, in contrast to the control groups consisting of a cell-free gel and an ECs-only gel.

Besides fibronectin, fibulin-1 is also involved in vascularization processes. The immunostained fluoromicrographs (Fig. 6) showed that fibulin-1 had a deposition pattern similar to fibronectin (Fig. 5). Cell -free skin ECM hydrogels and EC-seeded hydrogels contained negligible amounts of fibulin- 1, while ECs co-

cultured with fibroblasts, deposited greater amounts of fibulin-1 (Fig. 6). The cross-sectional quantitative densitometry revealed that fibulin-1 was deposited solely around cells, irrespective of them being in single or co-culture (Suppl. Fig. S4D - F). The qualitative assessments of the fluorographs were corroborated by both the AUC for the intensities of fibulin- 1, as well as their intensity peaks: irrespective of EC type, their co-culture with fibroblasts markedly increased fibulin-1 deposition (Suppl. Fig. S4E, F).

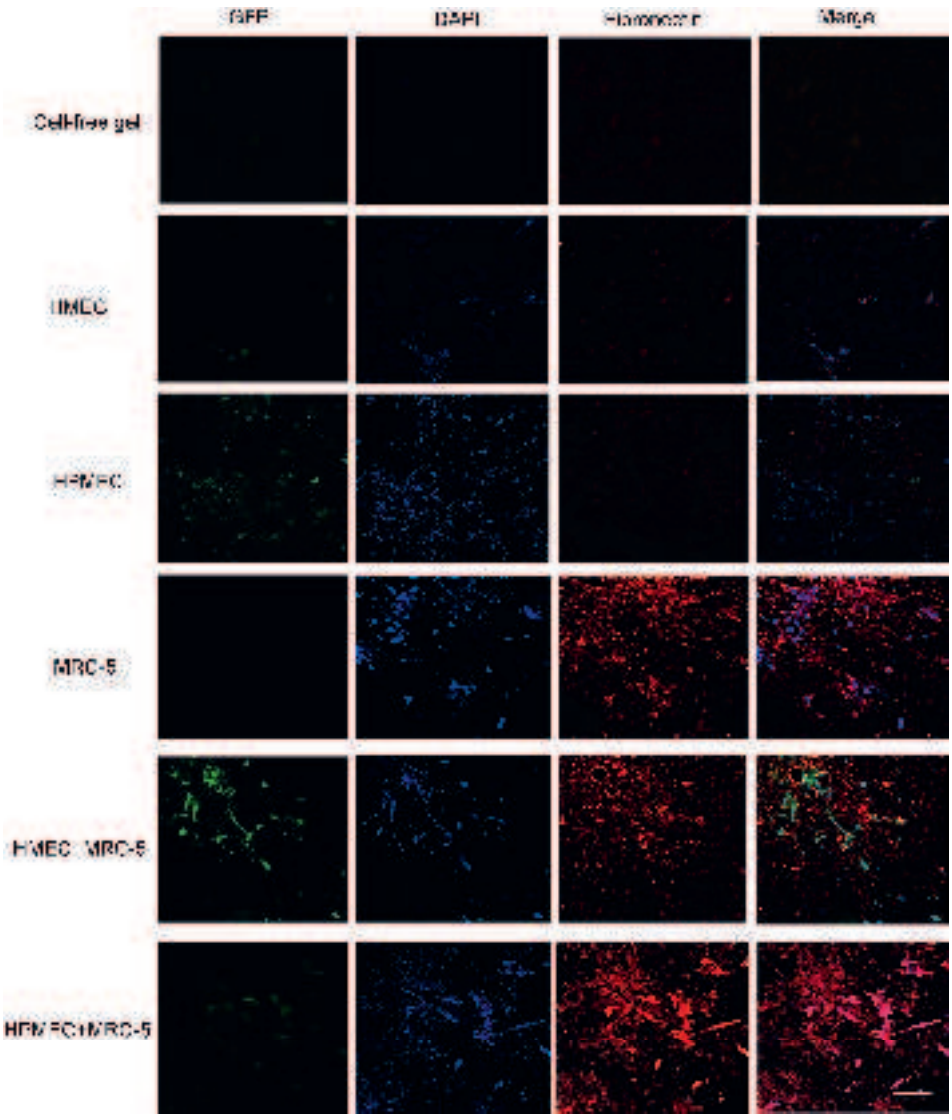

Figure 5. Fluoromicrographs of fibronectin-staining. Representative images of fibronectin staining of 4 μm sections of paraffin-embedded hydrogels. Merged images: green – GPF-labeled HMEC and HPMEC, red – fibronectin, blue – nuclei (DAPI). Scale bar: 58 μm.

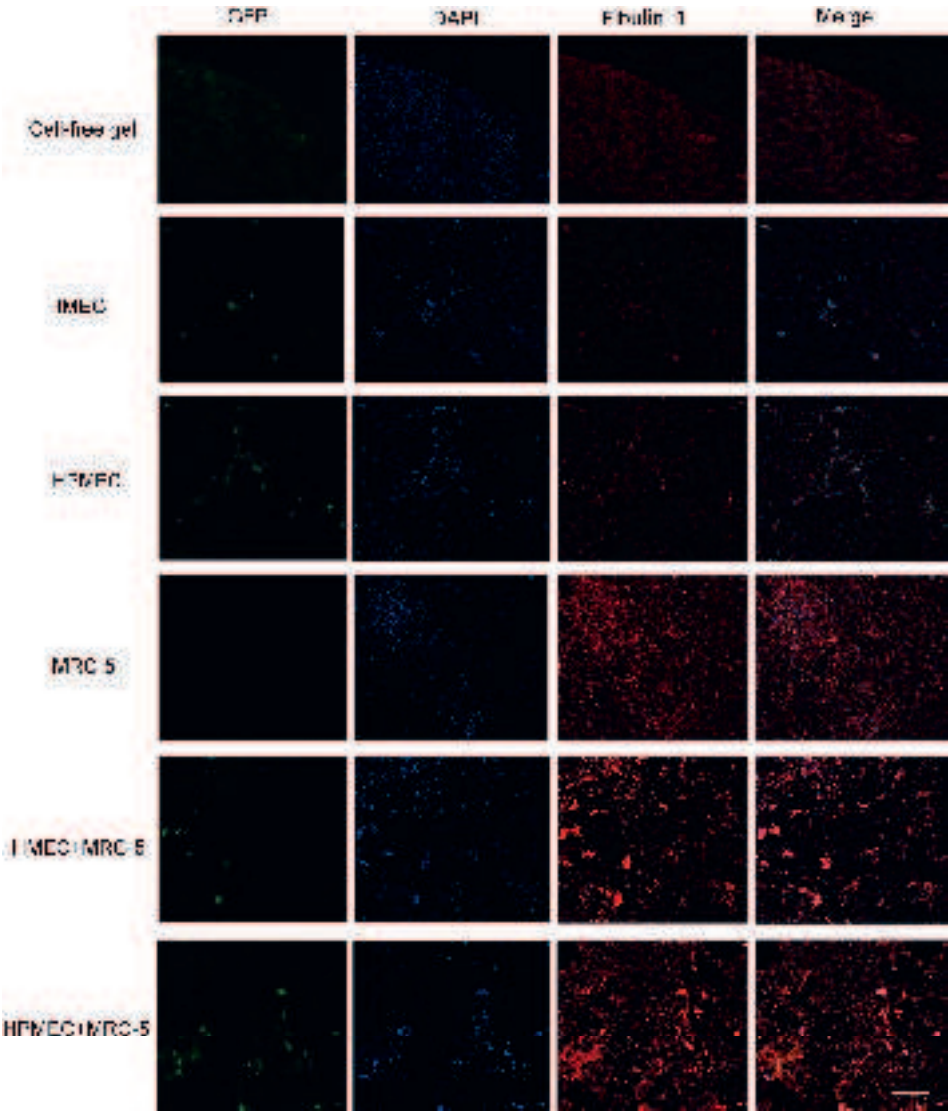

Figure 6. Fluoromicrographs of fibulin-1 staining. Representative images of fibulin-1 staining of 4 μm sections of paraffin-embedded hydrogels. Merged images: green – GPF-labeled HMEC and HPMEC, red – fibronectin, blue – nuclei (DAPI). Scale bar: 58 μm.

4. Discussion

In this study, we tested the hypothesis that fibroblasts promote vascularization and remodeling of skin-derived ECM hydrogels. Our main results were that the presence of fibroblasts alters the architecture and mechanical properties of ECM hydrogels, whilst also changing the biochemical ECM constituents. The altered architecture by fibroblasts resulted in changes of porosity of the ECM fiber meshes and diameter during VNF by microvascular ECs. Fibroblasts engaged in intimate contact with newly formed endothelial tubes akin to pericytes. Furthermore, the organization and alignment of collagen fibers within the skin ECM hydrogel were also altered by the interaction of fibroblasts with ECs. The biochemical composition of the ECM hydrogel was modified through the fibroblasts' deposition of fibronectin and fibulin-1.

In our study, we discovered that ECs have the ability to form vascular structures in skin-derived ECM hydrogels and that fibroblasts enhance VNF formation. We also observed that skin ECM hydrogel provides a conductive environment for VNF formation, which may serve as a model for in vivo vascularization e.g. during wound healing. This suggests that skin-derived ECM hydrogels are a suitable biomaterial that replicate several properties of skin ECM in vivo.

The impact of fibroblast-induced matrix remodeling and mechanical signaling on angiogenesis is less well-understood than the impact of e.g. hypoxia and growth factor signaling. An earlier study suggested that EC tube formation in 3D fibrin gels was primarily influenced by the presence of surrounding fibroblasts, rather than the composition of the surrounding medium [41]. In our study, as visualized in the 3D imaging, a proportion of the MRC-5 fibroblasts aligned closely with the ECs. Whisler et al. observed that there was a physical interaction between ECs and fibroblasts cocultured in fibrin hydrogel, as evidenced by the elongation of fibroblasts along the external walls of vascular tubes [42]. This implies that fibroblasts may affect VNF formation through juxtracrine signaling or other factors, such as modulation of the ECM, rather than solely through fibroblast-derived paracrine factors.

The formation of highly branched vascular networks, in pure collagen hydrogels, correlates with the mechanical properties of these hydrogels [43, 44]. Previously, we showed that microvascular ECs (HPMEC) engage in VNF in cardiac-derived

ECM hydrogels in a seeding density and time-dependent fashion [26]. Thus, VNF likely depends both on the physical and biochemical nature of the surrounding matrix. Indeed, we also showed that fibroblast- augmented VNF increased the stiffness of the skin-derived ECM hydrogel, while simultaneously reducing its stress relaxation. This suggests that part of the increased VNF is due to fibroblasts that actively remodel the ECM. In contrast, others showed that an increase in ECM density reduces the number of vascular tubes, yet it promotes the formation of thicker, deeper networks and more stable lumens in other biomaterials such as mixed collagen-fibronectin hydrogels which are much stiffer materials [45, 46]. On the other hand, an increased ECM density hindered network formation and adding fibroblasts to EC-embedded 3D gels resulted in increased VNF regardless of matrix density [47]. As for the definition of higher stiffness, variations in the Young's modulus range were observed across these studies, attributable to disparities in the methodologies employed for stiffness assessments and the diverse materials under consideration [48]. This conflicting evidence might pertain to the challenge of quantifying 3D VNF. Moreover, we observed a greater variability in stiffness within hydrogels in which fibroblasts were co-cultured with ECs in comparison to groups with ECs cultured independently. A study by Juliar et al. demonstrated that the co-culture of fibroblasts with ECs induced stiffness heterogeneities in fibrin hydrogels during VNF [49]. The substantial variability in stiffness of skin ECM hydrogel may also be caused by the effects of fibroblast on the peri-endothelial stiffness. This effect may be influenced by the new generated ECM-binding proteins, such as fibronectin and fibulin. In addition, previous research examining co-culture of fibroblasts and ECs within synthetic polyethylene glycol (PEG) hydrogels also demonstrated a correlation between fibronectin deposition and the stiffening of the hydrogel [50].

Natural biomaterials possess viscoelastic properties, characterized by the presence of both an elastic component (stiffness) and a viscous component, which are both key to vascularization [51]. However, the impact of matrix viscosity on ECs is relatively unexplored. In general, the stress relaxation rate of ECM-derived biomaterials decreases with increasing stiffness. In our study, no differences in viscosity were observed between any of our hydrogels after day 1. However, after 5 days of culturing, the viscosity of the hydrogels containing fibroblasts co-cultured with ECs was higher compared to the groups with ECs cultured alone. We suggest that this increase in viscosity may be attributed to the

degradation/rearrangement of ECM proteins during the VNF process, which potentially increased the fluidity of the ECM hydrogel.

In this study, we employed second harmonics generation microscopy to investigate architectural changes in collagen fibers at the macroscale level, which has not been previously addressed in other published studies related to 3D culturing in biomaterials. Collagens, particularly types I and III, are the most abundant ECM proteins in the skin, and both exhibit SHG properties. SHG imaging is a valuable technique to examine ECM structure [40, 52, 53]. High-resolution images from backward propagating SHG can be used to identify newly synthesized immature collagen or collagen turnover in older tissues. In our study, the collagen fibrils observed in the cocultured groups exhibited high density. This coincided with the abundant deposition of newly formed, fibronectin and fibulin-1 by fibroblasts which likely contributed to the observed increased matrix density. The ultrastructural analyses also showed that fibroblasts appear to facilitate migration of ECs and tube formation through degradation of the ECM causing an increased porosity around VNF areas. In contrast, in the hydrogels that only contained ECs, collagen fibrils exhibited a relatively high degree of alignment, forming entangled bundles composed of long fibers. These newly formed fibrils displayed a heterogeneous distribution, filling the pores between the fibers observed in SEM images and impeding the migration and interconnection of ECs.

The nanometer to micrometer-scaled topography of ECM-based hydrogels is dictated by the arrangement and structural attributes of fibers. Altogether, these characteristics dictate the architecture, geometry, pores and interconnectivity which are all sensed by embedded cells. The topography influences cellular phenotype and function such as ECM remodeling by fibroblasts and vascularization by ECs [54, 55]. VNF might be enhanced by physical nano topography, while also being dependent on the cell type. Our research showed that the achieved diameter of the skin ECM fiber was EC- type-dependent. The differences in fiber characteristics seen between HMEC with fibroblast and HMEC alone were absent when comparing those hydrogels with HPMEC. VNF also changed surface chemistry, and surface features [56]. In our study, the generation of new proteins and degradation of existing proteins in the cast hydrogels, as well as changes in fiber structure, are attributed to the behavior of cells, and conversely, influenced cell behavior.

Our research substantiated that fibroblast-generated newly deposited ECM, at least fibronectin and fibulin-1, facilitates ECs sprouting and tube formation. Fibronectin is an ECM protein which modulates interactions between endothelial and perivascular cells in order to modulate VNF. It is essential for vascularization, evidenced by the non-viability of mice lacking fibronectin [57]. Our study confirmed that fibronectin was mainly generated by fibroblasts adjacent to ECs. Fibronectin was also observed to be closely associated with the newly deposited collagen fibrils, as seen in our merged images of fibronectin and SHG. Fibulin-1 is also an ECM glycoprotein [58]. The function of fibulin-1-ECM interactions is not yet completely explored, with some studies suggesting it binds to other ECM protein like fibronectin and can promote the stabilization of ECM [59]. Also, fibulin-1 regulates cell migration such as required for VNF [60]. Our skin ECM hydrogels seeded with ECs alone contained little fibulin-1. Fibroblasts were the main contributor to the secretion of fibulin-1, and the fibulin-1 was mainly located around the ECs when the hydrogels also contained fibroblasts, similar to the pattern of fibronectin deposition. We acknowledge a limitation in our study, as we did not undertake additional experiments to delve into the potential mechanisms underlying the role of fibulin-1. In vivo, ECs attract mural, mesenchymal, cells through secretion of platelet-derived growth factor – BB (PDGF-BB). Our results do not solve the ‘chicken or egg’ question i.e. whether the fibroblast-derived fibulin-1 and fibronectin attracted ECs or that ECs attracted fibroblasts or even perhaps both. The fact that only a proportion of the fibroblasts had integrated in the vascular tubes suggests that ECs migrated to fibroblasts which subsequently engaged in intimate contact after PDGF stimulation.

Conclusion

This study elucidates the dynamic process of matrix remodeling through the interaction between fibroblasts and ECs, resulting in changes in the architectural and chemical characteristics of the ECM. Our organ-derived ECM 3D culturing model provides valuable insights into the role of fibroblasts in vessel formation and wound healing, advancing our understanding of these processes.

Acknowledgements

Part of the work has been performed in the UMCG Microscopy and Imaging

Center (UMIC), sponsored by NWO (175-010-2009-023). We acknowledge the support from Klaas Sjollema towards the utilization of microscopes at UMIC in this study. J.K.B. received unrestricted research funds from Boehringer Ingelheim (unrelated to this work) and was supported by Nederlandse Organisatie voor Wetenschappelijk Onderzoek (NWO) Aspasia-premie subsidienummer (015.013.010).

Author contributions

M.Z.: conceptualization, methodology, investigation, formal analysis, and writing. F.Z., X.Z., L.A.B.: investigation and methodology. J.K.B.: conceptualization and writing. M.C.H.: conceptualization and writing. All authors have read and agreed to the published version of the manuscript.

Declaration of generative AI and AI-assisted technologies in the writing process:

During the preparation of this work, the authors used ChatGPT-3.5 (San Francisco, USA) in order to improve language. After using this tool/service, all authors reviewed and edited the content as needed and take full responsibility for the content of the publication.

References

[1] H. Brem, O. Stojadinovic, R.F. Diegelmann, H. Entero, B. Lee, I. Pastar, M. Golinko, H. Rosenberg, M. Tomic-Canic, Molecular markers in patients with chronic wounds to guide surgical debridement, Mol. Med. 13 (1–2) (2007) 30–39.

[2] G. Han, R. Ceilley, Chronic wound healing: a review of current management and treatments, Adv. Ther. 34 (3) (2017) 599–610.

[3] S. Guo, L.A. Dipietro, Factors affecting wound healing, J. Dent. Res. 89 (3) (2010) 219–229.

[4] A. Gosain, L.A. DiPietro, Aging and wound healing, World J. Surg. 28 (3) (2004) 321–326.

[5] P. Carmeliet, Angiogenesis in health and disease, Nat. Med. 9 (6) (2003) 653–660. [6] N. Raina, R. Rani, M. Gupta, Chapter 8 - angiogenesis: aspects in wound healing, in: S. Chatterjee (Ed.), Endothelial Signaling in Vascular Dysfunction and Disease, Academic Press, 2021, pp. 77–90.

[7] K.E. Johnson, T.A. Wilgus, Vascular endothelial growth factor and angiogenesis in the regulation of cutaneous wound repair, Adv. Wound Care 3 (10) (2014) 647–661.

[8] B.S. Brooke, S.K. Karnik, D.Y. Li, Extracellular matrix in vascular morphogenesis and disease: structure versus signal, Trends Cell Biol. 13 (1) (2003) 51–56.

[9] P. Lu, V.M. Weaver, Z. Werb, The extracellular matrix: a dynamic niche in cancer progression, J. Cell Biol. 196 (4) (2012) 395–406.

[10] M. Marchand, C. Monnot, L. Muller, S. Germain, Extracellular matrix scaffolding in angiogenesis and capillary homeostasis, Semin. Cell Dev. Biol. 89 (2019) 147–156.

[11] S. Wang, X. Li, M. Parra, E. Verdin, R. Bassel-Duby, E.N. Olson, Control of endothelial cell proliferation and migration by VEGF signaling to histone deacetylase 7, Proc. Natl. Acad. Sci. USA 105 (22) (2008) 7738–7743.

[12] D.R. Senger, S.R. Ledbetter, K.P. Claffey, A. Papadopoulos-Sergiou, C. Peruzzi, M. Detmar, Stimulation of endothelial cell migration by vascular permeability factor/vascular endothelial growth factor through cooperative mechanisms involving the alphavbeta3 integrin, osteopontin, and thrombin, Am. J. Pathol. 149 (1) (1996) 293.

[13] M. Ahmed, C. Ffrench-Constant, Extracellular matrix regulation of stem cell behavior, Curr. stem cell rep. 2 (2016) 197–206.

[14] F. Caiado, S. Dias, Endothelial progenitor cells and integrins: adhesive needs, Fibrogenesis Tissue Repair 5 (1) (2012) 4.

[15] K.H. Vining, D.J. Mooney, Mechanical forces direct stem cell behaviour in development and regeneration, Nat. Rev. Mol. Cell Biol. 18 (12) (2017) 728–742.

[16] S.W. Kim, H.Z. Zhang, L. Guo, J.M. Kim, M.H. Kim, Amniotic mesenchymal stem cells enhance wound healing in diabetic NOD/SCID mice through high angiogenic and engraftment capabilities, PLoS One 7 (7) (2012), e41105.

[17] A.C. Newman, M.N. Nakatsu, W. Chou, P.D. Gershon, C.C. Hughes, The requirement for fibroblasts in angiogenesis: fibroblast-derived matrix proteins are

essential for endothelial cell lumen formation, Mol. Biol. Cell 22 (20) (2011) 3791–3800.

[18] G. Seghezzi, S. Patel, C.J. Ren, A. Gualandris, G. Pintucci, E.S. Robbins, R. L. Shapiro, A.C. Galloway, D.B. Rifkin, P. Mignatti, Fibroblast growth factor-2 (FGF-2) induces vascular endothelial growth factor (VEGF) expression in the endothelial cells of forming capillaries: an autocrine mechanism contributing to angiogenesis, J. Cell Biol. 141 (7) (1998) 1659–1673.

[19] P. Carmeliet, VEGF as a key mediator of angiogenesis in cancer, Oncology 69 (Suppl 3) (2005) 4–10.

[20] G. Hajmousa, E. Przybyt, F. Pfister, G.A. Paredes-Juarez, K. Moganti, S. Busch, J. Kuipers, I. Klaassen, M.J.A. van Luyn, G. Krenning, H.P. Hammes, M.C. Harmsen, Human adipose tissue-derived stromal cells act as functional pericytes in mice and suppress high-glucose-induced proinflammatory activation of bovine retinal endothelial cells, Diabetologia 61 (11) (2018) 2371–2385.

[21] V. Terlizzi, M. Kolibabka, J.K. Burgess, H.P. Hammes, M.C. Harmsen, The pericytic phenotype of adipose tissue-derived stromal cells is promoted by NOTCH2, Stem Cell. 36 (2) (2018) 240–251.

[22] E. Przybyt, M.J. van Luyn, M.C. Harmsen, Extracellular matrix components of adipose derived stromal cells promote alignment, organization, and maturation of cardiomyocytes in vitro, J. Biomed. Mater. Res. 103 (5) (2015) 1840–1848.

[23] F.D. Martinez-Garcia, J.A. van Dongen, J.K. Burgess, M.C. Harmsen, Matrix metalloproteases from adipose tissue-derived stromal cells are spatiotemporally regulated by hydrogel mechanics in a 3D microenvironment, Bioengineering (Basel) 9 (8) (2022).

[24] L.E. Tracy, R.A. Minasian, E.J. Caterson, Extracellular matrix and dermal fibroblast function in the healing wound, Adv. Wound Care 5 (3) (2016) 119–136.

[25] J. Xu, G.-P. Shi, Vascular wall extracellular matrix proteins and vascular diseases, Biochim. Biophys. Acta (BBA) - Mol. Basis Dis. 1842 (11) (2014) 2106–2119.

[26] M. Zhang, V.E. Getova, F.D. Martinez-Garcia, T. Borghuis, J.K. Burgess, M. C. Harmsen, From macro to micro: comparison of imaging techniques to detect vascular network formation in left ventricle decellularized extracellular matrix hydrogels, Gels 8 (11) (2022) 729.

[27] E.W. Ades, F.J. Candal, R.A. Swerlick, V.G. George, S. Summers, D.C. Bosse, T. J. Lawley, HMEC-1: establishment of an immortalized human microvascular endothelial cell line, J. Invest. Dermatol. 99 (6) (1992) 683–690.

[28] V. Krump-Konvalinkova, F. Bittinger, R.E. Unger, K. Peters, H.A. Lehr, C. J. Kirkpatrick, Generation of human pulmonary microvascular endothelial cell lines, Lab. Invest. 81 (12) (2001) 1717–1727.

[29] V.E. Getova, J.A. van Dongen, L.A. Brouwer, M.C. Harmsen, Adipose tissue-derived ECM hydrogels and their use as 3D culture scaffold, Artif. Cells, Nanomed. Biotechnol. 47 (1) (2019) 1693–1701.

[30] W.H. Burgess, T. Mehlman, R. Friesel, W.V. Johnson, T. Maciag, Multiple forms of endothelial cell growth factor. Rapid isolation and biological and chemical characterization, J. Biol. Chem. 260 (21) (1985) 11389–11392.

[31] J.P. Jacobs, C.M. Jones, J.P. Baille, Characteristics of a human diploid cell designated MRC-5, Nature 227 (5254) (1970) 168–170.

[32] G. Carpentier, S. Berndt, S. Ferratge, W. Rasband, M. Cuendet, G. Uzan, P. Albanese, Angiogenesis analyzer for ImageJ — a comparative morphometric analysis of "endothelial Tube Formation Assay" and "fibrin bead Assay", Sci. Rep. 10 (1) (2020), 11568.

[33] R.H.J.d. Hilster, P.K. Sharma, M.R. Jonker, E.S. White, E.A. Gercama, M. Roobeek, W. Timens, M.C. Harmsen, M.N. Hylkema, J.K. Burgess, Human lung extracellular matrix hydrogels resemble the stiffness and viscoelasticity of native lung tissue, Am. J. Physiol. Lung Cell Mol. Physiol. 318 (4) (2020) L698–L704.

[34] F.D. Martinez-Garcia, R.H.J. de Hilster, P.K. Sharma, T. Borghuis, M.N. Hylkema, J. K. Burgess, M.C. Harmsen, Architecture and composition dictate viscoelastic properties of organ-derived extracellular matrix hydrogels, Polymers 13 (18) (2021) 3113.

[35] R.H.J. de Hilster, P.K. Sharma, M.R. Jonker, E.S. White, E.A. Gercama, M. Roobeek, W. Timens, M.C. Harmsen, M.N. Hylkema, J.K. Burgess, Human lung extracellular matrix hydrogels resemble the stiffness and viscoelasticity of native lung tissue, Am. J. Physiol. Lung Cell Mol. Physiol. 318 (4) (2020) L698–L704.

[36] E. Wershof, D. Park, D.J. Barry, R.P. Jenkins, A. Rullan, A. Wilkins, K. Schlegelmilch, I. Roxanis, K.I. Anderson, P.A. Bates, E. Sahai, A Fiji macro for quantifying pattern in extracellular matrix, Life Sci. Alliance 4 (3) (2021).

[37] A. Sawaguchi, T. Kamimura, A. Yamashita, N. Takahashi, K. Ichikawa, F. Aoyama, Y. Asada, Informative three-dimensional survey of cell/tissue architectures in thick paraffin sections by simple low-vacuum scanning electron microscopy, Sci. Rep. 8 (1) (2018) 7479.

[38] N.A. Hotaling, K. Bharti, H. Kriel, C.G. Simon, DiameterJ: a validated open source nanofiber diameter measurement tool, Biomaterials 61 (2015) 327–338.

[39] G. Tjin, P. Xu, S.H. Kable, E.P. Kable, J.K. Burgess, Quantification of collagen I in airway tissues using second harmonic generation, J. Biomed. Opt. 19 (3) (2014), 36005.

[40] G. Cox, E. Kable, A. Jones, I. Fraser, F. Manconi, M.D. Gorrell, 3-Dimensional imaging of collagen using second harmonic generation, J. Struct. Biol. 141 (1) (2003) 53–62.

[41] C.K. Griffith, C. Miller, R.C. Sainson, J.W. Calvert, N.L. Jeon, C.C. Hughes, S. C. George, Diffusion limits of an in vitro thick prevascularized tissue, Tissue Eng. 11 (1–2) (2005) 257–266.

[42] J. Whisler, S. Shahreza, K. Schlegelmilch, N. Ege, Y. Javanmardi, A. Malandrino, A. Agrawal, A. Fantin, B. Serwinski, H. Azizgolshani, C. Park, V. Shone, O. O. Demuren, A. Del Rosario, V.L. Butty, N. Holroyd, M.C. Domart, S. Hooper, N. Szita, L.A. Boyer, S. Walker-Samuel, B. Djordjevic, G.K. Sheridan, L. Collinson, F. Calvo, C. Ruhrberg, E. Sahai, R. Kamm, E. Moeendarbary, Emergent mechanical control of vascular morphogenesis, Sci. Adv. 9 (32) (2023) eadg9781.

[43] F. Bordeleau, B.N. Mason, E.M. Lollis, M. Mazzola, M.R. Zanotelli, S. Somasegar, J. P. Califano, C. Montague, D.J. LaValley, J. Huynh, N. Mencia-Trinchant, Y. L. Negr´on Abril, D.C. Hassane, L.J. Bonassar, J.T. Butcher, R.S. Weiss, C. A. Reinhart-King, Matrix

stiffening promotes a tumor vasculature phenotype, Proc. Natl. Acad. Sci. U. S. A. 114 (3) (2017) 492–497.

[44] N. Yamamura, R. Sudo, M. Ikeda, K. Tanishita, Effects of the mechanical properties of collagen gel on the in vitro formation of microvessel networks by endothelial cells, Tissue Eng. 13 (7) (2007) 1443–1453.

[45] A.W. Chung, H.C. Yang, M.K. Sigrist, G. Brin, E. Chum, W.A. Gourlay, A. Levin, Matrix metalloproteinase-2 and-9 exacerbate arterial stiffening and angiogenesis in diabetes and chronic kidney disease, Cardiovasc. Res. 84 (3) (2009) 494–504.

[46] A. Shamloo, S.C. Heilshorn, Matrix density mediates polarization and lumen formation of endothelial sprouts in VEGF gradients, Lab Chip 10 (22) (2010) 3061–3068.

[47] C.M. Ghajar, X. Chen, J.W. Harris, V. Suresh, C.C. Hughes, N.L. Jeon, A.J. Putnam, S.C. George, The effect of matrix density on the regulation of 3-D capillary morphogenesis, Biophys. J. 94 (5) (2008) 1930–1941.

[48] C.O. Crosby, J. Zoldan, Mimicking the physical cues of the ECM in angiogenic biomaterials, Regen Biomater 6 (2) (2019) 61–73.

[49] B.A. Juliar, M.T. Keating, Y.P. Kong, E.L. Botvinick, A.J. Putnam, Sprouting angiogenesis induces significant mechanical heterogeneities and ECM stiffening across length scales in fibrin hydrogels, Biomaterials 162 (2018) 99–108.

[50] B.A. Juliar, J.A. Beamish, M.E. Busch, D.S. Cleveland, L. Nimmagadda, A. J. Putnam, Cell-mediated matrix stiffening accompanies capillary morphogenesis in ultra-soft amorphous hydrogels, Biomaterials 230 (2020), 119634.

[51] X. Zhao, Multi-scale multi-mechanism design of tough hydrogels: building dissipation into stretchy networks, Soft Matter 10 (5) (2014) 672–687.

[52] E. Brown, T. McKee, E. DiTomaso, A. Pluen, B. Seed, Y. Boucher, R.K. Jain, Dynamic imaging of collagen and its modulation in tumors in vivo using secondharmonic generation, Nat. Med. 9 (6) (2003) 796–800.

[53] R.M. Williams, W.R. Zipfel, W.W. Webb, Multiphoton microscopy in biological research, Curr. Opin. Chem. Biol. 5 (5) (2001) 603–608.

[54] K. Cai, J. Bossert, K.D. Jandt, Does the nanometre scale topography of titanium influence protein adsorption and cell proliferation? Colloids Surf. B Biointerfaces 49 (2) (2006) 136–144.

[55] D. Khang, J. Choi, Y.-M. Im, Y.-J. Kim, J.-H. Jang, S.S. Kang, T.-H. Nam, J. Song, J.W. Park, Role of subnano-, nano-and submicron-surface features on osteoblast differentiation of bone marrow mesenchymal stem cells, Biomaterials 33 (26) (2012) 5997–6007.

[56] I.A. Janson, A.J. Putnam, Extracellular matrix elasticity and topography: materialbased cues that affect cell function via conserved mechanisms, J. Biomed. Mater. Res. 103 (3) (2015) 1246–1258.

[57] E.L. George, E.N. Georges-Labouesse, R.S. Patel-King, H. Rayburn, R.O. Hynes, Defects in mesoderm, neural tube and vascular development in mouse embryos lacking fibronectin, Development 119 (4) (1993) 1079–1091.

[58] W.S. Argraves, H. Tran, W.H. Burgess, K. Dickerson, Fibulin is an extracellular matrix and plasma glycoprotein with repeated domain structure, J. Cell Biol. 111 (6 Pt 2) (1990) 3155–3164.

[59] K. Balbona, H. Tran, S. Godyna, K.C. Ingham, D.K. Strickland, W.S. Argraves, Fibulin binds to itself and to the carboxyl-terminal heparin-binding region of fibronectin, J. Biol. Chem. 267 (28) (1992) 20120–20125.

[60] G. Kostka, R. Giltay, W. Bloch, K. Addicks, R. Timpl, R. F¨assler, M.-L. Chu, Perinatal lethality and endothelial cell abnormalities in several vessel compartments of fibulin-1-deficient mice, Mol. Cell Biol. 21 (20) (2001) 7025–7034.

Supplementary data

Videos available on request from m.zhang02@umcg.nl, or https://www.sciencedirect.com/science/article/pii/S2590006423003022#sec2

Suppl Video 1: VNF by EGFP-HMEC VNF on day five scanned by cell discoverer 7. Scanning was through a depth of 108 µm.

Suppl Video 2: VNF by EGFP-HPMEC on day five scanned by cell discoverer 7. Scanning was through a depth of 72 µm.

Suppl Video 3: VNF by co-cultured EGFP-HMEC and dTomato-MRC-5 on day five scanned by cell discoverer 7. Scanning was through a depth of 72 µm.

Suppl Video 4: VNF by co-cultured EGFP-HPEMC and dTomato-MRC-5 on day five scanned by cell discoverer 7. Scanning was through a depth of 52 µm.

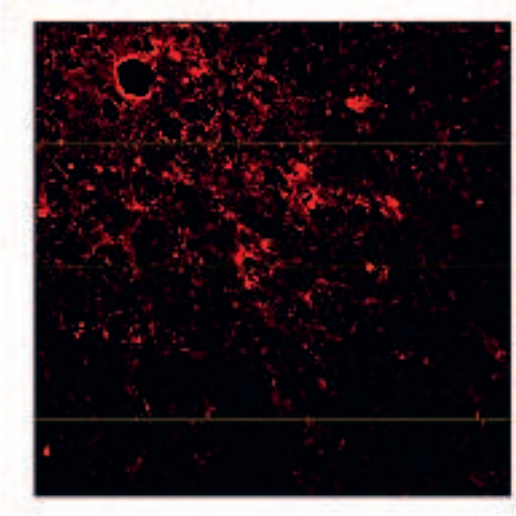

Fig.S1. Schematic diagram of histogram analysis. The yellow lines were drawn at predetermined consistent positions (top, middle, and bottom) within each image. Histograms of fluorescence signal intensity were reported along each line in each image.

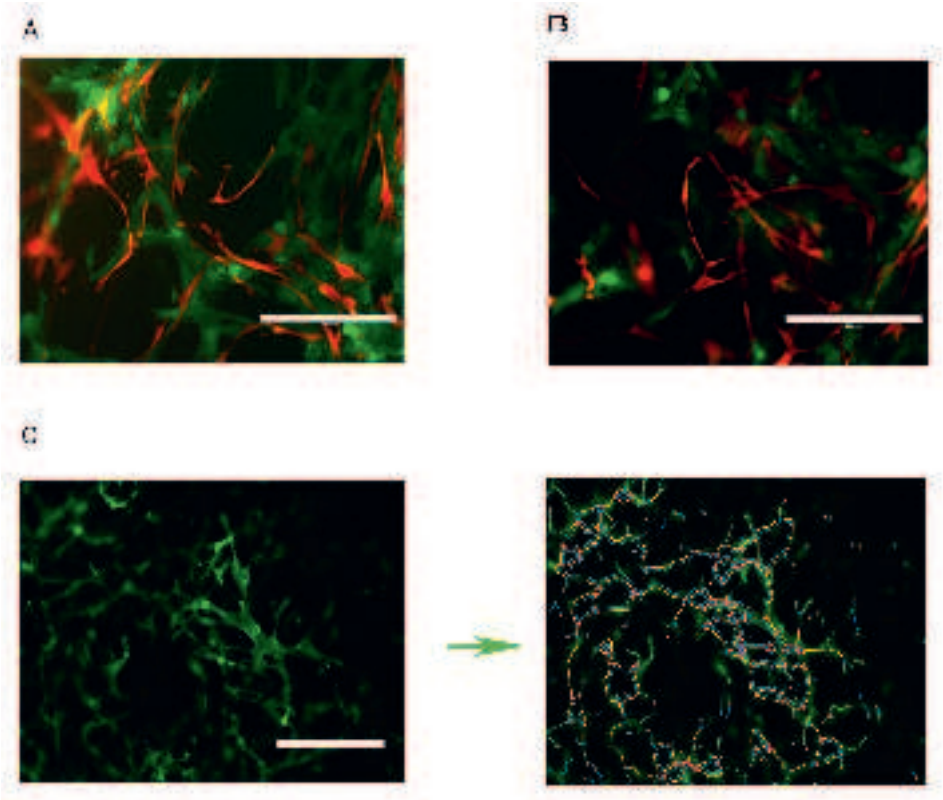

Fig.S2. Fibroblasts align closely to endothelial tubes. (A) The cells were cultured in 48-well plates in skin hydrogel for a period of five days. Co-cultures of HMEC (green) with MRC-5 (red) cells were observed under both the GFP and the Texas red filters. Scale bars represent 200 μm. (B) The cells were cultured in 48-well plates for a period of five days. Co-cultures of HPMEC (green) with MRC-5 (red) cells were observed under both the GFP and the Texas red filters. Scale bars represent 200 μm. (C) Initial image enlargement of the network formed by HPMEC cocultured with fibroblast and the VNF formed by HPMEC analyzed by endothelial tube formation assays. Branches are denoted in green, segments in magenta, junctions are encapsulated in red and surrounded by blue, meshes are indicated in cyan, and the master tree, composed of segments linked by master junctions, is depicted in yellow.

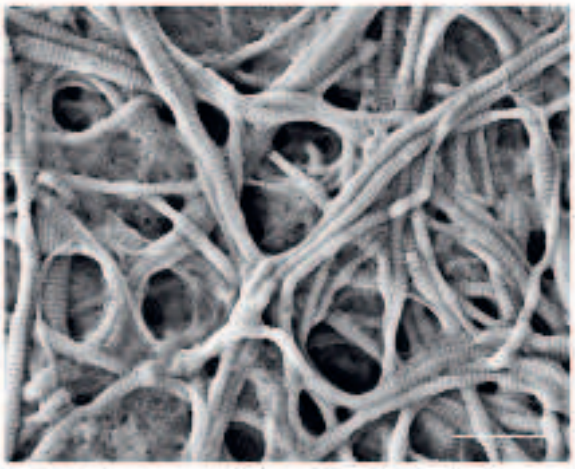

Fig.S3. Fibers of the matrix were visualized by SEM at 5,0000 (50k). Scale bar: 1 µm.

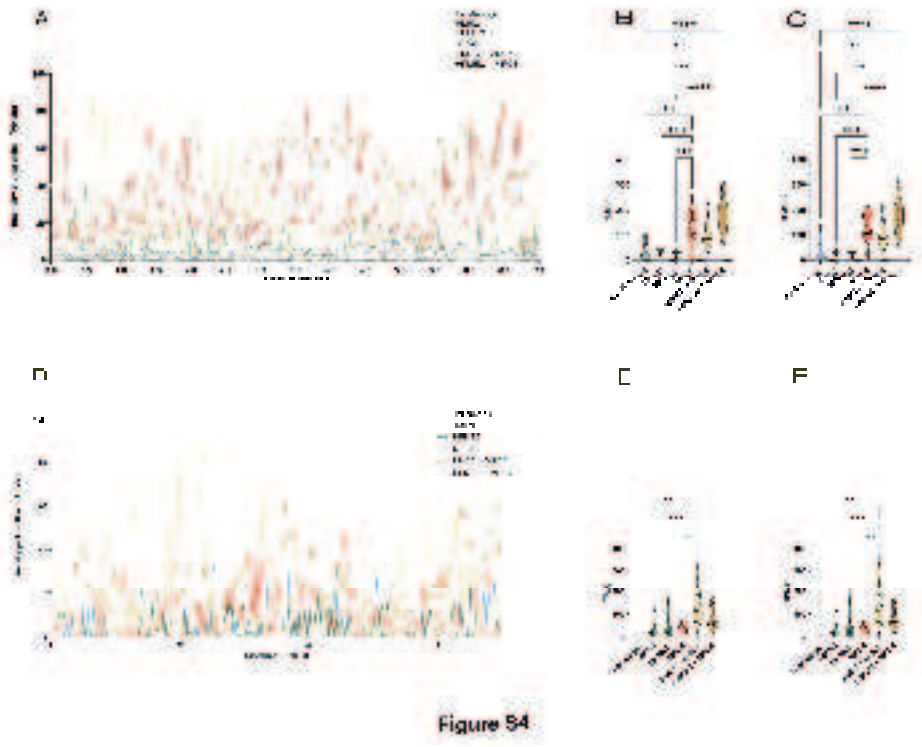

Fig.S4. Analysis of fibronectin and fibulin-1staining intensity. (A) cross-sectional intensity profile through three representative images. (B) Total area under the curve

(TAUC) of the intensity profile of the images. (C) Total peak area under the curve (TPAUC) of the intensity profile of the images. Each dot represents one measurement of a line. Three lines are in the same position for every sample. The data were generated from three independent experiments. (D) cross-sectional intensity profile through three representative images. (E) TAUC of the intensity profile of the images. (F) TPAUC of the intensity profile of the images. Each dot represents one measurement of a line. Three lines are in the same position for every sample. The data were generated from three independent experiments. Statistical testing by one-way ANOVA gel, * $p < 0.05$, ** $p < 0.01$.*** $p < 0.001$.

Chapter 4

Physical properties and biochemical composition of extracellular matrix-derived hydrogels dictate vascularization potential in an organ-dependent fashion

Meng Zhang [1,2], **Fenghua Zhao [2,3]**, Yuxuan Zhu[4], Linda A. Brouwer [1], Hasse Van der Veen[1], Janette K. Burgess [1,2,5] and Martin C. Harmsen [1,2, 5]

1 University of Groningen, University Medical Center Groningen, Department of Pathology and Medical Biology, Hanzeplein 1 (EA11), 9713 GZ Groningen, The Netherlands

2 University of Groningen, University Medical Center Groningen, W.J. Kolff Institute for Biomedical Engineering and Materials Science-FB41, A. Deusinglaan 1, 9713 AV Groningen, The Netherlands

3 University of Groningen, University Medical Center Groningen, Department of Biomedical Engineering-FB40, A. Deusinglaan 1, 9713 AV Groningen, The Netherlands

4 Department of Computer Science, Rensselaer Polytechnic Institute, Troy, NY 12180, USA

5 University of Groningen, University Medical Center Groningen, Groningen Research Institute for Asthma and COPD (GRIAC), Hanzeplein 1 (EA11), 9713 AV Groningen, The Netherlands

ACS Applied Materials & Interfaces

https://doi.org/10.1021/acsami.4c05864

Chapter 4

Abstract: The inherent extracellular matrix (ECM) originating from a specific tissue impacts the process of vascularization, specifically vascular network formation (VNF) orchestrated by endothelial cells (ECs). The specific contribution towards these processes of ECM from highly disparate organs such as the skin and lungs remain a relatively unexplored area. In this study, we compared VNF and ECM remodeling mediated by microvascular ECs within gel, lung, and combinations thereof (hybrid) ECM hydrogels. Irrespective of the EC source, the skin-derived ECM hydrogel exhibited a higher propensity to drive and support VNF compared to both lung and hybrid ECM hydrogels. There were distinct disparities in the physical properties of the three types of hydrogels, including viscoelastic properties and complex architectural configurations including fiber diameter, pore area, and numbers among the fibers. The hybrid ECM hydrogel properties were unique and not the sum of the component ECM parts. Furthermore, cellular ECM remodeling responses varied, with skin ECM hydrogels promoting matrix metalloproteinase 1 (MMP1) secretion, while hybrid ECM hydrogels exhibited increased MMP9, fibronectin, and collagen IV deposition. Principal Component Analysis (PCA) indicated that the influence of a gel's mechanical properties on VNF was stronger than the biochemical composition. These data indicate that the organ-specific properties of an ECM dictate its capacity to support VNF, while intriguingly showing that ECs respond to more than just the biochemical constituents of an ECM. The study suggests potential applications in regenerative medicine by strategically selecting ECM origin or combinations to manipulate vascularization, offering promising prospects for enhancing wound healing through pro-regenerative interventions.

Keywords: Vascularization, Extracellular matrix, ECM hydrogel, Endothelial cells, biomechanics.

1. Introduction

Regeneration of organs and tissues after damage demands vascularization to reinstate adequate perfusion, which is essential to facilitate the exchange of gas, nutrients, and waste, as well as to enable the recruitment and influx of immune cells [1-3]. Upon acute skin damage, wound healing depends on the proliferation and migration of resident mesenchymal cells and proper vascularization[4].

Traditional therapeutic approaches face several obstacles when it comes to the vascular regeneration treatment of skin diseases. One of the challenges is the biocompatibility of applied materials that should support healing[5]. Also, traditional treatment may not adequately stimulate or support endogenous vascular formation[6]. To address these limitations, novel approaches, such as biomaterials or regenerative medicine, are being explored to promote targeted and effective vascularization.

The ECM hydrogel derived from natural tissues is a promising biomaterial for directing vascularization by endothelial cells. Natural ECM hydrogels facilitate tissue reconstruction in vivo[7-9], while porcine ECM hydrogels are biocompatible and augment skin wound healing in rats through upregulated vascularization[10]. It appears that ECM hydrogels preserve the biochemical complexity, nanostructure, and biological inductive properties inherent in the native matrix[11]. ECM hydrogels derived from different organs show a large overlap in biochemical composition[12, 13]. However, despite the similarities in the bulk biochemical composition among organ-derived ECM hydrogels, each hydrogel still possesses distinct characteristics associated with its respective organ source. For instance, the lung ECM hydrogel lacks glycosaminoglycans (GAGs), while conversely, these were found to be relatively higher in the skin ECM hydrogel. Moreover, the collagen I content in the lung ECM hydrogel was observed to be lower compared to the skin ECM hydrogel. These variations extend beyond biochemical composition and encompass differences in mechanical properties, including stiffness and viscosity, as well as in the fibrous microstructure[14]. The specific biological consequences of these variances remain to be elucidated. The manner in which these diverse ECM hydrogels impact fundamental processes occurring in tissues and organs, such as vascularization, remains a topic to be explored.

Over the preceding decades, considerable focus has been directed towards vascularization from the endothelial cell's perspective, while little is known regarding the impact of the ECM's origin and physical attributes[15]. Therefore, we set out to explore differences in vascularization and ECM remodeling between skin ECM hydrogel, lung ECM hydrogel and tested the hypothesis that equally mixed skin and lung ECM hydrogels (referred to as "hybrid ECM hydrogel" hereafter) improve vascularization in vitro.

2. Materials and methods

2.1 Hydrogel Synthesis

Porcine skin and lung were purchased from a slaughterhouse (Kroon Vlees, Groningen, The Netherlands). The generation of decellularized ECM was performed as described previou17In short, Skin tissue was dissected (1 cm^3) and combined with ice-cold Dulbecco's phosphate-buffered saline (DPBS) (Lonza Walkersville, Inc., Walkersville, MD, USA) before being finely divided in a kitchen blender (Bourgini, Breda, The Netherlands) with DPBS to create a paste. This tissue paste was subjected to sonication using an Ultrasonic homogenizer (Sigma Aldrich, Amsterdam, the Netherlands) at 100% power for one minute. The paste was then washed with DPBS twice and separated by centrifugation at 3000 x g until the supernatant was transparent. Subsequent incubation occurred with 0.05% trypsin in DPBS (Thermo Fisher Scientific, Waltham, MA, USA) at 37 °C with consistent shaking for four hours. After two further washes with PBS, the slurry underwent overnight incubation in Milli-Q® water at 37°C with continuous agitation. Next, the tissue homogenate was treated with excess saturated NaCl (6M) for three hours, 1% SDS, 1% Triton X-100, and 1% sodium deoxycholate in Milli-Q® water, along with 30 µg/mL DNase (Roche Diagnostics GmbH, Mannheim, Germany) in 1.3 mM $MgSO_4$ and 2 mM $CaCl_2$. These incubations were maintained under shaking at 37°C overnight. Between treatments, the homogenate was washed three times with Milli-Q® water. Finally, the homogenate was washed with DPBS for an hour six times and then replaced with 70% ethanol for overnight sterilization at room temperature.

The lung tissue was dissected (1 cm^3), with cartilaginous airways and large blood vessels removed. The remaining procedure was identical except that the lung

homogenate underwent two rounds of treatment: 0.1% Triton X-100, 2% sodium deoxycholate, 1 M NaCl solution at 37 °C with shaking, followed by 30 µg/mL DNase in 1.3 mM $MgSO_4$ and 2 mM $CaCl_2$, 10 mM Tris pH 8 at 4 °C with constant shaking. The skin and lung ECM samples were frozen in liquid nitrogen and lyophilized with a freeze dryer (Labconco, Kansas City, MO, USA), then ground into a fine powder using an ULTRA-TURRAX (IKA, Staufen, Germany).

To prepare hydrogels, 20 mg/mL of ECM powder was digested with 2 mg/mL of porcine pepsin (Sigma-Aldrich, St. Louis, MO, USA) in 0.01M HCl under constant agitation at room temperature; the skin ECM powder required 24 hours of digestion and the lung ECM powder 48 hours. Post-digestion, the ECM was neutralized by adding 1/10th volume 0.1M NaOH and subsequently 1/10th volume 10xDPBS, forming an isotonic, neutral pH ECM pregel, stored at 4°C until use.

2.2 3D Cell Culture

Human pulmonary microvascular endothelial cells (HPMEC-ST1.6R[17] HPMEC in the text), Johannes Gutenberg University, Mainz, Germany) and Human microvascular endothelial cells (HMEC-1[18], HMEC in the text) were retrovirally tagged with EGFP (green fluorescence) by third-generation VSV-pseudotyped replication-deficient lentiviruses[19]. The media and other culture information of HMEC and HPMEC were consistent with those reported in the previously study[16]. $0.5x10^6$ HPMEC or HMEC were suspended in 10 µL of culture media which was carefully and homogeneously mixed with 200 µL of skin or lung or skin and lung ECM pregel mixed in1:1 (100µL for each type of pregel). The cell-gel mixtures were cast into single wells of 48-well plates and incubated at 37°C for 45 min to solidify the gel. Subsequently, 500 µL of endothelial culture medium was added to the wells. Hydrogels without cells were used as controls.

2.3 Fluorescence cell imaging

After 5 days of culturing at 37ºC 5% CO_2, inverted fluorescence microscopy (EVOS model M5000, Thermo Fisher) was used to acquire fluoromicrographs to visualize the vascular-like network formation (VNF) by HPMEC and HMEC. Both HPMEC and HMEC were visualized using GPF ‘light cubes’ ($\lambda^{ex}/\lambda^{em}$

470/510nm). VNF was further processed with the Endothelial Tube Formation Assay—angiogenesis analyzer in Fiji[20]. The micrographs compressed the original 3D VNF onto a 2D plane which displaced genuine branched tubes and tubes that crossed each other at different planes in the gel. Because no suitable 3D imaging and quantification software was available to analyze our images, we decided to process all images in this way.

2.4 Characterization of the mechanical properties

The gels loaded with cells were subjected to uniaxial compression at three locations using a 2.5 mm plunger using a low-load compression tester (LLCT) and 20% compression (0.2 strain) in 1sec[12, 21]. The compression sites were positioned at least 2 mm away from the edge of the gel and were separated by 2 mm or more from each other. Stress relaxation test was conducted under 'wet' mode and at room temperature. The LLCT load cell and linear positioning for control and data were acquired using LabVIEW 7.1 software[22]. During compression, the increase in stress was continuously monitored to derive the elastic modulus from the stress-strain curve's slope. Upon reaching a strain of 0.2, it was maintained at this level for 100 seconds, while continuously monitoring the stress. The percentage stress relaxation was calculated by comparing the stress at t = 0 s and t = 100 s.

2.5 Hydrogel Ultrastructure

The hydrogel ultrastructure was examined using scanning electron microscopy (SEM). After culturing, the fixation of hydrogels and the sample preparation for SEM performed as described in previous published research[16]. The hydrogels were visualized at magnifications of 5,000×, 10,000×, and 25,000×, (resp. 5K, 10K and 25K) operating at 3 kV using the Zeiss Supra 55 scanning electron microscope (Carl Zeiss NTS GmbH). Fibers surrounding the cells were assessed '25K' micrographs using the Diameter J plugin in Fiji[23].

2.6 Immunofluorescence staining

Thin paraffin sections (4 μm) were deparaffinized and rehydrated. For antigen retrieval, slides were incubated in 10 mM citric acid (pH 6) at 85°C overnight. Slides were washed with demi water and PBS and subsequently blocked in 4% BSA for 15 min at room temperature. Afterward, the slides were incubated for 1

hours with first antibody (Table 1) at room temperature. After that, the slides were washed with PBS 3 times and incubated with secondary antibody (Table 2) for 1h. Opal 650 (Akoya Biosciences, 1:200) was used for fibronectin to amplify the signal. Opal 650 diluted in 0.1M borate buffer with 0.003% hydrogen peroxide (Merck, Darmstadt, Germany) and incubated with slides for 15 mins. The slides were washed with demi water 3 times and incubated with DAPI (Merck 1:5,000) for 10 min. These staining images were generated by SP8 confocal microscope (Leica, Wetzlar, Germany).

Table 1: The information of the first antibody.

First antibody	Host	Company	Concentration
Fibronectin	Rabbit	ab6584, Abcam	1:100
Ki67	Rabbit	ab211536, Abcam	1:300
MMP1	Rabbit	ab52631, Abcam	1:100
MMP9	Rabbit	Meridian Rd.61101	1:100
Collagen IV	Goat	1340-01, Southern Biotech	1:100

Table 2: The information of the second antibody.

Second antibody	Corresponding first antibody	Host	Company	Concentration
Immunoglobulins/HRP	Fibronectin	Goat	P0448, Dako	1:200
Alexa Fluor™ 647	Ki67	Donkey	A31573, Invitrogen	1:300
Alexa Fluor™ 647	MMP1	Donkey	A31573, Invitrogen	1:300
Alexa Fluor™ 647	MMP9	Donkey	A31573, Invitrogen	1:300
Alexa Fluor™ 555	Collagen IV	Rabbit	A21431, Invitrogen	1:300

The staining images obtained were analyzed with CellProfiler v 4.2.5. For each sample, a total of three images (n = 3) were randomly selected to quantify the expression levels of MMP1, MMP9, fibronectin, and collagen IV, as well as the number of nuclei (i.e. cells) per image. The quantification of protein expression per cell was determined by dividing the overall protein expression by the number of nuclei observed in each image. Additionally, the ratio of Ki67 positive nuclei was calculated as the fraction of the number of positive Ki67 nuclei divided by the total number of nuclei to obtain the proliferation index.

2.7 Principal Component Analysis

PCA was performed on a dataset which records material property and VNF, to explore the correlation between the extent of tube formation and material characteristics. PCA diminishes the dataset's dimensionality by identifying a reduced set of variables that retains most of the information present in the larger set.

In our experiment, the data matrix $X \in R50 \times 20$, which consisted of 50 samples and 20 features. All variables were normalized using Min-Max normalization, scaling the data to a specified range (default: 0 to 1) to mitigate the influence of scale differences between features on the PCA algorithm. The PCA algorithm was implemented using the sklearn library in Python[24]. By observing the scatter plots of the samples after performing PCA, patterns and trends in the samples could be identified. If there is a clear linear relationship between the original features and the PCA results, a high correlation will exist between the original features and the PCA results. To achieve consistency in the positive and negative values of PC1, PC2, and PC3, where positive values indicate a positive impact on the VNF, we standardize by assigning the opposite numerical values to all components of PC1 and PC3. A higher PC value signifies a more substantial positive contribution to VNF.

2.8 Statistical analysis

All statistical analyses were conducted using GraphPad Prism v9.2.0 (GraphPad Company, San Diego, CA, USA). Prior to analysis, all data underwent outlier detection utilizing the robust regression and outlier removal (ROUT) test. Subsequently, one-way analysis of variance (ANOVA) was employed for data analysis. Significance was determined at the $p < 0.05$ level in the respective

statistical tests. Components with absolute PC values in PCA exceeding the median are deemed significant for VNF.

3. Results

3.1 Skin-derived ECM hydrogel enhances VNF by ECs irrespective of their organ-specific origin

Spontaneous VNF and formation of branched and extensive vascular-like structures by HMEC and HPMEC was observed in all three distinct ECM hydrogels after 5 days of culture (Fig. 1A, green).

The VNF by HMEC in skin ECM hydrogels was consistently higher than in lung ECM hydrogels for all four measured parameters (Figs. 1B-E). Specifically, the number of nodes was 477.2 ± 129.4 in skin ECM hydrogels and 279.9 ± 184.3 in lung ECM hydrogels ($p=0.0269$); the number of junctions was 135.6 ± 37.35 in skin ECM hydrogels and 79.4 ± 51.8 in lung ECM hydrogels ($p=0.0224$). Moreover, the number of branches and total branching length were 80.9 ± 17.5 and 12,255 ± 2,681 pixels in skin ECM hydrogels respectively, whereas in lung ECM hydrogels, these values were lower resp. 58.2 ± 24.5 ($p=0.0267$) and 7,897 ± 4,089 pixels ($p=0.0150$). The VNF by HMEC in hybrid ECM hydrogels did not differ from skin ECM hydrogels or lung ECM hydrogels due to the large variation in responses (Fig. 1B-E).

Like VNF by HMEC, VNF by HPMEC (Fig. 1F-I) was also highest in skin ECM hydrogels, but notably, this was only in comparison to hybrid ECM hydrogels. while only the number of junctions, but not the number of branches or total branching length in lung ECM hydrogels was lower than in skin ECM hydrogels. The number of HPMEC-generated nodes was 532.3 ± 213.1 in skin ECM hydrogels and 299.8 ± 136.6 in hybrid ECM hydrogels ($p= 0.0123$), and the reduced number of junctions was 188.6 ± 80.6 in skin ECM hydrogels and 101.3 ± 61.8 in hybrid ECM hydrogels ($p=0.0057$).

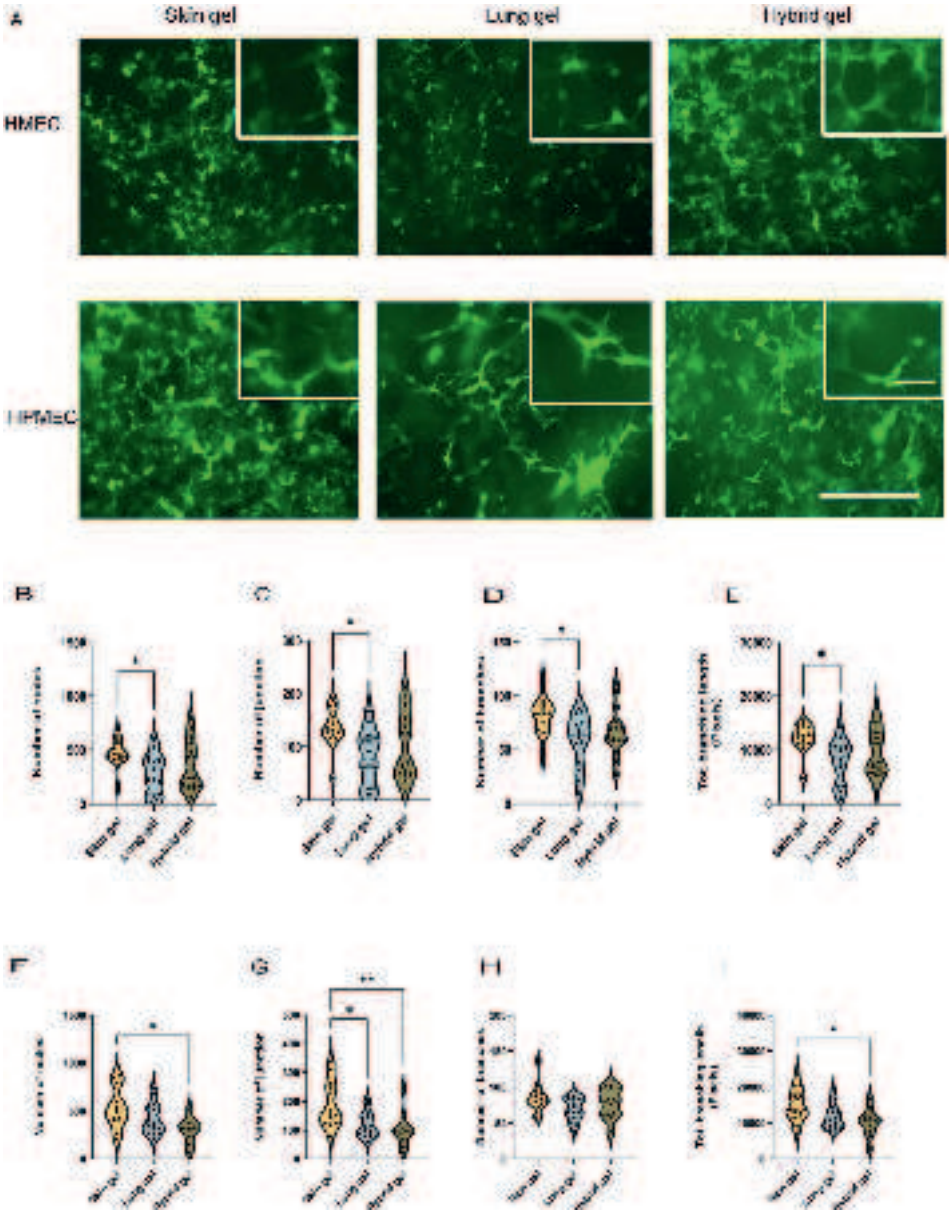

Figure 1. VNF by ECs was visualized in three different ECM hydrogels. (A) EGFP-expressing HMECs or HPMECs (green) were seeded in skin, lung, and hybrid hydrogels in 48-well plates and cultured for 5 days. Scale bar: 400 μm. (B) Quantification of nodes formed by HMEC in three distinct hydrogel types was done with FIJI software. (C) Quantification of the number of master junctions formed by HMEC in three distinct hydrogel types. (D) Quantification of the number of branches produced by HMEC in three distinct hydrogel types. (E) Quantification of total branching length generated

byHMECin three distinct hydrogel types. (F) Quantification of the number of nodes produced by HPMEC in three distinct hydrogel types. (G) Quantification of the number of master junctions produced by HPMEC in three distinct hydrogel types. (H) Quantification of the number of branches produced by HPMEC in three distinct hydrogel types. (I) Quantification of total branching length produced by HPMEC in three distinct hydrogel types. The data are from 7 independent experiments. Three different random regions of interest (ROI) were measured for every single sample, and each dot represents a measurement of a randomized region. One-way ANOVA comparing gels, $*p < 0.05$, $**p < 0.01$.

3.2 The proliferation of HPMEC is highest in skin ECM hydrogels after five days of culturing

Considering that (irrespective of gel type) HMEC and HPMEC had similar VNF patterns but the HPMEC being slightly higher, we continued our experiments with HPMEC only. HPMEC had elongated in the skin ECM hydrogels within one day (Fig. 2A, top row, green), whereas at day 1, cells remained rounded in the lung and hybrid ECM hydrogels. At day 1 and irrespective of gel type, approx. 50% of HPMEC were proliferating as judged by the Ki67 expression (Fig. 2B). Albeit, that skin ECM hydrogels tended to promote proliferation more than lung or hybrid ECM hydrogels or alternatively, lung and hybrid ECM hydrogels tended to inhibit proliferation more. These differences maintained at five days when the percentage proliferation of HPMEC in skin ECM hydrogels was higher than in lung ECM hydrogels (Fig. 2C, 59% ± 28% vs 30% ± 9%, p=0.0378). The variation in the proliferation of HPMEC in hybrid ECM hydrogels was too large and did not differ from either skin or lung ECM hydrogels.

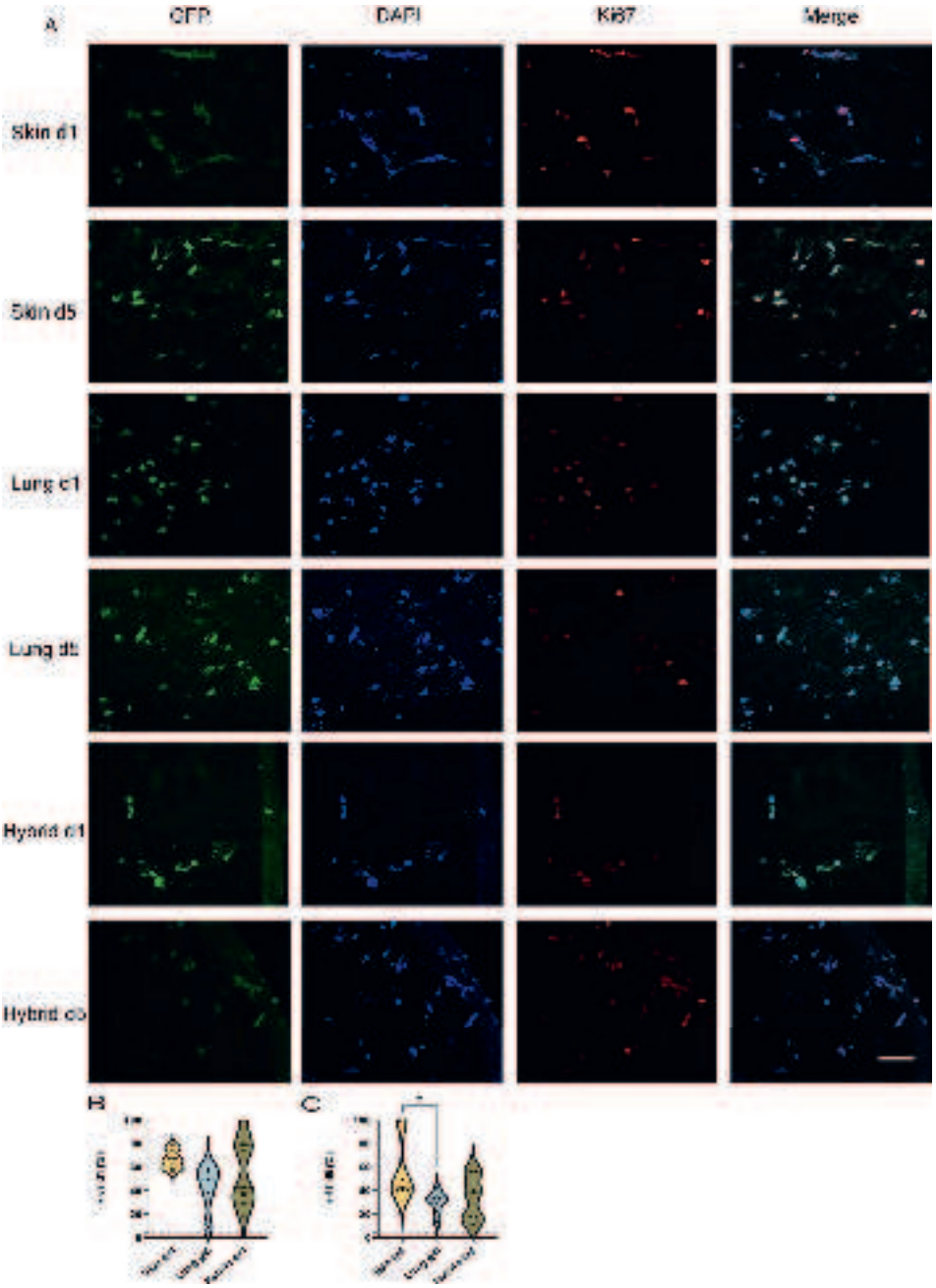

Figure 2. Comparison of Ki67 expression in HPMEC seeded in three distinct ECM hydrogels. (A) Representative fluoromicrographs of 4 μm sections of paraffin-embedded skin, lung, and hybrid ECM hydrogels loaded with HPMEC. Merged images: green, GPF-labeled HPMEC; red, Ki67; blue, nuclei (DAPI). Scale bars: 58 μm. (B) Comparison of

the percentage of Ki67 positive nuclei in the three different gels at day 1. (C) Comparison of the percentage of Ki67 positive nuclei in the three different gels on day 5.

3.3 The physical properties of different organ-derived ECM hydrogels change during VNF

Hydrogels' stiffness and stress relaxation were measured using a low-load compression tester (LLCT). Both were determined after 20% strain and relaxation for 100s. The stiffness of the cell-free skin ECM hydrogels was lower than lung ECM hydrogels (Suppl. Fig. S1A). At 24 hours post-seeding, the stiffness of the skin ECM hydrogels was lower than lung ECM hydrogels (Fig. 3A, 0.45 ± 0.16kPa vs 1.35 ± 0.41kPa, $p<0.0001$) and hybrid ECM hydrogels (0.45 ± 0.16k Pa vs 1.03 ± 0.37kPa, $p=0.0025$). After five days of culture, the stiffness of the HPMEC-loaded gels did not differ, irrespective of the hydrogel origin. It was observed that both the lung and hybrid ECM hydrogels exhibited a reduction in firmness compared to their initial state on day 1, a change not observed in the skin ECM hydrogel. (Fig. 3A, $p<0.0001$).

Hydrogels also comprise a viscous component that dictates stress relaxation. Cell-free skin ECM hydrogel reached close to 100% stress relaxation, which was higher than cell-free lung and hybrid ECM hydrogel (Suppl. Fig. S1B). However, this difference disappeared in HPMEC-seeded hydrogels already at day 1 (Fig. 3B). Prolonged culturing (5 days) decreased the stress relaxation of the skin ECM hydrogel compared to the hybrid ECM hydrogel (72.8% ± 12.5% vs 84.0% ± 12.1%, $p=0.0322$).

Differential viscoelastic properties are discernible among various organ-derived hydrogel substrates. Skin ECM hydrogel was softer than the other two hydrogels, which may contribute to the augmentation of VNF. Conversely, the activities of ECs, including vascularization and proliferation, lead to significant modifications in the physical attributes of physical characteristics of ECM.

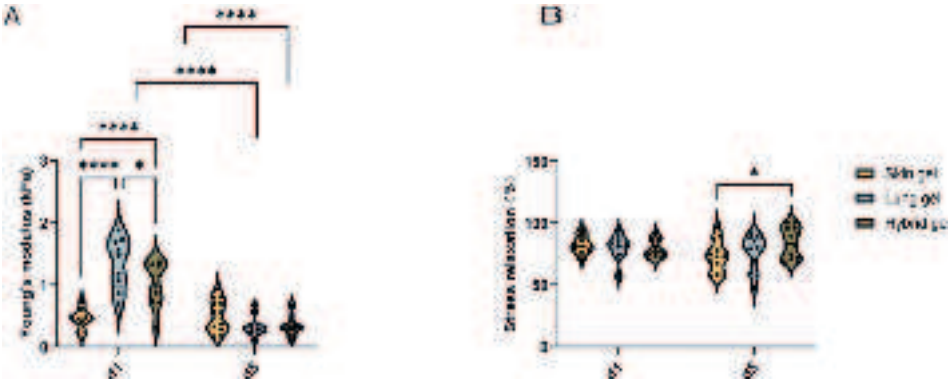

Figure 3. Comparison of the physical characteristics of three ECM hydrogels. (A) Stiffness of skin, lung, and hybrid ECM hydrogels loaded with HPMEC at days 1 and 5. (B) Total stress relaxation of skin, lung, and hybrid ECM hydrogel was loaded with HPMEC at days 1 and 5. After compressing the skin ECM hydrogel for 20%, the stress relaxation was recorded for 100 s.

3.4 The ultrastructure of hydrogels depends on the organ origin and cellular influence

The ultrastructure of the hydrogel was examined using SEM (Fig. 4). Irrespective of the presence of cells, skin, lung, and hybrid ECM hydro each showed a distinct network of erratically organized fibers that were discernable even at lower magnifications ('5K', Fig. 4). The fiber mesh in the lung ECM hydrogel exhibited a notably denser configuration, characterized by numerous fine pores, in contrast to the skin and hybrid ECM hydrogels. Among these, the pores within the fiber network of the skin ECM hydrogel were the largest, while those in the hybrid ECM hydrogel were intermediate in size. Following the seeding of cells within all types of the ECM hydrogels, the matrix surrounding HPMEC underwent reorganization, characterized by the noticeable thickening of fibers and the formation of pores.

By analyzing the fibers surrounding the cells, the average fiber diameter in lung ECM hydrogels was calculated; this always smaller than in skin or hybrid ECM hydrogels, irrespective of the presence of HPMEC (Fig. 4B). Specifically, the average diameter of the fibers in cell-free skin ECM hydrogels was larger than in lung ECM hydrogel (Fig. 4B, 10.57 ± 0.42 vs 8.128 ± 0.2299, $p<0.0001$). Additionally, the average diameter of the fibers in the hybrid ECM hydrogel was

intermediate between skin and lung ECM hydrogels (Fig. 4B). Furthermore, the diameter of fibers in the skin and hybrid ECM hydrogels remained larger than that of the lung ECM hydrogel on both day 1 and day 5 (Fig. 4B, skin vs lung ECM hydrogel on day 1: 11.5 ± 0.6 vs 8.6 ± 0.3, $p<0.001$; on day 5: 10.8 ± 1.1 vs 8.7 ± 0.4, $p<0.001$; hybrid vs lung ECM hydrogel on day 1: 11.2 ± 1.2 vs 8.6 ± 0.3, $p<0.001$; on day 5: 10.0 ± 1.0 vs 8.7 ± 0.4, $p<0.001$). Comparing the HPMEC-loaded ECM hydrogel to the cell-free ECM hydrogel, the fibers in the HPMEC-loaded ECM hydrogel showed increased thickness at day 1, regardless of the gel type (Suppl. Fig. S2A, $p<0.001$). At day 5, the fibers' diameter in the lung ECM hydrogel remained thicker compared to cell-free lung ECM hydrogel, whereas the diameter of the fibers in the skin and hybrid ECM hydrogels did not show differences compared to the respective cell-free ECM hydrogels. The fiber diameters of the ECM hydrogel proximal to the HPMEC did not differ from fibers distal to the HPMEC after five days (Suppl. Fig. S2D).

The size (Fig. 4C) and numbers of pores (Fig. 4D) depended on the presence of cells as well as ECM origin. The average size of the 'mesh holes' between fibers (Mean Pore Area) was larger in cell-free skin ECM hydrogel and hybrid ECM hydrogel compared to the lung ECM hydrogel (Fig. 4C, skin ECM hydrogel vs lung ECM hydrogel: 1,046 ± 240.4 vs 702.9 ± 142.9, $p< 0.001$; hybrid ECM hydrogel: lung ECM hydrogel: 1,006 ± 131.0 vs 702.9 ± 142.9, $p<0.001$). The pore areas in the skin ECM hydrogels and hybrid ECM hydrogels were larger than in the lung ECM hydrogel at day 1 (Fig. 4C). This disparity with lung ECM hydrogels persisted even after five days of HPMEC culturing in skin ECM hydrogels (Fig. 4C, 1,197 ± 448.9 vs 622.3 ± 190.1, $p=0.0007$), yet the mean pore area of lung ECM hydrogels had increased by day 5 to similar levels as hybrid ECM hydrogels (Fig. 4C). Pore areas of seeded skin and hybrid ECM hydrogels it did not differ upon culturing for one and five days compare to the cell -free ECM hydrogel (Suppl. Fig. S2B). Intriguingly, at day one, the pore area in HPMEC-seeded lung ECM hydrogels was smaller than cell-free ECM hydrogel and day 5 gels (Suppl. Fig. S2B). Also, the pore area of the hybrid ECM hydrogel proximal to the HPMEC was lagger than it was distal to the HPMEC after five days (Suppl. Fig. S2E).

In contrast, the number of pores in the skin ECM hydrogel were less than in the lung ECM hydrogel (Fig. 4D, 182.0 ± 13.7 vs 353.2 ± 38.6, $p<0.0001$), and also lower than in hybrid ECM hydrogel (182.0 ± 13.7 vs 277.7 ± 40.94, $p=0.0002$).

While the differences in the number of pores were maintained at one day post-seeding, the average number of pores in skin and hybrid ECM hydrogels had increased at day five post-seeding and were similar to lung ECM hydrogels (Fig. 4D). Furthermore, the number of pores in HPMEC-seeded skin ECM hydrogels did not change compared to cell-free ECM hydrogel at days one and five (Suppl. Fig. S2C). In contrast, the number of pores had decreased at day one in HPMEC-seeded lung ECM hydrogels compared to the cell-free lung ECM hydrogels ($p=0.0465$), and this decrease continued at day five ($p=0.0107$) compared to day 1. Similarly, the number of pores had decreased in HPMEC-seeded hybrid ECM hydrogels at day 1 ($p=0.0016$). The number of pores in the skin ECM hydrogel and hybrid ECM hydrogel remained lower than that in the lung ECM hydrogel after HPMEC seeding on day 1 (Fig. 4D, skin vs lung ECM hydrogel:175.9 ± 25.8 vs 314.3 ± 35.4, $p<0.001$; hybrid vs lung ECM hydrogel: 179.1 ± 42.2 vs 314.3 ± 35.4, $p<0.001$). The number of pores around the HPMEC was higher than those distal from the HPMEC in the lung ECM hydrogels after five days culturing (Suppl. Fig. S2F, $p=0.00211$). However, regarding the proliferation of HPMEC and remodeling of ECM, no differences were observed among the three gels at day five (Fig. 4D).

The ultrastructure analyses revealed that the hybrid ECM hydrogels exhibited a composite architecture, representing a combination of the skin and lung ECM hydrogels. ECs changed the architecture of their 3D microenvironment over time. The differences in fiber diameter and pore area persisted among the three gels, notwithstanding a reduction of these differences by endothelial cell activities.

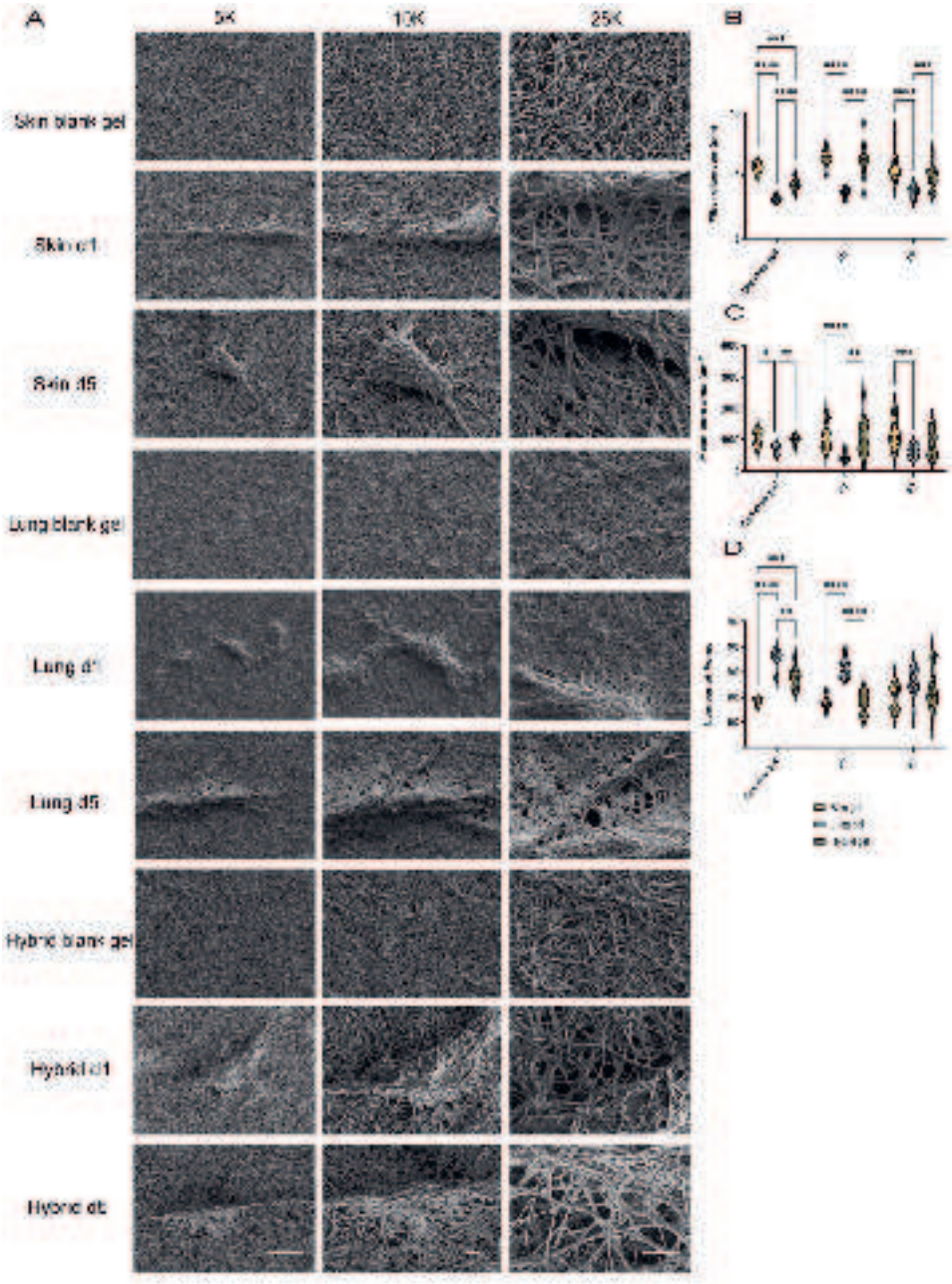

Figure 4. Ultrastructure of the extracellular matrix. (A) Fibers of the matrix in skin, lung, and hybrid ECM hydrogels and fibers of three distinct types of hydrogels loaded with HPEMC at days 1 and 5 at three different magnifications: 5, 10, and 25K. Scale bars represent 10 μm in 5K. Scale bars represent 2 μm in 10 and 25K. (B) Analyses of the mean fiber diameter of cell-free skin, lung, and hybrid ECM hydrogel and Mean fiber

diameter of HPMEC-loaded skin, lung, and hybrid ECM hydrogel at days 1 and 5. (C) Analyses of the mean pore area within the fiber mesh of cell-free skin, lung, and hybrid ECM hydrogels. Mean pore area of HPMEC-loaded skin, lung, and hybrid ECM hydrogels at days 1 and 5. (D) Analyses of the number of pores within the fiber mesh of cell-free skin, lung, and the hybrid ECM hydrogel. The number of pores within the fiber mesh of HPMEC-loaded skin, lung, and hybrid ECM hydrogels at days 1 and 5.

3.5 Degradation of hydrogels is organ dependent

To investigate whether the changes in pore area and number were attributed to the degradation of the ECM hydrogel by HPMEC during VNF, we examined the presence of the archetype ECM-degrading proteases MMP1 and MMP9 by immunofluorescent staining. Cell-free ECM hydrogels were devoid of detectable levels of MMP1 (Suppl. Fig. 3). During HPMEC VNF on day 1 and day 5, no more than minimal MMP1 expression was observed in the lung and hybrid ECM hydrogels (Fig. 5A, red). In contrast, the skin ECM hydrogel showed significant MMP1 deposition as early as after one day of culturing (Fig. 5B), and its expression remained higher than that in the lung ECM hydrogel after five days (Fig. 5C, 0.0189 ± 0.0158 vs 0.00583 ± 0.00719, $p=0.0363$). Interestingly, the differences in MMP1 expression between the skin ECM hydrogel and hybrid ECM hydrogel on day 1 (Fig. 5B) disappeared after five days (Fig. 5C). MMP1 was predominantly localized around cells, with scattered deposition more distally in the hydrogel.

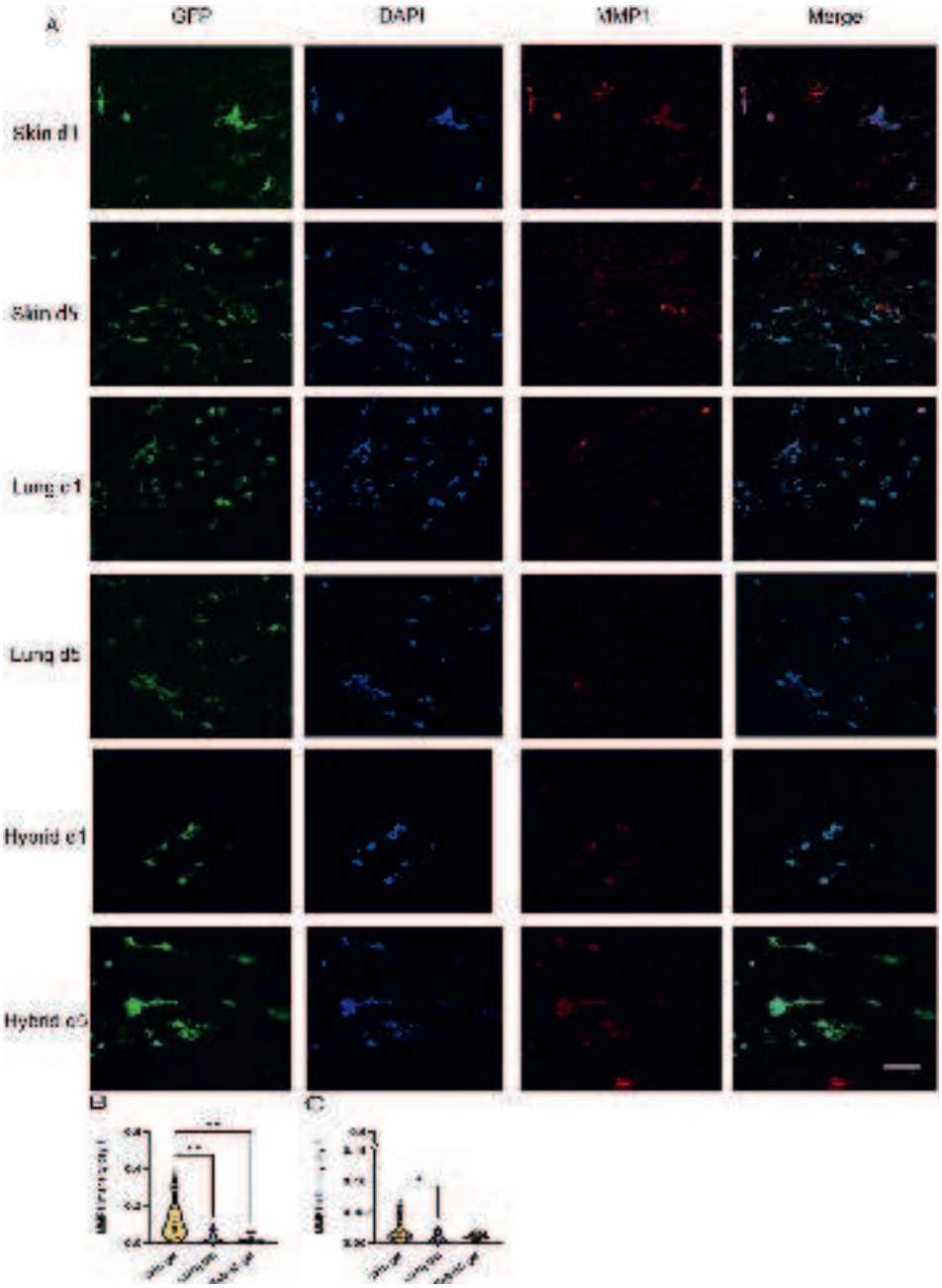

Figure 5. Fluoromicrographs of MMP1 staining. (A) Representative images of fibronectin staining of 4 μm sections of paraffin-embedded hydrogels. Merged images: green, GPF-labeled HPMEC; red, MMP1; blue, nuclei (DAPI). Scale bar: 58 μm. (B) Comparison of the MMP1 intensity per nuclei among three different gels at day 1. (C) Comparison of MMP1 intensity per nuclei among three different gels at day 5.

Additionally, MMP9 was assessed through immunofluorescent staining. In contrast to MMP1, cell-free lung (and hybrid) ECM hydrogels revealed minimal staining of MMP9 (Suppl. Fig. 4). To ensure standardization, the expression level of MMP9 in the HPMEC-loaded hydrogel was normalized against the expression level of MMP9 in the cell-free gel, as described in the methods section. The localization of MMP9 was observed not only in the proximity of HPMEC but also in distal areas of the ECM hydrogel (Fig. 6A, red). Intriguingly, the deposition of MMP9 in the hybrid ECM hydrogel did not exhibit an intermediate level between the skin and lung; instead, its expression was higher than both the deposition in the skin ECM hydrogel and the lung ECM hydrogel on day 1 (Fig. 6B) and day 5 (Fig. 6C).

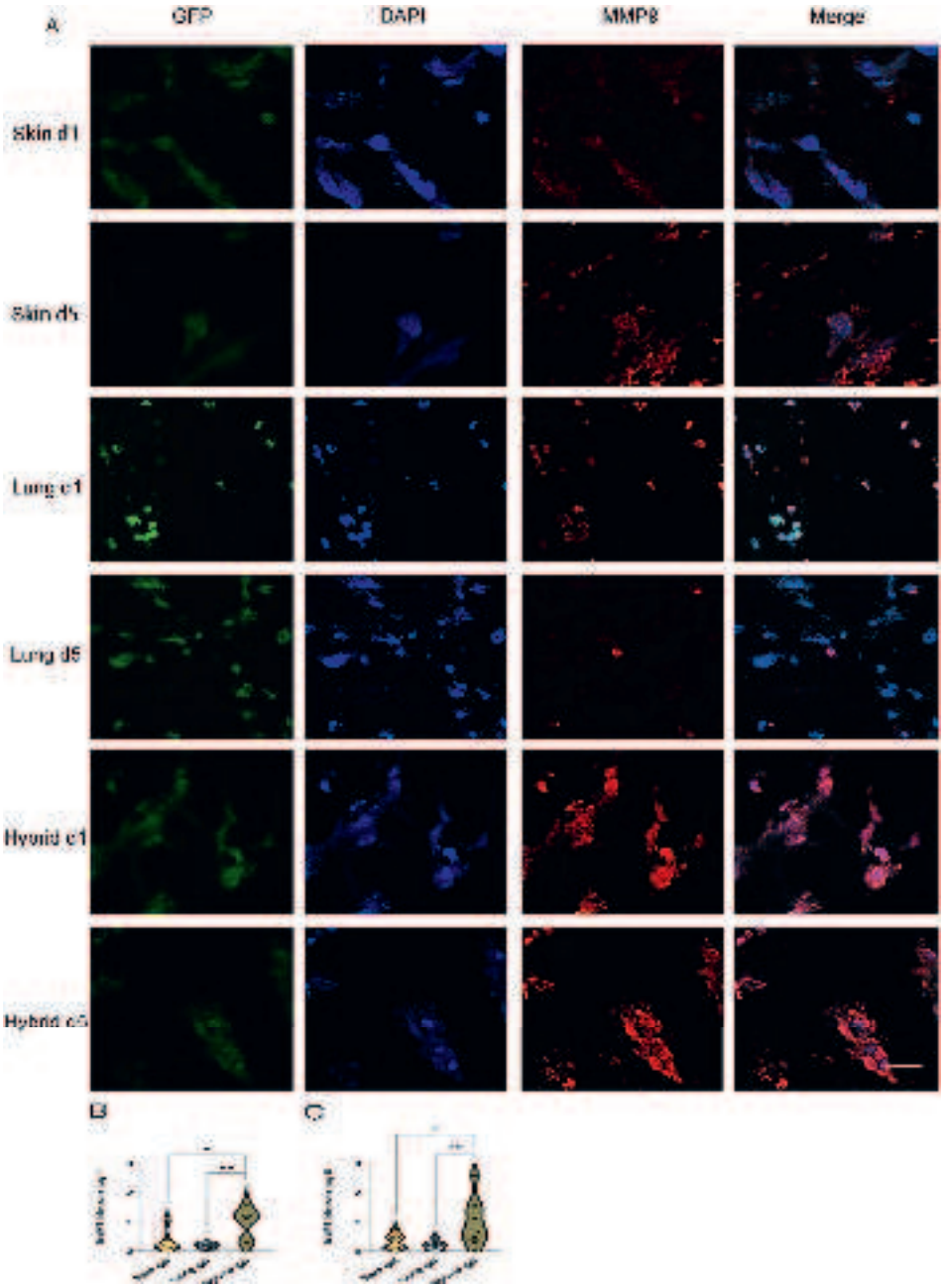

Figure 6. Fluoromicrographs of MMP9 staining. (A) Representative images of fibronectin staining of 4 μm sections of paraffin-embedded hydrogels. Merged images: green, GPF labeled HPMEC; red, MMP9; blue, nuclei (DAPI). Scale bar: 58 μm. (B) Comparison of the MMP9 intensity per nuclei among three different gels at day 1. (C) Comparison of MMP9 intensity per nuclei among three different gels at day 5.

3.6 VNF directs novel deposition of vasculogenic ECM components in an organ-dependent fashion.

All three types of cell-fee ECM hydrogels contained no detectable fibronectin (Suppl. Fig. 5). After one day of culturing, HPMEC-seeded hybrid ECM hydrogels showed a strong deposition of fibronectin (Fig. 7A), which remained on day 5. In contrast, only minimal fibronectin deposition had occurred in the skin and lung ECM hydrogels at days one and five. The cross-sectional fluorescence intensity on day 1 and day 5 was analyzed by CellProfiler (Fig. 7B.C). The expression of fibronectin in hybrid ECM hydrogel was higher than in skin ECM hydrogel on day 1 (Fig. 7B, 0.658 ± 0.516 vs 0.118 ± 0.132, $p= 0.0128$) and day 5 (Fig. 7C, 0.381 ± 0.255 vs 0.164 ± 0.0831, $p= 0.0247$).

Besides fibronectin, the basement membrane constituent collagen IV is also involved in vascularization processes. The immunostained fluoromicrographs showed that collagen IV had a deposition pattern similar to fibronectin. Cell-free hydrogels harbored negligible amounts of collagen IV (Suppl. Fig. 6). The deposition of collagen IV by HPMEC was reminiscent of fibronectin (Fig. 8A-C). Again, at days one and five, minimal deposition had occurred in skin and lung ECM hydrogels while hybrid gels showed a high deposition compared to lung ECM hydrogels on day five (Fig. 8C, 0.286 ± 0.167 vs 0.082 ± 0.039, $p=0.0110$).

An overview of the measurements made throughout the summary is provided in Tabe 3.

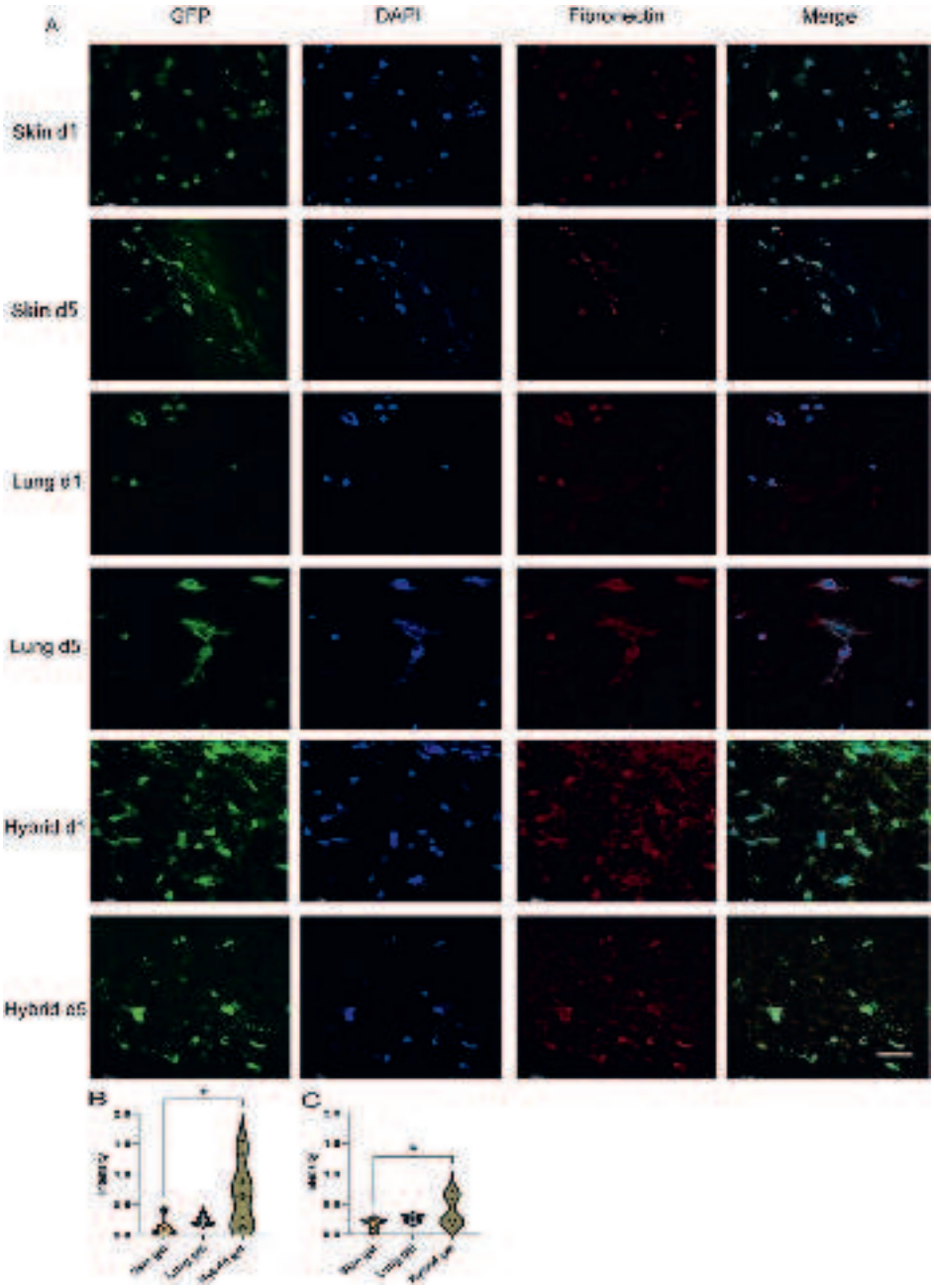

Figure 7. Fluoromicrographs of fibronectin-staining. (A) Representative images of fibronectin staining of 4 μm sections of paraffin-embedded hydrogels. Merged images: green, GPF-labeled HPMEC; red, fibronectin; blue, nuclei (DAPI). Scale bar: 58 μm. (B) Comparison of the fibronectin intensity per nuclei among three different gels at day 1. (C) Comparison of fibronectin intensity per nuclei among three different gels at day 5.

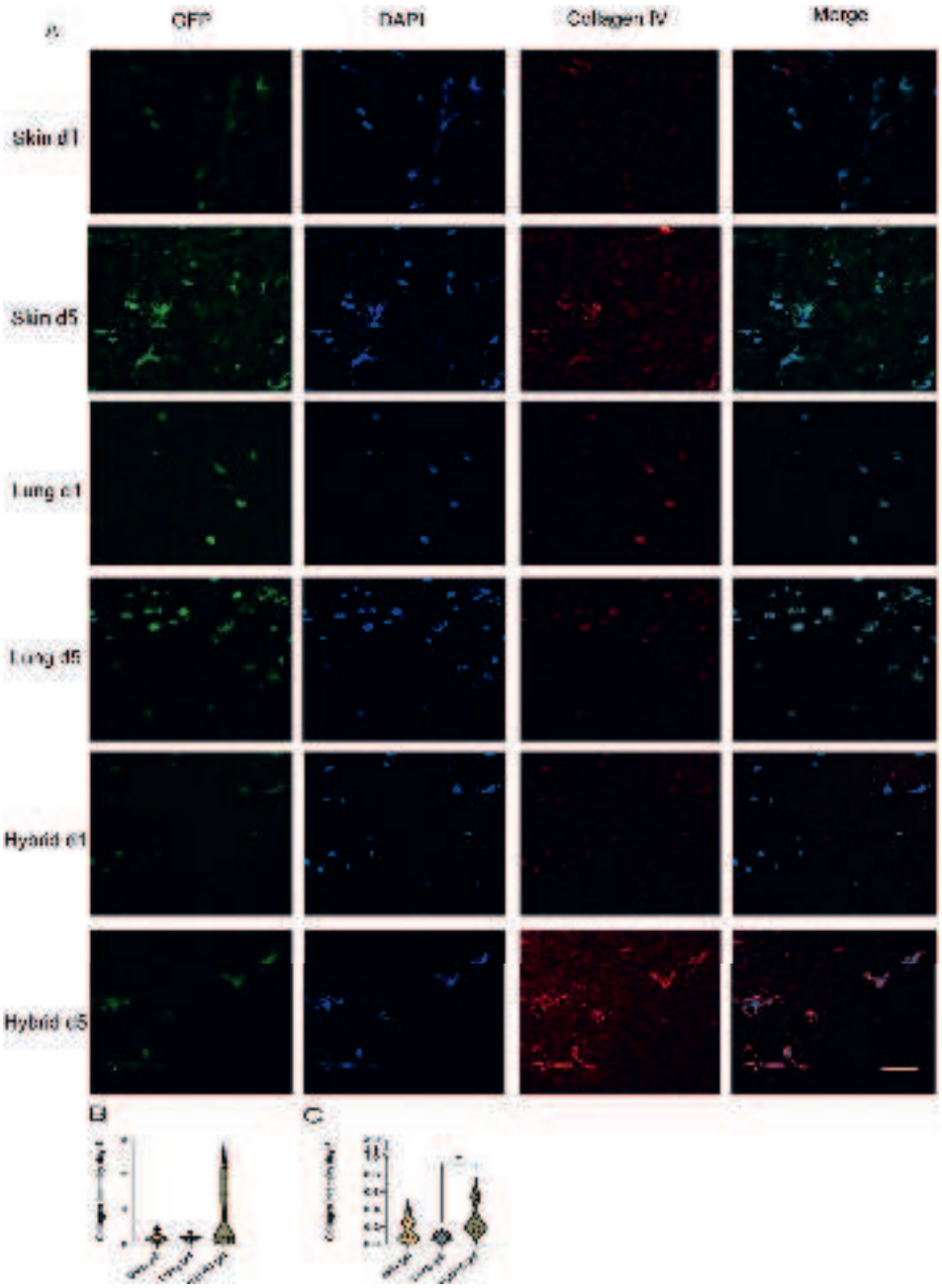

Figure 8. Fluoromicrographs of collagen IV staining. (A) Representative images of fibronectin staining of 4 μm sections of paraffin-embedded hydrogels. Merged images: green, GPF-labeled HPMEC; red, collagen IV; blue, nuclei (DAPI). Scale bar: 58 μm. (B) Comparison of collagen IV intensity per nuclei among three different gels at day 1. (C) Comparison of collagen IV intensity per nuclei among three different gels at day 5. The

data are from 3 independent experiments. Three randomly selected ROIs were measured for every single sample, and each dot represents a measurement of a randomized region. One-way ANOVA comparing gel, $*p < 0.05$.

Table 3: summary of the measurements of all parameters in the three hydrogels on day 1 and day 5. The more + marked, the higher value recorded.

Features	**Skin ECM hydrogel**		**Lung ECM hydrogel**		**Hybrid ECM hydrogel**	
Time point	day 1	day 5	day 1	day 5	day 1	day 5
Stiffness	+	+	+++	+	++	+
Total stress relaxation	+	+	+	+	+	++
Fiber diameter	++++	++++	+	++	+++	+++
Mean Pore Area	++++	++++	+	++	+++	+++
Number of Pores	++	++	+++	++	++	++
Ki67	+++	++	++	+	++	++
MMP 1	+++	++	+	+	+	++
MMP9	++	++	+	+	+++	+++
Fibronectin	+	+	+	+	++	+
collagen IV	+	+	+	+	+	++

3.7 Principal Component Analyses

To further understand the interrelationship between, on the one hand VNF and on the other hand, culture times, cellular responses and matrix changes, we performed a Principal Component Analysis (PCA). In these analyses we did not take into consideration the different types of hydrogels. Principal components that defined the VNF-dependent variable “total branching length” were analyzed and 3D plotted. The components of gels and cell responses were categorized at two time points: day 1 and day 5. On day 1, there was no evident clustering of data points observed between the variables measured in this study (Suppl. Fig. 7A). In contrast, the 3D PCA scatter plots on day 5 showed distinct and discernible clustering (Suppl. Fig. 7B), which indicated a strong correlation between the PCA-derived component groups and the VNF. We further dissected the PCA

clusters to reveal hitherto unknown relationships between the parameters we had measured and VNF. We elected to examine the number of principal components that collectively accounted for a minimum of 60% of the cumulative variance within the data. Upon the inclusion of the third principal component, as shown in the scree plots (Suppl. Fig. 8), the cumulative proportion of variance explained exceeded the threshold of 60%. The relative influence of the three principal components (PC1, PC2 and PC3) on day 5 individually accounted for 40.1%, 13.5%, and 10.0% of the data description.

Table 4 presents the correlations or weights of the parameters we measured to each principal component. We selected the average arbitrary value of PC at ±0.21365 as the threshold for assessing the contribution of features in relation to VNF. Given the samples with longer total branching length were generally clustering at the back left-hand quadrant of the 3D plot (negative arbitrary values on PC1 and PC3 but positive arbitrary values on PC2 axes) (dots with red shades), we standardized all components as described in methods for easier understanding. Features with contributions more than 0.21365 arbitrary units were interpreted as having a strong positive impact on VNF, whereas those less than -0.21365 arbitrary units were construed as needing to be reduced to allow VNF. In PC1 PCA indicated a lower stiffness, slim fiber diameter with small but plentiful pores was the ideal environment for VNF. In PC2 the combination of lower stiffness, increased stress relaxation, a reduced number of pores and enhanced presence of collagen IV supported VNF. In PC3 the less presence of collagen IV, MMP1 and MMP9 with slim fiber diameters and reduced total stress relaxation with endothelial cells that had a lower rate of proliferation supported enhanced VNF.

Table 4: Contributions of the measured variables within each principal component group. Units are arbitrary units.

Feature	PC1	PC2	PC3
Stiffness	-0.3762	-0.3143	
Total stress relaxation		0.7496	0.2517
Fiber diameter	-0.4656		-0.2198
Mean Pore Area	-0.5192		
Number of Pores	0.4788	-0.2913	
Ki67 ratio	-0.2686		-0.3100
MMP 1			-0.2731
MMP9			-0.4526
Collagen IV		0.3685	-0.6657

4. Discussion

In this study, we examined the impact of various organ-derived hydrogels on VNF by ECs. We found that skin ECM-derived hydrogels are the most potent enhancers of VNF and endothelial cell proliferation, compared to ECM-derived hydrogels from lung or a hybrid of both ECM sources. Our second main finding was that mechanical properties of the hydrogels influenced VNF and subsequent ECM remodeling in a time and organ (mixture)-dependent fashion. Principal mechanical properties of the gel included stiffness, viscosity, the number and the area of the pores, diameter exert a more pronounced influence on the VNF than the biochemical proteins such as MMP9, fibronectin, and collagen IV. Finally, hybrid ECM hydrogels did not influence VNF or associated processes in a manner that mirrors the "average" effects observed with skin and lung ECM hydrogels.

The process of vascularization involves a complex interaction between ECs and their ECM environment. Underlying mechanisms remain elusive. The morphology of biomaterial fibers influences cell adhesion, proliferation, and orientation[25]. Larger pores affect cell seeding, distribution, migration, and further neovascularization in vivo[26-28]. Our research facilitated the evaluation

of the mutual interactions between ECs and the ECM across a span of time. PCA indicated that more small pores within the fiber matrix contributed to the enhancement of VNF when the fibers were thinner. An optimal ECM architecture is one characterized by pores that are sufficiently spacious to facilitate easy cell penetration into the internal spaces, while simultaneously preventing excessive pore size that might hinder cells from effectively extending and stretching between the fibers[29]. Our PCA results were in alignment with this finding. An adequate number of pores within the ECM hydrogel, serving as a positive factor, offered ample space for cell proliferation, thereby promoting VNF. Conversely, when the pore areas were excessively large, the ECs were unable to establish connections with one another, thus acting as a negative factor inhibiting VNF in our study.

The ultrastructure of ECM hydrogel also impacted the proliferation of ECs [30]. PCA revealed that a reduced Ki67, indicative of proliferation, stood out as another primary determinant for VNF on day 5. Lower proliferation of HPMEC in lung and hybrid ECM hydrogels as compared to skin ECM hydrogels was beneficial for VNF on day 5, whereas the excessive proliferation within the skin ECM hydrogel led to the cellular occupation of pores among the ECM hydrogel fibers, potentially limiting VNF.

Understanding the influence of ECM stiffness on ECs holds significant importance [31]. In collagen or fibrin hydrogels or on ECM-coated polyacrylamide gels, an increased stiffness of the ECM hampered VNF[32], resulting in shorter, thicker, slower-growing sprouts, fewer branching points, and reduced network connectivity[33-35]. Nonetheless, this stiffness-induced effect also promotes the formation of larger and more stable lumens[36, 37]. Our results in native organ-derived ECM hydrogels corroborate these findings. The stiffer lung ECM hydrogels had less VNF than skin ECM hydrogels. Moreover, as per the results of the PCA, it was found that the stiffness of gels on day 5 was a strong regulatory factor, with reduced stiffness promoting VNF in both PC1 and PC2.

The architectural and stiffness changes during VNF are mediated through matrix remodeling as well as through pulling forces that are exerted by the cells on the fiber networks. During wound healing and the associated vascularization processes, ECM remodeling is a dynamic spatiotemporally regulated process. Remodeling of ECM during vascularization, is a balance of degradation by

MMPs[38, 39] and deposition of vasculogenic ECM components, like fibronectin and collagen IV. Our results show that MMPs are upregulated in the ECM during VNF and may contribute to decreases in stiffness that negatively correlate with VNF. The stiffness of hybrid ECM hydrogel decreased after five days culturing, corresponded with the highest expression of MMP9 among three types of gels. The gelatinase MMP9 can degrade collagen IV [40] which was highly expressed in the hybrid ECM hydrogel. These findings suggested that a regulatory feedback loop exists between expression levels of MMP9 and collagen IV in hybrid ECM hydrogels. Importantly, this shows that ECs in hybrid ECM hydrogels do not respond merely as the average responses of ECs in both individual gels but rather have a defined response to this unique environment.

MMP1 mediated ECM degradation facilitated the VNF of ECs[41]. MMP1 expression in skin ECM hydrogels was highly expressed compared to the other gels. According to the outcomes derived from the PCA, MMP1 was identified as one of the contributing features that augment VNF in PC3. We assume that highly expressed MMP1 was the consequence of over proliferation of the ECs. During VNF when ECs needed more space to build the branches and mesh within the hydrogels, they facilitated this through the expression of MMPs. Regarding fibronectin, there was more dispersed distribution and a higher level of expression in the hybrid ECM hydrogels. Fibronectin appeared to have supported cell adhesion of ECs during VNF in skin and lung ECM hydrogels, while in hybrid ECM hydrogels it may also have mainly acted to stabilize the ECM by bridging collagen fibers[42]. The extent of the contribution of the deposition of fibronectin to the VNF formation requires more investigation, as it did not feature in our PCA analyses. In terms of biochemistry, the hybrid ECM hydrogel did not demonstrate an intermediary behavior between the skin and lung ECM hydrogels, despite its physical properties (stiffness, viscosity, fiber diameter, pore size and number of the pores) falling between those of the skin and lung ECM hydrogels.

In this research, PCA was performed on the ECs phenotype and ECM property dataset to draw correlations between ECs response and ECM properties to establish correlations between ECs responses and ECM attributes. PCA stands as a powerful method to predict the significance of individual features within a multifactorial biomaterial affecting VNF. After analyzing 10 features including physical characters (viscoelasticity and architecture) and biochemical features pertaining to ECM turnover, the physical properties were shown to influence the

VNF more than the biochemical properties. However, we have not yet investigated the specific influence of distinct chemical components, such as collagen I and GAGs, originally present in the three different gels, nor did we consider the individual compositions of the three different hydrogels in these analyses. Also, it is challenging to definitively attribute the lower significance of biochemical proteins secreted by ECs, such as MMPs and fibronectin, to VNF, as it remains unclear whether this outcome is a consequence of the physical properties or if physical properties indeed play a more dominant role in VNF. The therapeutic ramifications of our findings are that by mixing different organ-derived ECM hydrogels it is possible to 'tweak' its influence on vascularization.

Conclusion

This study shows that VNF by HPMEC in ECM hydrogels or mixtures, depends on the organ origin of the ECM. The mutual interaction showed that the initial physical properties of the gels, influence VNF while at later stages cellular driven changes in gels' physical properties also influence the process.

Acknowledgements

We acknowledge the support from Klaas Sjollema towards the utilization of microscopes at UMIC in this study. M.Z was supported by Stichting De Cock-Hadders foundation (Project number 2023-11). J.K.B. was supported by Nederlandse Organisatie voor Wetenschappelijk Onderzoek (NWO) Aspasia-premie subsidienummer (015.013.010).

Reference:

1. Goel, S., D.G. Duda, L. Xu, L.L. Munn, Y. Boucher, D. Fukumura, and R.K. Jain, Normalization of the vasculature for treatment of cancer and other diseases. Physiol Rev, 2011. **91**(3): p. 1071-121.
2. Brust, M., O. Aouane, M. Thiébaud, D. Flormann, C. Verdier, L. Kaestner, M.W. Laschke, H. Selmi, A. Benyoussef, T. Podgorski, G. Coupier, C. Misbah, and C. Wagner, The plasma protein fibrinogen stabilizes clusters of red blood cells in microcapillary flows. Sci Rep, 2014. **4**: p. 4348.
3. Julier, Z., A.J. Park, P.S. Briquez, and M.M. Martino, Promoting tissue regeneration by modulating the immune system. Acta Biomater, 2017. **53**: p. 13-28.
4. Eming, S.A., P. Martin, and M. Tomic-Canic, Wound repair and regeneration: mechanisms, signaling, and translation. Sci Transl Med, 2014. **6**(265): p. 265sr6.
5. Kolimi, P., S. Narala, D. Nyavanandi, A.A.A. Youssef, and N. Dudhipala, Innovative Treatment Strategies to Accelerate Wound Healing: Trajectory and Recent Advancements. Cells, 2022. **11**(15).
6. Han, G. and R. Ceilley, Chronic Wound Healing: A Review of Current Management and Treatments. Adv Ther, 2017. **34**(3): p. 599-610.
7. Kobayashi, M., J. Kadota, Y. Hashimoto, T. Fujisato, N. Nakamura, T. Kimura, and A. Kishida, Elastic Modulus of ECM Hydrogels Derived from Decellularized Tissue Affects Capillary Network Formation in Endothelial Cells. Int J Mol Sci, 2020. **21**(17).
8. Correa, S., A.K. Grosskopf, H. Lopez Hernandez, D. Chan, A.C. Yu, L.M. Stapleton, and E.A. Appel, Translational Applications of Hydrogels. Chem Rev, 2021. **121**(18): p. 11385-11457.
9. Saldin, L.T., M.C. Cramer, S.S. Velankar, L.J. White, and S.F. Badylak, Extracellular matrix hydrogels from decellularized tissues: Structure and function. Acta Biomater, 2017. **49**: p. 1-15.
10. Vriend, L., J.A. van Dongen, V. Sinkunas, L.A. Brouwer, H.J. Buikema, L.F. Moreira, R. Gemperli, L. Bongiovanni, A. de Bruin, B. van der Lei, C.P. Camargo, and M.C. Harmsen, Limited Efficacy of Adipose Stromal Cell Secretome-Loaded Skin-Derived Hydrogels to Augment Skin Flap Regeneration in Rats. Stem Cells Dev, 2022. **31**(19-20): p. 630-640.
11. Badylak, S.F., D.O. Freytes, and T.W. Gilbert, Extracellular matrix as a biological scaffold material: Structure and function. Acta Biomaterialia, 2009. **5**(1): p. 1-13.
12. Martinez-Garcia, F.D., R.H.J. de Hilster, P.K. Sharma, T. Borghuis, M.N. Hylkema, J.K. Burgess, and M.C. Harmsen, Architecture and Composition Dictate Viscoelastic Properties of Organ-Derived Extracellular Matrix Hydrogels. Polymers, 2021. **13**(18): p. 3113.
13. Liguori, G.R., T.T.A. Liguori, S.R. de Moraes, V. Sinkunas, V. Terlizzi, J.A. van Dongen, P.K. Sharma, L.F.P. Moreira, and M.C. Harmsen, Molecular and Biomechanical Clues From Cardiac Tissue Decellularized Extracellular Matrix Drive Stromal Cell Plasticity. Front Bioeng Biotechnol, 2020. **8**: p. 520.

14. Martinez-Garcia, F.D., R.H.J. de Hilster, P.K. Sharma, T. Borghuis, M.N. Hylkema, J.K. Burgess, and M.C. Harmsen, Architecture and Composition Dictate Viscoelastic Properties of Organ-Derived Extracellular Matrix Hydrogels. Polymers (Basel), 2021. **13**(18).

15. Hynes, R.O., The extracellular matrix: not just pretty fibrils. Science, 2009. **326**(5957): p. 1216-9.

16. Zhang, M., F. Zhao, X. Zhang, L.A. Brouwer, J.K. Burgess, and M.C. Harmsen, Fibroblasts alter the physical properties of dermal ECM-derived hydrogels to create a pro-angiogenic microenvironment. Materials Today Bio, 2023. **23**: p. 100842.

17. Krump-Konvalinkova, V., F. Bittinger, R.E. Unger, K. Peters, H.A. Lehr, and C.J. Kirkpatrick, Generation of human pulmonary microvascular endothelial cell lines. Lab Invest, 2001. **81**(12): p. 1717-27.

18. Ades, E.W., F.J. Candal, R.A. Swerlick, V.G. George, S. Summers, D.C. Bosse, and T.J. Lawley, HMEC-1: establishment of an immortalized human microvascular endothelial cell line. J Invest Dermatol, 1992. **99**(6): p. 683-90.

19. Getova, V.E., J.A. van Dongen, L.A. Brouwer, and M.C. Harmsen, Adipose tissue-derived ECM hydrogels and their use as 3D culture scaffold. Artif Cells Nanomed Biotechnol, 2019. **47**(1): p. 1693-1701.

20. Carpentier, G., S. Berndt, S. Ferratge, W. Rasband, M. Cuendet, G. Uzan, and P. Albanese, Angiogenesis Analyzer for ImageJ — A comparative morphometric analysis of "Endothelial Tube Formation Assay" and "Fibrin Bead Assay". Scientific Reports, 2020. **10**(1): p. 11568.

21. Hilster, R.H.J.d., P.K. Sharma, M.R. Jonker, E.S. White, E.A. Gercama, M. Roobeek, W. Timens, M.C. Harmsen, M.N. Hylkema, and J.K. Burgess, Human lung extracellular matrix hydrogels resemble the stiffness and viscoelasticity of native lung tissue. American Journal of Physiology-Lung Cellular and Molecular Physiology, 2020. **318**(4): p. L698-L704.

22. de Hilster, R.H.J., P.K. Sharma, M.R. Jonker, E.S. White, E.A. Gercama, M. Roobeek, W. Timens, M.C. Harmsen, M.N. Hylkema, and J.K. Burgess, Human lung extracellular matrix hydrogels resemble the stiffness and viscoelasticity of native lung tissue. Am J Physiol Lung Cell Mol Physiol, 2020. **318**(4): p. L698-l704.

23. Hotaling, N.A., K. Bharti, H. Kriel, and C.G. Simon, DiameterJ: A validated open source nanofiber diameter measurement tool. Biomaterials, 2015. **61**: p. 327-338.

24. Pedregosa, F., G. Varoquaux, A. Gramfort, V. Michel, B. Thirion, O. Grisel, M. Blondel, P. Prettenhofer, R. Weiss, and V. Dubourg, Scikit-learn: Machine learning in Python. the Journal of machine Learning research, 2011. **12**: p. 2825-2830.

25. Cai, S., C. Wu, W. Yang, W. Liang, H. Yu, and L. Liu, Recent advance in surface modification for regulating cell adhesion and behaviors. Nanotechnology Reviews, 2020. **9**(1): p. 971-989.

26. Milleret, V., T. Hefti, H. Hall, V. Vogel, and D. Eberli, Influence of the fiber diameter and surface roughness of electrospun vascular grafts on blood activation. Acta Biomaterialia, 2012. **8**(12): p. 4349-4356.

27. Yao, T., H. Chen, M.B. Baker, and L. Moroni, Effects of Fiber Alignment and Coculture with Endothelial Cells on Osteogenic Differentiation of Mesenchymal Stromal Cells. Tissue Eng Part C Methods, 2020. **26**(1): p. 11-22.

28. Almonacid Suarez, A.M., I. van der Ham, M.G.L. Brinker, P. van Rijn, and M.C. Harmsen, Topography-driven alterations in endothelial cell phenotype and contact guidance. Heliyon, 2020. **6**(6): p. e04329.

29. Lowery, J.L., N. Datta, and G.C. Rutledge, Effect of fiber diameter, pore size and seeding method on growth of human dermal fibroblasts in electrospun poly(ε-caprolactone) fibrous mats. Biomaterials, 2010. **31**(3): p. 491-504.

30. Tsou, Y.-H., J. Khoneisser, P.-C. Huang, and X. Xu, Hydrogel as a bioactive material to regulate stem cell fate. Bioactive Materials, 2016. **1**(1): p. 39-55.

31. Hu, M., F. Jia, W.P. Huang, X. Li, D.F. Hu, J. Wang, K.F. Ren, G.S. Fu, Y.B. Wang, and J. Ji, Substrate stiffness differentially impacts autophagy of endothelial cells and smooth muscle cells. Bioact Mater, 2021. **6**(5): p. 1413-1422.

32. Ghajar, C.M., X. Chen, J.W. Harris, V. Suresh, C.C.W. Hughes, N.L. Jeon, A.J. Putnam, and S.C. George, The Effect of Matrix Density on the Regulation of 3-D Capillary Morphogenesis. Biophysical Journal, 2008. **94**(5): p. 1930-1941.

33. Krishnan, R., D.D. Klumpers, C.Y. Park, K. Rajendran, X. Trepat, J. van Bezu, V.W. van Hinsbergh, C.V. Carman, J.D. Brain, J.J. Fredberg, J.P. Butler, and G.P. van Nieuw Amerongen, Substrate stiffening promotes endothelial monolayer disruption through enhanced physical forces. Am J Physiol Cell Physiol, 2011. **300**(1): p. C146-54.

34. Huynh, J., N. Nishimura, K. Rana, J.M. Peloquin, J.P. Califano, C.R. Montague, M.R. King, C.B. Schaffer, and C.A. Reinhart-King, Age-Related Intimal Stiffening Enhances Endothelial Permeability and Leukocyte Transmigration. Science Translational Medicine, 2011. **3**(112): p. 112ra122-112ra122.

35. Schnellmann, R., D. Ntekoumes, M.I. Choudhury, S. Sun, Z. Wei, and S. Gerecht, Stiffening Matrix Induces Age-Mediated Microvascular Phenotype Through Increased Cell Contractility and Destabilization of Adherens Junctions. Adv Sci (Weinh), 2022. **9**(22): p. e2201483.

36. Effects of the Mechanical Properties of Collagen Gel on the In Vitro Formation of Microvessel Networks by Endothelial Cells. Tissue Engineering, 2007. **13**(7): p. 1443-1453.

37. Shamloo, A. and S.C. Heilshorn, Matrix density mediates polarization and lumen formation of endothelial sprouts in VEGF gradients. Lab on a Chip, 2010. **10**(22): p. 3061-3068.

38. Stamenkovic, I., Extracellular matrix remodelling: the role of matrix metalloproteinases. J Pathol, 2003. **200**(4): p. 448-64.

39. Alexander, J. and J.W. Elrod, Extracellular matrix, junctional integrity and matrix metalloproteinase interactions in endothelial permeability regulation. Journal of anatomy, 2002. **200**(6): p. 561-574.

40. Zeng, Z.S., A.M. Cohen, and J.G. Guillem, Loss of basement membrane type IV collagen is associated with increased expression of metalloproteinases 2 and 9 (MMP-2 and MMP-9) during human colorectal tumorigenesis. Carcinogenesis,

1999. **20**(5): p. 749-55.

41. Merfeld-Clauss, S., N. Gollahalli, K.L. March, and D.O. Traktuev, Adipose tissue progenitor cells directly interact with endothelial cells to induce vascular network formation. Tissue Eng Part A, 2010. **16**(9): p. 2953-66.

42. Sottile, J. and D.C. Hocking, Fibronectin polymerization regulates the composition and stability of extracellular matrix fibrils and cell-matrix adhesions. Mol Biol Cell, 2002. **13**(10): p. 3546-59.

Supplementary data

Supplementary data is available free of charge at https://pubs.acs.org/doi/10.1021/acsami.4c05864

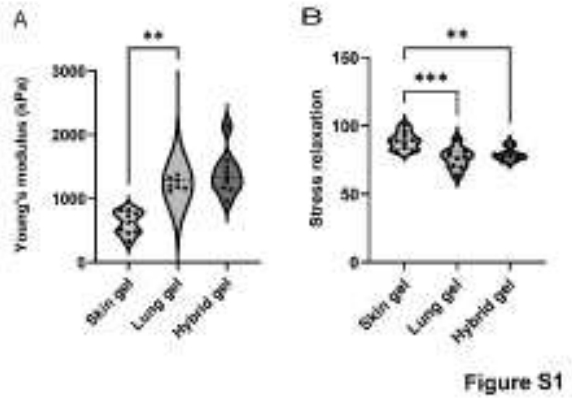

Fig.S1. Comparison of physical characteristics of three distinct types of cell-free ECM hydrogels. (A) Stiffness of skin, lung, and hybrid ECM hydrogel. (B) Total stress relaxation of skin, lung, and hybrid ECM hydrogel. The data are from three independent experiments. Three randomly selected ROIs were measured for every single sample, and each dot represents a measurement of a randomized region. one-way ANOVA comparing gel, ** $p < 0.01$, **** $p << 0.0001$.

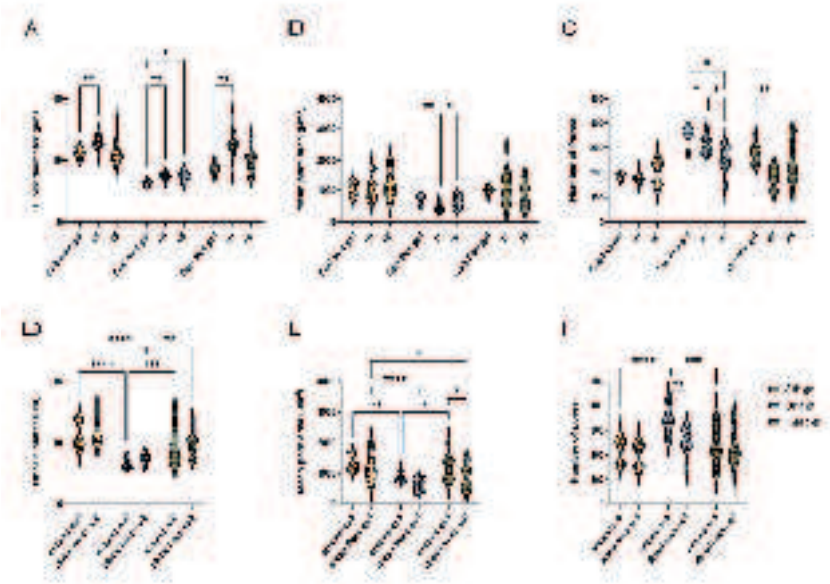

Figure S2

Fig.S2. Comparison of the microstructure of the fibers and pores. (A) Comparison of mean fiber diameter among cell-free ECM hydrogel, and HPMEC-loaded skin at day 1 and 5 in skin, lung and hybrid ECM hydrogel respectively. (B) Comparison of mean pore area among cell-free ECM hydrogels, and HPMEC-loaded hydrogels at day 1 and 5 culture in skin, lung, and hybrid ECM hydrogels respectively. (C) Comparison of the number of pores within the fiber mesh among cell-free ECM hydrogel, and HPMEC-loaded hydrogels at day 1 and 5 in skin, lung, and hybrid ECM hydrogels respectively. (D) Comparison of mean fiber diameter of three distinctive hydrogels around the HPMEC and distal from the HPMEC at day 1 5 days. (E) Comparison of mean pore area of three distinctive hydrogels proximal and distal to the HPMEC at day 1 5 days. (F) Comparison of the number of pores within the fiber mesh of three distinctive hydrogels proximal and distal to the HPMEC at day 1 5. The data are from 3 independent experiments. 5 randomly selected ROIs were measured for every single sample, each dot represents a measurement of a randomized region. Tukey's multiple comparisons test, * $p < 0.05$, ** $p < 0.01$, *** $p < 0.001$, **** $p << 0.0001$.

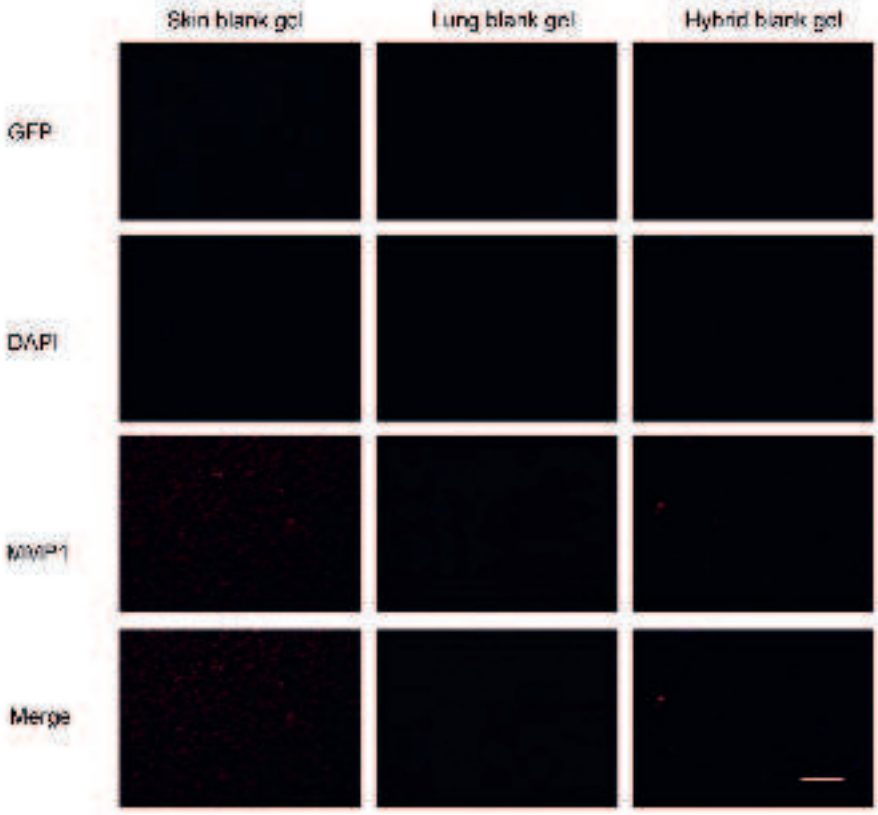

Figure S3

Figure S3. Fluoromicrographs of MMP1 staining of three distinctive cell-free hydrogels. GPF-labeled HPMEC, red – MMP1, blue – nuclei (DAPI). Scale bar: 58 μm.

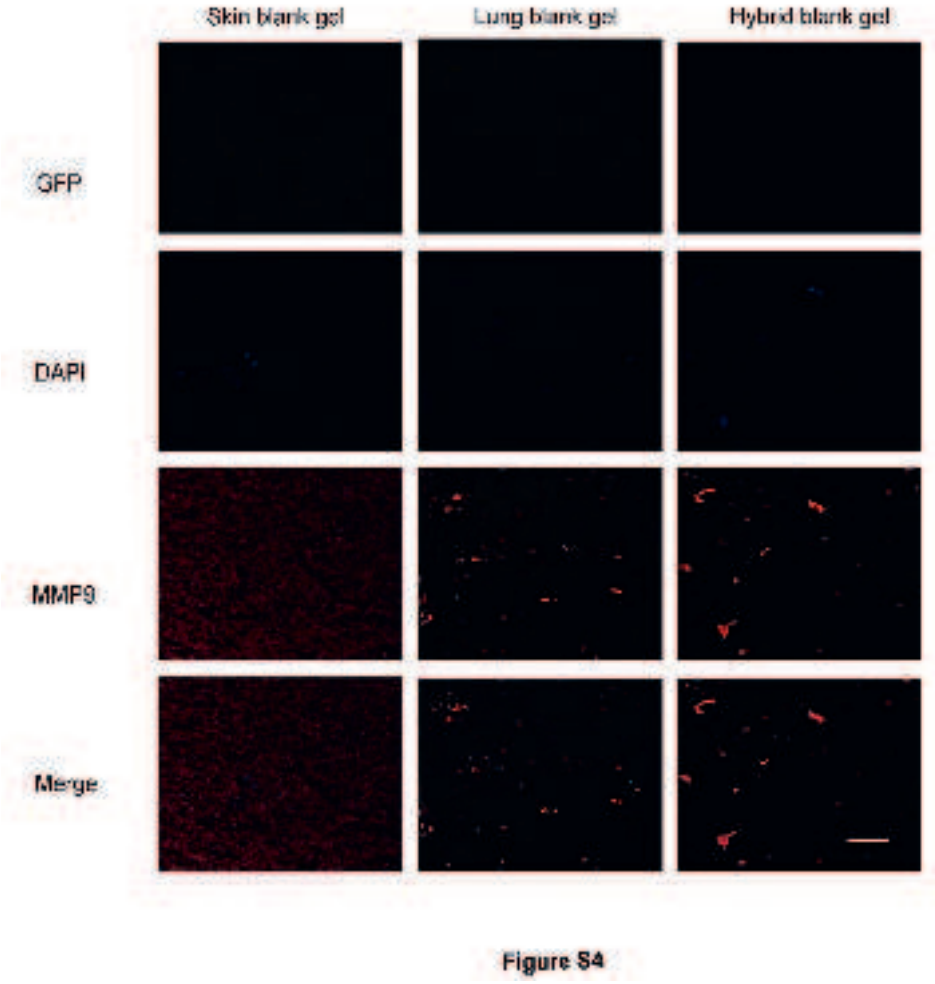

Figure S4. Fluoromicrographs of MMP9 staining of three distinctive cell-free hydrogels. GPF-labeled HPMEC, red – MMP9, blue – nuclei (DAPI). Scale bar: 58 μm.

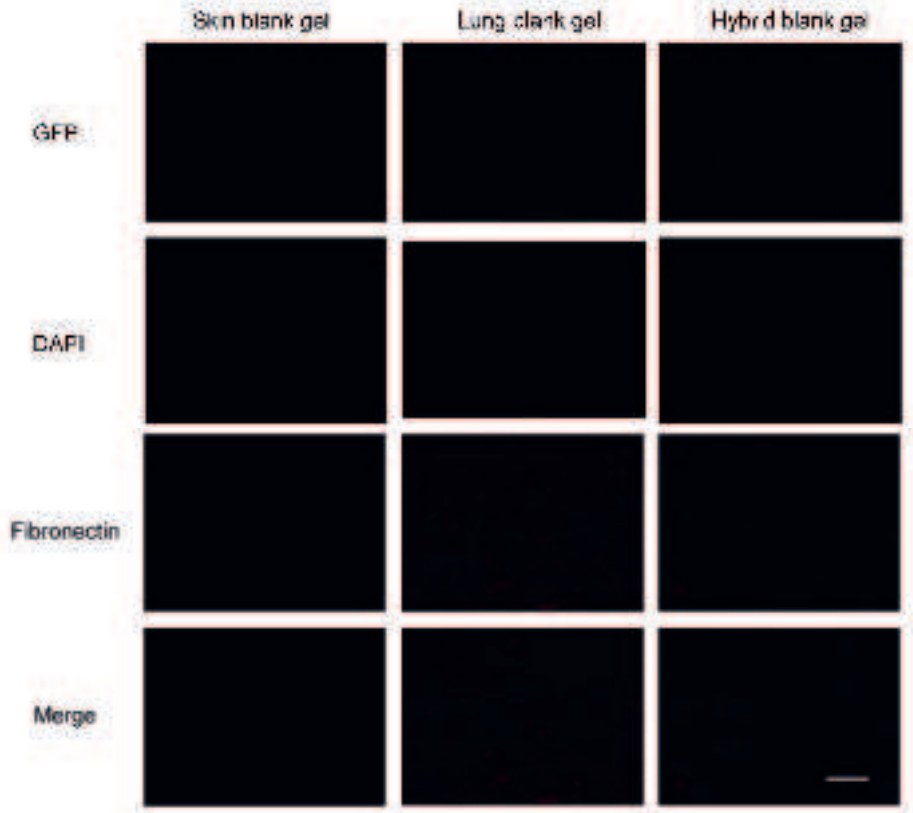

Figure S5. Fluoromicrographs of fibronectin staining of three distinctive cell-free hydrogels. GPF-labeled HPMEC, red – fibronectin, blue – nuclei (DAPI). Scale bar: 58 μm.

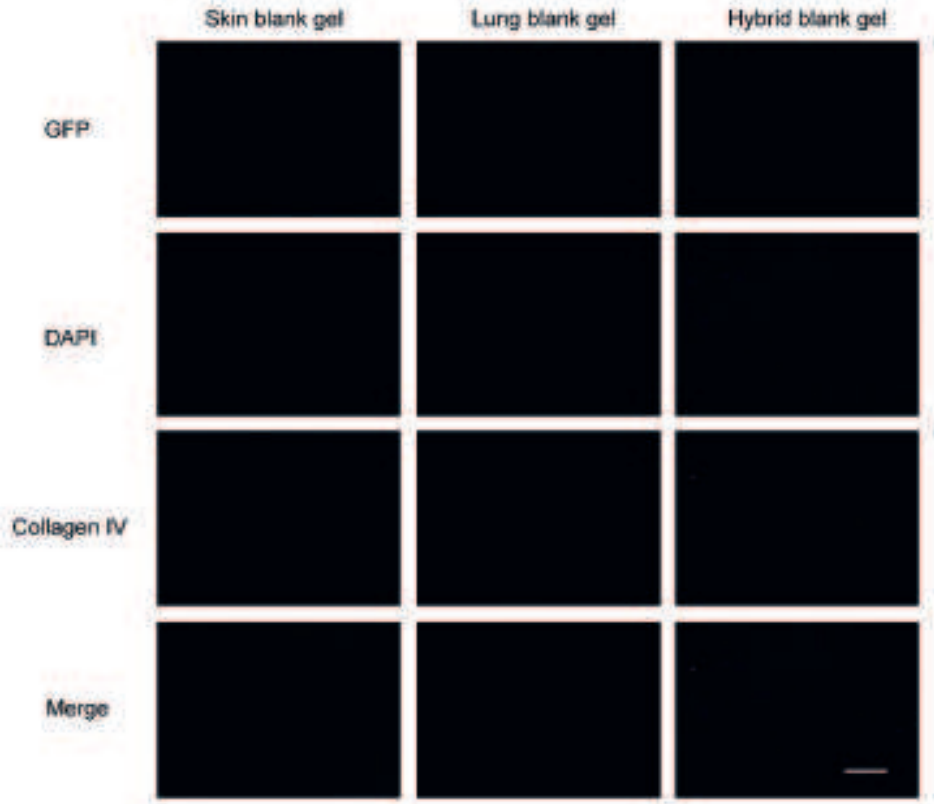

Figure S6

Figure S6. Fluoromicrographs of collagen IV staining of three distinctive cell-free hydrogels. GPF-labeled HPMEC, red – collagen IV, blue – nuclei (DAPI). Scale bar: 58 μm.

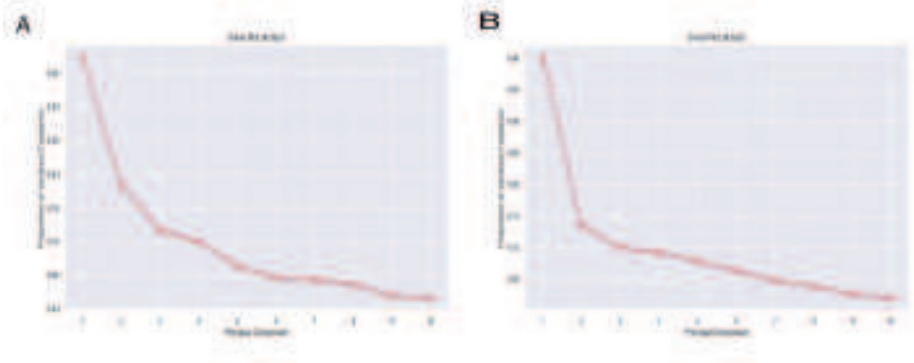

Figure S7

Figure S7. Scree plot representing proportion of principal component within measured features in three types of ECM hydrogels. (A) Scree plot representing proportion of principal component of three types of hydrogels on day 1. (B) Scree plot representing proportion of principal component of three types of hydrogels on day 5.

Chapter 5

An *in vitro* model of fibrosis using crosslinked native extracellular matrix-derived hydrogels to modulate biomechanics without changing composition

Mehmet Nizamoglu [a b 1], Roderick H.J. de Hilster [a b 1], **Fenghua Zhao [c d]**, Prashant K. Sharma [c d], Theo Borghuis [a], Martin C. Harmsen [a b c], Janette K. Burgess [a b c]

a University of Groningen, University Medical Centre Groningen, Department of Pathology and Medical Biology, Hanzeplein 1 (EA11), 9713 GZ Groningen, The Netherlands

b University of Groningen, University Medical Centre Groningen, Groningen Research Institute for Asthma and COPD (GRIAC), Hanzeplein 1 (EA11), 9713 AV Groningen, The Netherlands

c University of Groningen, University Medical Centre Groningen, W.J. Kolff Institute for Biomedical Engineering and Materials Science-FB41, A. Deusinglaan 1, 9713 AV Groningen, The Netherlands

d University of Groningen, University Medical Centre Groningen, Department of Biomedical Engineering-FB40, A. Deusinglaan 1, 9713 AV Groningen, The Netherlands

1 These authors contributed equally

Acta Biomaterialia

https://doi.org/10.1016/j.actbio.2022.05.031

Abstract: Extracellular matrix (ECM) is a dynamic network of proteins, proteoglycans and glycosaminoglycans, providing structure to the tissue and biochemical and biomechanical instructions to the resident cells. In fibrosis, the composition and the organization of the ECM are altered, and these changes influence cellular behaviour. Biochemical (i. e. protein composition) and biomechanical changes in ECM take place simultaneously in vivo. Investigating these changes individually in vitro to examine their (patho)physiological effects has been difficult. In this study, we generated an in vitro model to reflect the altered mechanics of a fibrotic microenvironment through applying fibre crosslinking via ruthenium/sodium persulfate crosslinking on native lung ECM-derived hydrogels. Crosslinking of the hydrogels without changing the biochemical composition of the ECM resulted in increased stiffness and decreased viscoelastic stress relaxation. The altered stress relaxation behaviour was explained using a generalized Maxwell model. Fibre analysis of the hydrogels showed that crosslinked hydrogels had a higher percentage of matrix with a high density and a shorter average fibre length. Fibroblasts seeded on ruthenium-crosslinked lung ECM-derived hydrogels showed myofibroblastic differentiation with a loss of spindle-like morphology together with greater α-smooth muscle actin (α-SMA) expression, increased nuclear area and circularity without any decrease in the viability, compared with the fibroblasts seeded on the native lung-derived ECM hydrogels. In summary, ruthenium crosslinking of native ECM-derived hydrogels provides an exciting opportunity to alter the biomechanical properties of the ECM-derived hydrogels while maintaining the protein composition of the ECM to study the influence of mechanics during fibrotic lung diseases. STATEMENT OF SIGNIFICANCE: Fibrotic lung disease is characterized by changes in composition and excessive deposition of extracellular matrix (ECM). ECM fibre structure also changes due to crosslinking, which results in mechanical changes. Separating the changes in composition and mechanical properties has been difficult to date. In this study, we developed an in vitro model that allows alteration of the mechanical changes alone by applying fibre crosslinking in native lung ECM-derived hydrogels. Characterisations of the crosslinked hydrogels indicated the model mimicked mechanical properties of fibrotic lung tissue and reflected altered fibre organisation. This ECM-based fibrosis model provides a method to preserve the native protein composition

while altering the mechanical properties providing an important tool, not only for lung but also other organ fibrosis.

Keywords: Crosslinking; ECM hydrogel; Extracellular matrix; Fibrosis; Lung; Maxwell model; Ruthenium; Viscoelasticity

1. Introduction

Extracellular matrix (ECM) is the structural component of every tissue, formed by a complex network of proteins, glycosaminoglycans and proteoglycans [1]. The highly tissue-specific nature of the ECM is dictated by the presence of a defined grouping of matrisome elements, incorporating demarcated ratios of ECM proteins [2]. These distinctions also result in different mechanical properties of the ECM, depending on the origin of the tissue [3]. Next to being structural support for the cells, the ECM provides biochemical and biomechanical cues to cells *in vivo* [4]. As such, it has proven challenging to mimic and incorporate the ECM structure and mechanics into (*in vitro)* studies regarding the structure and function of the ECM in health and disease. In fibrotic lung diseases, not only is the ECM composition altered but also its mechanical properties, resulting in higher stiffness and decreases in stress relaxation [5,6]. All the changes that are evident within a fibrotic ECM have been revealed to instruct cells and influence their responses to contribute to the progression of fibrosis, as reported and reviewed elsewhere [7–13].

To investigate the mechanical properties of (fibrotic) ECM *in vitro*, the ECM is often mimicked using hydrogels. ECM-derived hydrogels, which have been introduced to the field in the last decade, are a promising alternative to other types of hydrogels such as collagen, gelatine, or hyaluronic acid [14]. ECM hydrogels, which are developed from native decellularized tissue, retain most of the native ECM composition and, in general, resemble the mechanical properties of the parent tissue [6]. The most common method to produce hydrogels from ECM is to digest decellularized ECM powder with porcine pepsin at low pH with constant agitation [14]. Our recent study illustrated the preparation of ECM-derived hydrogels from human decellularized lung ECM, and established that the mechanical properties of the diseased (fibrotic) lung ECM-derived hydrogels resembled the mechanics of the decellularized fibrotic lung ECM [6]. Fibrotic lung ECM (both in native and hydrogel form) showed decreased viscoelastic stress relaxation compared to control lung ECM [6]. The stiffness of fibrotic lung tissue was ~10 times higher than its hydrogel counterpart, possibly due to the absence of chemical crosslinks and lung-resident cells in the ECM hydrogel. Previous studies showed that the composition of fibrotic lung ECM is different to that seen in control lung due to dysregulation of the ECM

degradation/deposition processes resulting in an aberrant ECM [15]. To investigate the separate influences on the cells of the altered mechanical properties or ECM composition in the fibrotic microenvironment, advanced and innovative *in vitro* models are needed. Recently, altering the mechanical properties of methacrylate or thiol functionalized ECM-derived hydrogels using click-chemistry has been shown [16,17]. Given that these processes rely on interactions with amine groups of lysine or arginine amino acids, which are known to be parts of cell binding domains including GFOGER, IKVAV or RGD, the implications of methacrylation or thiolation of ECM proteins on cellular functions still need to be explored [16,18–20]. Alternatively, chemical crosslinking has been applied to ECM-derived hydrogels using harsh chemicals such as glutaraldehyde or genipin, but cytotoxicity limits their use when cells are present in the hydrogel [21]. Another option is using near visible light UV-induced ruthenium/sodium persulfate (SPS) crosslinking, which has been employed on several other types of hydrogels (gelatine or fibrin) with and without cells present in the hydrogels [22,23]. The higher wavelength (405 nm) of the crosslinking light, which decreases the cytotoxicity, and the lack of requirement for any additional functionalization on the target material are the main advantages of this crosslinking method [24]. Using ruthenium/SPS crosslinking to reinforce the mechanical stability of the ECM-derived hydrogels has recently been reported by Kim et al. [25]; however, the implications of altering the mechanical properties of the hydrogels without changing the (bio)chemical composition have yet to be explored in terms of fibrosis and for developing *in vitro* models for fibrosis research.

In this study, we aimed to develop an *in vitro* model for examining the influence of mechanical properties of the fibrotic microenvironment by using native lung-derived ECM hydrogels (LdECM), which were generated using ruthenium/SPS crosslinking. We hypothesized that the ruthenium crosslinking would increase the stiffness of lung-derived ECM hydrogels (Ru-LdECM), while the viscoelastic relaxation would decrease, to then trigger pro-fibrotic activation of lung fibroblasts.

2. Materials and methods

2.1. Porcine lung decellularization

Porcine lungs (~6-month, female) were purchased from a local slaughterhouse (Kroon Vlees, Groningen, the Netherlands). The lung was dissected, cartilaginous airways and large blood vessels removed, before cutting into ~1 cm^3 cubes that were homogenized in a kitchen blender prior to decellularization. The lung homogenate was decellularized as previously described [26,27]. In short, the homogenate was repeatedly washed with Milli-Q® water and centrifuged at 3000 x g until the supernatant was completely clear. The sedimented material went through two rounds of sequential treatment with 0.1% Triton X-100 (Sigma-Aldrich, St. Louis, MO, USA), 2% sodium deoxycholate (Sigma-Aldrich), 1 M NaCl solution and 30 µg/mL DNase (Sigma-Aldrich) in $MgSO_4$ (Sigma-Aldrich) 1.3 mM and $CaCl_2$ (Sigma-Aldrich) 2 mM, 10 mM Tris pH8 (Sigma-Aldrich) solution each for 24 h at 4 °C with constant shaking, except for the DNase treatments, which were at 37 °C with shaking. The volume ratio of tissue homogenate to decellularization/washing solution was always 1:10. Between treatments, the homogenate was washed three times with Milli-Q® water, with centrifugation at 3000 x g between washes. After two cycles of decellularization, the tissue homogenate was sterilised by adding 0.18% peracetic acid and 4.8% ethanol, and left shaking at 4 °C for 24 h. After tissue sterilization the resultant decellularized ECM was washed three times with sterile Dulbecco's phosphate-buffered saline (DPBS) and stored in sterile DPBS containing 1% penicillin-streptomycin (Gibco Invitrogen, Carlsbad, CA, USA) at 4 °C (Fig. 1A).

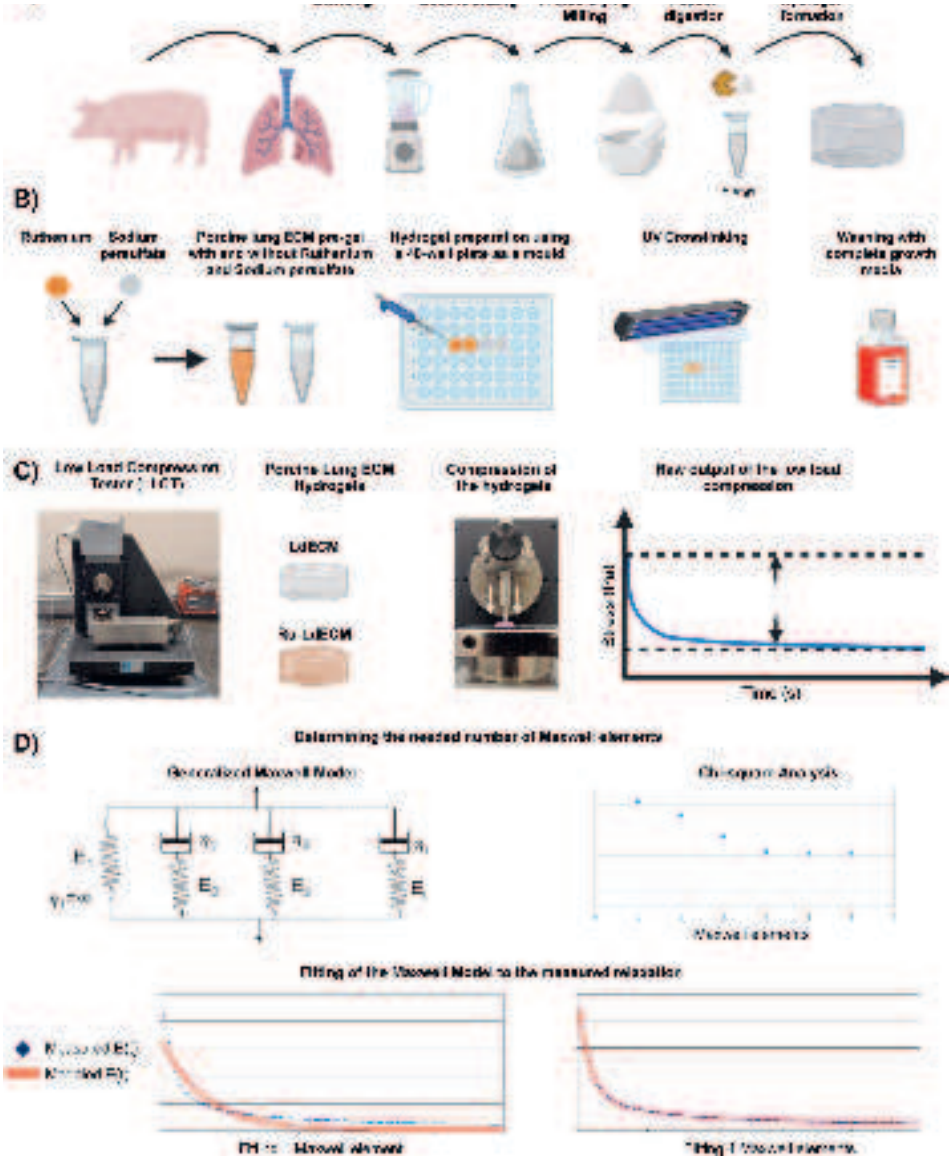

Fig. 1. Schematic representation of the methodology. (A) Porcine lung ECM hydrogel preparation. Porcine lungs were blended, decellularized and freeze-dried before grinding to a fine powder. Afterwards, the ECM powder was pepsin digested to prepare the pre-gel solution which can form hydrogels after incubating at 37 °C. (B) Fibre crosslinking of porcine lung ECM hydrogels. Lung derived-ECM (LdECM) hydrogels were used as is or mixed with ruthenium and sodium persulfate solutions before casting to 48-well plates. Afterwards, the pre-gel solutions were incubated at 37 °C and UV-crosslinked. (C) Mechanical characterization of the uncrosslinked and ruthenium crosslinked ECM

hydrogels. Low Load Compression Tester (LLCT) was used to determine the stiffness and stress relaxation of LdECM and Ru-LdECM hydrogels. The stress relaxation was modelled with a Maxwell elements system, and a chi^2 analysis was used to determine the number of Maxwell elements to fit the measured relaxation. Figure created with BioRender.

2.2. Hydrogel preparation

The decellularized lung ECM was snap-frozen in liquid nitrogen and lyophilized with a FreeZone Plus lyophilizer (Labconco, Kansas City, USA), before being ground into a powder with an A11 Analytical mill (IKA, Staufen, Germany). For solubilization, 20 mg/mL of ECM powder was digested with 2 mg/mL porcine pepsin (Sigma-Aldrich) in 0.01 M HCl under constant agitation at RT for 48 h [28]. Digestion was stopped by neutralising the pH with 0.1 M NaOH and the solution was brought to 1X PBS with one-tenth volume 10X PBS to generate the lung ECM pre-gel solution which was stored at 4 °C indefinitely.

A ruthenium Visible Light Photo initiator (400–450 nm) kit (Advanced BioMatrix, San Diego, California, US) containing pentamethyl cyclopentadienyl bis(triphenylphosphine) ruthenium(II) chloride (CAS Number: 92361-49-4, hereafter referred as ruthenium) and sodium persulfate (CAS: 7775-27-1) was used to crosslink the LdECM hydrogels (Fig. 1B). 20 µL of each ruthenium (37.4 mg/mL) and sodium persulfate (119 mg/mL) solutions were added per 1 mL of ECM hydrogel. The control gel received the same volume of sterile ddH_2O water. In the dark, both the ruthenium-containing gel and the control gel without ruthenium were pipetted (200 µL) into a 48-well plate and incubated at 37 °C for 1 h. After the hydrogels had settled, crosslinking of the ECM by photoinitiated ruthenium was triggered by exposing the samples to UV/Visible light from 4.5 cm distance using 2 × 9 W UV lamps (405 nm) (20 mW/cm^2 light intensity) for 5 min to generate Ru-LdECM hydrogel (Fig. 1B). Finally, the gels were immersed in 400 µL of Dulbecco's Modified Eagle Medium (DMEM) Low Glucose growth media (Lonza) supplemented with 10% foetal bovine serum (FBS), 1% penicillin-streptomycin and 1% GlutaMAX (Gibco) (hereafter referred as complete growth medium), and were washed 3X with media before cell seeding in order to remove excess (both reacted and unreacted) ruthenium and sodium persulfate.

2.3. Characterization of the mechanical properties

Both LdECM and Ru-LdECM hydrogels were made as described in hydrogel preparation. The gels were subjected to uniaxial compression with a 2.5 mm diameter plunger at three different locations, at least 2 mm away from the gel border and ensuring 2 mm or more between each compression site (Fig. 1C). The stress relaxation test was performed with a low-load compression tester (LLCT) at RT as described previously [6,26,29]. The LabVIEW 7.1 program was used for the LLCT load cell and linear positioning for control and data acquisition. The resolution in position, load, and time determination was 0.001 mm, 2 mg, and 25 ms, respectively, and the compression speed was controlled in feedback mode. Samples were compressed to 20% of their original thickness (strain $\varepsilon = 0.2$) at a deformation speed of 20%/s (strain rate $\dot{\varepsilon} = 0.2\ s^{-1}$). The deformation was held constant for 100 s and the stress continuously monitored. During compression, the required stress was plotted against the strain. In this plot, a linear increase in stress as a function of strain was observed between a strain of 0.04 and 0.1; the slope of the line fit to this region was taken as Young's modulus. Young's modulus essentially describes the stiffness of a material [30]. Since the Young's modulus of the viscoelastic gel depends on the strain rate, values reported here are valid only at a strain rate of 0.2 s^{-1}.

After compression, the required stress to maintain a constant strain of 0.2 s^{-1}, continuously decreases with time, which is a clear indication of the viscoelastic nature of the hydrogels and called stress relaxation. The shape of the stress relaxation curve was mathematically modelled with a generalized Maxwell model (2) (Fig. 1C). The continuously changing stress [$\sigma(t)$] was converted into continuously changing stiffness [$E(t)$] by dividing with the constant strain of 0.2 s^{-1}. Obtained $E(t)$ values were fitted to Eq. (1) to obtain the relaxation time constants (τ_i), and Eq. (2) provided relative importance (R_i) for each Maxwell element.

$$E(t) = E_1 e^{-t/\tau_1} + E_2 e^{-t/\tau_2} + E_3 e^{-t/\tau_3} + \dots E_n e^{-t/\tau_n} \quad (1)$$

$$R_i = 100.\frac{E_i}{\sum_{i=1}^{n} E_i} \quad (2)$$

where i varies from 1 to 4 or from 1 to 3 when necessary. The optimal number of Maxwell elements was determined with the chi-square function expressed by Eq. 3 (typically 3 or 4) and visually matching the modelled stress relaxation curve to

the measured curve (Fig. 1C).

$$x^2 = \sum_{j=0}^{100} \left(\frac{E_j - E(t_j)}{\sigma_j} \right) \quad (3)$$

where j varies from 0 to 100 s, E_j is the experimentally measured value at time j, $E(t_j)$ is the fit value at time j calculated with Eq. 1, and σ_j is the standard error that the LLCT makes because of inherent errors in position, time, and load measurements.

2.4. Histological characterisation of ECM hydrogel fibre structure

LdECM and Ru-LdECM hydrogels were prepared and washed as described above and fixed with 2% paraformaldehyde (PFA; Sigma-Aldrich) in PBS at RT for 20 min. The gels were then embedded in 1% Ultrapure agarose (Invitrogen, Waltham, MA, USA) before using a graded alcohol series to dehydrate followed by paraffin embedding. Sections (4 µm) were deparaffinised, and stained with 0.1% Picrosirius Red (PSR; Sigma-Aldrich) in 1.3% aqueous solution of picric acid to visualize collagens and their network. Slides were mounted with Neo-Mount® Mounting Medium (Merck, Darmstadt, Germany).

2.5. Cell culture

MRC-5 foetal lung fibroblasts (n = 5) were cultured in complete growth medium. The MRC-5s were washed with Hank's Balanced Salt Solution (HBSS; Gibco), harvested using 0.25% Trypsin-EDTA (Gibco) and centrifuged at 500 x g for 5 min. Cells were resuspended in 1 mL complete growth media and counted with a NucleoCounter NC-200™ (Chemometec, Allerod, Denmark). Fibroblasts were seeded on top of pre-prepared and washed LdECM and Ru-LdECM hydrogels in complete growth media with the seeding density 10.000 cells/gel. The cells were cultured on the gels for 1 or 7 days. Gels used for live/dead staining were stained with the live/dead stain and were subsequently harvested. Gels intended for immunofluorescent imaging were fixed in 2% PFA in PBS for 30 min. After fixation, hydrogels were washed three times with PBS and stored in PBS containing 1% penicillin-streptomycin at 4 °C until analyses.

2.6. Live/dead staining

Cell viability of the MRC-5 cells cultured on LdECM and Ru-LdECM hydrogels

was assessed after 1 and 7 days using Calcein AM (Thermo Scientific, Breda, the Netherlands) to stain live cells and propidium iodide (PI; Sigma-Aldrich) for staining dead cells, as previously described [31]. The hydrogels were first washed with HBSS and then incubated with serum free media containing 5 µM Calcein AM and 2 µM PI, for 1 hour at 37 °C. After incubation, fluorescent images were captured using a EVOS Cell Imaging System (Thermo Scientific) with GFP (509 nm) and Texas Red (615 nm) channels.

2.7. Immunofluorescence staining

The hydrogels were treated with avidin/biotin blocking kit (ThermoFisher) before being incubated with 0.5 µg/mL biotinylated wheat germ agglutinin (Vector Laboratories, Burlingame, USA) for 20 min at 37 °C. Then the hydrogels were washed and permeabilized by incubating with 0.5% v/v Triton X-100 in HBSS for 10 min at RT and subsequently blocked in 2.5% v/v BSA + 0.1% Triton-X 100 in HBSS for 30 min at RT. Endogenous peroxidase activity was blocked by 30 min incubation in a 0.3% hydrogen peroxide solution. Afterwards, the hydrogels were incubated overnight with a mouse anti-human α-smooth muscle actin antibody (DAKO, Glostrup, Denmark) at 4 °C. A rabbit-anti-mouse antibody conjugated with peroxidase (DAKO) and streptavidin conjugated with Alexa Fluor 555 (ThermoFisher) were used as a second step for 45 min at room temperature staining for α-SMA was then developed by Opal650 tyramide (Akoya Biosciences, Marlborough MA, USA) according to the manufacturer's instructions. After staining with 0.1 µg/mL DAPI solution (Merck), the hydrogels were mounted with Citifluor Mounting Medium (Science Services, Munich, Germany) and fluorescence microscopy was performed to acquire images.

2.8. Imaging and image analysis

Fluorescent images of PSR-stained LdECM and Ru-LdECM hydrogel sections were generated with Leica SP8 X white light laser confocal microscope (Leica, Wetzlar, Germany), λ_{ex}561 nm / λ_{em} 566/670 nm at 40x magnification. TWOMBLI plugin for FIJI ImageJ was used to assess the number of fibres, end points, branching points, total fibre length and alignment, lacunarity, high density matrix (HDM) and curvature of the fibres as previously described (*Supplementary Fig. 1*) [26,32]. Fluorescent images of cell-seeded hydrogels stained for α-SMA, wheat germ agglutinin and DAPI were generated with Leica

SP8 confocal microscope (Leica, Wetzlar, Germany), using λ_{ex}627 nm / λ_{em}650 nm for α-SMA, λ_{ex}555 nm / λ_{em}580 nm for wheat germ agglutinin and λ_{ex}359 nm / λ_{em}457 nm for DAPI at 40X and 63X magnifications. Five separate images per sample (n = 5) were used to calculate the stiffness-induced changes in the expression of α-SMA, nuclei area and eccentricity (which is also described as inverse circularity) (Supplementary Fig. 2). Expression of α-SMA per nuclei was calculated using built-in functions for measuring area in ImageJ. CellProfiler 4.2.1 software was used to analyse the nuclei characteristics on the DAPI-stained images as previously described [33]. Circularity of the samples were calculated from the eccentricity values using the Eq. (4).

$$Circularity\ (n) = 1 - Eccentricity\ (n) \quad (4)$$

2.9. Statistical analysis

All statistical analyses were performed using GraphPad Prism v9.1.0 (GraphPad Company, San Diego, USA). Data are presented as mean values with standard deviation (SD). All data were tested for outliers using the robust regression and outlier removal (ROUT) test and analysed for normality using Shapiro-Wilk and Q-Q plots (*Supplementary Fig. 3*). For the data that were normally distributed, differences between control porcine lung ECM hydrogel and ruthenium crosslinked ECM hydrogels generated from the same batch of LdECM and used in the same experiment were tested by paired t-test to compare the effect of crosslinking between different experiments. For the data that were not normally distributed, Mann-Whitney test was used to compare the effect of crosslinking between different experiments. All data were considered significantly different when $p < 0.05$.

3. Results

3.1. Ruthenium crosslinking increases hydrogel stiffness

Both LdECM and Ru-LdECM solutions were able to form hydrogels after incubating at 37 °C. UV/Visible light crosslinking did not result in a macroscopic change in the LdECM hydrogels. Ru-LdECM hydrogels (and the solution before the crosslinking) had a bright orange colour due to the ruthenium addition.

Stiffness measurements on LdECM and Ru-LdECM hydrogels were performed

using a low-load compression tester (LLCT). Ruthenium crosslinking increased the stiffness of the Ru-LdECM 5-10-fold (p = 0.0026, paired t-test) (Fig. 2).

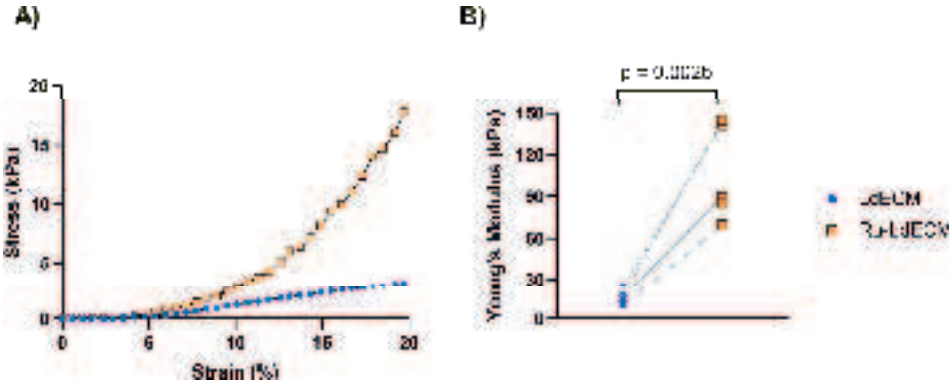

Fig. 2. Comparison of stiffness of control and ruthenium-crosslinked hydrogels. LdECM and Ru-LdECM hydrogels were mechanically tested using Low Load Compression Tester (LLCT) with a fixed 20% strain ratio. (A) Representative stress-strain curve for LdECM and Ru-LdECM hydrogels. (B) Comparison of stiffness of LdECM and Ru-LdECM hydrogels. Each dot represents the mean of three independent measurements on the same hydrogel for each sample (n = 5). Applied test: Paired t-test to compare the LdECM and Ru-LdECM hydrogels that were generated in the same experimental batch (as indicated by the connecting lines in the graph). LdECM: Lung-derived ECM Hydrogels, Ru-LdECM: Ruthenium-crosslinked Lung-derived ECM Hydrogels.

3.2. Decreased stress relaxation rate in ruthenium-crosslinked ECM hydrogels

The stress relaxation behaviour of both the LdECM and RU-LdECM hydrogels were measured after applying 20% strain using LLCT measurement. The average stress relaxation profiles of both groups over 100 s are visualized in Fig. 3A. Ru-LdECM hydrogels did not reach 100% stress relaxation during the 100 s monitored, while some LdECM hydrogels achieved 100% stress relaxation. In addition to the decreased total stress relaxation percentage (in 100s) in the Ru-LdECM hydrogels, the relaxation profile was different. The rate of stress relaxation slowed down earlier in the crosslinked hydrogels. To assess the dynamic differences in the initial stress relaxation behaviour patterns in both groups the time to reach 50% total stress relaxation was compared. LdECM hydrogels reached 50% stress relaxation in significantly shorter time compared

to the Ru-LdECM hydrogels. (p = 0.0054, paired t-test) (Fig. 3B).

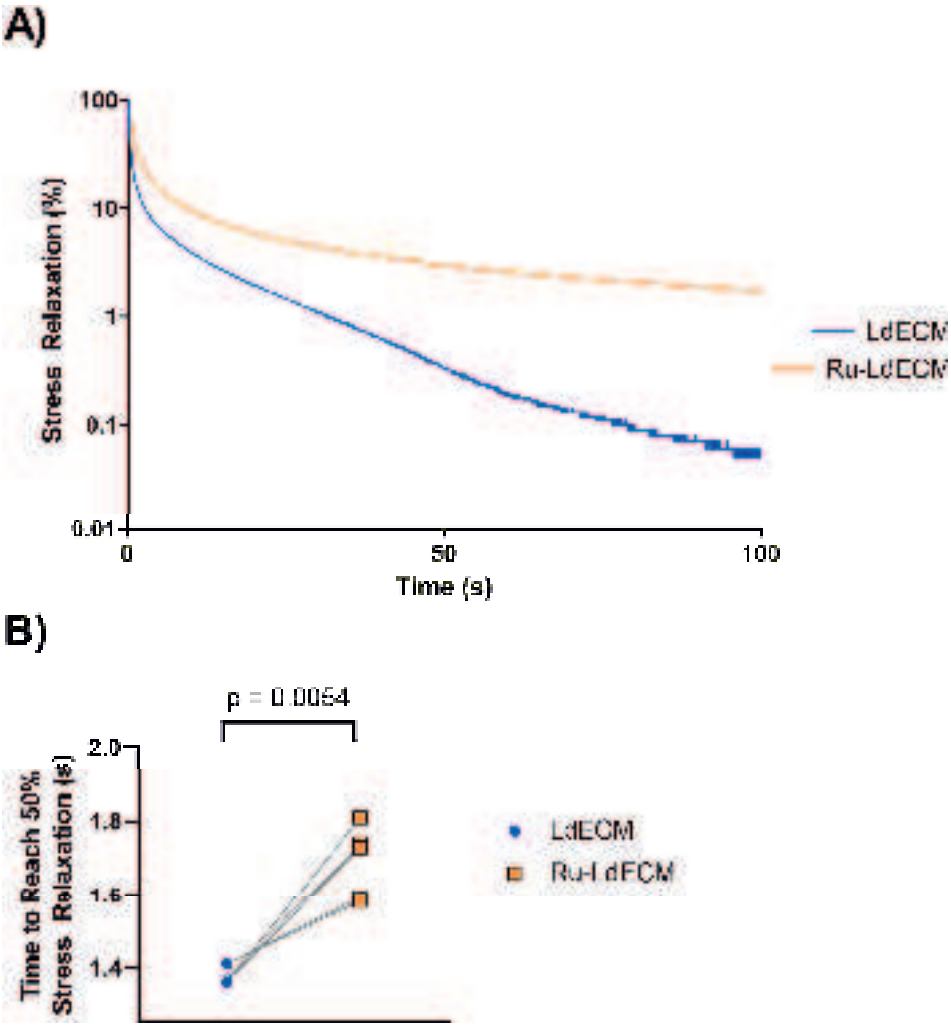

Fig. 3. Stress relaxation in control and ruthenium-crosslinked ECM-derived hydrogels. After compressing the LdECM and Ru-LdECM hydrogels using Low Load Compression Tester (LLCT) with a fixed 20% strain ratio, the stress relaxation behaviour was recorded over 100s period. (A) Average stress relaxation behaviour over 100 s duration. (B) Time taken to reach 50% stress relaxation. Each dot represents the mean of three independent measurements on the same hydrogel for each sample (n = 5). Applied test: Paired t-test to compare the LdECM and Ru-LdECM hydrogels that were generated in the same experimental batch (as indicated by the connecting lines in the graph). LdECM: Lung-derived Extracellular Matrix Hydrogels, Ru-LdECM: Ruthenium-crosslinked Lung-derived Extracellular Matrix Hydrogels.

3.3. Altered relaxation profile in ruthenium-crosslinked ECM hydrogels

Since the ECM hydrogels are a viscoelastic material with various elastic (e.g., ECM proteins) and viscous components (e.g., water, bound water), we mathematically modelled this using a generalized Maxwell model. This approach allowed the total relaxation data to be split into Maxwell elements that can theoretically be attributed to physical components in the hydrogels. Each of these Maxwell elements are responsible for a part of the total relaxation (relative importance), as well as occurring within a specific time window during the relaxation process. The distribution of the time constants of these different elements and their respective relative importance are presented in Fig. 4. The stress relaxation of the LdECM hydrogels could be modelled with 3 Maxwell elements while Ru-LdECM hydrogels needed 4 Maxwell elements. Next to the difference in the number of Maxwell elements required to explain the relaxation profiles, the time constants of the elements differed between the two groups: the first element was significantly faster in the LdECM hydrogels ($p = 0.002$, paired t-test) while the third element took longer in the LdECM hydrogels ($p = 0.002$, paired t-test) compared to the Ru-LdECM (Fig. 4A).

The relative importance of the Maxwell elements was used to assess the individual contribution of each element to the total stress relaxation over the 100 s (Fig. 4B). In both types of hydrogels, the first element made the greatest contribution to the stress relaxation profile, although the percentage contribution was significantly lower in the Ru-LdECM hydrogels compared with the LdECM hydrogels ($p = 0.002$, paired t-test). The contribution of the second Maxwell element was the second largest in both groups while the relaxation profile of the Ru-LdECM hydrogels had a significant increase in the contribution of this element compared to uncrosslinked hydrogels ($p = 0.0002$, paired t-test). The third element had the lowest percentage contribution in LdECM hydrogels, with this contribution being lower than this element in its ruthenium-crosslinked counterpart ($p = 0.002$, paired t-test).

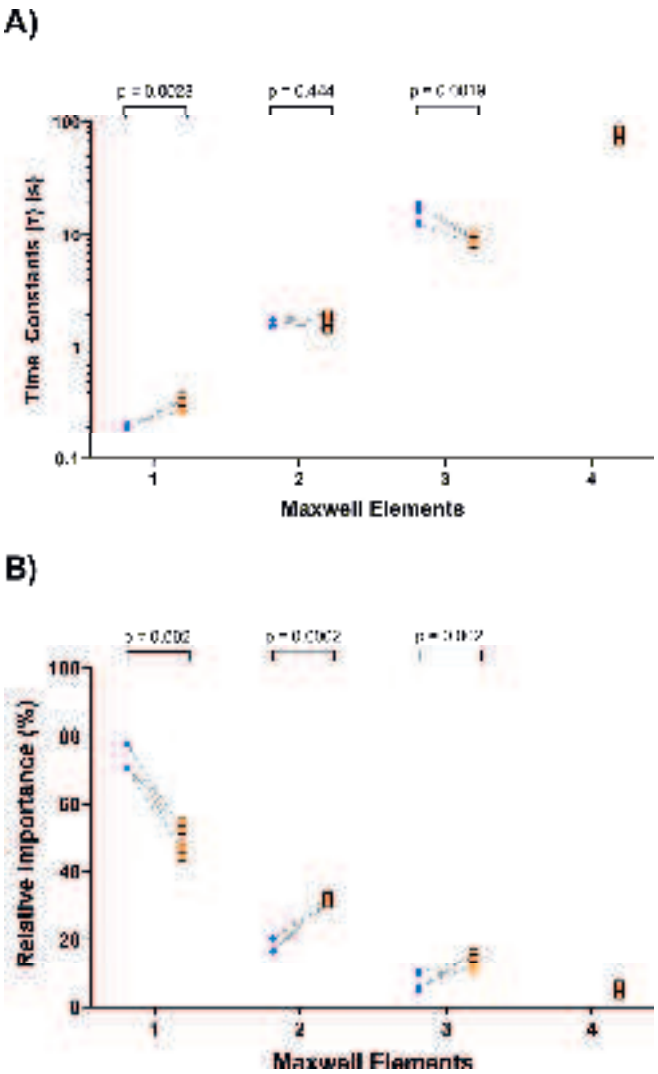

Fig. 4. Analysis of the stress relaxation behaviour through the generalized Maxwell model system. The relaxation profiles of the both types of hydrogels over 100 s period was mathematically modelled using a Maxwell model system and the relative importance values of the Maxwell Elements were determined. (A) Time constants for each Maxwell element for LdECM and Ru-LdECM hydrogels. (B) Relative importance (%) of the each Maxwell element for LdECM and Ru-LdECM hydrogels. Each dot represents the mean of three independent measurements on the same hydrogel (n = 5). Applied test: Paired t-test to compare the LdECM and Ru-LdECM hydrogels that were generated in the same experimental batch (as indicated by the connecting lines in the graph). LdECM: Lung-derived ECM Hydrogels, Ru-LdECM: Ruthenium-crosslinked Lung-derived ECM Hydrogels.

3.4. Increased density and decreased alignment of fibres in lung ECM hydrogels after ruthenium crosslinking

Ru-LdECM hydrogels had a denser fibre network compared to LdECM hydrogels (Fig. 5A). The average fibre length was shorter in Ru-LdECM than LdECM hydrogels ($p = 0.0026$, paired *t*-test). While the normalized numbers of endpoints and branchpoints did not differ between LdECM and Ru-LdECM hydrogels, the percentage of area with high density matrix (HDM) was greater in Ru-LdECM hydrogels compared with LdECM hydrogels ($p = 0.0146$, paired t-test). Alignment of the fibres in Ru-LdECM hydrogels was lower than LdECM hydrogels ($p = 0.0048$, paired t-test) (Fig. 5B–G).

The differences in the curvature of the fibres with different length were compared in LdECM and Ru-LdECM hydrogels. Curvature of the fibres with shorter length (< 40 μm) were higher in the crosslinked hydrogels, suggesting that shorter fibres were more bent in Ru-LdECM hydrogels while curvature of the longer fibres was not different between these two groups (Table 1).

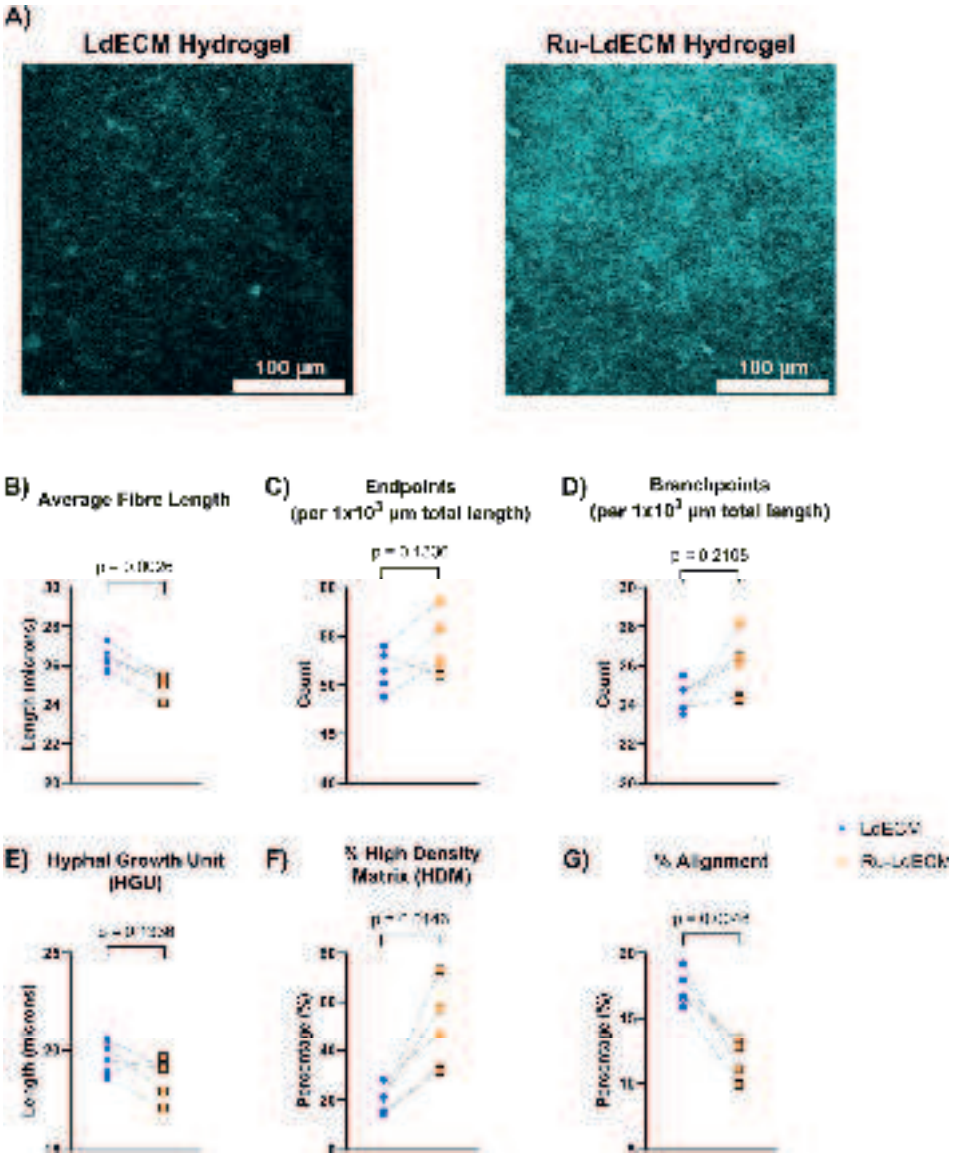

Fig. 5. Picrosirius red staining on LdECM and Ru-LdECM and fibre characteristics analysis on the collagen network. LdECM and Ru-LdECM hydrogels were stained using Picrosirius red staining and generated fluorescent images were analysed using TWOMBLI plugin in FIJI ImageJ. (A) Representative images of Picrosirius red staining on LdECM and Ru-LdECM hydrogels, scale bars: 100 µm. (B) Average Fibre Length, (C) Endpoints per 1000 µm total length, (D) Branchpoints per 1000 µm total length, (E) HGU, (F) % of High Density Matrix (HDM), (G) % fibre Alignment. Each dot represents the mean of measurements of 5 different randomized regions on the fluorescent images of

Picrosirius red staining for each sample (n = 5). Applied statistical test: paired t-test to compare the LdECM and Ru-LdECM hydrogels that were generated in the same experimental batch (as indicated by the connecting lines in the graph). LdECM: Lung-derived ECM Hydrogels, Ru-LdECM: Ruthenium-crosslinked Lung-derived ECM Hydrogels.

Table 1. TWOMBLI analysis for the curvature of fibres with different lengths. All results show mean ± standard deviation of n = 5. Each analysis was performed using averages of 5 different randomized regions on the fluorescent images of Picrosirius red staining for each sample. LdECM: Lung-derived ECM Hydrogels, Ru-LdECM: Ruthenium-crosslinked Lung-derived ECM Hydrogels. Applied statistical test: paired-t test to compare the LdECM and Ru-LdECM hydrogels that were generated in the same experimental batch. $P < 0.05$ was considered statistically significant.

Fibre Length	Average Curvature (Δ°)		P values
	LdECM	Ru-LdECM	
10 µm fibres	42.40 ± 0.92	44.98 ± 0.89	0.019
20 µm fibres	53.47 ± 0.98	56.02 ± 0.92	0.022
30 µm fibres	59.12 ± 0.71	60.84 ± 0.86	0.027
40 µm fibres	62.55 ± 0.51	63.29 ± 1.02	0.12
50 µm fibres	64.32 ± 0.79	64.60 ± 0.84	0.58

3.5. Ruthenium crosslinking does not affect fibroblast viability but induces altered morphology

After 1 day of culture, no dead cells were observed and the fibroblasts were viable on both types of hydrogels (Fig. 6). The viability of the fibroblasts did not change over a 7-day culture period (*Supplementary Fig. 4*). On both gels the fibroblasts appeared to be lying flat on the surface of the hydrogels; however, the fibroblasts on LdECM hydrogels displayed a more spindle-shaped morphology, while fibroblasts on Ru-LdECM gels were more hypertrophic and displayed more protrusions, suggesting a more migratory phenotype for fibroblasts on Ru-

LdECM hydrogels. At day 7, a fully confluent monolayer was present on both control and crosslinked hydrogels with no differences in viability.

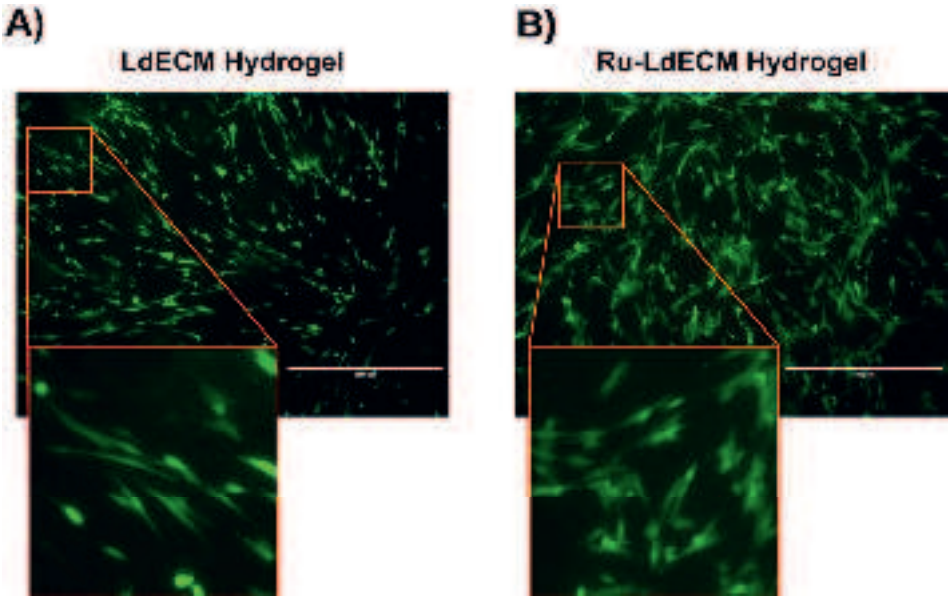

Fig. 6. Live/dead staining on MRC-5 fibroblasts seeded on LdECM and Ru-LdECM hydrogels on day 1 using Calcein AM (green) and propidium iodide (red). (A) MRC-5 fibroblasts cultured on the LdECM hydrogels, (B) MRC-5 fibroblasts cultured on Ru-LdECM hydrogels. Scale bar: 1000 μm. Results are representative for all experiments ($n = 5$). LdECM: Lung-derived ECM Hydrogels, Ru-LdECM: Ruthenium-crosslinked Lung-derived ECM Hydrogels.

3.6. Ruthenium crosslinking of ECM hydrogel promotes differentiation of fibroblasts to myofibroblasts

Fibroblasts seeded on Ru-LdECM hydrogels had higher expression of α-SMA when compared to LdECM hydrogel-seeded fibroblasts (Fig. 7). In addition to the stronger expression of α-SMA, the organization of the cytoskeleton was altered in the fibroblasts seeded on the Ru-LdECM hydrogels (Fig. 7B, lower row). When these images were quantified using ImageJ, fibroblasts seeded on Ru-LdECM hydrogels had significantly higher α-SMA expression per nuclei ($p < 0.0001$) compared with the fibroblasts seeded on LdECM hydrogels (Fig. 8A). These myofibroblast-like characteristics were also accompanied by a change in the nuclear morphology.

At day 7, the nuclei in the fibroblasts on Ru-LdECM hydrogels had an altered morphology as illustrated by the higher area ($p < 0.0001$, Mann-Whitney test) with an increased circularity ($p < 0.0001$, Mann-Whitney test) compared with the fibroblasts seeded on LdECM hydrogels (Fig. 8, B and C).

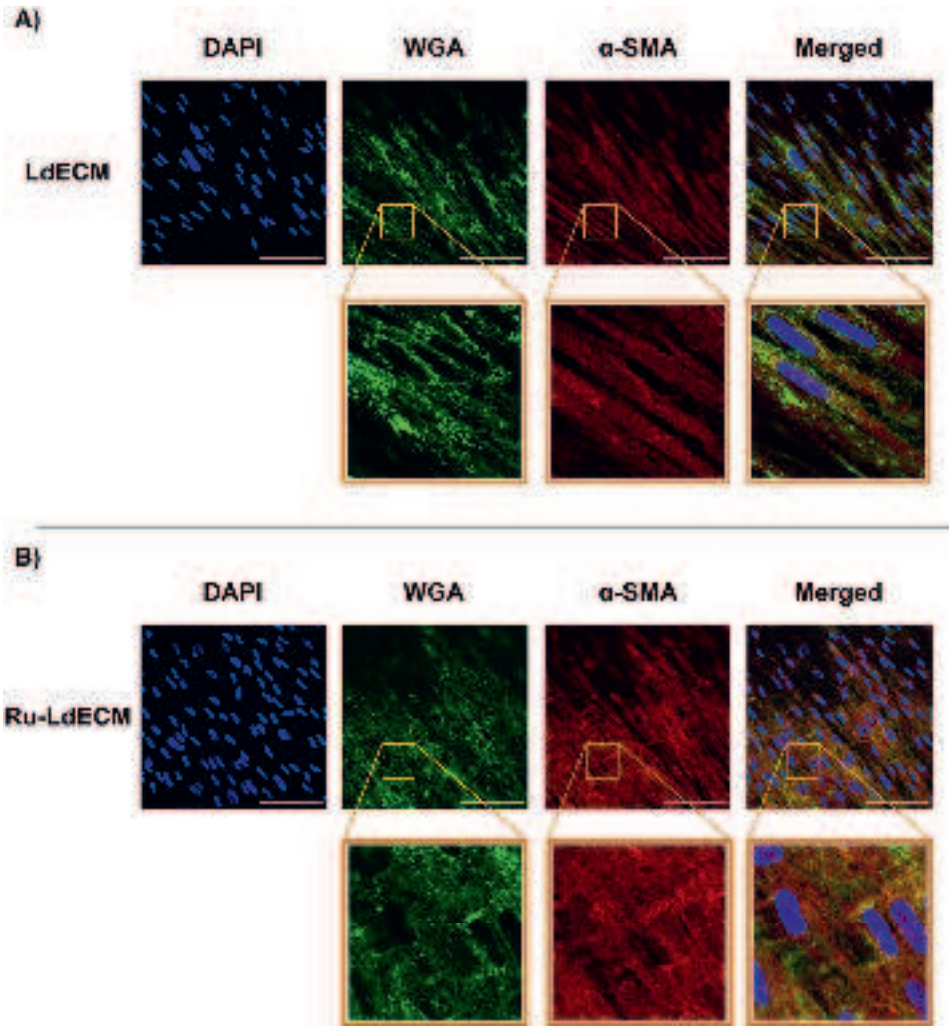

Fig. 7. Fluorescence images for the comparison of cell nuclei (DAPI), cell membrane (WGA) and cytoskeleton (α-SMA) on MRC-5 fibroblasts seeded on LdECM and Ru-LdECM hydrogels at day 7. (A) Top row: Stained LdECM hydrogels imaged at original objective magnification 40 ×, bottom row: digitally magnified versions of the respective images (B) Stained Ru-LdECM hydrogels imaged at original objective magnification 40 ×, bottom row: digitally magnified versions of the respective Scale bars:

100 µm. LdECM: Lung-derived ECM Hydrogels, Ru-LdECM: Ruthenium-crosslinked Lung-derived ECM Hydrogels. WGA: Wheat germ agglutinin, α-SMA: alpha smooth muscle actin.

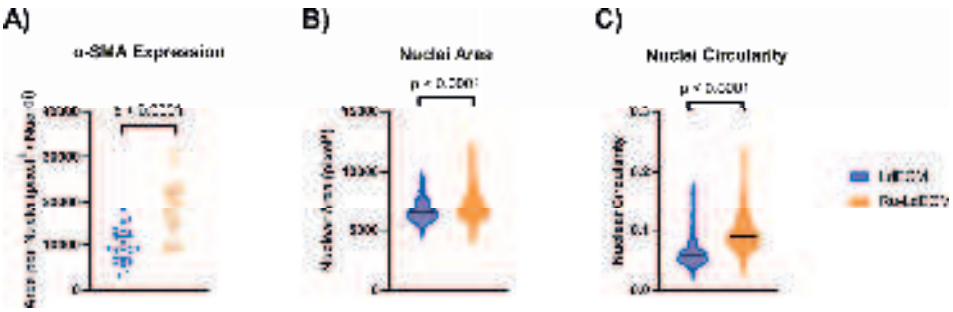

Fig. 8. Comparison of the fibroblasts seeded on LdECM and Ru-LdECM hydrogels. α-SMA and DAPI-stained fluorescent images of the fibroblasts were analysed using the ImageJ and CellProfiler software to compare the α-SMA expression per nuclei, the nuclear area and circularity. (A) Quantification of the α-SMA expression per cell nuclei imaged in the fluorescent images. (B) Comparison of nuclear area of fibroblasts seeded on LdECM and Ru-LdECM. (C) Nuclear circularity of the fibroblasts seeded on LdECM and Ru-LdECM hydrogels. For panel A, each data point represents the quantification of the images generated from different randomized regions ($n = 5$ per hydrogel) from different hydrogels ($n = 5$ total). Applied statistical test: Mann-Whitney test. For panels B and C, each data point represents measurement on an individual nucleus for the respective characteristic, in total from 5 different randomized regions on the fluorescent images of DAPI staining for each sample ($n = 5$). Applied statistical test: Mann-Whitney test. α-SMA: alpha-smooth muscle actin, LdECM: Lung-derived ECM Hydrogels, Ru-LdECM: Ruthenium-crosslinked Lung-derived ECM Hydrogels.

4. Discussion

In this study we describe a model that enables modulation of the mechanical properties of an ECM without changing the composition. Using this model, we illustrated that by modulating the crosslinks between ECM fibres, the stiffness and stress relaxation properties of the ECM-derived hydrogels were altered. The crosslinking influenced the ECM fibre characteristics with a higher percentage of high density matrix and lower percentage of alignment being evident within the hydrogels treated with ruthenium. Fibroblasts grown on the surface of the

crosslinked hydrogels displayed more myofibroblast-like characteristics. The features of this model illustrate that it would provide an innovative research tool for investigating the importance of biomechanical changes in fibrotic diseases.

The increase in stiffness caused by ruthenium crosslinking in the LdECM hydrogels is similar to the increase in stiffness seen in fibrotic lung diseases such as idiopathic pulmonary fibrosis (IPF) [15]. Booth et al. measured the stiffness of whole non-IPF and IPF human lungs before and after decellularization and found that the fibrotic regions of the IPF lung often reached a stiffness of 100 kPa or more, a vast increase compared to that of normal lung which has an average stiffness of 1.96 kPa [15]. The increased stiffness of IPF human lung was still present in hydrogels when compared to hydrogels generated from control human lungs, albeit proportionally reduced when compared to the intact lung tissue [6]. Recreating the (patho)physiological stiffness is essential to study the corresponding behaviour of cells during fibrotic diseases [34]. Ruthenium crosslinking on ECM-derived hydrogels provides an ideal opportunity to recreate the (patho)physiological stiffness. This is due to the fact that it does not require additional modifications on the ECM itself, enabling the modification of the mechanical properties while keeping the biochemical composition of the ECM constant. Thus these hydrogels mimic only the altered mechanical properties observed in fibrotic diseases. Ruthenium crosslinking relies on the crosslinking of the tyrosine amino acids and the potential for employing this strategy on the ECM-derived hydrogels has recently been demonstrated by Kim et al. [25]. The ruthenium crosslinking of the ECM in our model allows us to recreate the (patho)physiological mechanical environment in a fibrotic lung. This method can most likely be adapted to generate tissue specific fibrotic environments that are representative of many organ microenvironments.

Different rheology measuring techniques will yield slightly different results and have specific benefits. A study by Polio et al. used cavitation rheology, micro-indentation, tensile testing and small amplitude oscillatory shear rheometry on porcine lung and found that each technique resulted in a different Young's modulus [35]. A previous study shows the difference in viscoelastic properties of human lung ECM hydrogels and intact (patho)physiological counterparts where the hydrogels had a lower stiffness and higher total relaxation [6]. The first Maxwell element was the main contributor to the stress relaxation in hydrogels whereas with lung tissue this was more equally divided amongst the elements.

ECM hydrogels are reconstituted solutions of decellularized and enzyme-digested ECM proteins and therefore they lack the chemical crosslinks and the cellular components present in intact and native ECM. This is most likely why the stress relaxation and Young's modulus of the hydrogels differs from intact tissue. Introducing the crosslinks back into the hydrogel as well as tissue specific cells who will remodel their local environment over time can possibly be the factor to bridge the gap that still exists between hydrogel models and native tissue.

Stress relaxation has been found to be an important mechanism that can regulate cellular fate and behaviour [36]. Ruthenium crosslinked LdECM hydrogels had a lower and more complex stress relaxation than uncrosslinked LdECM hydrogels, similar to that of IPF human lung compared to normal human lung [6]. To date, attributing individual Maxwell elements to specific components of a hydrogel such as water, small molecules, cells, or type of crosslinks formed in the ECM remains difficult in absence of a dedicated systematic study [37]. However, the fourth Maxwell element (with a relaxation time constant of ~100 s) for Ru-LdECM hydrogels required to describe their relaxation profile can be attributed to the secondary ECM network formed through the ruthenium crosslinking since this is the only difference between the two tested hydrogels. A similar difference in stress relaxation was found between control and fibrotic human lung ECM-derived hydrogels, showing three Maxwell elements in control hydrogels and 4 Maxwell elements in fibrotic hydrogels [6]. While the differences in species might complicate comparisons between porcine and human lung-derived hydrogels with respect to mechanical properties, the presence of a fourth Maxwell element in a Ru-LdECM hydrogels suggests that these hydrogels were able to resemble the stress relaxation behaviour of fibrotic lung ECM-derived hydrogels.

Ruthenium crosslinking of ECM hydrogels led to a more dense ECM network reflective of tissue changes in fibrotic diseases. Crosslinking the ECM fibres together in LdECM hydrogels resulted in lower fibre lengths and more dense matrix packed areas. In fibrotic lung diseases like IPF, topography and organization of the ECM are altered, as recently summarized elsewhere [38]. Through post-translational modifications and crosslinking of the collagen network by the lysyl oxidase (LO) family of enzymes, lung ECM in IPF has been reported to be more mature and organized, compared to non-IPF lung ECM [39,40]. The denser matrix with a high degree of crosslinking is a key feature of fibrotic lung disease and protects the ECM from proteolysis [41]. The overall

organization of the ECM in IPF is decreased when compared to normal lungs, a characteristic which was also present in the Ru-LdECM hydrogels as seen in the lower alignment [42]. Similar values in normalized numbers of endpoints and branchpoints suggest that fibre integrity was not affected during the crosslinking and existing branches were crosslinked. The shorter fibres in crosslinked hydrogels might be explained with the increased curvature in these samples: the effect of crosslinking on curvature of fibres with respect to the fibre length was prominent in shorter fibres (<40 μm) while longer fibres did not have differences among the two groups. These observations indicate that the ruthenium-crosslinking mainly influences the shorter fibres and decreases the average fibre length. Together with the mechanical characterization data, these results show that the mechanical properties were altered through the changes in the alignment and density of the matrix (HDM) in the crosslinked hydrogels.

One of the most important components of the fibrotic microenvironment is the (myo)fibroblasts and their responses to the altered ECM. In our model, the cells remained viable and the fibroblasts seeded on crosslinked hydrogels lost their spindle-like morphology that we observed on the native LdECM hydrogels. This observation is in parallel with previously reported studies showing the effect of stiffness on human lung fibroblasts [43]. As a response to the altered mechanical properties in Ru-LdECM hydrogels, the fibroblasts have displayed more myofibroblast-like characteristics. Increased α-SMA expression and altered organization have been previously reported in lung fibroblasts as a response to increasing stiffness of their environment [43,44]. Parallel to these previous studies, IPF fibroblasts have been reported to have higher levels of α-SMA expression both at gene [45] and protein [46] levels, compared with non-disease control lung-derived fibroblasts. In addition, another study reported that myofibroblast differentiation was not triggered by an isolated increase in the fibre density of synthetic 3D culture while keeping the stiffness of the environment constant [47]. This observation is also in concert with our results as both stiffness and the fibre organization are altered in Ru-LdECM hydrogels. The accompanying changes in the nuclear morphology was also in agreement with the influence of increased stiffness [48]. As reviewed by Wang et al., nuclear mechanotransduction as a response to a stiffer microenvironment (such as in fibrosis) has yet to be completely understood; however, such a change can result in altered gene regulation or nuclear transportation of cytoplasmic

factors [49]. Another implication of the altered nuclear morphology due to increased stiffness was shown to influence the differentiation of mesenchymal stromal cells [50]. These demonstrated changes on the seeded fibroblasts in our study suggest that the biomechanical properties of the fibrotic microenvironment were replicated in our model.

Our study utilizes a crosslinking strategy on native ECM-hydrogels using a ruthenium complex and sodium persulfate, as described recently by Kim et al. [25]. While this innovative approach has its advantages, our study has also some limitations. First of all, assessing the amounts of excess (unreacted) ruthenium and sodium persulfate remaining in the hydrogels was not possible with our current methodology; however, our future research is looking into further optimizing the amount of ruthenium and sodium persulfate in the reaction. In this study, we have seeded the fibroblasts on top of the hydrogels (2D) instead of seeding them within the hydrogel network. Although a 3D environment would represent the physiological situation in the body, a 2D culture system was preferred in this study to ensure proper visualization of the cell viability and morphology. Our study reports a model for examining the influence of biomechanical changes of the fibrotic microenvironment without investigating any gene and protein output from the fibroblasts. Although the influence of a fibrotic biomechanical microenvironment on fibroblasts have been shown to promote a pro-fibrotic phenotype both in gene and protein levels (as reviewed in [5,51]), such investigations are beyond the scope of this study. Lastly, the power of Maxwell modelling of the stress relaxation profiles of the native and crosslinked ECM hydrogels has not been completely realized and seems to remain as a mathematical exercise. The reason is that unlike other research areas e.g. microbial biofilms where relaxation constants has been linked to the composition [52], for hydrogels this systematic study is not yet available. With that, such modelling still proves useful in terms of analysing the altered stress relaxation behaviour.

Conclusion

This study demonstrates the mechanical characterization of an *in vitro* ECM-based fibrosis model for advancement of investigations on effects of a fibrotic microenvironment on the cells. The next step for this model is to investigate how changes in the stiffness or viscoelastic relaxation can instruct the cells for further profibrotic responses, especially in a 3-dimensional setting. In addition, fibre characteristics analysis revealed that the changes in the fibre organization (alignment, density, curvature) accompany the altered pattern in the viscoelastic stress relaxation behaviour. More research on the influence of these altered fibre characteristics on the profibrotic activation of different cells (fibroblasts, macrophages…) have yet to be explored. Overall, this study shows the preparation and the characterization of an *in vitro* fibrosis model. Such advanced *in vitro* models for fibrosis research will improve our understanding on de-coupling the mechanical changes from the biochemical changes taking place in fibrosis.

Declaration of Competing Interest

RHJH, FZ, TB, PKS, MCH have no conflicts to declare. MN and JKB receive unrestricted research funds from Boehringer Ingelheim.

Acknowledgements

The authors thank Albano Tosato for the assistance with graphical abstract preparation. Nederlandse Organisatie voor Wetenschappelijk Onderzoek (NWO) Aspasia-premie grant number 015.013.010 awarded to JKB.

References:

[1] A.D. Theocharis, S.S. Skandalis, C. Gialeli, N.K. Karamanos, Extracellular matrix structure, Adv. Drug. Deliv. Rev. 97 (2016) 4–27.

[2] C. Frantz, K.M. Stewart, V.M. Weaver, The extracellular matrix at a glance, J. Cell Sci. 123 (Pt 24) (2010) 4195–4200.

[3] L.D. Muiznieks, F.W. Keeley, Molecular assembly and mechanical properties of the extracellular matrix: a fibrous protein perspective, Biochim. Biophys. Acta (BBA) Mol. Basis Dis. 1832 (7) (2013) 866–875.

[4] J.K. Burgess, T. Mauad, G. Tjin, J.C. Karlsson, G. Westergren-Thorsson, The extracellular matrix - the under-recognized element in lung disease? J. Pathol. 240 (4) (2016) 397–409.

[5] D.J. Tschumperlin, G. Ligresti, M.B. Hilscher, V.H. Shah, Mechanosensing and fibrosis, J. Clin. Invest. 128 (1) (2018) 74–84.

[6] R.H.J. de Hilster, P.K. Sharma, M.R. Jonker, E.S. White, E.A. Gercama, M. Roobeek, W. Timens, M.C. Harmsen, M.N. Hylkema, J.K. Burgess, Human lung extracellular matrix hydrogels resemble the stiffness and viscoelasticity of native lung tissue, Am. J. Physiol. Lung Cell. Mol. Physiol. 318 (4) (2020) L698–L704.

[7] K.E.C. Blokland, S.D. Pouwels, M. Schuliga, D.A. Knight, J.K. Burgess, Regulation of cellular senescence by extracellular matrix during chronic fibrotic diseases, Clin. Sci. 134 (20) (2020) 2681–2706 (Lond.).

[8] G.F. Vasse, M. Nizamoglu, I.H. Heijink, M. Schleputz, P. van Rijn, M.J. Thomas, J.K. Burgess, B.N. Melgert, Macrophage-stroma interactions in fibrosis: biochemical, biophysical, and cellular perspectives, J. Pathol. 254 (4) (2021) 344–357.

[9] A.J. Haak, Q. Tan, D.J. Tschumperlin, Matrix biomechanics and dynamics in pulmonary fibrosis, Matrix Biol. 73 (2018) 64–76.

[10] J. Herrera, C.A. Henke, P.B. Bitterman, Extracellular matrix as a driver of progressive fibrosis, J. Clin. Invest. 128 (1) (2018) 45–53.

[11] M.E. Blaauboer, F.R. Boeijen, C.L. Emson, S.M. Turner, B. Zandieh-Doulabi, R. Hanemaaijer, T.H. Smit, R. Stoop, V. Everts, Extracellular matrix proteins: a positive feedback loop in lung fibrosis? Matrix Biol. 34 (2014) 170–178.

[12] M.W. Parker, D. Rossi, M. Peterson, K. Smith, K. Sikstrom, E.S. White, J.E. Connett, C.A. Henke, O. Larsson, P.B. Bitterman, Fibrotic extracellular matrix activates a profibrotic positive feedback loop, J. Clin. Invest. 124 (4) (2014) 1622–1635.

[13] M. Nizamoglu, J.K. Burgess, The multi-faceted extracellular matrix: unlocking its secrets for understanding the perpetuation of lung fibrosis, Curr. Tissue Microenviron. Rep. (2022).

[14] L.T. Saldin, M.C. Cramer, S.S. Velankar, L.J. White, S.F. Badylak, Extracellular matrix hydrogels from decellularized tissues: structure and function, Acta Biomater. 49 (2017) 1–15.

[15] A.J. Booth, R. Hadley, A.M. Cornett, A.A. Dreffs, S.A. Matthes, J.L. Tsui, K. Weiss, J.C. Horowitz, V.F. Fiore, T.H. Barker, B.B. Moore, F.J. Martinez, L.E. Niklason, E.S. White, Acellular normal and fibrotic human lung matrices as a culture system for in vitro investigation, Am. J. Respir. Crit. Care Med. 186 (9) (2012) 866–876.

[16] C.L. Petrou, T.J. D'Ovidio, D.A. Bolukbas, S. Tas, R.D. Brown, A. Allawzi, S. Lindstedt, E. Nozik-Grayck, K.R. Stenmark, D.E. Wagner, C.M. Magin, Clickable decellularized extracellular matrix as a new tool for building hybrid-hydrogels to model chronic fibrotic diseases in vitro, J. Mater. Chem. B 8 (31) (2020) 6 814–6 826.

[17] D.O. Visscher, H. Lee, P.P.M. Van Zuijlen, M.N. Helder, A. Atala, J.J. Yoo, S.J. Lee, A photo-crosslinkable cartilage-derived extracellular matrix bioink for auricular cartilage tissue engineering, Acta Biomater. 121 (2021) 193–203.

[18] J.W. Nichol, S.T. Koshy, H. Bae, C.M. Hwang, S. Yamanlar, A. Khademhosseini, Cell-laden microengineered gelatin methacrylate hydrogels, Biomaterials 31 (21) (2010) 5536–5544.

[19] J. Pupkaite, J. Rosenquist, J. Hilborn, A. Samanta, Injectable shape-holding collagen hydrogel for cell encapsulation and delivery cross-linked using thiol-michael addition click reaction, Biomacromolecules 20 (9) (2019) 3475–3484.

[20] N. Huettner, T.R. Dargaville, A. Forget, Discovering cell-adhesion peptides in tissue engineering: beyond RGD, Trends Biotechnol. 36 (4) (2018) 372–383.

[21] K. Vyborny, J. Vallova, Z. Koci, K. Kekulova, K. Jirakova, P. Jendelova, J. Hodan, S. Kubinova, Genipin and EDC crosslinking of extracellular matrix hydrogel derived from human umbilical cord for neural tissue repair, Sci. Rep. 9 (1) (2019) 10674.

[22] K.S. Lim, B.J. Klotz, G.C.J. Lindberg, F.P.W. Melchels, G.J. Hooper, J. Malda, D. Gawlitta, T.B.F. Woodfield, Visible light cross-linking of gelatin hydrogels offers an enhanced cell microenvironment with improved light penetration depth, Macromol. Biosci. 19 (6) (2019) e190 0 098.

[23] J.Y. Hsieh, M.T. Keating, T.D. Smith, V.S. Meli, E.L. Botvinick, W.F. Liu, Matrix crosslinking enhances macrophage adhesion, migration, and inflammatory activation, APL Bioeng. 3 (1) (2019) 016103.

[24] M. Keating, M. Lim, Q. Hu, E. Botvinick, Selective stiffening of fibrin hydrogels with micron resolution via photocrosslinking, Acta Biomater. 87 (2019) 88–96.

[25] H. Kim, B. Kang, X. Cui, S.H. Lee, K. Lee, D.W. Cho, W. Hwang, T.B. Woodfield, K.S. Lim, J. Jang, Light-activated decellularized extracellular matrix-based bioinks for volumetric tissue analogs at the centimeter scale, Adv. Funct. Mater. (2021) 2011252.

[26] F.D. Martinez-Garcia, R.H.J. de Hilster, P.K. Sharma, T. Borghuis, M.N. Hylkema, J.K. Burgess, M.C. Harmsen, Architecture and composition dictate viscoelastic properties of organ-derived extracellular matrix hydrogels, Polymers 13 (18) (2021) (Basel).

[27] R.A. Pouliot, P.A. Link, N.S. Mikhaiel, M.B. Schneck, M.S. Valentine, F.J. Kamga Gninzeko, J.A. Herbert, M. Sakagami, R.L. Heise, Development and characterization of a naturally derived lung extracellular matrix hydrogel, J. Biomed. Mater. Res. A 104 (8) (2016) 1922–1935.

[28] R.A. Pouliot, B.M. Young, P.A. Link, H.E. Park, A.R. Kahn, K. Shankar, M.B. Schneck, D.J. Weiss, R.L. Heise, Porcine lung-derived extracellular matrix hydrogel properties are dependent on pepsin digestion time, Tissue Eng. Part C Methods 26 (6) (2020) 332–346.

[29] P. Sharma, H. Busscher, T. Terwee, S. Koopmans, T. van Kooten, A comparative study on the viscoelastic properties of human and animal lenses, Exp. Eye Res. 93 (5) (2011) 6 81–6 88.

[30] W.D. Callister, D.G. Rethwisch, Materials Science and Engineering: An Introduction, 9th ed., John Wiley & Sons, New York, 2017.

[31] F.D. Martinez-Garcia, M.M. Valk, P.K. Sharma, J.K. Burgess, M.C. Harmsen, Adipose tissue-derived stromal cells alter the mechanical stability and viscoelastic properties of gelatine methacryloyl hydrogels, Int. J. Mol. Sci. 22 (18) (2021) 10153.

[32] E. Wershof, D. Park, D.J. Barry, R.P. Jenkins, A. Rullan, A. Wilkins, K. Schlegelmilch, I. Roxanis, K.I. Anderson, P.A. Bates, E. Sahai, A FIJI macro for quantifying pattern in extracellular matrix, Life Sci Alliance 4 (3) (2021).

[33] C. Mcquin, A. Goodman, V. Chernyshev, L. Kamentsky, B.A. Cimini, K.W. Karhohs, M. Doan, L. Ding, S.M. Rafelski, D. Thirstrup, W. Wiegraebe, S. Singh, T. Becker, J.C. Caicedo, A.E. Carpenter, CellProfiler 3.0: next-generation image processing for biology, PLoS Biol. 16 (7) (2018) e2005970.

[34] A. Marinkovi ´c, F. Liu, D.J. Tschumperlin, Matrices of physiologic stiffness potently inactivate idiopathic pulmonary fibrosis fibroblasts, Am. J. Respir. Cell Mol. Biol. 48 (4) (2013) 422–430.

[35] S.R. Polio, A.N. Kundu, C.E. Dougan, N.P. Birch, D.E. Aurian-Blajeni, J.D. Schiffman, A.J. Crosby, S.R. Peyton, Cross-platform mechanical characterization of lung tissue, PLoS One 13 (10) (2018) e0204765.

[36] O. Chaudhuri, L. Gu, D. Klumpers, M. Darnell, S.A. Bencherif, J.C. Weaver, N. Huebsch, H.P. Lee, E. Lippens, G.N. Duda, D.J. Mooney, Hydrogels with tunable stress relaxation regulate stem cell fate and activity, Nat. Mater. (2016) 326–334.

[37] B.W. Peterson, H.C. van der Mei, J. Sjollema, H.J. Busscher, P.K. Sharma, A distinguishable role of eDNA in the viscoelastic relaxation of biofilms, mBio (2013) American Society for Microbiologye00497-13.

[38] J.K. Burgess, M.C. Harmsen, Chronic lung diseases: entangled in extracellular matrix, Eur. Respir. Rev. 31 (163) (2022) 210202.

[39] G. Tjin, E.S. White, A. Faiz, D. Sicard, D.J. Tschumperlin, A. Mahar, E.P.W. Kable, J.K. Burgess, Lysyl oxidases regulate fibrillar collagen remodelling in idiopathic pulmonary fibrosis, Dis. Model. Mech. 10 (11) (2017) 1301–1312.

[40] J.K. Burgess, T. Mauad, G. Tjin, J.C. Karlsson, G. Westergren-Thorsson, The extracellular matrix –the under-recognized element in lung disease? J. Pathol. (2016).

[41] C.J. Philp, I. Siebeke, D. Clements, S. Miller, A. Habgood, A.E. John, V. Navaratnam, R.B. Hubbard, G. Jenkins, S.R. Johnson, Extracellular matrix cross-linking enhances fibroblast growth and protects against matrix proteolysis in lung fibrosis, Am. J. Respir. Cell Mol. Biol. 58 (5) (2018) 594–603.

[42] D.S. James, A.N. Jambor, H.Y. Chang, Z. Alden, K.B. Tilbury, N.K. Sandbo, P.J. Campagnola, Probing ECM remodeling in idiopathic pulmonary fibrosis via second harmonic generation microscopy analysis of macro/supramolecular collagen structure, J. Biomed. Opt. 25 (1) (2019) 1–13.

[43] S. Asano, S. Ito, K. Takahashi, K. Furuya, M. Kondo, M. Sokabe, Y. Hasegawa, Matrix stiffness regulates migration of human lung fibroblasts, Physiol. Rep. 5 (9) (2017).

[44] F. Liu, J.D. Mih, B.S. Shea, A.T. Kho, A.S. Sharif, A.M. Tager, D.J. Tschumperlin, Feedback amplification of fibrosis through matrix stiffening and COX-2 suppression, J. Cell Biol. 190 (4) (2010) 693–706.

[45] J. Jaffar, S.H. Yang, S.Y. Kim, H.W. Kim, A. Faiz, W. Chrzanowski, J.K. Burgess, Greater cellular stiffness in fibroblasts from patients with idiopathic pulmonary fibrosis, Am. J. Physiol. Lung Cell. Mol. Physiol. 315 (1) (2018) L59–L65.

[46] K.M. Roach, H. Wulff, C. Feghali-Bostwick, Y. Amrani, P. Bradding, Increased constitutive αSMA and Smad2/3 expression in idiopathic pulmonary fibrosis myofibroblasts is KCa3.1-dependent, Respir. Res. 15 (1) (2014).

[47] D.L. Matera, K.M. DiLillo, M.R. Smith, C.D. Davidson, R. Parikh, M. Said, C.A. Wilke, I.M. Lombaert, K.B. Arnold, B.B. Moore, B.M. Baker, Microengineered 3D pulmonary interstitial mimetics highlight a critical role for matrix degradation in myofibroblast differentiation, Sci. Adv. 6 (37) (2020).

[48] A. Galarza Torre, J.E. Shaw, A. Wood, H.T.J. Gilbert, O. Dobre, P. Genever, K. Brennan, S.M. Richardson, J. Swift, An immortalised mesenchymal stem cell line maintains mechano-responsive behaviour and can be used as a reporter of substrate stiffness, Sci. Rep. 8 (1) (2018).

[49] N. Wang, J.D. Tytell, D.E. Ingber, Mechanotransduction at a distance: mechanically coupling the extracellular matrix with the nucleus, Nat. Rev. Mol. Cell Biol. 10 (1) (2009) 75–82.

[50] J. Swift, I.L. Ivanovska, A. Buxboim, T. Harada, P.C.D.P. Dingal, J. Pinter, J.D. Pajerowski, K.R. Spinler, J.W. Shin, M. Tewari, F. Rehfeldt, D.W. Speicher, D.E. Discher, Nuclear Lamin-A scales with tissue stiffness and enhances matrix-directed differentiation, Science 341 (6149) (2013) 1240104.

[51] M.A.T. Freeberg, A. Perelas, J.K. Rebman, R.P. Phipps, T.H. Thatcher, P.J. Sime, Mechanical feed-forward loops contribute to idiopathic pulmonary fibrosis, Am. J. Pathol. 191 (1) (2021) 18–25.

[52] B.W. Peterson, H.C. van der Mei, J. Sjollema, H.J. Busscher, P.K. Sharma, A distinguishable role of eDNA in the viscoelastic relaxation of biofilms, MBio 4 (5) (2013) e00497-13.

Supplementary Figures

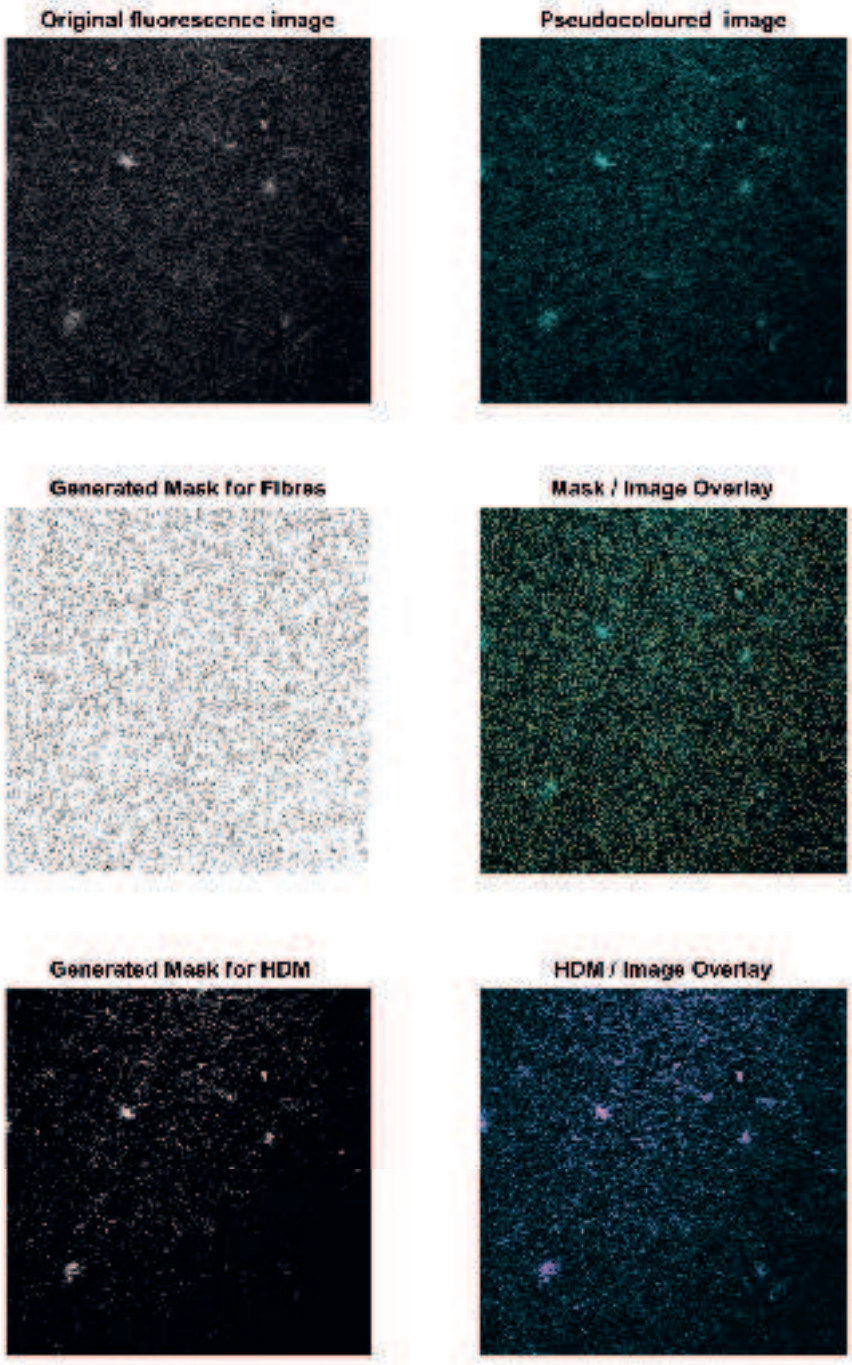

Supplementary Figure 1: Example of the masks and HDM generated through TWOMBLI analysis and their overlays with the original images.

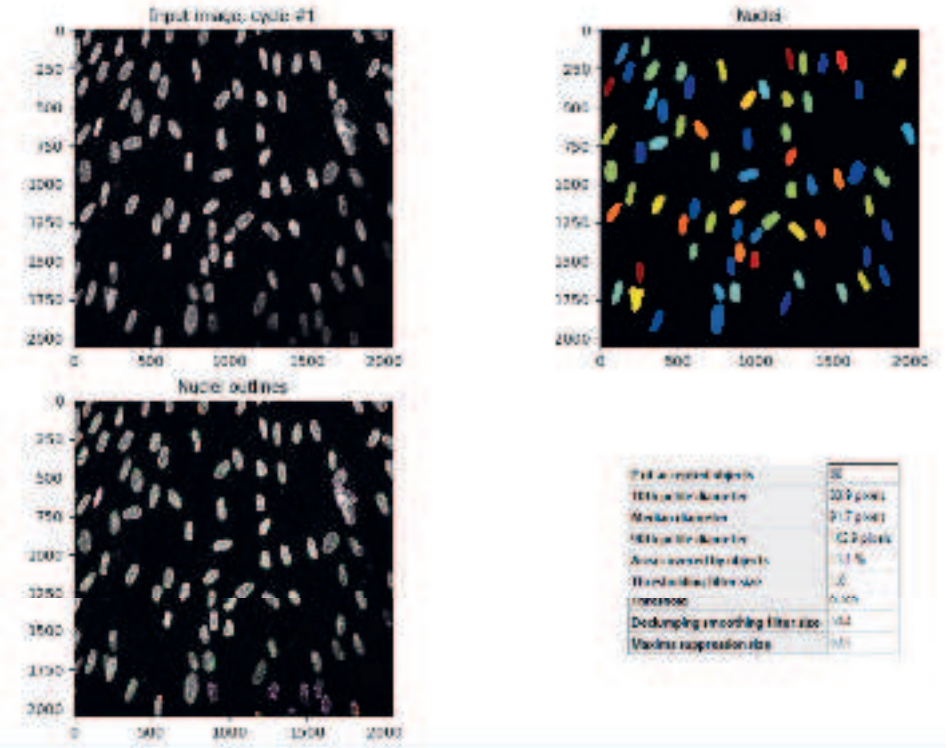

Supplementary Figure 2: Example pipeline of the CellProfiler software for the nuclei analysis.

A)

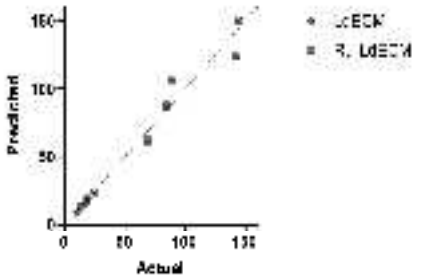
Normal QQ plot - Stiffness
Predicted
Actual

B)

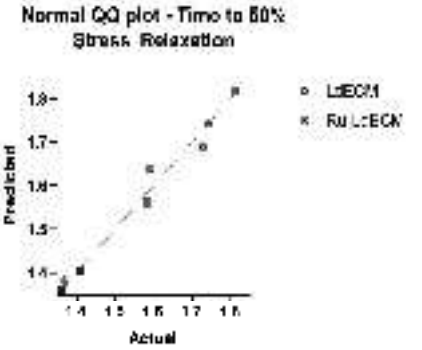
Normal QQ plot - Time to 50% Stress Relaxation
Predicted
Actual

C)

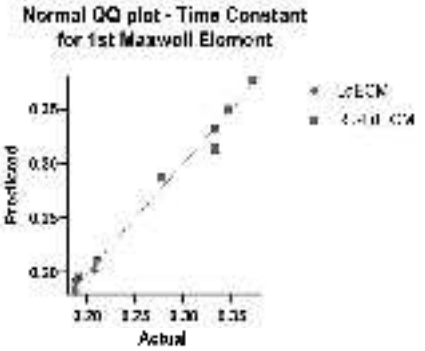
Normal QQ plot - Time Constant for 1st Maxwell Element
Predicted
Actual

D)

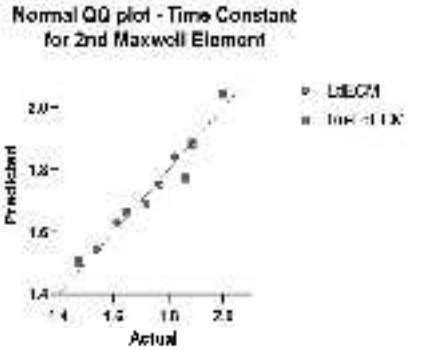
Normal QQ plot - Time Constant for 2nd Maxwell Element
Predicted
Actual

E)

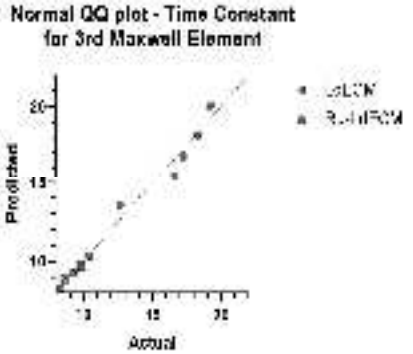
Normal QQ plot - Time Constant for 3rd Maxwell Element
Predicted
Actual

F)

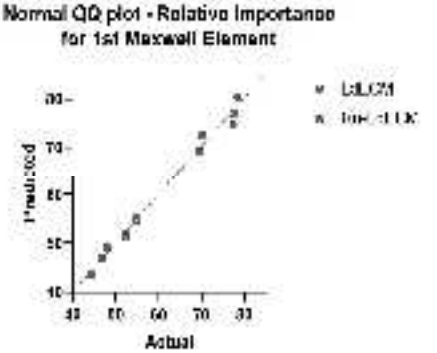
Normal QQ plot - Relative Importance for 1st Maxwell Element
Predicted
Actual

G)

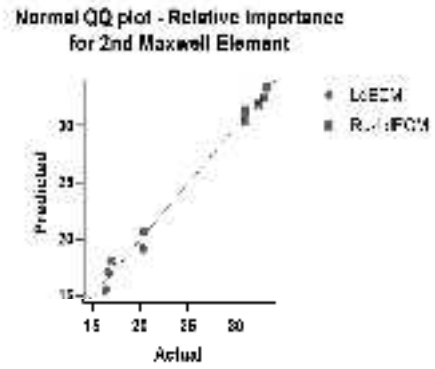
Normal QQ plot - Relative Importance for 2nd Maxwell Element
Predicted
Actual

H)

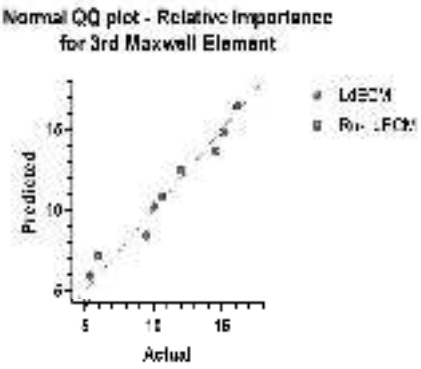
Normal QQ plot - Relative Importance for 3rd Maxwell Element
Predicted
Actual

I)

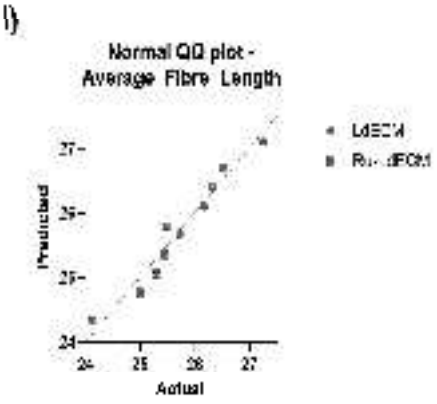
Normal QQ plot - Average Fibre Length
Predicted
Actual

J)

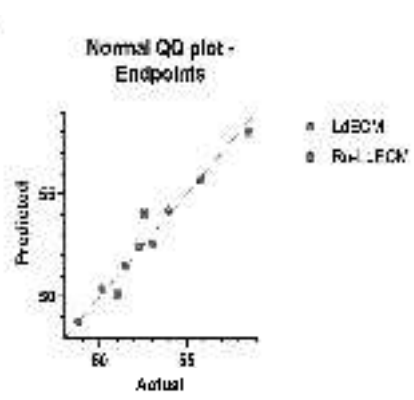
Normal QQ plot - Endpoints
Predicted
Actual

K)

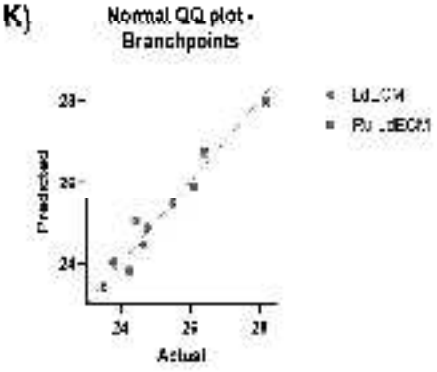
Normal QQ plot - Branchpoints
Predicted
Actual

L)

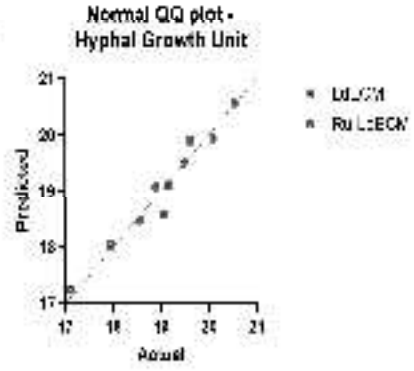
Normal QQ plot - Hyphal Growth Unit
Predicted
Actual

M)

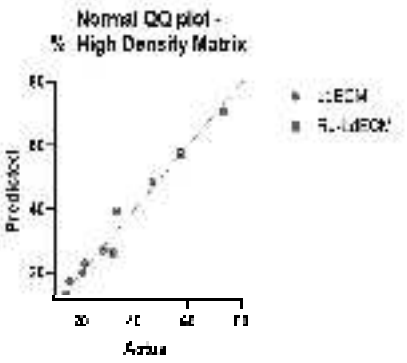
Normal QQ plot -
% High Density Matrix
Predicted
Actual

N)

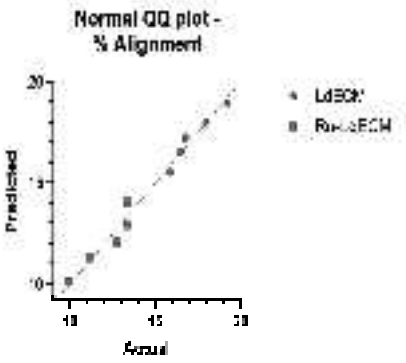
Normal QQ plot -
% Alignment
Predicted
Actual

O)

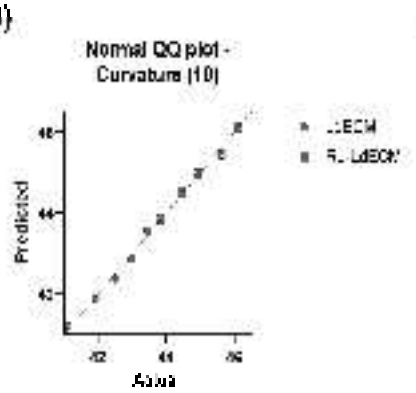
Normal QQ plot -
Curvature (10)
Predicted
Actual

P)

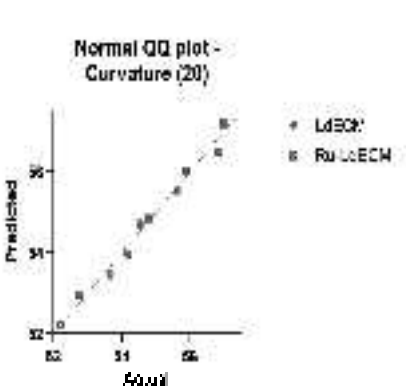
Normal QQ plot -
Curvature (20)
Predicted
Actual

R)

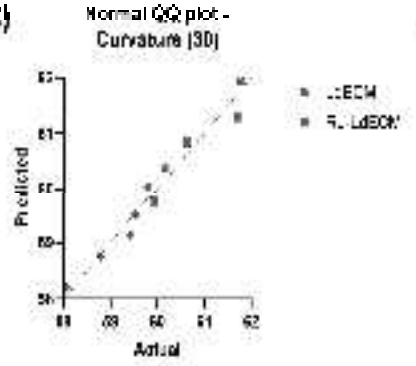
Normal QQ plot -
Curvature (30)
Predicted
Actual

S)

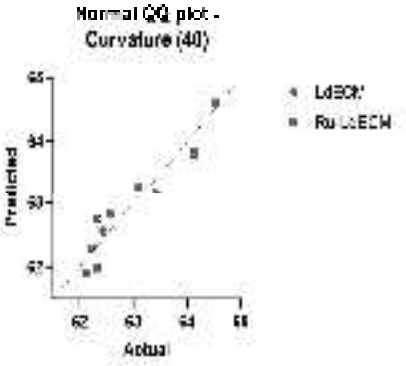
Normal QQ plot -
Curvature (40)
Predicted
Actual

T)

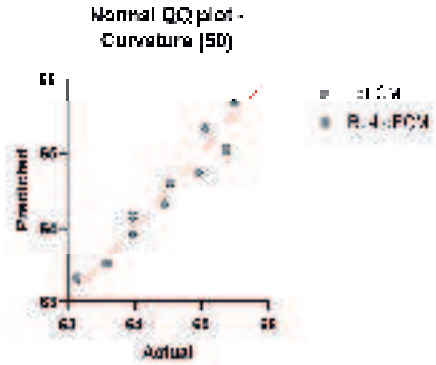

Supplementary Figure 3: Q-Q plots for the normality assessments of the data analyzed using parametric tests. A) Stiffness, B) Time to 50% Stress Relaxation, C) Time Constant for 1st Maxwell Element, D) Time Constant for 2nd Maxwell Element, E) Time Constant for 3rd Maxwell Element, F) Relative Importance for 1st Maxwell Element, G) Relative Importance for 2nd Maxwell Element, H) Relative Importance for 3rd Maxwell Element, I) Average Fibre Length, J) Number of Endpoints, K) Number of Branchpoints, L) Hyphal Growth Unit, M) % High Density Matrix, N) % Alignment, O) Curvature (10 µm fibres), P) Curvature (20 µm fibres), R) Curvature (30 µm fibres), S) Curvature (40 µm fibres), T) Curvature (50 µm fibres).

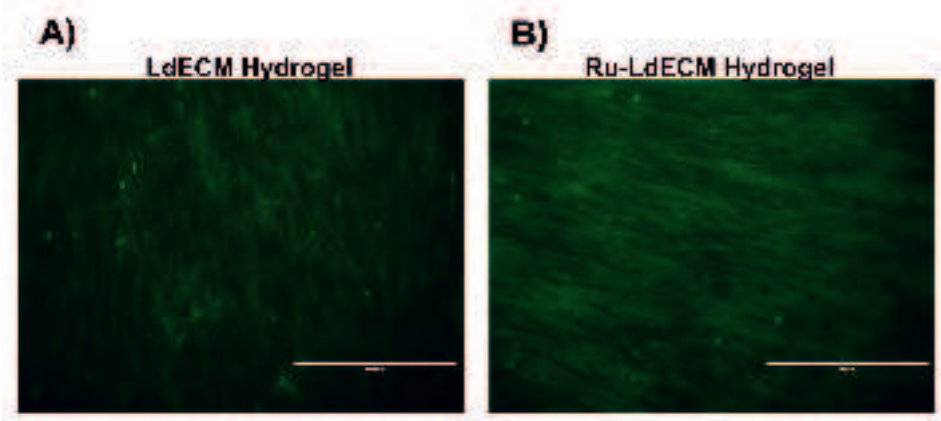

Supplementary Figure 4: Example image of the live/dead staining at day 7.

Chapter 6

Fibroblast alignment and matrix remodeling induced by a stiffness gradient in skin-derived extracellular matrix hydrogel

Fenghua Zhao[a,b,c], Meng Zhang[a,c], Mehmet Nizamoglu[c,d], Hans Kaper[a,b], Linda A. Brouwer[c], Theo Borghuis[c], Janette K. Burgess[a,c,d,#], Martin C. Harmsen[a,c,d,#], Prashant K. Sharma[a,b,#]

a University of Groningen, University Medical Centre Groningen, W.J. Kolff Institute for Biomedical Engineering and Materials Science-FB41, A. Deusinglaan 1, 9713 AV Groningen, The Netherlands

b University of Groningen, University Medical Centre Groningen, Department of Biomaterials and Biomedical Technology-FB40, A. Deusinglaan 1, 9713 AV Groningen, The Netherlands

c University of Groningen, University Medical Centre Groningen, Department of Pathology and Medical Biology, Hanzeplein 1 (EA11), 9713 GZ Groningen, The Netherlands

d University of Groningen, University Medical Centre Groningen, Groningen Research Institute for Asthma and COPD (GRIAC), Hanzeplein 1 (EA11), 9713 AV Groningen, The Netherlands

[#] These authors contributed equally

Acta Biomaterialia

https://doi.org/10.1016/j.actbio.2024.05.018

Chapter 6

Abstract: Large skin injuries heal as scars. Stiffness gradually increases from normal skin to scar tissue (20x higher), due to excessive deposition and crosslinking of extracellular matrix (ECM) mostly produced by (myo)fibroblasts. Using a custom mold, skin-derived ECM hydrogels (dECM) were UV crosslinked after diffusion of ruthenium (Ru) to produce a Ru-dECM gradient hydrogel. The Ru diffusion gradient equates to a stiffness gradient and models physiology of the scarred skin. Crosslinking in Ru-dECM hydrogels results in a 23-fold increase in stiffness from a stiffness similar to that of normal skin. Collagen fiber density increases in a stiffness-dependent fashion while stress relaxation also alters, with one additional Maxwell element necessary for characterizing Ru-dECM. Alignment of fibroblasts encapsulated in hydrogels suggests that the stiffness gradient directs fibroblasts to orientate at ~45 ° in regions below 120 kPa. In areas above 120 kPa, fibroblasts decrease the stiffness prior to adjusting their orientation. Furthermore, fibroblasts remodel their surrounding ECM in a gradient-dependent fashion, with rearrangement of cellsurrounding ECM in high-stiffness areas, and formation of interlaced collagen bundles in low-stiffness areas. Overall, this study shows that fibroblasts remodel their local environment to generate an optimal ECM mechanical and topographical environment.

Keywords: gradient stiffness, extracellular matrix hydrogel, fibroblasts, collagen, scarring

1. Introduction

The skin is the largest organ of the human body. Appropriate healing of the skin after injury is necessary to restore the barrier function [1, 2]. Dermal wound healing is a spatio-temporally regulated process. It involves four defined and overlapping stages: coagulation, inflammation, proliferation, and remodeling/fibrosis [3-5]. However, if not properly regulated, accumulation of extracellular matrix (ECM) and tissue stiffening during the last stage of wound healing can lead to pathological dermal scarring [6]. The pivotal cells involved in fibrosis are fibroblasts and their differentiated form - myofibroblasts, as these remodel ECM [7, 8]. Numerous fibroblasts migrate to the injured area and produce collagens to replace the fibrin clot formed during the coagulation phase of the wound healing process. During the remodeling phase, fibroblasts are activated and differentiate into myofibroblasts [9]. These myofibroblasts express more α-smooth muscle actin than fibroblasts and are contractile, as well as migratory [10]. They act as natural stitches to keep wounds closed, which they then fill with ECM components such as collagens. The wound then enters the final stage of remodeling. During the remodeling process, various factors, such as hypoxia in the wound, continued inflammatory stimulation, excessive wound tension, can lead to continued deposition and disordered arrangement of collagens. Finally, if the wound healing becomes dysregulated, the deposited collagen is heavily crosslinked by the persistent and chronically activated myofibroblasts to form fibrosis, rather than undergoing apoptosis at the time when the tissue structural integrity is restored [11, 12].

An important element of skin fibrosis is the gradient of stiffness in the ECM that extends from the healthy dermis into the scar [13-15]. In fact, stiffness gradients also occur in other pathological conditions *in vivo* such as fibrosis of liver, heart, lungs and kidney [16-19]. Furthermore, because the ECM provides attachment sites for cell adhesion receptors, changes in the biophysical tissue microenvironment directly influences the behavior and function of fibroblasts and may dictate phenotypic changes e.g. to myofibroblasts [20]. The mechanics of ECM affect the cytoskeleton, matrix adhesion, cell proliferation and differentiation of fibroblasts cultured in two-dimensions (2D) [21-25]. As cells naturally exist in complex three-dimensional (3D) ECM networks [26], current studies shift towards 3D culturing to better understand how matrix mechanical

properties affect cell phenotype [27]. Dermal fibroblasts in 3D culture in matrices of different stiffnesses showed that, unlike cells that expand more with increasing 2D stiffness, high stiffness in 3D causes cells to round up and change towards a pro-inflammatory, pro-remodeling state [28-30]. Most of these *in vitro* studies apply uniform stiffness substrates, in which the gradient of stiffness changes of tissue ECM *in vivo* is not replicated. Such uniform stiffness substrates limit potential studies on how fibroblasts are influenced by diverse biophysical environments *in vivo*. In addition, the widely used hydrogels, whether natural hydrogels such as collagen, hyaluronic acid, chitosan, or synthetic hydrogels such as polyvinyl alcohol (PVA) and polyacrylic acid (PAA), do not sufficiently approximate the complex natural biochemical environment for interrogating cell responses, either in composition or structure [31-35].

To address this challenge, we established an *in vitro* scar model with stiffness gradients using skin-derived decellularized ECM (dECM) hydrogel. These dECM hydrogels comprise the natural ECM components and mimic the physiological environment of (scarred) skin. This experimental system builds on our previous study in which we developed a non-cytotoxic method to uniformly modulate the stiffness of lung-derived dECM hydrogel by introducing visible UV (UV/vis) - induced ruthenium (Ru)/sodium persulfate (SPS) crosslinking [36]. In the presence of visible light and a cross-linker electron acceptor SPS, Ru^{2+} is photolytically oxidized to Ru^{3+}. The presence of Ru^{3+} can oxidize aromatic residues such as in tyrosine residues in proteins. The free tyrosyl radical then reacts with another free tyrosyl radical to form a covalent dityrosine bond i.e. crosslinking neighboring protein chains. dECM hydrogels cross-linked with Ru not only have increased stiffness levels, but also have increased higher density matrix percentages and smaller average fiber lengths. In the current study, we introduced Ru crosslinking into skin-derived dECM to generate the stiffness gradient hydrogels. We investigated the physical characteristics of these gradients and their influence on fibroblasts in particular pertaining to ECM remodeling.

2. Experimental Methods

2.1. Decellularization of porcine skin tissue

Porcine skin tissue was obtained from a local abattoir (Kroon Vlees, Groningen, the Netherlands). The epidermis and subcutaneous fat were removed. Then the

remaining dermal tissue was cut into ~ 3 mm x 3 mm x 3 mm cubes which were homogenized in a kitchen blender (Bourgini, Breda, The Netherlands) until a paste was formed, while keeping the temperature below 37 °C. The homogenized skin was decellularized as we described previously (Figure 1A) [37, 38]. Briefly, the minced tissue was washed with Dulbecco's phosphate-buffered saline (DPBS) and then sonicated for 1 minute at 100 % power. Next, 0.05 % trypsin (Thermo Fisher Scientific, US) dissolved in DPBS was used to digest the tissue slurry, followed by deep digestion using subsequent incubations in saturated 6 M NaCl solution, 1 % sodium dodecyl sulfate (SDS) (Sigma-Aldrich, US), 1 % Triton X-100 (Sigma-Aldrich, US) and 1 % sodium deoxycholate (Sigma-Aldrich, US), which were all dissolved in distilled water and each added to the tissue slurry for 24 h incubations at 37 °C with shaking. Washing 3 times with distilled water after each step was undertaken to remove residual digestive. The volume of solution at each step was 5-fold more than the tissue volume. Next, residual DNA was digested with 30 μg/mL DNase (Sigma-Aldrich, US) in 10 mM Tris-HCl buffer with pH 8, 1.3 mM $MgSO_4$ (Sigma-Aldrich, US) and 2 mM $CaCl_2$ (Sigma-Aldrich, US) for 24 h at 37 °C with shaking. Then, three volumes of 70 % ethanol were used to sterilize the decellularized ECM (dECM) tissue overnight with shaking. At the end, dECM tissue was frozen in liquid nitrogen and lyophilized with a FreeZone Plus lyophilizer (Labconco, US). The Ultra-Turrax (IKEA, Germany) with liquid nitrogen crushed the lyophilized dECM tissue into a fine powder which was stored in an airtight plastic bottle at -20 °C.

2.2. Preparation of dECM pre-gel

The dECM (20 mg/mL) powder was added to 0.01 M hydrochloric acid (HCl) with 2 mg/mL pepsin and digested in a sterile glass vial while mixing using a magnetic stirring bar at 500 rpm at room temperature for 24h. The homogeneously dissolved ECM solution was neutralized to pH 7.4 with 0.1 M NaOH to stop digestion and adjusted to 1x PBS by adding one-tenth volume 10x PBS. This so-called dECM pre-gel was stored at 4°C.

2.3. Making gradient stiffness skin dECM hydrogels

A polylactic acid (PLA) front-mold, designed to enable the generation of our gradient hydrogel, was printed using a 3D printer (ULT216931, Ultimaker S3, Netherlands) (figure 1B) (See printing script in Suppl. materials). Liquid

polydimethylsiloxane (PDMS, Sylgard 184, Dow Corning, Netherlands) composed of the elastomer and the cross-linker in a 10:1 ratio by weight, was then poured into the PLA mold, until it completely filled it. A microscope slide (25mm x 76mm, Thermo Fisher Scientific, US) was placed on top of the mold and the solution was cured at 50°C overnight. Then, the cast PDMS back-mold with the tightly adhered microscope slide was separated from the PLA front-mold (See Figure S1 for details). The PDMS back-mold contained a cuboidal space of 10 mm x 8 mm x 1.5 mm (120 mm^3) connected to a cylindrical space of radius 19 mm and height 1.5 mm (425 mm^3). The cylindrical to cuboidal volume ratio was 3.5.

The cylindrical space was first filled by placing a plug with a thin layer of parafilm, before the dECM pre-gel was poured into the cuboidal space. The dECM pre-gel filled PDMS mold was incubated at 37 °C for 1 hour to allow for thermal gelation. The plug was carefully removed from the cylindrical space and the cross-linker solution was poured into this space (Figure 1B). The cross-linker solution was prepared using a ruthenium visible light photo initiator (400-450 nm) kit (Advanced BioMatrix, US) containing pentamethyl cyclopentadienyl bis(triphenylphosphine) ruthenium (II) chloride (CAS Number: 92361-49-4, hereafter referred as ruthenium (Ru)) and sodium persulfate (SPS, CAS: 7775-27-1). A series of ruthenium concentrations (0, 1.5 mM, 3 mM, 6 mM, and 15 mM coupled with 30 mM sodium persulfate in sterile DPBS were prepared and added to the cylindrical space of the mold. Then the mold was placed in a cell incubator at 37 °C for 3 h, to allow for lateral diffusion of ruthenium and sodium persulfate into the gel to generate a concentration gradient. After 3 h the cross-linker solution was removed from the mold reservoir and the hydrogel with ruthenium gradient was photo crosslinked by placing at a 4.5 cm distance from two 9 W lamps emitting UV A light at 405 nm for 5 min (UV/vis light density: 20 mW/cm^2) (Figure 1C). Under the UV/vis exposure, ruthenium catalyzed the covalent bond formation of di-tyrosine dimers between protein chains in dECM hydrogel (Figure 1D). The hydrogels (10mm×8mm×1.5mm) with stiffness gradient (Figure 1C) were labeled as Ru0-dECM, Ru1.5-dECM, Ru3-dECM, Ru6-dECM, and Ru15-dECM, respectively. The hydrogels were then incubated in 6 mL DPBS for 4 hours at 37 °C to keep them moist before testing the mechanical properties. After our initial validation experiments, we selected ruthenium/sodium persulfate of 3 mM Ru / 30 mM SPS (Ru3-dECM) as the final

concentration for all subsequent experiments (referred to as Ru-dECM), the control gel (dECM hydrogel) was then prepared by adding the same volume and concentration of cross-linker solution without UV/vis light exposure.

2.4. Mechanical properties

2.4.1. μLLCT measurements

The stiffness of dECM and Ru-dECM hydrogels were assessed by using a micro low-load compression tester (μLLCT, UMCG, Groningen, The Netherlands) at room temperature. The μLLCT performed micron-scale multi-point automatic testing on hydrogels, which is helpful to determine stiffness gradients at multiple areas along the hydrogel. The μLLCT consists of a micro force sensing probe FT-S1000 (Femto Tools, Switzerland) with a 50×50 μm square tip area mounted on a precision linear stage Q522.230 (PI, Karlsruhe, Germany) and a bottom plate which can be moved on the x and y axes (Figure 2A). Data acquisition and stage control were carried out using a program written in MATLAB software (MathWorks® Inc., Natick, US). The μLLCT probe tip was slowly brought in contact with the hydrogel and hydrogel compressed to measure the stiffness of the hydrogel. Hydrogel properties were determined at 15 discrete and equidistant points spread over 9 mm between the high Ru concentration end to low Ru concentration end. At each testing point the hydrogel was compressed to 90 % of its original thickness (imposed strain, ε of 0.1) at a deformation speed of 10 %/s (strain rate, $\dot{\varepsilon}$ of $0.1 s^{-1}$) and kept compressed for 5 s. Next, the probe was elevated 300μm and moved to next testing point position until all 15 points were tested. During the initial 1 second compression step, the applied force, F, was converted to stress, σ, by dividing F by the area of cross-section, A, of the probe tip (A=2500 μm^2). The deformation was converted into strain, ε, by dividing the compression depth by the original thickness of the hydrogel sample. Stress was plotted as a function of strain and the slope of the linear fit was taken as the Young's modulus in Pascals (Pa or N/m^2) which is indicative of the hydrogel stiffness at that testing point and a strain rate ($\dot{\varepsilon}$) of 0.1 s^{-1}.

2.4.2. LLCT measurement

The viscoelastic properties (stiffness, stress relaxation) of the gradient hydrogels, were tested using the low-load compression tester (LLCT, (Mytri Aeldoom, the Netherland) fitted with a 0.5mmϕ probe. LabVIEW 7.2 (National Instruments,

Austin, US) was used to control the LLCT and for data acquisition. The LLCT probe was used to compress the hydrogel to 80% of its original thickness at a deformation rate of 20 % s^{-1} (Strain rate, $\dot{\varepsilon} = 0.2\ s^{-1}$). Same as the μLLCT, the slope of the linear part of the stress-strain curve was taken as the Young's modulus (Pa or N/m^2), which is indicative of the stiffness of the hydrogel. After compression, a constant strain of 20% was kept for 50 s. The required stress continuously decreased with time ($\sigma(t)$) due to the viscoelastic nature of the hydrogel, which is stress relaxation. The stress ($\sigma(t)$) was converted into relaxing stiffness ($E(t)$) by dividing with the constant strain of 0.2. A Maxwell function i.e., *Eq. 1* was fitted to $E(t)$ to get the values of E_i and τ_i for individual Maxwell elements. The τ_i was the relaxation time constant for each individual Maxwell element. *Eq. 2* was used to represent relative importance (R_i) for each Maxwell element (ME) parallelly placed in the generalized Maxwell model. For natural materials, multiple elements are necessary to explain the experimentally observed stress relaxation behavior. The minimum number of MEs necessary to explain the stress relaxation behavior of a measured hydrogel was determined by monitoring the decrease in chi-square function expressed by *Eq. 3* with the addition of each new element, starting with only 1 in the beginning. When no further decrease in chi-square function was observed, then that number was used as the minimum number of MEs. In general, for replicate measurements the same minimum number of MEs were found to be necessary.

$$E(t) = E_1 e^{t/\tau_1} + E_2 e^{t/\tau_2} + E_3 e^{t/\tau_3} + \cdots + E_n e^{t/\tau_n} \quad (1)$$

$$R_i = {E_i}/{E_1 + E_2 + E_3 + \cdots + E_n} \quad (2)$$

$$\chi^2 = \sum_{j=0}^{200} \left[\frac{E_j - E(t_j)}{\sigma_j}\right] \quad (3)$$

2.5. 3D Cell culture

Primary human dermal neonatal fibroblasts (HDFn, PCS-201-010™, ATCC, US) were cultured in growth media composed of high glucose (25mM) Dulbecco's Modified Eagle's Medium (DMEM, Lonza, Switzerland), 10% fetal bovine serum (FBS, Gibco, Germany), 1% glutamine (BioWhittaker®, Verviers, Belgium) and 1% penicillin/streptomycin (Gibco, Paisley, UK). Upon reaching

90% confluency, the cells were harvested using 0.25% Trypsin-EDTA (Gibco, US) in DPBS and then the cell numbers were counted using a NucleoCounter NC-200 TM (Chemometec, Allerod, Denmark). Next, the cells were collected through centrifuging at 500 x g and resuspended in 50 µL growth media. The resuspended cells were mixed gently with the dECM pre-gel at a density of 1.7 x 10^6 cells /mL. Next, the mold was inserted into a well of a 4-well rectangular dish (Thermo Scientific™ 167063, US; Figure S5). The cell–pre-gel mixtures were cast into the cuboid space of mold (Figure 1B) while the connected cylinder groove part was completely closed off with a plug. After the pre-gel was incubated at 37°C for one hour to allow complete thermal gelation, the plug in the cylinder groove was removed and replaced with cross-linking solution (DPBS with 3mM ruthenium and 30mM sodium persulfate for Ru-dECM; pure DPBS for dECM). Next, the mold was incubated at 37°C for 3h, after which the ruthenium and sodium persulfate had diffused into the gel and generate a gradient stiffness under photo crosslinking at 405nm for 5 min. Following, 7 mL of growth media was added to each well.

2.6. Live-Dead staining

Cell viability and morphology were determined by staining live cells, dead cells, and cell nuclei using Calcein AM (C1430- Thermo Fisher Scientific, US), propidium iodide (PI; P4170, Sigma Aldrich, US) and Hoechst (Hoechst 33342, Thermo Fisher Scientific, US) dyes respectively. After culturing for 4 h, 1 d and 5 d, the hydrogels were removed from the mold and washed three times with DPBS and then incubated with staining solution (5 µM Calcein AM, 3 µM PI in DPBS, 8 µM Hoechst). From this step onwards, aluminum foil was used to protect the hydrogel from light. After incubating for 30 min at 37 °C, the samples were washed twice with DPBS to remove excess staining solution, and then serum-free medium was added to maintain cell viability. Finally, the hydrogels were transferred to a 35 mm glass bottom dish (Thermo Scientific™, C150680, UK) and imaged within 2 hours using a Zeiss Cell Discoverer 7 imaging system (Zeiss, Jena, Germany) with GFP (509 nm) and Texas Red (615 nm), DAPI (405 nm) channels. The cell orientation in both Ru-dECM and dECM gel was characterized using Fiji with orientation J macro [39]. Cell morphology in both Ru-dECM and dECM hydrogels was analyzed based on Calcein AM stained of living fibroblasts: average spreading area of HDFn fibroblasts was evaluated

using Fiji; cell aspect ratio was calculated using the plug-in PAT-GEOM [40] in Fiji.

2.7. Histological characterization of protein fiber structure

Hydrogel ultrastructure was investigated using scanning electron microscopy (SEM). After Ru crosslinking of the skin dECM pre-gel, the cell-free Ru-dECM and dECM hydrogels were fixed with 2.5 % glutaraldehyde (111-30-8, Sigma, Darmstadt, Germany) and 2% paraformaldehyde (PFA; Sigma-Aldrich) in PBS at 4 °C overnight. After fixation, 2 % agarose (Invitrogen, US) in DPBS was used to pre-embed hydrogels to avoid shrinkage of the hydrogel during dehydration. Next, the hydrogels were stepwise dehydrated through a graded ethanol series before embedding them in paraffin. Then, the paraffin-embedded hydrogels were cut into 50 μm thick sections which were mounted onto glass coverslips (size 18 × 18 mm, Merk, Catalog #BR470045). After drying, the sections were deparaffinized in xylene and rehydrated in a series of 100 %, 96 %, and 70 % ethanol. Dry sections were glued on top of 6 mm SEM pin stubs (Agar Scientific, Stansted, UK) and carbon coated using a Leica EM ACE600 sputter coater device (Leica Microsystems B.V., Amsterdam, Netherlands). Hydrogels were visualized at 25,000× magnification, at 3 kV with a Zeiss Supra 55 STEM (Carl Zeiss NTS GmbH). The analyses were performed from images of three independent hydrogels using Fiji with the plugin DiameterJ[41].

2.8. Histological characterization of ECM protein fiber structure

After 4 h, 1 d, and 5 d cell culture, hydrogels were fixed in 2 % PFA in DPBS overnight. Then, the samples were pre-embedded / dehydrated / paraffin embedded as described above in section 2.7. The paraffin-embedded hydrogels were cut into 4 μm thin sections. The sections were deparaffinized and stained with Hoechst (8 μM in DPBS) for 15 min followed by 0.1 % picrosirius red (PSR; Sigma-Aldrich) in 1.3 % aqueous solution of picric acid (Sigma-Aldrich) to visualize the cell nuclei and collagen fibers respectively. After washing with 3 changes of dH_2O and 3 changes of 0.5 % acetic acid, the sections were mounted with 0.7 % acetic acid in glycerol. The slides were stored at 4 ℃, in the dark, before they were imaged.

2.9 Immunofluorescence staining

Before immunofluorescent staining, the 4 μm deparaffinized sections were heated in 10 mM citrate buffer pH 6 at 85 ◦C for 4 h for antigen retrieval. Then sections were incubated in 0.3 % hydrogen peroxide (H_2O_2, Merck, Germany) for 30 min to block endogenous peroxidase activity. After 3 times washing with Tris Buffered Saline buffer (TBS, Thermo Fisher Scientific), the sections were blocked with 4 % bovine serum albumin (BSA) in TBS for 15 min and subsequently incubated at room temperature for 2 h with the primary antibody Ki67 (ab16 6 67, Abcam, rabbit anti-human, 1:200) for detecting cell proliferation. After 3 times washing with TBS, the peroxidase-conjugated goat-anti-rabbit secondary antibody (Thermo Fisher Scientific, catalog #A32731, 1:200) was added for one hour at room temperature, followed by color development by incubation with the Opal 570 (Akoya Biosciences, Marlborough MA, US, 1:200) diluted in 0.1 M borate buffer with 0.003 % hydrogen peroxide (Merck, Darmstadt, Germany). Finally, the sections were treated with DAPI (Thermo fisher scientific, Lot:2328978, US) (1:50 0 0) in DPBS for 30 min. The sections were mounted using Citifluor mounting medium (Science Services, Munich, Germany) and stored at 4 ° in the dark before acquiring images.

2.10. Section imaging and image analyzing

The cell live-dead staining images were obtained by scans using the Zeiss Cell discoverer 7 imaging system as described above. The fluorescent images of stained PSR and Hoechst sections were generated with the fluorescence slide scanner Olympus VS200（Olympus Corporation, Japan) at 40x magnification using λ_{ex} 561 nm / λ_{em} 670 nm for PSR and λ_{ex} 405nm / λ_{em} 455nm for Hoechst. The intensity of PSR-stained collagen fibers was analyzed with Fiji [42]. Fluorescent images of Ki67 and DAPI staining were generated with a Leica SP8 X laser confocal microscope (Leica, Wetzlar, Germany) using λ_{ex} 561nm / λ_{ex} 617 nm and λ_{ex} 405nm / λ_{em} 455 nm at 40 x magnification. CellProfiler 4.2.1 software was used to quantify the percentage of Ki67 positive fibroblasts [43].

2.11. Statistical analysis

All statistical analyses were performed using GraphPad Prism v9.2.0 (GraphPad Company, San Diego, CA, US). All data are shown as mean ± standard deviation from the experiments that were performed with least five independent experiments. The figure legends indicate the sample size associated with each

experiment. Normality of the data was tested with a QQ plot and a Shapiro-Wilk test [44]. When normality was confirmed, a one-way or two-way analysis of variance (ANOVA) was employed for data analysis. When data were not normally distributed, Mann-Whitney test and Kruskal-Wallis test were used for data analyses. All data were considered significantly different at $p < 0.05$.

3. Results

3.1. Characterizations of the stiffness gradient of Ru-dECM hydrogel under variable Ru working concentrations

In the custom mold, controlled by Fick's laws of diffusion, Ru naturally diffused from one end of the hydrogel to the other due to the concentration differences. The flow rate of a substance (i.e., the amount of substance passing through a unit area per unit time) is linearly related to the concentration gradient. This resulted in the generation of a gradient in Ru concentration along the hydrogel over time. Since the rate of the cross-linking reaction depends on the concentration of Ru present at any location within the hydrogel, the degree of cross-linking of the hydrogel also exhibited a gradient distribution. As a result, control dECM hydrogels (Ru: 0mM) had a consistent (low) stiffness throughout the entire gel, while all four gels with Ru concentrations (Ru: 1.5, 3, 6, 15 mM) yielded stiffness gradients which extended to the stiffness seen in the control at their far end (Figure 2B), as measured by μLLCT. The main differences of these gradients were the inclines of the curves. The gradient induced by 1.5 mM Ru extended over a distance of 3.1 mm and had a slope of -130.3 kPa/mm. In contrast, the gradient induced by 3 mM Ru extended over a distance of 5 mm with a slope of -118.4 kPa/mm, while the gradient induced by 6mM Ru and 15 mM Ru extended over a distance of 3.8 mm with a slope of -38.7 kPa/mm and 4.4 mm with -120.5 kPa/mm. Because 3 mM Ru yielded the widest gradient, this was selected for further experiments, referred to from here on as Ru-dECM. Subsequently, the stiffness gradient region of Ru-dECM spanning from 2 mm to 7 mm was selected as the focus of our research and divided into 10 equal-distant zones of 0.5 mm each (Figure 2C). For high accuracy, a μLLCT with 50×50 μm square probe was used here to identify the stiffness gradients. However, this procedure was time-consuming and μLLCT had limited ability to detect stress relaxation. Therefore, in subsequent viscoelasticity testing of hydrogels LLCT was performed with a

0.5 mm diameter round probe. Due to differences in probe size, the stiffness values obtained with μLLCT differed slightly from LLCT values, yet the shape of the stiffness curves was retained.

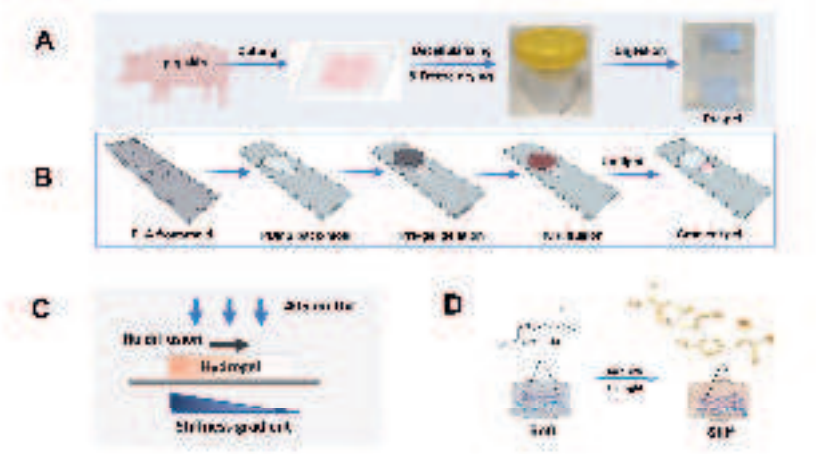

Figure 1. Schematic outlining the steps in designing and creating a gradient stiffness hydrogel. A) Porcine skin decellularization and ECM (dECM) pre-gel preparation. Porcine skin was blended, decellularized, freeze-dried and ground to a fine powder. Afterwards, the ECM powder was pepsin digested to prepare the pre-gel solution. B) Polydimethylsiloxane (PDMS) mold fabrication to enable gradient stiffness dECM hydrogel generation. Polylactic acid (PLA) pre-mold was first three dimensionally (3D) printed, and liquid PDMS was poured into the PLA mold which was subsequently covered by a glass microscope slide and incubated overnight to allow the development of a tight connection between the PDMS mold and the glass. This PDMS mold contained a cylindrical space connected to a cuboidal space. The dECM pre-gel solutions were poured into the cuboid space while blocking the cylindrical space with a plug (shown in dark grey color). After the thermal gelation of the pre-gel, the plug was removed and a Ru crosslinking solution (shown in red color) was poured and incubated for 3 h to allow for diffusion of ruthenium (Ru) and sodium persulfate (SPS) into the gel, followed by UV/vis crosslinking. C) A schematic diagram of introducing Ru crosslinks in the hydrogel to create the stiffness-gradient hydrogel. D) A schematic of the chemical change induced during the visible UV light activated dityrosine synthesis using the Ruthenium kit for the ECM crosslinking: Ruthenium catalyses the formation of dityrosine dimers between protein chains. Figure created with BioRender.

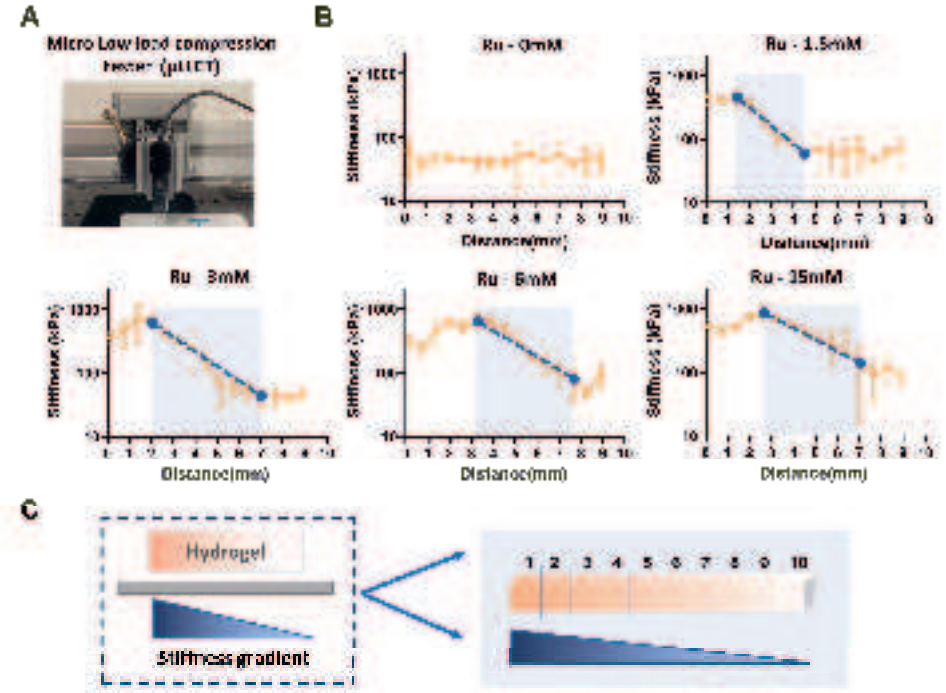

Figure 2. Stiffness of dECM hydrogel after the diffusion of a series of initial Ru concentrations and UV/vis crosslinking. A) Micro low-load compression tester (μLLCT) used for measuring stiffness in compression mode. Using MATLAB software, the system automatically captured the stress-strain curve (the slope is the Young's modulus indicative of stiffness) at 15 points spread over a 9 mm distance in the horizontal direction from high Ru concentration end to low Ru concentration end. B) Stiffness gradients of Ru-dECM hydrogels for different initial Ru concentration. Each dot represents the mean ± standard deviation generated from measurement on five independent experiments (n=5). The grey box length represents the span of the stiffness gradient; the blue dashed line represents the slope of the stiffness gradient. C) A schematic for dividing the entire stiffness gradient of Ru-dECM hydrogel into 10 zones for all the subsequent analyses.

3.2. Regulation of viscoelastic mechanical properties of cell-free dECM hydrogels by Ru-introduced crosslinking

First, without encapsulating cells, the effect of Ru-introduced crosslinking on the mechanical properties of dECM hydrogels was explored. The stiffness of cell-free Ru-dECM under the LLCT test ranged from 459 ± 92 kPa to 20 ± 7 kPa over 5 mm and dECM hydrogel stiffness remained constant at 8 ± 2 kPa (Fig. 3 A). To compare the effects of hydrogels with different stiffness values on subsequent encapsulating of cells, zones 2, 5, and 8 were selected to represent high, medium, and low stiffness zones of the gradient. This yielded stiffness values for zone 2: 349 kPa, zone 5: 107 kPa, and for zone 8: 32 kPa. Stress relaxation curves for cellfree Ru-dECM and dECM hydrogels at 4 h under constant deformation in 50 s showed a relaxation of over 93.2 % in both hydrogels in all zones (Fig. 3 B). The time to reach 50 % stress relaxation also did not differ between Ru-dECM and dECM hydrogels and was less than 1 s (Fig. 3 C). Mathematical fitting of the relaxation curves with the generalized Maxwell model, yielded three elements for control dECM hydrogels and four elements for crosslinked hydrogels (Fig. 3D). Each Maxwell element was characterized by a relaxation time constant (τ) and its relative importance (Ri). The τ values are presented in Table 1, and the Ri values are plotted in Fig. 3D. At 4 h post-crosslinking, the shortest ME1 ($\tau \sim 0.2$ s, Table 1) had the largest relative contribution irrespective of crosslinking. ME1 contributed approximately 65 % of the relaxation curve in dECM hydrogels while it accounted for 45–55 % in Ru-dECM hydrogels. In cell-free Ru-dECM, the contributions of the ME2, ME3 and ME4 decreased successively, while ME2 and ME3 contributed equally (~20 % each) for dECM hydrogels. The relaxation time constants (τ) of these four MEs in gradient stiffness hydrogels were 0.2 s, 1.3 s, 6.6 s, and 71 s (Table 1), respectively. The relaxation constant (τ) of each element was unaffected by the hydrogel stiffness (i.e. it remained the same in zone 2, zone 5 and zone 8). The τ of the three MEs in dECM hydrogels were 0.2 s, 2.1 s, and 16 s (Table 1), respectively. From the analysis of the time constants, the additional ME (ME4) needed to explain the relaxation in Ru-dECM corresponded to the relaxation time constant of 71 s.

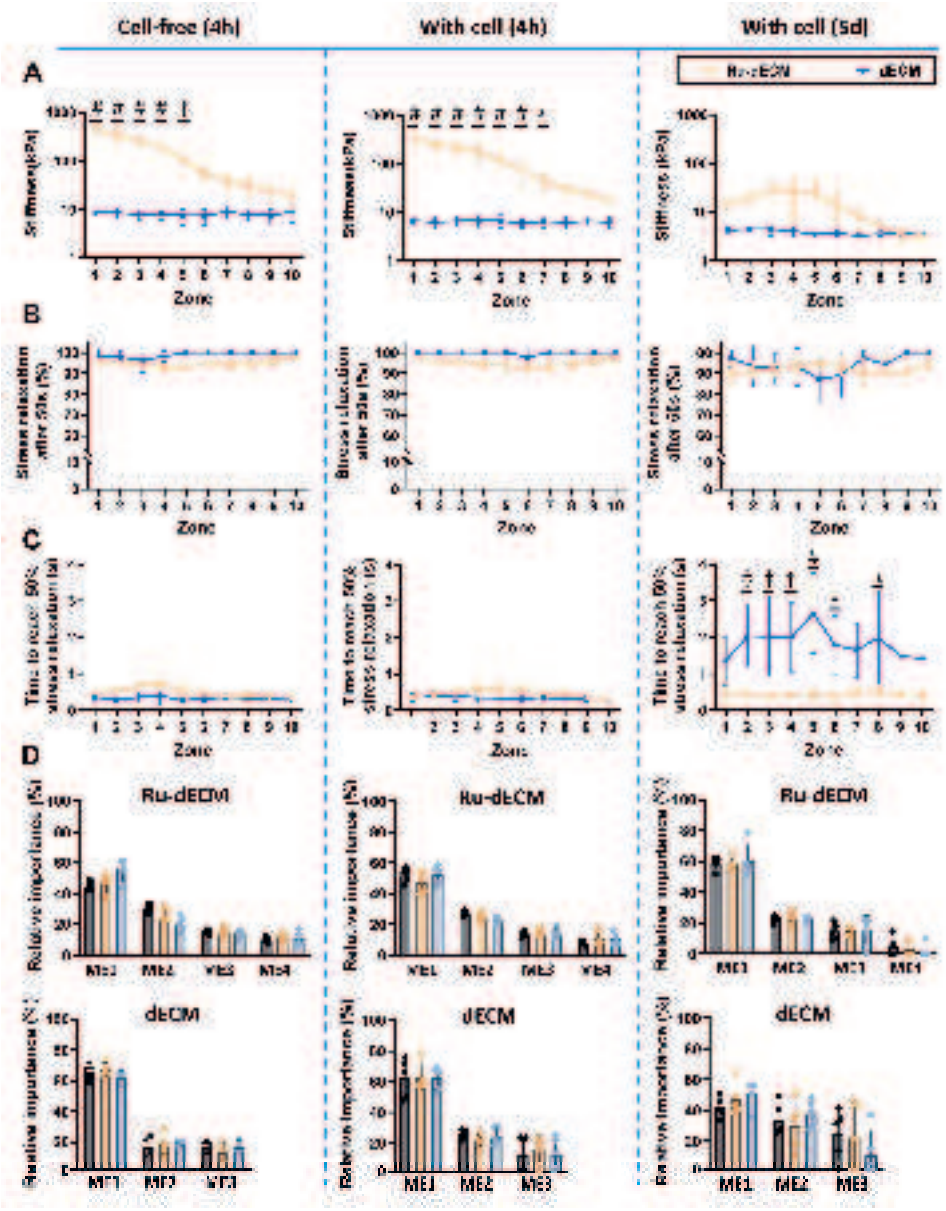

Figure 3. Mechanical properties of both Ru-dECM and dECM hydrogels with and without encapsulated human dermal neonatal fibroblasts (HDFn) at 4h and 5d. A) The stiffness of Ru-dECM and dECM hydrogels. B) Average stress relaxation behavior over 50 s duration. After compressing hydrogels using LLCT with a fixed 20% strain ratio, the stress relaxation behavior was recorded over 50 s period. C) Time taken to reach 50 % stress relaxation. D) Analysis of the stress relaxation behavior through the generalized Maxwell model system. The relaxation profiles of the both types of hydrogels with and

without encapsulated cells over 50 s period was mathematically modelled using a Maxwell model system and the contribution (relative importance R_i) of each Maxwell element to the total relaxation were determined. Each dot represents the mean ± standard deviation (SD) of five independent measurements on the same hydrogel for each sample (n = 5). Statistical significance was analyzed by two-way ANOVA to compare each zone of Ru-dECM hydrogels with the corresponding zone of dECM hydrogels. (ns or unmarked, not significant; *, $p< 0.05$; ‡, $p < 0.01$; †, $p < 0.001$; #, $p < 0.0001$).

3.3. Regulation of hydrogel mechanical properties by encapsulated HDFn cells

Upon 3D encapsulation of HDFn cells in the hydrogels (4 h culturing), the stiffness gradient of Ru-dECM changed from an initial range of 459 ± 92 to 20 ± 7 kPa in cell free Ru-dECM to 323 ± 97 to 22 ± 3 kPa in cell encapsulated Ru-dECM, whereas the dECM hydrogel's stiffness changed from approximately 8 ± 2 kPa in the absence of cells to about 6 ± 2 kPa in the presence of encapsulated cells (Fig. 3 A). This observed small decrease in the stiffness gradient range was due to the fact that after cells were encapsulated in the hydrogel, the cells (as added elements in the hydrogel) also contributed to the overall stiffness. The stiffnesses of zones 2, 5, and 8, which represented high stiffness, medium stiffness and low stiffness, were 254 kPa, 120 kPa, and 31 kPa respectively after encapsulating the cells for 4 h. After 5 d, the gradient stiffness range was still maintained in the cell-free Ru-dECM hydrogel (Figure S2). A reduction in the magnitude of the stiffness occurred due to the swelling of the hydrogel under medium immersion (stiffness of cell-free Ru-dECM at 4 h ranged from 459 ± 92 kPa to 20 ± 7 kPa and changed to 269 ± 66 kPa to 11 ± 4 kPa at 5 d; The stiffness of cell-free dECM remained constant, with a stiffness of 8 ± 2 kPa at 4 h to 8 ± 2 kPa at 5 d (Figure S2)). Intriguingly, the stiffness gradient of cell-encapsulated Ru-dECM had vanished after 5d especially within the high stiffness part and the previously observed significant difference of stiffness between Ru-dECM and dECM at 4 h was no longer present by day 5 (Fig. 3 A). The stiffness values of cell- encapsulated Ru-dECM at 5 d spanned from 27 ± 19 kPa to 3 ± 1 kPa and hovered at 4 ± 0.1 kPa for dECM.

Both Ru-dECM and dECM, when loaded with cells, retained their stress relaxation profiles, exceeding 87 % relaxation across all assessed durations, mirroring the cell-free hydrogels (Fig. 3 B). The relaxation rate (time to reach 50 %

stress relaxation) in cell encapsulated Ru-dECM hydrogel after 5d culture remained consistent at approximately 0.5 s. In contrast, the cell encapsulated dECM hydrogel had a protracted relaxation time (lower relaxation rate) at day 5 (τ~2.0 s) compared to that at 4 h (τ~0.5 s) (Fig. 3 C). The requisite number of MEs remained unaltered after 5d for both cells encapsulated and unencapsulated hydrogels; three elements for dECM and four for Ru-dECM (Table 1 and Fig. 3 D). After 4 h culture, the time constants (τ) of the MEs closely reflected those in cell-free hydrogels, shown by τ_1 0.2 s, τ_2 1.3 s and τ_3 6.8 s, with unique element 4 for τ_4 74 s in Ru-dECM and τ_1 0.3 s, τ_2 2.2 s and τ_3 12 s in dECM (Table 1). The relative importance corresponding to each element had not changed after 4 h cell encapsulation. After 5 d culture, although the presence of cells did not affect the number of ME, the characteristics of the MEs changed significantly compared to the initial 4 h stage (Fig. 3 D). The τ values expanded for each element, with $\tau_1 \leq 1$ s, $1 < \tau_2 \leq 10$ s, $10 < \tau_3 \leq 60$ s, and the fourth element was $60 < \tau_4 \leq 150$ s (Table 1). Concurrently, alterations in the Ri of elements within both hydrogels were noted, displaying an increase in ME1 and a decrease for ME4 for Ru-dECM hydrogel, while there was a decrease in ME1 and an increase in ME2 & ME3 for dECM hydrogel.

Table 1. Relaxation time constants (τ) in seconds (s) of each Maxwell element for both of Ru-dECM and dECM hydrogels with and without encapsulated cells. Zones 2, 5 and 8 correspond to high, medium and low stiffness regions on the gradient hydrogel.

		Ru-dECM				dECM		
Time		τ_1	τ_2	τ_3	τ_4	τ_1	τ_2	τ_3
4h	zone2	0.3	1.3	6.5	75.4	0.2	1.6	17.1
	zone5	0.2	1.4	7.1	71.3	0.2	2.2	22.1
cell	zone8	0.2	1.2	6.3	64.9	0.3	2.4	8.5
free	**Average**	**0.2**	**1.3**	**6.6**	**70.5**	**0.2**	**2.1**	**16.0**
4h	zone2	0.3	1.3	6.4	69.0	0.3	2.8	13.5
	zone5	0.3	1.4	7.0	71.6	0.3	2.2	12.0
with	zone8	0.2	1.3	7.2	81.2	0.2	1.9	9.6
cell	**Average**	**0.2**	**1.3**	**6.8**	**73.9**	**0.3**	**2.2**	**11.7**
5d	zone2	0.3	2.0	48.0	193.8	0.4	7.0	31.9
	zone5	0.3	2.1	34.0	122.2	0.7	9.7	56.5
with	zone8	0.3	3.8	76.8	108.6	0.8	10.7	47.2
cell	**Average**	**0.3**	**2.6**	**52.9**	**141.5**	**0.6**	**9.1**	**45.2**

3.4 Stiffness gradient does not affect the viability, migration and proliferation of HDFn, but causes changes in cell morphology and orientation

At all-time points at least 85 % of the encapsulated fibroblasts were alive irrespective of the hydrogel crosslinking. Encapsulated cells (4 h) appeared rounded but had adopted a more stretched morphology after 1 d of culture (Fig. 4). This spindle-shaped morphology remained in both groups after 5 d culture albeit that fibroblasts tended to spread randomly in soft control gels, while these elongated more in a single direction in Ru-dECM gels. Cell spreading area and aspect ratio analyses revealed distinct morphological preferences of fibroblasts encapsulated within hydrogels over a one-day period (Figure S4). Notably, cells exhibited a pronounced spindle-shaped morphology with an aspect ratio of 2.0 in the soft dECM gel, while within the gradient stiffness of Ru-dECM, the aspect ratio of cells gradually increased as stiffness decreased, transitioning from 1.4 in zone 2 to 2.0 in zone 8 meaning that stiffness inhibited cell stretching. By day 5, the Ru-dECM induced elongation of fibroblasts up to an aspect ratio of 3.9 in all zone 2, 5 and 8, contrasting with the 2.9 aspect ratio observed in the soft dECM gel in which fibroblasts also had continued to stretch (Figure S4). While cell area increased with extended culture time, it remained unaffected by variations in mechanical cues and changes in cell shape. In control gels, cell densities appeared higher than in Ru-crosslinked gels. Yet, this related to the approximately 50% size reduction of the dECM hydrogel area (Figure S5).

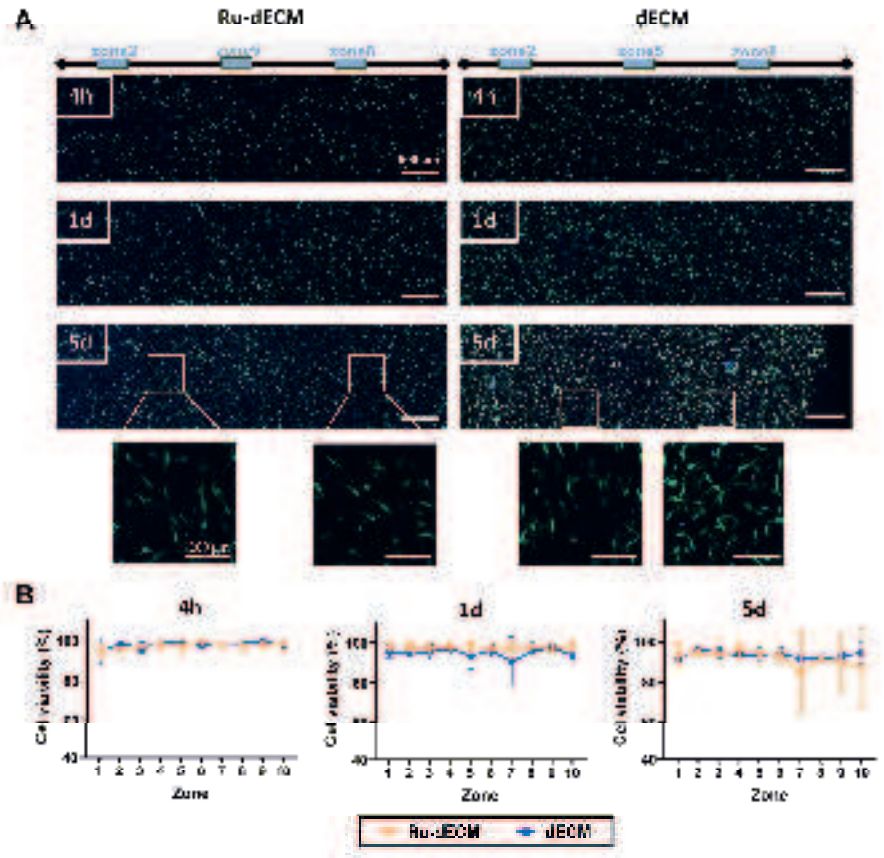

Figure 4. Live/dead staining on HDFn fibroblasts seeded in Ru-dECM and dECM hydrogels at 4h, 1d and 5d. A) Cells were stained with Calcein AM (green) for living cells, propidium iodide (red) for dead cells and Hoechst (blue) for cell nuclei. Scale bars depict 500 µm. B) Cell viability percentage was calculated based on ImageJ quantification of fluorescently labelled cells. Each dot represents the mean ± standard deviation (SD) of three independent measurements on the same hydrogel for each sample (n = 3). Statistical significance was analyzed by two-way ANOVA to compare each zone of Ru-dECM hydrogels with the corresponding zone of dECM hydrogels (ns or unmarked, not significant).

We quantified the angular arrangement of the fibroblasts within the different hydrogels at 1 d and 5 d After 1 d the cells exhibited an orientation pattern within defined zones of the Ru-dECM hydrogel, with the degree of orientation appearing to be related to the stiffness range the cells experienced (Fig. 5 B). More cells aligned between −80 ° to −30 ° relative to the stress axis (stiff to soft) in zone 5

and −60 ° to −30 ° in zone 8. This arrangement did not appear in zone 2 which was the region with the high stiffness (~254 kPa). As we reported in the previous section: the fibroblasts cultured in 3D in the Ru-dECM hydrogel remodeled the hydrogel during the 5 d of culture to modulate the stiffness to decrease it within the initially high stiffness zones significantly to achieve a stiffness range between 27.2 to 3.2 kPa across the breadth of the hydrogel. In apparent response to these changes in mechanics, on the fifth day, the fibroblasts that had previously experienced a gradient stiffness in their environment in the Ru-dECM hydrogel all adopted a uniform cell orientation at an approximately −45 ° angular orientation to the gradient axis (stiff to soft) (Figure5). To represent the three-dimensional arrangement of cells in the hydrogel, the length (10 mm), width (8 mm), and height (1.5 mm) of the hydrogel were defined as the X, Y, and Z axes, respectively. Obviously, the x-axis is the gradient axis where the stiffness gradient exists. The cell directional alignment was found to only occur in the XYplane rather than along the Z-axis. In contrast, in control dECM gels the cells maintained their random orientation throughout the culture period.

Ki67 immunofluorescence staining showed that the stiffness gradient did not affect the proliferation of fibroblasts. The proliferation indexes of HDFn (percentage of Ki67 positive cells) cultured in Ru-dECM and dECM were less than 10% after 1 d and 5 d (Figure S6). There was also no difference in the number of proliferating cells in each zone in any of the hydrogels regardless of the time in culture. In addition, there were no differences in the number of cells in each zone in any of the hydrogels (Figure S6C). The uniform distribution of cell numbers throughout the gradient stiffness hydrogel may suggest the absence of cell migration (prominent durotaxis) under the conditions of our experiment. However, this was an indirect observation, and further investigation would be required to substantiate this observation.

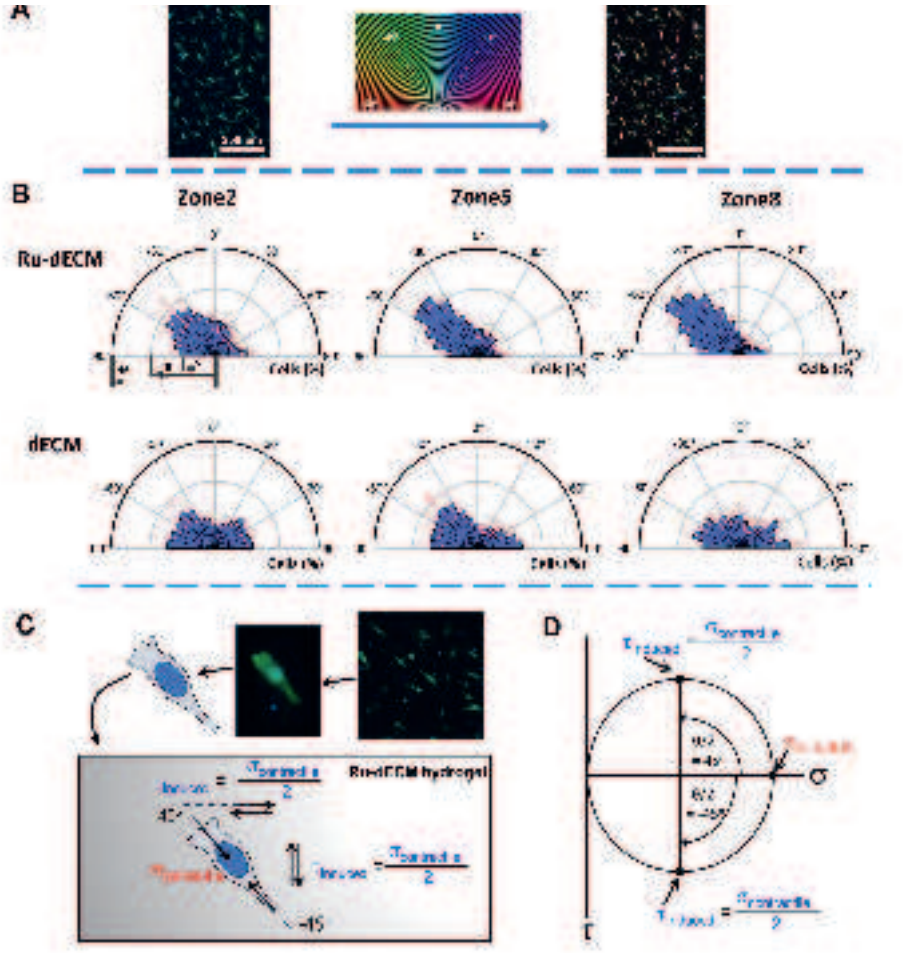

Figure 5. Distribution of HDFn cells orientation in Ru-dECM and dECM hydrogels after 5d. A) Orientation J software package as the plugin for Fiji evaluated the orientation of HDFn cells generating a visual representation of the orientation based on the circular HSB color map coding. The left panel is a representative fluorescence micrograph of HDFn cells in zone 5 of Ru-dECM hydrogel stained for living cells (Calcein AM (green)), dead cells (propidium iodide (red)) and cell nuclei (Hoechst (blue)); the middle panel is the circular HSB color map coding; and the right panel is the color-coded orientation survey for the HDFn cells in zone 5. Scale bar: 250 μm. B) Orientation distributions of HDFn cells in zones 2, 5 and 8 in Ru-dECM and dECM hydrogels after 5d. C) A 2D schematic showing that cells maximized the induced shear stress on the hydrogel along and across to the gradient by aligning themselves 45° to the long axis. D) A plain strain Mohr's circle showing how the contractile normal stresses cause maximum possible induced shear stresses on the hydrogel along and across the long axis with a magnitude of half of the contractile normal stresses.

3.5. The ECM fiber structure observation in no cell-encapsulated dECM and Ru-dECM hydrogels

The ultrastructure of the hydrogel was visualized by SEM (Figure. S7A) at 25,0 0 0x magnification. Irrespective of the Ru crosslinking, the skin-derived ECM hydrogels comprised a network of randomly organized fibers, with the fibers showing a striped repeat pattern typical for collagen fibers. However, the arrangement of fibers in Ru-dECM was denser than that in dECM, especially in zone2 of Ru-dECM. Moreover, the diameter of the fibers in zone2 of Ru-dECM were significantly greater than that in zone5 of Ru-dECM and the control dECM. The 'percentage of pores' corresponds to the proportion of pore area relative to the entire image. While the number of pores in the RuECM hydrogel did not differ from control dECM hydrogel (Figure S7C), Ru crosslinking reduced the fraction of mesh holes compared to control dECM gel (Ru-dECM zone2: 0.33 ± 0.09; Ru-dECM zone5: 0.42 ± 0.04; Ru-dECM zone8: 0.50 ± 0.03; dECM: 0.50 ± 0.003 (Figure S7D). In contrast, Ru crosslinking in hydrogels had no influence on the intersection density (the intersection number per μm2) (Figure S7E).

3.6 Time-dependent matrix fiber remodeling in cell-encapsulated dECM and Ru-dECM hydrogels

Cells encapsulated in the hydrogels, altered collagen architecture and increased the fiber density in Ru-dECM hydrogels compared to those in the dECM hydrogels (Fig. 6 A). The increase in collagen fiber density was stiffness dependent in the Ru-dECM hydrogels. The PSR stained collagen fibers for dECM hydrogel at 4 h appeared diffused and homogeneously dense in all zones. In contrast, the fiber density for the Ru-dECM at 4 h was greater in the vicinity of zone 1 and lower near the softer end of the gradient i.e. zone 10. This was also evident from the mean fluorescence intensity (MFI) of collagen fibers per unit area which was determined using Fiji (Fig. 6 B). Ru-induced crosslinking increased the MFI in the cell-loaded Ru-dECM hydrogel, where the MFI in the softest part (zone 10) of Ru-dECM at 4 h was similar to that in control dECM hydrogel (Fig. 6 B), while the intensity of the collagen fiber fluorescence signal increased towards zone 1.

The striking feature in the Ru-dECM hydrogel after 5 d of cell culture was the appearance of voids (pores) within the collagen network in zones 1–4 and the

decreased MFI in zone 3 - 8 compared to 4 h (Fig. 6 B). The fiber intensity in the softest part (zone 10) of Ru-dECM hydrogel was similar to that observed in control dECM hydrogel, showing the formation of defined interlaced collagen fiber bundles (Fig. 6 A) and the increased MFI (Fig. 6 B).

In detailed view, the collagen fibers surrounding fibroblasts in zones 2, 5, and 8 after 5 days, showed the fibers had been reorganized compared to freshly encapsulated (4 h) fibroblasts (Figure S8). In zone 2 (high stiffness) of Ru-dECM, larger pores had appeared in the immediate vicinity of encapsulated fibroblasts. This suggested that fibroblasts had degraded the collagen and /or rearranged the collagen fibers' assembly pattern through exertion of pulling/pushing forces upon the fibers or both. Within zones 5 and 8 (medium and low stiffness) of Ru-dECM respectively, the fibroblasts demonstrated interconnectivity with the surrounding fibers and there were no pores in the collagen fiber network appearing around the cells. In dECM hydrogels, the pattern of fiber bundle assembly in the matrix surrounding the cells was clearly visible. (Figure S8).

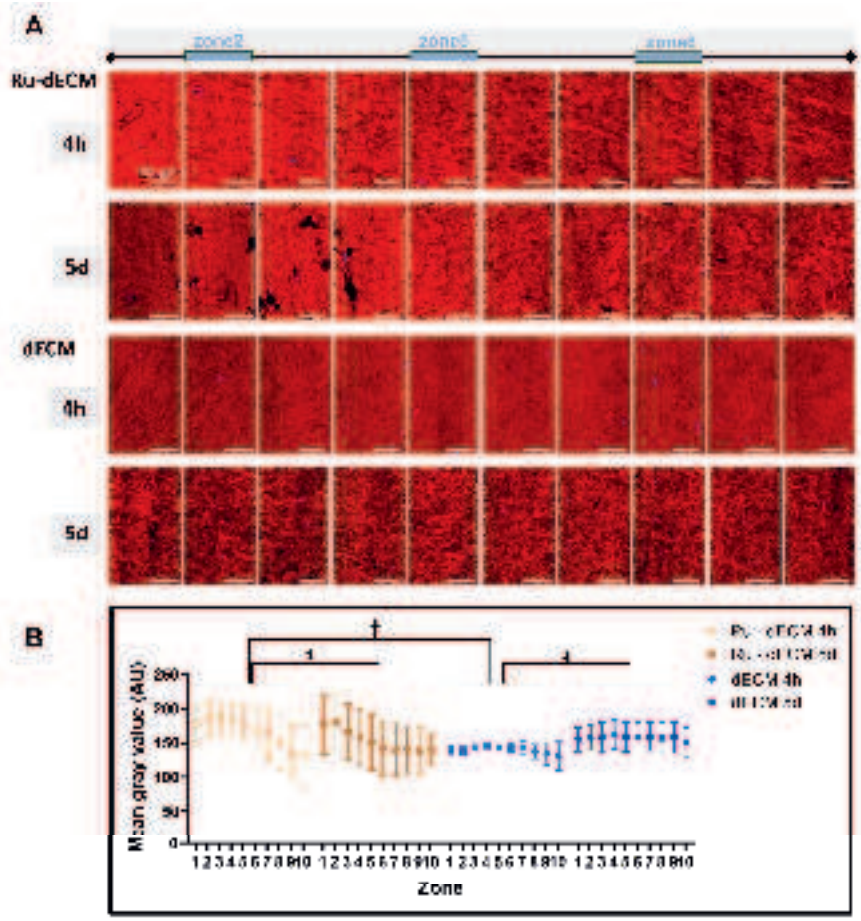

Figure 6. Picrosirius red staining on Ru-dECM and dECM hydrogel slices and fiber characteristics analysis on the collagen network. Ru-dECM and dECM hydrogel slices were stained using Picrosirius red staining and generated fluorescent images were analyzed using FIJI ImageJ. A) Representative images of Picrosirius red staining on Ru-dECM and dECM hydrogel slices after 4h and 5d cell culturing. (cell nuclei-blue (Hoechst); collagen fiber-red (PSR)) Scale bars: 100 μm. B) Quantification for fiber Mean grey value (Integrated Density/Area, Integrated Density: the sum of the fluorescent signal pixels of all collagen fibers in an area) for 10 zones in Ru-dECM and dECM hydrogels. Each dot represents the mean ± standard deviation (SD) of five independent measurements on the same hydrogel for each sample (n = 5). Statistical significance was analyzed by one-way ANOVA through comparing the area below the curve data (*, $p < 0.05$; †, $p < 0.001$).

4. Discussion

The biomechanical dynamics of scar tissue formation after skin injury has been a focus of interest in histopathology and regenerative medicine. Our goal was to construct an *in vitro* model to elucidate the responses of dermal fibroblasts to a stiffness gradient. A major outcome of this study was the establishment of a versatile skin-derived ECM hydrogel platform with gradient stiffness starting at ~20 kPa and enabling a 23-fold log linear increase over 5 mm generated using Ruthenium diffusion and UV/vis crosslinking. The Ru-dECM hydrogel exhibited stress relaxation behavior which required an extra ME to describe the relaxation pattern over the 3 required for the dECM hydrogel. Coinciding with the increasing gradient of stiffness, the collagen fiber density also increased. Furthermore, encapsulated fibroblasts re-oriented from a random alignment to 45° angle relative to the direction of the gradient stiffness that was present when the hydrogels were established with Ru-dECM, but not in dECM, after 5 d. Finally, the fibroblasts remodeled their surrounding matrix to reach their optimal conditions, regardless of the initial stiffness in their environment. Regarding mechanical changes, the fibroblast activity over the 5 d caused the disappearance of the gradient stiffness of Ru-dECM, the extension of the ME time constants (τ) both in Ru-dECM and dECM hydrogels (Figure 3D, Table 1 and Table S1) and the decrease in relaxation rate in cell encapsulated dECM gels after 5 d.

Our model provides an ideal platform for *in vitro* reconstruction of the physiological stiffness of normal skin and scars. In our model, the stiffness obtained in dECM hydrogel (8 ± 2 kPa) was comparable to the normal dermis (12 ± 4 kPa, Figure S3). In fibrotic skin the stiffness was observed to increase up to 20-fold compared to healthy skin dermis and in our Ru-dECM model we were able to achieve a 23-fold increase at the stiff end as compared to the soft end of our hydrogel [45, 46]. Recently, a series of physically/photopolymerized cross-linked hydrogels have been used to systematically investigate the effects of gradient stiffness substrates on cell behavior [47]. However, these studies primarily focused on a single natural polymer such as hyaluronic acid or synthetic hydrogels such as polyacrylic acid and their effects on cell behavior in 2D. Notably, our skin-derived gradient stiffness hydrogels and encapsulated fibroblast 3D cultures were developed to be the first system that can replicate the natural biochemical environment of cells in terms of composition, structure, and

dimensions. Furthermore, our strategy of Ru diffusion and UV/vis crosslinking can potentially be utilized to model other fibrotic tissues (e.g., pulmonary fibrosis, cirrhosis) and assess their related cellular responses, using the respective organ derived ECMs.

Ruthenium crosslinking depends on the covalent chemical crosslinking formed between tyrosines, known as di-tyrosine bonds [48]. It is noteworthy that the Ru-induced covalent bonds within the hydrogels introduced an additional Maxwell element-ME4 (which had the longest relaxation time constant), which was necessary when fitting the relaxation curve description and was accompanied by the redistributed relative importance of each ME. Typically, ME1, which is usually of the highest relative importance, can be attributed to the redistribution of the most abundant and fastest-moving free water molecules in the hydrogel. Other MEs may correspond to small molecules, cells, or types of crosslinks formed in the ECM [49]. However, compared to skin tissue, both hydrogels exhibited significantly higher total stress relaxation percentage in 50 s and a faster initial relaxation rate. This aligns with a previous study, where a dECM hydrogel derived from human lung tissue displayed a higher total relaxation than its derivative tissue [50], likely due to the complete removal of cells, reconfiguration of ECM proteins and the (partial) disruption of chemical crosslinks during decellularization.

Additionally, SEM images showed that the ECM structure comprised of randomly organized fibers both in non-crosslinked and crosslinked hydrogels. However, crosslinking had caused a decreased porosity, and simultaneously increased the fiber diameter due to an increase of the tight connections between fibrils. Moreover, the observed changes in collagen fiber density of cell-encapsulated Ru-dECM (4 h) directly correlated with the degree of crosslinking, consistent with our prior research of lung-derived dECM hydrogels in which crosslinking resulted in a denser collagen matrix with decreased fiber lengths [36]. The notable density increase of collagen fibers at the stiffer end of the Ru-dECM mirrors the highly crosslinked outcome of scar ECM *in vivo*, providing an optimal environment for studying how fibroblasts inherently respond to increases in matrix stiffness and crosslinking.

Matrix stiffness directs the morphology and migration of fibroblasts [51, 52]. Different from 2D where increased adhesion, proliferation, average cell area and

aspect ratio of fibroblasts have been observed towards the stiffer end of surfaces [25], the fibroblasts cultured in the 3D stiffness gradient only exhibited a high aspect ratio (~3.9) and an oriented arrangement (~ -45° angular orientation) after 5d while there were no significant changes in cell spreading area, cell proliferation and migration. Our data strongly suggest that the prior experience of a stiffness gradient is an essential requirement to motivate cell alignment, because no cell alignment was observed in the dECM hydrogels. This observation is consistent with studies that indicate cell morphology and orientation are influenced by the steepness (slope) of the gradient [53, 54]. Furthermore, a relatively low stiffness (≤ 120 kPa) environment is necessary for enabling cell alignment: this can be observed in Figure 5B where at day 1 the cell alignment is only observed for zones 5 and 8 with stiffnesses ≤ 120 kPa. In zone 2 alignment was only observed at day 5 when the stiffness had been reduced below 120 kPa by the cellular activities (Figure 5B).

To our knowledge we are the first to observe this stiffness gradient induced cell alignment in 3D cultures. Fibroblasts sensed the stimulation of the stiffness gradient and exerted tension on the surrounding ECM to achieve orientation. High stiffness is driving encapsulated fibroblasts to remodeling i.e. reduce stiffness. Below a threshold stiffness, fibroblasts that had previously experienced the gradient, gain the ability to align to the longitudinal (gradient) axis of the hydrogel. Since we did not observe preferred alignment of the collagen fibers the reasons for cell alignment could be related to generation of internal stresses in the hydrogel caused by cellular contractile forces. The cellular contractile force in dECM hydrogel caused shrinkage of the hydrogels at day 5 (Figure S5), akin to the contracture observed in dermal scar tissue. Ru-dECM hydrogels, on the other hand, resisted shrinking by opposing the cellular contractile forces through the Ru induced covalent bonds in their matrix network [55, 56]. Alignment of cells to 45° could possibly be interpreted as an effort by the cells to maximize the leverage of their longitudinal contractile normal stress ($\sigma_{contractile}$) on the 3D shear stresses ($\tau_{induced}$) necessary for hydrogel shrinking, which now occurs along and across the long axis of the Ru-dECM hydrogel (Figure 5C and D) [57].

The cells orientated randomly in the dECM non-covalently bonded hydrogels and these hydrogels contract because the contractile stresses applied by the cells individually to their local environment are collectively enough to overcome the

resistance to shrinkage. Therefore, there is no reason for these cells to change their orientation. However, for cells in the RuECM crosslinked hydrogel the covalent bonded matrix offered additional resistance to shrinkage thus the cells needed to align themselves in an orientation where the effect of their individual contractile forces is maximized and could challenge the resistance offered by the hydrogel.

A solid metal or ceramic object is composed of interconnected (bonded via metallic, covalent or ionic bonds) atoms or molecules, similarly a plastic material or hydrogel is composed of interconnected (through physical interactions or covalent bonds) polymers. As a consequence to external or internal stresses the solid objects deform, which is measured in terms of strain (e.g. shrinkage of dECM gels). Only, two type of stresses can exist in a solid object namely, normal (pulling/pushing) or shear (sliding) stress. The interconnections in solid objects cause the normal stresses active in one direction to transform and manifest themselves on other direction as shear stresses or *vice versa*. This phenomenon of stress transformation in 2D is visualized through the Mohr's circle [58] as depicted in Fig. 5D which shows that if normal contractile stresses pull on the hydrogel then at 45° orientation these normal stresses transform and induce a certain maximum shear stresses and this happens along and across the hydrogel if all the cells align themselves 45° to the longitudinal (gradient) hydrogel axis.

Changes in cell alignment were driven by mechano-transduction signaling in the fibroblasts. Mechanical cues from the surrounding matrix also cause fibroblasts to induce matrix remodeling and regulation of mechanical properties [7, 59]. Our results showed that fibroblast-mediated ECM remodeling is governed by the stiffness value of the cell-surrounding ECM. The Ru-crosslinking at the stiffer end of the gradient resulted in a denser collagen network structure (seen at 4 h), which, in the presence of fibroblasts, underwent specific remodeling of the cell surrounding matrix to reach the optimal conditions for the fibroblasts over an extended culture time (5 d). After 5d, the fibroblasts degraded collagen and /or re-assembled collagen fibers to induce a decrease in stiffness at the stiffest regions of Ru-dECM. In addition, the fibroblasts rearranged the random ECM matrix into dense fiber bundles over short ranges in the softest part i.e. zone 10 of Ru-dECM and whole of dECM, which is consistent with the typical basket-weave structure that exists in normal dermal tissue [26]. Interestingly, fibroblasts also modulated the viscoelasticity of dECM hydrogels by slowing down the rate

of stress relaxation both for dECM and Ru-dECM hydrogels (Table S1) accompanied by a redistribution of the relative importance of individual MEs, which we hypothesize is related to the increased collagen intermolecular forces in the hydrogel and the resulting increased plasticity.

Conclusion

In conclusion, Ruthenium diffusion followed by UV/vis crosslinking of skin-derived ECM gave rise to a stiffness gradient Ru-dECM hydrogel with a 23-fold increase in stiffness. This hydrogel provides a promising *in vitro* 3D model for elucidating fibroblast responses to stiffness gradients seen in scar transitions. The findings in this study suggest the stiffness gradient within the *in vitro* scar model directs fibroblast's alignment in regions below 120 kPa stiffness. Fibroblasts remodel the matrix within their vicinity in regions with stiffness higher than 120 kPa causing a decrease in stiffness. Overall, this study adds to understanding of how the mechanics of fibrosis affects resident fibroblasts. This model can be further extended to *in vitro* engineering of different tissues such as heart and liver and used as a platform for fibrotic disease modeling studies in different tissue systems. However, as our platform is a model it will not fully capture the complexity of *in vivo* scar formation and remodeling processes. Our platform, however, does allow to dissect the interaction between tissue fibroblasts and tissue-derived ECM as a function of a stiffness gradient. Scar tissue stiffness can vary significantly due to factors such as the age of the scar and individual healing responses. We plan to explore these aspects in future work, seeking to better understand the nuances of tissue stiffness gradients, fibroblast behavior, and scar formation in the context of wound healing and tissue engineering.

Author contributions

F.Z.: conceptualization, methodology, investigation, formal analysis, interpretation of the data and writing. M.Z., M.N., H.K., L.A.B., T.B.: investigation and methodology. J.K.B.: conceptualization, interpretation of the data, and writing. M.C.H.: conceptualization, interpretation of the data, and writing. P.K.S.: conceptualization, interpretation of the data, and writing. All authors have read, edited and agreed to the final version of the manuscript.

Declaration of Competing Interest

The authors declare no conflict of interest.

Acknowledgements

Part of the work has been performed at the UMCG Imaging and Microscopy Center (UMIC), which is sponsored by NWO-grants 175-010-2009-023. The authors thank Klaas Sjollema for the assistance with utilization of microscopes at UMIC. The authors would like to thanks China Scholarship Council and the GSMS in the University of Groningen for the financial support to FZ (Grant No. 202006240071). Nederlandse Organisatie voor Wetenschappelijk Onderzoek (NWO) Aspasia-premie subsidienummer 015.013.010 awarded to JKB.

References:

[1] J.F. Almine, S.G. Wise, A.S. Weiss, Elastin signaling in wound repair, Birth Defects Res C Embryo Today 96(3) (2012) 248-57.

[2] H. Sorg, D.J. Tilkorn, S. Hager, J. Hauser, U. Mirastschijski, Skin Wound Healing: An Update on the Current Knowledge and Concepts, Eur Surg Res 58(1-2) (2017) 81-94.

[3] A.F. Spielman, M.F. Griffin, J. Parker, A.C. Cotterell, D.C. Wan, M.T. Longaker, Beyond the Scar: A Basic Science Review of Wound Remodeling, Adv Wound Care (New Rochelle) 12(2) (2023) 57-67.

[4] J.M. Reinke, H. Sorg, Wound repair and regeneration, Eur Surg Res 49(1) (2012) 35-43.

[5] H.E. Talbott, S. Mascharak, M. Griffin, D.C. Wan, M.T. Longaker, Wound healing, fibroblast heterogeneity, and fibrosis, Cell Stem Cell 29(8) (2022) 1161-1180.

[6] L. Moretti, J. Stalfort, T.H. Barker, D. Abebayehu, The interplay of fibroblasts, the extracellular matrix, and inflammation in scar formation, J Biol Chem 298(2) (2022) 101530.

[7] B. Li, J.H. Wang, Fibroblasts and myofibroblasts in wound healing: force generation and measurement, J Tissue Viability 20(4) (2011) 108-20.

[8] L. Van De Water, S. Varney, J.J. Tomasek, Mechanoregulation of the Myofibroblast in Wound Contraction, Scarring, and Fibrosis: Opportunities for New Therapeutic Intervention, Adv Wound Care (New Rochelle) 2(4) (2013) 122-141.

[9] A.L. Rippa, E.P. Kalabusheva, E.A. Vorotelyak, Regeneration of Dermis: Scarring and Cells Involved, Cells 8(6) (2019).

[10] D.G. Janson, G. Saintigny, A. van Adrichem, C. Mahe, A. El Ghalbzouri, Different gene expression patterns in human papillary and reticular fibroblasts, J Invest Dermatol 132(11) (2012) 2565-72.

[11] A. Shpichka, D. Butnaru, E.A. Bezrukov, R.B. Sukhanov, A. Atala, V. Burdukovskii, Y. Zhang, P. Timashev, Skin tissue regeneration for burn injury, Stem Cell Res Ther 10(1) (2019) 94.

[12] J.J. Tomasek, G. Gabbiani, B. Hinz, C. Chaponnier, R.A. Brown, Myofibroblasts and mechano-regulation of connective tissue remodelling, Nat Rev Mol Cell Biol 3(5) (2002) 349-63.

[13] J. Godwin, D. Kuraitis, N. Rosenthal, Extracellular matrix considerations for scar-free repair and regeneration: insights from regenerative diversity among vertebrates, Int J Biochem Cell Biol 56 (2014) 47-55.

[14] T.R. Cox, J.T. Erler, Remodeling and homeostasis of the extracellular matrix: implications for fibrotic diseases and cancer, Dis Model Mech 4(2) (2011) 165-78.

[15] M. Xue, C.J. Jackson, Extracellular Matrix Reorganization During Wound Healing and Its Impact on Abnormal Scarring, Adv Wound Care (New Rochelle) 4(3) (2015) 119-136.

[16] S. Mueller, G. Millonig, L. Sarovska, S. Friedrich, F.M. Reimann, M. Pritsch, S. Eisele, F. Stickel, T. Longerich, P. Schirmacher, H.K. Seitz, Increased liver stiffness in alcoholic liver disease: differentiating fibrosis from steatohepatitis, World J Gastroenterol

16(8) (2010) 966-72.

[17] T.J.H. Narasimham L. Parinandi, Cardiovascular Signaling in Health and Disease, Cham (CH): Springer, 2022.

[18] J.K. Burgess, M.C. Harmsen, Chronic lung diseases: entangled in extracellular matrix, Eur Respir Rev 31(163) (2022).

[19] S. Rayego-Mateos, S. Campillo, R.R. Rodrigues-Diez, A. Tejera-Munoz, L. Marquez-Exposito, R. Goldschmeding, D. Rodriguez-Puyol, L. Calleros, M. Ruiz-Ortega, Interplay between extracellular matrix components and cellular and molecular mechanisms in kidney fibrosis, Clin Sci (Lond) 135(16) (2021) 1999-2029.

[20] B.R. Seo, X. Chen, L. Ling, Y.H. Song, A.A. Shimpi, S. Choi, J. Gonzalez, J. Sapudom, K. Wang, R.C. Andresen Eguiluz, D. Gourdon, V.B. Shenoy, C. Fischbach, Collagen microarchitecture mechanically controls myofibroblast differentiation, Proc Natl Acad Sci U S A 117(21) (2020) 11387-11398.

[21] T. Yeung, P.C. Georges, L.A. Flanagan, B. Marg, M. Ortiz, M. Funaki, N. Zahir, W. Ming, V. Weaver, P.A. Janmey, Effects of substrate stiffness on cell morphology, cytoskeletal structure, and adhesion, Cell Motil Cytoskeleton 60(1) (2005) 24-34.

[22] A. Jagiello, U. Castillo, E. Botvinick, Cell mediated remodeling of stiffness matched collagen and fibrin scaffolds, Sci Rep 12(1) (2022) 11736.

[23] A. Wahlsten, D. Rutsche, M. Nanni, C. Giampietro, T. Biedermann, E. Reichmann, E. Mazza, Mechanical stimulation induces rapid fibroblast proliferation and accelerates the early maturation of human skin substitutes, Biomaterials 273 (2021) 120779.

[24] F. Feng, M. Liu, L. Pan, J. Wu, C. Wang, L. Yang, W. Liu, W. Xu, M. Lei, Biomechanical Regulatory Factors and Therapeutic Targets in Keloid Fibrosis, Front Pharmacol 13 (2022) 906212.

[25] I. Hopp, A. Michelmore, L.E. Smith, D.E. Robinson, A. Bachhuka, A. Mierczynska, K. Vasilev, The influence of substrate stiffness gradients on primary human dermal fibroblasts, Biomaterials 34(21) (2013) 5070-7.

[26] R.A. Brown, In the beginning there were soft collagen-cell gels: towards better 3D connective tissue models?, Exp Cell Res 319(16) (2013) 2460-9.

[27] R.I. RI, R. do Amaral, R.L. Reis, A.P. Marques, C.M. Murphy, F.J. O'Brien, 3D-Printed Gelatin Methacrylate Scaffolds with Controlled Architecture and Stiffness Modulate the Fibroblast Phenotype towards Dermal Regeneration, Polymers (Basel) 13(15) (2021).

[28] C. Branco da Cunha, D.D. Klumpers, W.A. Li, S.T. Koshy, J.C. Weaver, O. Chaudhuri, P.L. Granja, D.J. Mooney, Influence of the stiffness of three-dimensional alginate/collagen-I interpenetrating networks on fibroblast biology, Biomaterials 35(32) (2014) 8927-36.

[29] Z. Zhao, G. Huang, Y. He, X. Zuo, W. Han, H. Li, Extracellular matrix stiffness regulates fibroblast differentiation by influencing DNA methyltransferase 1 expression through microtubule polymerization, bioRxiv 10 (2022) 1101.

[30] N. Migulina, R.H.J. de Hilster, S. Bartel, R.H.J. Vedder, M. van den Berge, A. Nagelkerke, W. Timens, M.C. Harmsen, M.N. Hylkema, C.A. Brandsma, J.K. Burgess, 3-D culture of human lung fibroblasts decreases proliferative and increases extracellular matrix remodeling genes, Am J Physiol Cell Physiol 326(1) (2024) C177-C193.

[31] S. Ishihara, H. Kurosawa, H. Haga, Stiffness-Modulation of Collagen Gels by Genipin-Crosslinking for Cell Culture, Gels 9(2) (2023).

[32] Y. Ren, H. Zhang, Y. Wang, B. Du, J. Yang, L. Liu, Q. Zhang, Hyaluronic Acid Hydrogel with Adjustable Stiffness for Mesenchymal Stem Cell 3D Culture via Related Molecular Mechanisms to Maintain Stemness and Induce Cartilage Differentiation, ACS Appl Bio Mater 4(3) (2021) 2601-2613.

[33] Z. Shariatinia, A.M. Jalali, Chitosan-based hydrogels: Preparation, properties and applications, Int J Biol Macromol 115 (2018) 194-220.

[34] Y. Liu, J. Mao, Z. Guo, Y. Hu, S. Wang, Polyvinyl alcohol/carboxymethyl chitosan hydrogel loaded with silver nanoparticles exhibited antibacterial and self-healing properties, Int J Biol Macromol 220 (2022) 211-222.

[35] Y. Liang, Y. Shen, X. Sun, H. Liang, Preparation of stretchable and self-healable dual ionically cross-linked hydrogel based on chitosan/polyacrylic acid with anti-freezing property for multi-model flexible sensing and detection, Int J Biol Macromol 193(Pt A) (2021) 629-637.

[36] M. Nizamoglu, R.H.J. de Hilster, F. Zhao, P.K. Sharma, T. Borghuis, M.C. Harmsen, J.K. Burgess, An in vitro model of fibrosis using crosslinked native extracellular matrix-derived hydrogels to modulate biomechanics without changing composition, Acta Biomater 147 (2022) 50-62.

[37] F.D. Martinez-Garcia, R.H.J. de Hilster, P.K. Sharma, T. Borghuis, M.N. Hylkema, J.K. Burgess, M.C. Harmsen, Architecture and Composition Dictate Viscoelastic Properties of Organ-Derived Extracellular Matrix Hydrogels, Polymers (Basel) 13(18) (2021).

[38] M. Zhang, V.E. Getova, F.D. Martinez-Garcia, T. Borghuis, J.K. Burgess, M.C. Harmsen, From Macro to Micro: Comparison of Imaging Techniques to Detect Vascular Network Formation in Left Ventricle Decellularized Extracellular Matrix Hydrogels, Gels 8(11) (2022).

[39] Z. Puspoki, M. Storath, D. Sage, M. Unser, Transforms and Operators for Directional Bioimage Analysis: A Survey, Adv Anat Embryol Cell Biol 219 (2016) 69-93.

[40] I.Z.W. Chan, M. Stevens, P.A. Todd, D. Silvestro, pat-geom: A software package for the analysis of animal patterns, Methods in Ecology and Evolution 10(4) (2019) 591-600.

[41] N.A. Hotaling, K. Bharti, H. Kriel, C.G. Simon, Jr., DiameterJ: A validated open source nanofiber diameter measurement tool, Biomaterials 61 (2015) 327-38.

[42] J. Schindelin, I. Arganda-Carreras, E. Frise, V. Kaynig, M. Longair, T. Pietzsch, S. Preibisch, C. Rueden, S. Saalfeld, B. Schmid, J.Y. Tinevez, D.J. White, V. Hartenstein, K. Eliceiri, P. Tomancak, A. Cardona, Fiji: an open-source platform for biological-image analysis, Nat Methods 9(7) (2012) 676-82.

[43] C. McQuin, A. Goodman, V. Chernyshev, L. Kamentsky, B.A. Cimini, K.W. Karhohs, M. Doan, L. Ding, S.M. Rafelski, D. Thirstrup, W. Wiegraebe, S. Singh, T. Becker, J.C. Caicedo, A.E. Carpenter, CellProfiler 3.0: Next-generation image processing for biology, PLoS Biol 16(7) (2018) e2005970.

[44] C.J. Morgan, Use of proper statistical techniques for research studies with small samples, Am J Physiol Lung Cell Mol Physiol 313(5) (2017) L873-L877.

[45] C. Huang, L. Liu, Z. You, B. Wang, Y. Du, R. Ogawa, Keloid progression: a stiffness

gap hypothesis, Int Wound J 14(5) (2017) 764-771.

[46] J. A. Clark, J. C. Y. Cheng, K. S. Leung, Mechanical properties of normal skin and hypertrophic scars, Burns 22 (6) (1996) 443–446.

[47] S.R. Polio, A.N. Kundu, C.E. Dougan, N.P. Birch, D.E. Aurian-Blajeni, J.D. Schiffman, A.J. Crosby, S.R. Peyton, Cross-platform mechanical characterization of lung tissue, PLoS One 13(10) (2018) e0204765.

[48] H. Kim, B. Kang, X. Cui, S.H. Lee, K. Lee, D.W. Cho, W. Hwang, T.B.F. Woodfield, K.S. Lim, J. Jang, Light-Activated Decellularized Extracellular Matrix-Based Bioinks for Volumetric Tissue Analogs at the Centimeter Scale, Advanced Functional Materials 31(32) (2021).

[49] B.W. Peterson, H.C. van der Mei, J. Sjollema, H.J. Busscher, P.K. Sharma, A distinguishable role of eDNA in the viscoelastic relaxation of biofilms, mBio 4(5) (2013) e00497-13.

[50] R.H.J. de Hilster, P.K. Sharma, M.R. Jonker, E.S. White, E.A. Gercama, M. Roobeek, W. Timens, M.C. Harmsen, M.N. Hylkema, J.K. Burgess, Human lung extracellular matrix hydrogels resemble the stiffness and viscoelasticity of native lung tissue, Am J Physiol Lung Cell Mol Physiol 318(4) (2020) L698-L704.

[51] S. Asano, S. Ito, K. Takahashi, K. Furuya, M. Kondo, M. Sokabe, Y. Hasegawa, Matrix stiffness regulates migration of human lung fibroblasts, Physiol Rep 5(9) (2017).

[52] K.E.C. Blokland, M. Nizamoglu, H. Habibie, T. Borghuis, M. Schuliga, B.N. Melgert, D.A. Knight, C.A. Brandsma, S.D. Pouwels, J.K. Burgess, Substrate stiffness engineered to replicate disease conditions influence senescence and fibrotic responses in primary lung fibroblasts, Front Pharmacol 13 (2022) 989169.

[53] C. Kayal, E. Moeendarbary, R.J. Shipley, J.B. Phillips, Mechanical Response of Neural Cells to Physiologically Relevant Stiffness Gradients, Adv Healthc Mater 9(8) (2020) e1901036.

[54] D. Joaquin, M. Grigola, G. Kwon, C. Blasius, Y. Han, D. Perlitz, J. Jiang, Y. Ziegler, A. Nardulli, K.J. Hsia, Cell migration and organization in three-dimensional in vitro culture driven by stiffness gradient, Biotechnol Bioeng 113(11) (2016) 2496-506.

[55] B.M. Baker, B. Trappmann, W.Y. Wang, M.S. Sakar, I.L. Kim, V.B. Shenoy, J.A. Burdick, C.S. Chen, Cell-mediated fibre recruitment drives extracellular matrix mechanosensing in engineered fibrillar microenvironments, Nat Mater 14(12) (2015) 1262-8.

[56] A. Lavrentieva, T. Fleischhammer, A. Enders, H. Pirmahboub, J. Bahnemann, I. Pepelanova, Fabrication of Stiffness Gradients of GelMA Hydrogels Using a 3D Printed Micromixer, Macromol Biosci 20(7) (2020) e2000107.

[57] R.C. Hibbeler, Engineering Mechanics: Statics, SI Units, Pearson Education Limited, London, UK, 2022.

[58] F. P. Beer, E. R. Jr., J. T. DeWolf, D. F. Mazurek, Mechanics of Materials-Seventh Edition, chapter 7.2: Mohr's Circle for Plane Stress, McGraw Hill, 2014, 492-502.

[59] A.K. Schroer, W.D. Merryman, Mechanobiology of myofibroblast adhesion in fibrotic cardiac disease, J Cell Sci 128(10) (2015) 1865-75.

Supplementary Materials:

Table S1. Extension on the relaxation time constants for Maxwell elements for Ru-dECM and dECM hydrogels after 5 days of fibroblast activity

	dECM			Ru-dECM			
	τ_1	τ_2	τ_3	τ_1	τ_2	τ_3	τ_4
4h	0.3	2.2	11.7	0.2	1.3	6.8	73.9
5d	0.6	9.1	45.2	0.3	2.6	52.9	141.5
Folds Prolongation	2	4.1	3.8	1.5	2	7.7	1.9

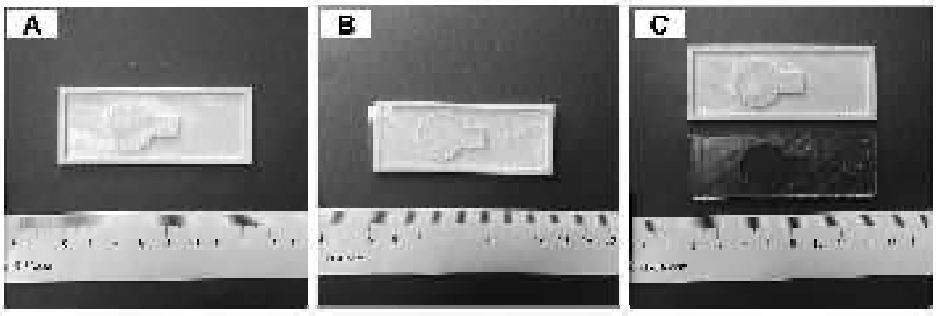

Figure S1. Processing to achieve polydimethylsiloxane (PDMS) back-mold. A) 3D printing polylactic acid (PLA) front-mold actual picture. Method: Firstly, computer 3D modeling software Solidworks was used to design modeling engineering drawing. The drawing was then printed using PLA material by an Ultimaker S5 desktop printer. The printer prints at 30mm/s, using a layer height of 0.2mm and an infill setting of 20%. After printing is completed, the surface and edges of the mold are sanded to make the surface flat and smooth, which ensures a tight fit between the PDMS subsequently filled into it and the covered microscope Slide; B) The PDMS back-mold formed in PLA front-mold post-mold; C) The PDMS back-mold separated from the PLA front-mold.

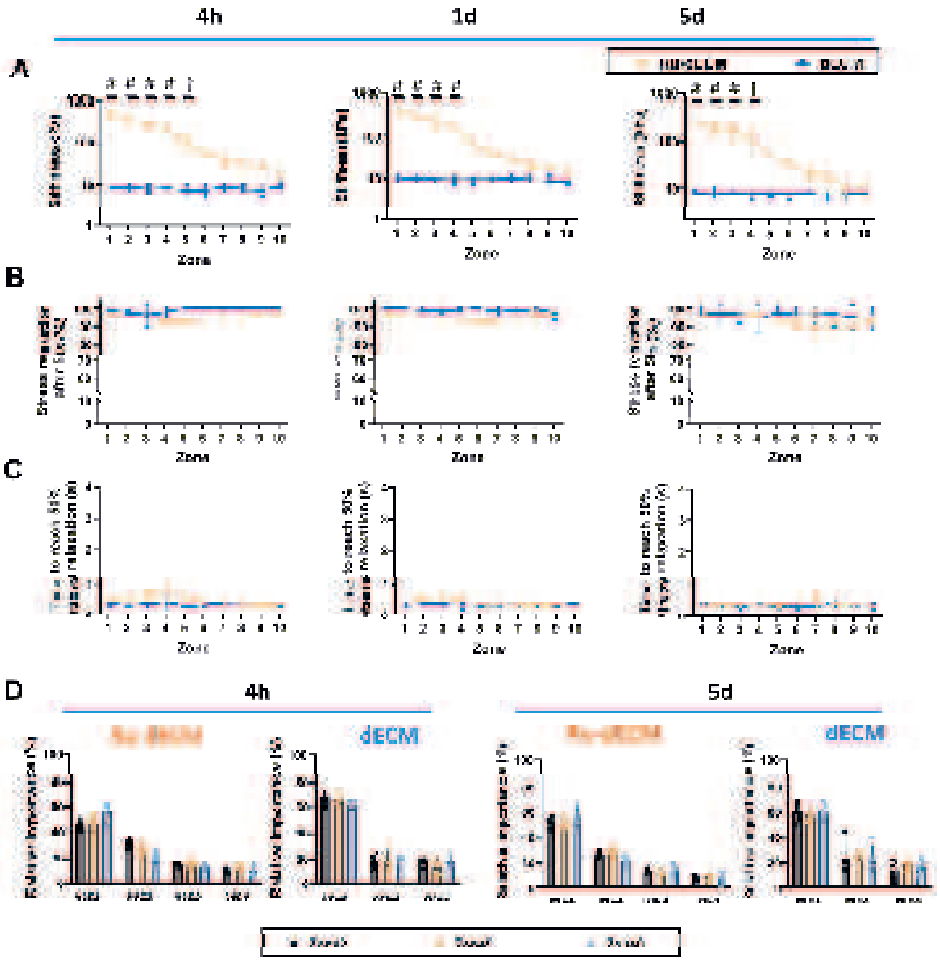

Figure S2. Mechanical properties of the Ru-dECM and dECM hydrogels without cells at 4h, 1d and 5d. A) The stiffness of Ru-dECM and dECM hydrogels. B) Total stress relaxation of the compressive force applied at 20% deformation over 50 s. C) Time taken to reach 50% stress relaxation. D) Analysis of the stress relaxation behavior through the generalized Maxwell model system. The relaxation profiles of both types of hydrogels over 50 s period was mathematically modeled using a Maxwell model system and the contributions (relative importance Ri) of each Maxwell element to the total relaxation were determined. For panel A, B and C, each dot represents the mean ± standard deviation generated from test on five independent hydrogels (n=5). For panel D, each dot represents the measurement from each of five independent hydrogels (n=5). Statistical significance

was analyzed by two-way ANOVA with post hoc testing comparing each zone of Ru-dECM hydrogels with the corresponding zone of dECM hydrogels. (*, $p < 0.05$; ‡, $p < 0.01$; †, $p < 0.001$; #, $p < 0.0001$.)

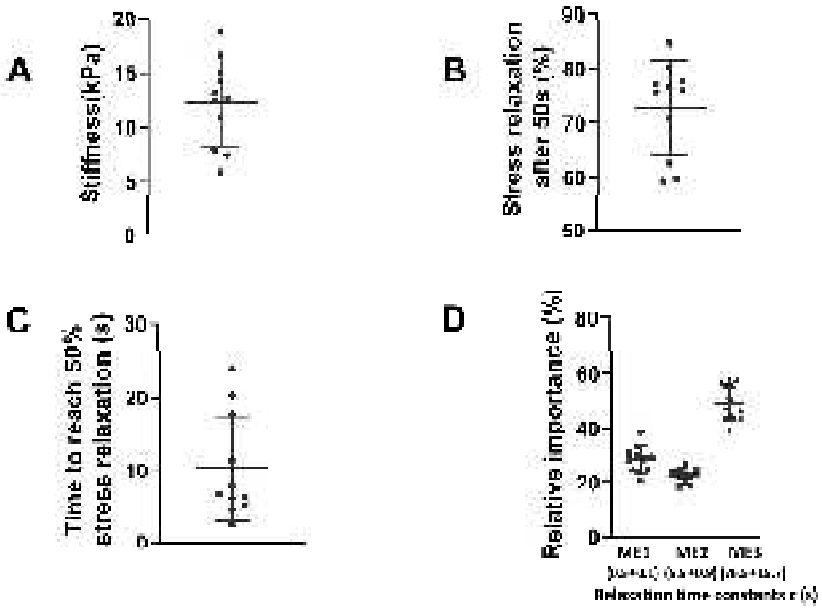

Figure S3. Mechanical properties of the normal human abdominal skin. A) The stiffness of the normal abdominal skin tissue. B) Total stress relaxation of the compressive force applied at 20% deformation over 50 s. C) Time taken to reach 50% stress relaxation. D) Analysis of the stress relaxation behavior through the generalized Maxwell model system. The relaxation profiles of the skin over 50 s period was mathematically modelled using a Maxwell model system and the relaxation time constants (τ) and the contribution (relative importance Ri) of each Maxwell element to the total relaxation were determined. The data are from eleven independent experiments and each dot represents a measurement (n=11).

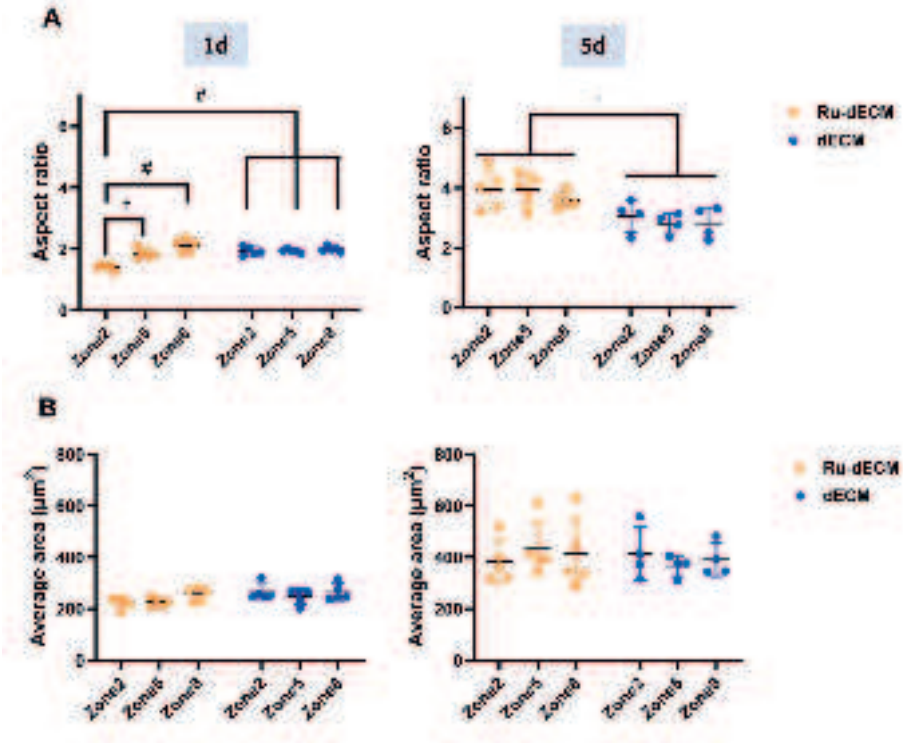

Figure S4. Cell morphology analysis based on Calcein AM staining of living HDFn fibroblasts encapsulated in Ru-dECM and dECM hydrogels at 1 d and 5 d. A) The aspect ratio of cells was calculated based on plugin PAT-GEOM in Fiji. B) Average area of HDFn fibroblasts was determined with Fiji. The data represents the mean ± standard deviation generated from measurement on five independent hydrogels (n=5). Statistical significance was analyzed by one-way ANOVA (*, $p < 0.05$; ‡, $p < 0.01$; †, $p < 0.001$; #, $p < 0.0001$).

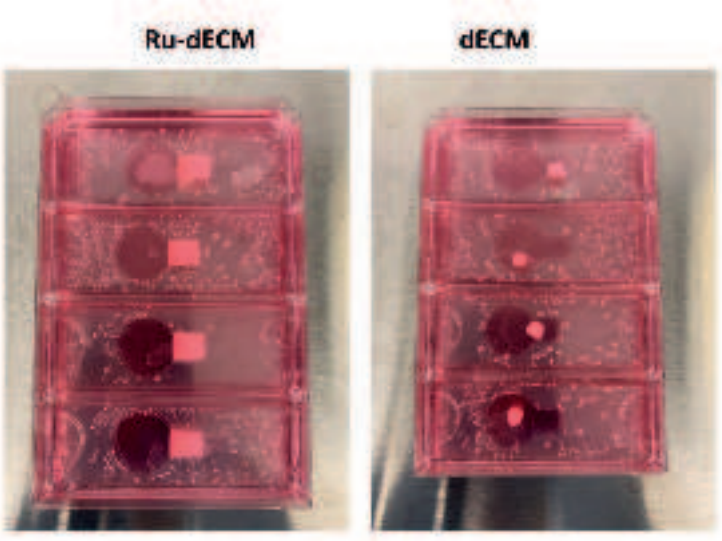

Figure S5. Shape of hydrogels of Ru-dECM and dECM at 5d.

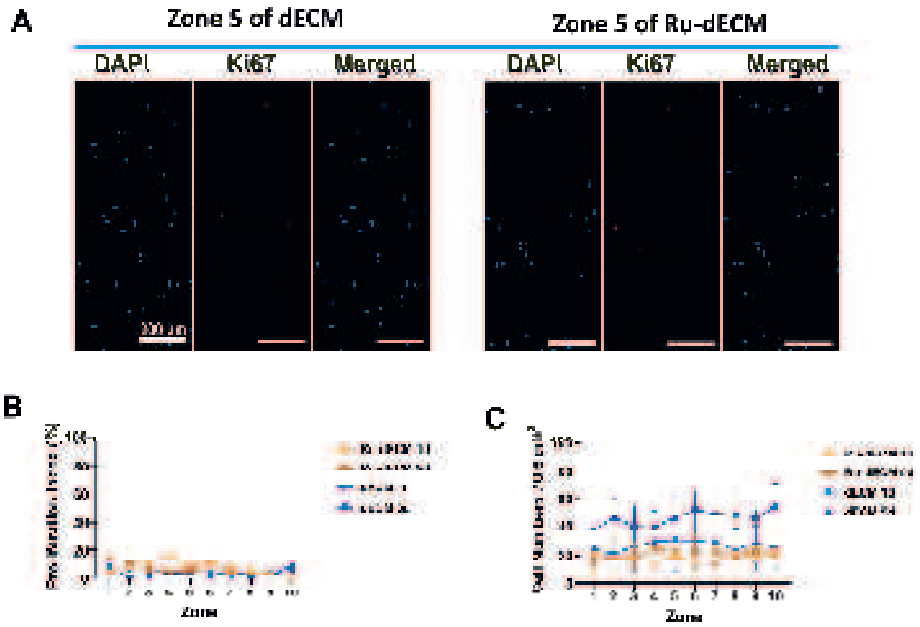

Figure S6. Proliferation index in HDFn fibroblast based on Ki67 positive cells in Ru-ECM and dECM hydrogels after 1d and 5d. A) Representative fluorescence images of Ki67 staining of Ru-dECM and dECM hydrogel slices at 1 day (cell nuclei-blue (DAPI) and Ki67-green (Ki67)). Scale bars: 200 μm. B) The proliferation index in HDFn--

Percentage of Ki67 positive cells. C) Nuclei numbers in 0.6 cm^2. Each dot represents as the mean ± standard deviation generated from measurement on five independent hydrogels (n=5). Statistical significance was analyzed by two-way ANOVA with post hoc testing comparing each zone of Ru-dECM hydrogels with the corresponding zone of dECM hydrogels. (ns or unmarked, not significant)

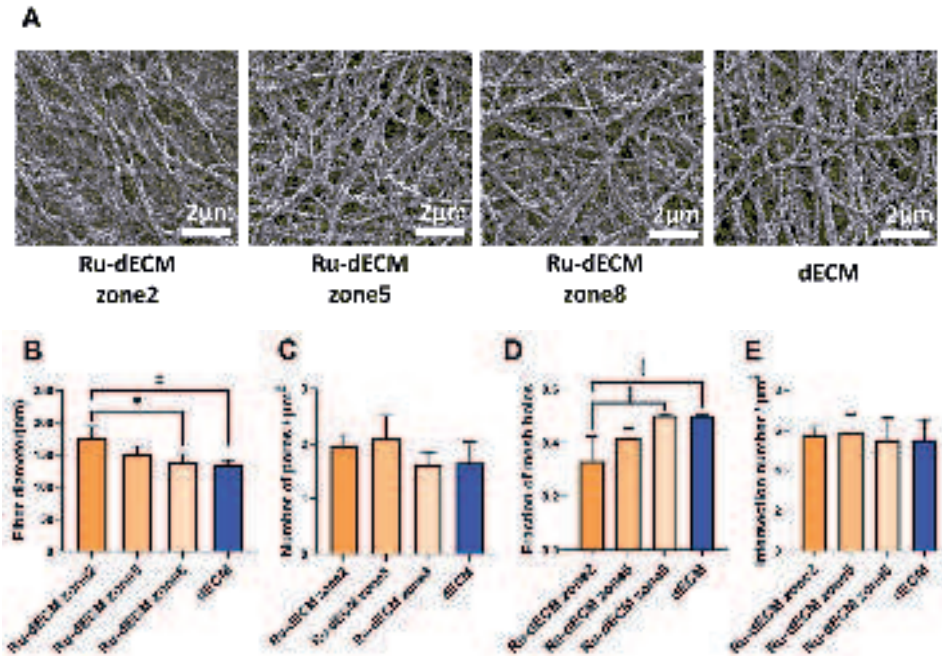

Figure S7. Ultrastructure of Ru-dECM at different positions and dECM hydrogels. A) Representative images of ECM fibers in Ru-dECM hydrogels at three different positions and dECM hydrogels according to scanning electron microscopy (SEM). Scale bars: 2 μm. Using the DiameterJ Plugin in Fiji the images were analyzed for B) Mean fiber diameter (nm). C) Number of pores per μm^2. D) Fraction of mesh holes which was defined as the pixels of total holes divided by the pixels of total image size. E) Intersection numbers per μm^2. The data were generated from three independent experiments for each sample (n=3). Statistical significance was analyzed by one-way ANOVA. ((*, $p < 0.05$; ‡, $p < 0.01$; †, $p < 0.001$; #, $p < 0.0001$)

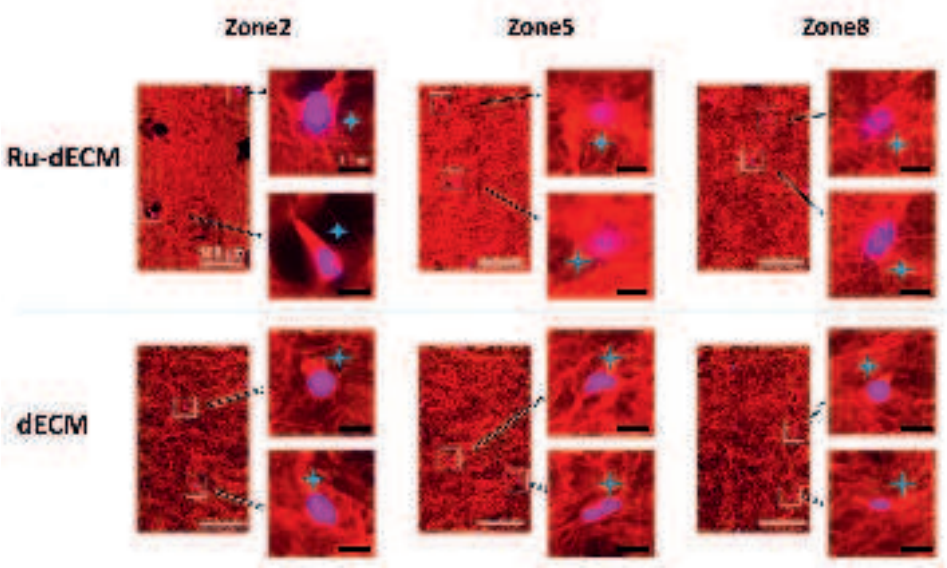

Figure S8. Enlarged micrographs of picrosirius red staining on Ru-dECM and dECM hydrogel sections. Representative images of picrosirius red staining on Ru-dECM and dECM hydrogel sections after 5d. Blue stars represent the ECM surrounding cells. The morphological changes of ECM architecture around cell nuclei can be observed in the photomicrographs. Scale bars: 100 μm.

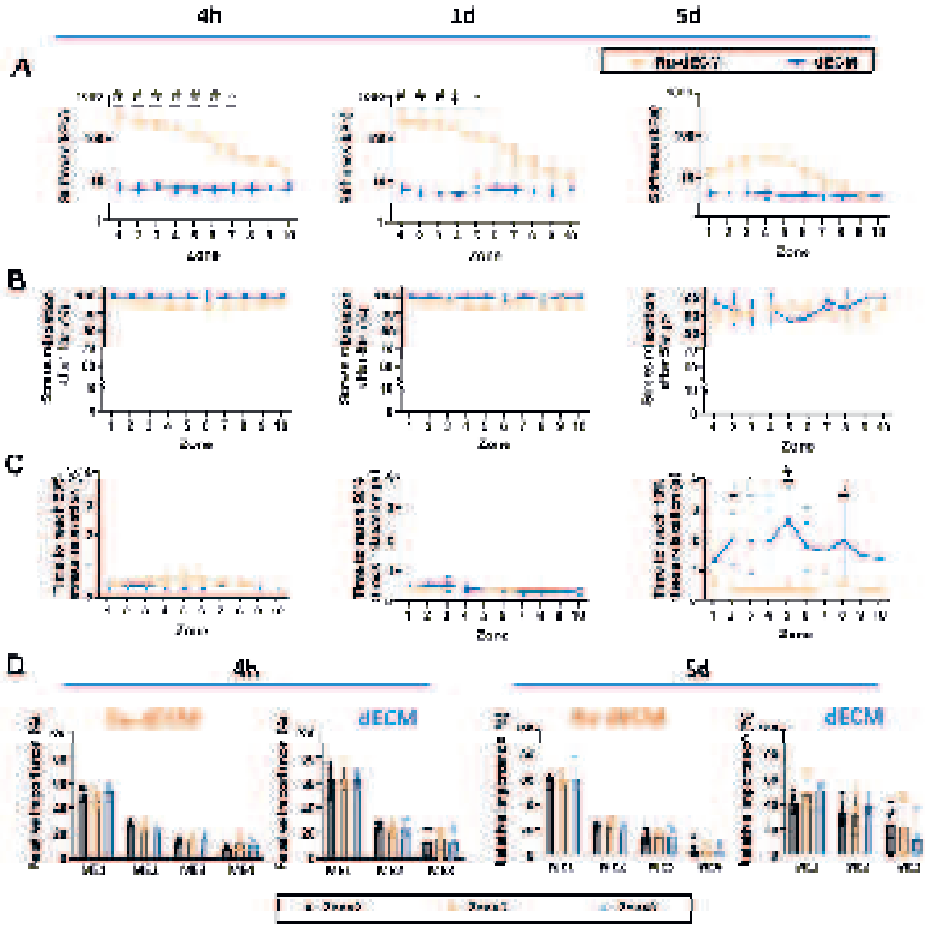

Figure S9. Mechanical properties of the HDFn cells cultured hydrogels of Ru-dECM and dECM at 4h, 1d and 5d. A) The stiffness of Ru-dECM and dECM hydrogels. B) Total stress relaxation of the compressive force applied at 20% deformation over 50 s. C) Time taken to reach 50% stress relaxation. D) Analysis of the stress relaxation behavior through the generalized Maxwell model system. The relaxation profiles of the both types of hydrogels with encapsulated cells over 50 s period was mathematically modelled using a Maxwell model system and the contribution (relative importance Ri) of each Maxwell element to the total relaxation were determined. Each dot is represented as the mean ± SD of five independent measurements (n=5). Statistical significance was analyzed by two-way ANOVA to compare each zone of Ru-dECM hydrogels with the corresponding zone of dECM hydrogels. (ns or unmarked, not significant; ∗, $p < 0.05$; ‡, $p < 0.01$; †, $p < 0.001$; #, $p < 0.0001$.

Chapter 7

Piezo1 regulates remodeling of skin-derived extracellular matrix by embedded umbilical cord mesenchymal stem cells in a stiffness dependent fashion

Fenghua Zhao[a,b], Theo Borghuis[b], Xue Zhang[b], Linda A. Brouwer[b], Janette K. Burgess[b,c,#], Prashant K. Sharma[a,#], Martin C. Harmsen[b,c,#]

a University of Groningen, University Medical Centre Groningen, Department of Biomaterials and Biomedical Technology-FB40, A. Deusinglaan 1, 9713 AV Groningen, The Netherlands

b University of Groningen, University Medical Centre Groningen, Department of Pathology and Medical Biology, Hanzeplein 1 (EA11), 9713 GZ Groningen, The Netherlands

c University of Groningen, University Medical Centre Groningen, Groningen Research Institute for Asthma and COPD (GRIAC), Hanzeplein 1 (EA11), 9713 AV Groningen, The Netherlands

[#] These authors contributed equally

This chapter is a manuscript in preparation.

Chapter 7

Abstract: Mechanotransduction, the process by which cells sense and respond to mechanical cues, is central to cellular behavior and matrix remodeling. Human mesenchymal stromal cells (MSCs), in particular umbilical cord-derived MSCs (UC-MSCs), have potential to facilitate tissue repair, however, how UC-MSCs sense and respond to changes in ECM stiffness, through mechanotransduction pathways, is not established. Using ruthenium-catalyzed photo-crosslinking, we engineered skin-derived extracellular matrix (ECM) hydrogels with tuned stiffnesses (1.2–17.7 kPa) while maintaining uniform, rapid stress relaxation (>83% within 100 s). This study examined the stiffness-dependent responses of UC-MSCs within these hydrogels and investigated the regulatory role of Piezo1 in these processes.

UC-MSC behavior was highly dependent on hydrogel stiffness. In soft hydrogels (1.2 kPa), cells exhibited little mechanosensing downstream effects, leading to matrix contraction and thus volume-driven stiffening without hole formation. In medium-stiffness hydrogels (3.4 kPa), cells adopted a spindle-shape and maintained ECM organization without hole formation. In stiff hydrogels (17.7 kPa), cells remained more rounded and promoted ECM degradation and localized hole formation, leading to a reduction in stiffness. Hydrogel volume-normalized analyses confirmed that stiffness changes in soft hydrogels were largely due to contraction, while in high stiffness hydrogels, they resulted from collagen degradation and/ or reorganization.

Piezo1 inhibition disrupted these stiffness-dependent remodeling processes, reducing contraction in soft hydrogels and attenuating ECM degradation in stiff hydrogels. pFAK expression increased with hydrogel stiffness but was significantly reduced by Piezo1 inhibition. Piezo1 inhibition did not affect stiffness-dependent expression of MMP2 and MMP14, suggesting that distinct mechanotransduction pathways may be involved. These results highlight Piezo1's role in stiffness-mediated ECM remodeling in UC-MSCs. While Piezo1 inhibition reduced ECM degradation in stiff gels, its potential as a therapeutic target for fibrosis modulation remains unclear.

1. Introduction

The extracellular matrix (ECM) provides mechanical and biochemical cues that profoundly influence cellular behavior, including morphology, differentiation, and function [1, 2]. Through a process known as mechanotransduction, cells sense and respond to these mechanical signals, often reshaping the ECM in turn. This dynamic interplay is crucial for maintaining tissue homeostasis and plays a central role in both physiological and pathological processes.

Mesenchymal cells, such as fibroblasts and mesenchymal stromal cells (MSCs), are potent ECM remodelers. Our previous studies have demonstrated that matrix stiffness regulates the expression of key ECM remodeling enzymes, such as matrix metalloproteinases (MMPs), in adipose-derived stem cells and fibroblasts. These MMPs facilitate ECM degradation and in so doing enable cells to generate an optimal mechanical environment [3-5]. Human MSCs, in particular umbilical cord-derived MSCs (UC-MSCs), have gained attention for their potential to facilitate injury repair and reduce, if not reverse, fibrosis through their secretory profile and ECM remodeling activities. For example, UC-MSCs attenuated liver fibrosis in a carbon tetrachloride (CCl_4)-induced rat model by inhibiting hepatic stellate cell activation and reducing excessive ECM deposition [6]. The underlying mechanisms by which UC-MSCs sense and respond to changes in ECM stiffness, through mechanotransduction pathways, remain incompletely understood.

Mechanotransduction involves several pathways that govern cellular responses to mechanical cues. Integrins, transmembrane receptors that mediate cell-ECM adhesion, are part of focal adhesions and recruit signaling kinases such as focal adhesion kinase (FAK). Activated (phospho-P) FAK activates downstream mediators, such as RhoA-ROCK (Ras homolog family member A (RhoA)- Rho-associated protein kinase (ROCK)), which regulates cytoskeletal dynamics by enhancing actomyosin contractility and tension. In addition, P-FAK interacts with the Hippo pathway, where YAP/TAZ (Yes-associated protein (YAP)/transcriptional coactivator with PDZ-binding motif (TAZ)) are activated and translocate to the nucleus to regulate mechanosensitive gene expression and control cell proliferation and differentiation. In addition to integrins, Piezo1, a large mechanically gated ion channel, mediates calcium influx in response to mechanical forces such as stretch, shear stress, and ECM stiffness.

A main pathological feature of fibrosis is excessive ECM deposition and increased matrix stiffness due to excessive crosslinking of collagens. Recent findings suggest that Piezo1 integrates mechanical signals to drive cellular responses and acts as a mechanosensitive regulator of fibrosis progression [7]. In a unilateral ureteral obstruction (UUO)-induced renal fibrosis model, increased ECM synthesis and stiffness activated Piezo1 in renal mesangial cells, and this was also seen in fibrotic human kidney tubules, including proximal tubular cells and collecting duct principal cells [8, 9]. Additionally, in vitro stimulation of Piezo1 using Yoda1 (a Piezo agonist) in human proximal tubular cells induced calcium influx, leading to activation of the calcium-dependent protease calpain-2, cleavage of talin-1, upregulation of integrin β1, and initiation of profibrotic responses [9]. Similarly, in both human and murine fibrotic skin, Piezo1 was found to be upregulated. Knockdown of Piezo1 in dermal fibroblasts attenuated fibrosis by disrupting a pro-inflammatory signaling cascade involving Wnt2/Wnt11 and CCL24 [10]. In osteoarthritic cartilage and chondrocytes under shear stress, Piezo1 was elevated and triggered calcium influx. Knockdown of Piezo1 inhibited YAP nuclear translocation and downregulated matrix-degrading enzymes MMP13 and ADAMTS5, ultimately reducing matrix degradation [11]. Together, these studies suggest that Piezo1 serves as an integrator of mechanical signals and regulation of fibrotic processes. Given the importance of mechanotransduction in regulating ECM remodeling and the therapeutic relevance of UC-MSCs in fibrosis, investigating how Piezo1 and related pathways influence UC-MSC responses to matrix stiffness may reveal important mechanisms underlying their regenerative function. This study investigated how matrix stiffness modulates UC-MSC phenotypes and ECM remodeling using 3D ECM hydrogels replicating the mechanical properties of healthy skin and fibrotic scars. By embedding UC-MSCs in tunable stiffness hydrogels, we explored the cells' viability, morphology, and remodeling capabilities. Focusing on key mechanosensors and pathways such as Piezo1, pFAK, and YAP, we aimed to uncover the roles of these components in stiffness-mediated responses. This research seeks to provide critical insights into the interplay between UC-MSCs and their mechanical microenvironment, advancing our understanding of ECM remodeling in health and disease.

2. Materials and Methods Cell culture

2.1. Cell isolation and culturing

Umbilical cord mesenchymal cells (UC-MSCs) were isolated from umbilical cord tissue that had been collected after birth and stored at 4°C for up to four days in umbilical cord buffer (40 mM potassium chloride, 0.14 M sodium chloride, 11 mM D-glucose, and 10 mM HEPES in sterile water, adjusted to pH 7.4 with 10 M HCl). The umbilical cords were obtained from anonymous donors in the Department of Gynecology who had provided informed consent for the use of their cord tissue (UMCG, Groningen, Netherlands). UC-MSCs were isolated by an experienced technician at the Endothelial Cell Facility, UMCG. Only umbilical cords that were at least 30 cm in length and free from significant twisting or large holes were selected and cut into 4-5 cm segments. These segments were washed twice with umbilical cord buffer before being carefully opened to expose the Wharton's Jelly, which was then dissected into small pieces (2-5 mm). These pieces were placed into wells of a 6-well plate, with 3-4 pieces per well. To promote tissue adhesion, the pieces were air-dried for 15 minutes, after which 2 mL of complete UC-MSC medium was added. The complete medium was prepared by adding 10% fetal bovine serum (FBS, Gibco, USA) that had been heat-inactivated at 56°C for 1 hour, 1% L-glutamine, and 1% penicillin/streptomycin (15140-122, Gibco) to DMEM medium containing 5mM glucose (BE12-707F, Lonza). The cultures were then incubated in a 5% CO_2 atmosphere at 37°C with minimal disturbance. The medium was refreshed every 3 days. Cells were cultured until they reached 70-100% confluence, at which point the tissue pieces were removed. The cells were then transferred to T25 flasks via enzymatic dissociation with 0.25% trypsin-EDTA (Gibco, USA), followed by neutralization with complete culture medium for further expansion. All cultures were routinely tested for mycoplasma contamination using a PCR screening and confirmed to be mycoplasma-free before use in experiments. After subculturing, P4 generation cells were used for flow cytometric analysis and differentiation potential evaluation. P5 to P6 generation cells were harvested and embedded into hydrogels for three-dimensional (3D) culture.

2.2. Flow cytometric analysis

Expression of UC-MSCs surface markers was determined using flow cytometry (FACS) staining. Cells were harvested from flasks by enzymatic dissociation with 0.25% trypsin-EDTA, followed by neutralization with complete culture medium. The cells were then counted using a NucleoCounter NC-200™ (Chemometec, Allerod, Denmark) and divided into tubes at a concentration of 1 × 10^6 cells per tube. After centrifugation at 300×g for 5 minutes at 4°C, the cells were resuspended in 100 µL FACS buffer (5 mg/mL BSA in PBS) and incubated for 30 minutes to block non-specific binding.

Fluorochrome-conjugated primary antibodies (all mouse anti-human) were added to the tubes at a final concentration of 10 µg/mL in 100 µL of FACS buffer containing the cells. The following antibodies were used: CD31-PE/Cy (IgG1, eBioscience, #25-0319-41), CD45-FITC (IgG1, IQ Products, #IQP-1), CD90-APC (IgG1, BD Pharmingen, #561), CD34-APC (IgG2a, Miltenyi Biotec, #130.090-954), CD44-FITC (IgG2b, Pharmingen, #555478), and CD105-PE/Cy (IgG1, eBioscience, #25-1057-4). The samples were incubated for 30 minutes at 4°C in the dark. To measure non-specific binding (assessing background signal from the antibody's fragment crystallizable region or the fluorochrome), isotype control antibodies were used: IgG1-PE/Cy (eBioscience, #25-4714-41), IgG2b-FITC (BD Pharmingen, #555742), IgG2a-APC (BD Pharmingen, #550882), IgG1-APC (IQ Products, #IQP-191A), and IgG1-FITC (IQ Products, #IQP-191F).

After incubation, cells were washed twice with FACS buffer, resuspended in 300 µL of FACS buffer, and analyzed by flow cytometry. Multiparametric flow cytometry was performed on 1 × 10^6 cells per sample using a BD FACSCanto II system (Becton Dickinson) with BD FACSDiva software. Data analysis was conducted using FlowJo software (FlowJo, LLC, Ashland), with the percentage of positive cells and the mean fluorescence intensity values calculated relative to isotype controls.

2.3. UC-MSCs differentiation induction

The UC-MSCs were seeded at a density of 10,000 cells/cm² in 24-well plates and cultured in complete medium until approximately 80% confluence. The culture medium was then replaced with differentiation induction media for adipogenic, osteogenic, and smooth muscle cell differentiation. Adipocyte induction medium was prepared by adding 0.1 µM dexamethasone (Gibco, A13449), 1 nM insulin

(ITS, Gibco, 41400-045), and 0.5 mM IBMX (3-isobutyl-1-methylxanthine, AppliChem, A0695) to the UC-MSCs complete medium. Osteoblast induction medium consisted of complete medium supplemented with 0.1 μM dexamethasone, 10 mM β-glycerophosphate (Sigma-Aldrich, G9422), and 0.05 mM ascorbic acid (Fisher Scientific, LC115309). Smooth muscle cell induction medium was prepared by adding 10 ng/mL transforming growth factor beta 1 (TGF-β1, PeproTech, Gibco, 1002110UG) to the complete medium.

The induction was conducted for 2 weeks in a 5% CO_2 atmosphere at 37°C during which period the medium was refreshed twice weekly. After media removal, cells were fixed with 2% paraformaldehyde (PFA; Sigma-Aldrich) in PBS for 15 minutes and washed with PBS for further differentiation characterization.

Adipogenic differentiation was evaluated by Oil Red O staining to visualize lipid vacuoles. The stock solution was prepared by dissolving 0.5 g Oil Red O (Sigma-Aldrich, O0625) in 100 mL isopropanol (Sigma-Aldrich, 190764), warming in a water bath, and filtering through a 0.45 μm filter. The working solution was made by mixing 30 mL of stock solution with 20 mL deionized water (dH_2O). Fixed and washed cells were rinsed with 60% isopropanol in dH_2O and stained with freshly prepared Oil Red O working solution for 15 minutes. Excess stain was removed by rinsing with 60% isopropanol. Nuclei were stained with hematoxylin for one minute, followed by rinsing with dH_2O.

Osteogenic differentiation was assessed by Alizarin Red staining to detect calcium deposition. Fixed and washed cells were incubated with 0.5% Alizarin Red (Sigma-Aldrich, A5533) in PBS for 10 minutes, followed by PBS washing. Nuclei were stained with hematoxylin and rinsed with dH_2O.

Myogenic differentiation was evaluated by immunohistochemistry for α-smooth muscle actin (α-SMA). Fixed cells were permeabilized with 0.25% Triton X-100 (Sigma-Aldrich, 9036-19-5) in PBS for 5 minutes, washed with PBS, and incubated with primary antibody against α-SMA (Rabbit anti-Human, Abcam, 124964, 1:250) for 1 hour at room temperature. After PBS washing, cells were incubated with a secondary antibody (Goat anti-Rabbit-HRP, Dako, P0448, 1:100) for 30 minutes. Cells were developed using 3,3'-diaminobenzidine (DAB) solution for 10 minutes and washed with dH_2O.

Finally, stained cells from all three differentiation groups were imaged using a brightfield microscope at 5x magnification (EVOS XL Core, Thermo Fisher Scientific, USA).

2.4. Generation of cell embedded ECM Hydrogels with different stiffnesses

To generate skin-derived decellularized ECM hydrogels with varying stiffnesses, we followed our previously published procedure [12, 13]. Briefly, porcine skin (purchased from a slaughterhouse, Kroon Vlees, Groningen, The Netherlands) was chopped and blended into a paste, then subjected to decellularization and freeze-drying to obtain dry skin-derived ECM. This ECM was subsequently ground into a powder and dissolved in 0.01 M hydrochloric acid containing 2% pepsin at a concentration of 20 mg/mL. After achieving a homogeneous solution, it was neutralized to form the dECM pre-gel which was kept at 4 °C.

To prepare the crosslinking solutions, 0.03 M and 0.06 M pentamethylcyclopentadienyl bis(triphenylphosphine) ruthenium (II) chloride (CAS: 92361-49-4, hereafter referred to as Ru) and 0.1 M sodium persulfate (SPS, CAS: 7775-27-1) were dissolved in PBS. For the experimental groups, 20 µL of either 0.03 M or 0.06 M Ru solution and 20 µL of 0.1 M SPS solution were added to 1 mL of dECM pre-gel and mixed thoroughly. This resulted in final concentrations of 0.58 mM Ru for the 0.03 M Ru solution group and 1.15 mM Ru for the 0.06 M Ru solution group. The final SPS concentration was 1.92 mM in both groups. In the control group, 40 µL of PBS was added instead. Harvested cells were then incorporated into the pre-gel mixture at a density of 2×10^6 cells/mL, and mixed carefully to achieve an even distribution. The cell-pre-gel mixture was carefully pipetted (200 µL) into each well of a 48-well plate and incubated at 37°C for 1 hour to allow hydrogel formation. Following gelation, the mixtures were exposed to UV light (from 4.5 cm distance using 2 × 9 W UV lamps (405 nm) (20 mW/cm^2 light intensity)) for 5 min to induce crosslinking. Following this, hydrogels were washed 3 times using 400 µL PBS to get rid of excess soluble Ru and SPS. After 4 hours of washing, 400 µL of UC-MSCs complete medium was added to each well for cell culturing. This process yielded hydrogels with three levels of different degrees of crosslinking: Ru0 (no crosslinker), Ru3 (0.58 mM Ru), and Ru6 (1.15 mM Ru), designed to mimic the stiffness range of normal human skin and fibrotic scar tissue.

2.5. Piezo1 modulation of UC-MSCs in 3D

The activity of Piezo1 in UC-MSCs was modulated using the Piezo1 agonist Yoda1 (1 μM, prepared as a 1:2000 dilution from a 2 mM stock in DMSO) (Sigma Aldrich, SML1558, Netherlands) and the antagonist GsMTx4 (5 μM, prepared as a 1:100 dilution from a 0.5 mM stock in PBS) (Abcam, ab141871, U.S.). Both were added to the complete medium following hydrogel generation and three PBS washes. As controls, complete medium containing 1:100 PBS served as the control for GsMTx4 treatments, while DMSO (1:2000 in complete medium) was used for Yoda1-treated controls. This experimental design yielded four distinct groups: Ctr, DMSO, Yoda1+DMSO, and GsMTx4. All treatments were maintained throughout the experiment, with treatments being refreshed each time the medium was replaced (every two days).

2.6 Mechanical properties measurement

The low load compression tester (LLCT, Mytri Aeldoom, the Netherland) was used to test the viscoelastic properties of hydrogels [14, 15]. To assess the physiological relevance of hydrogel stiffness, human abdominal skin was also measured. The skin sample was obtained as anonymized discarded surgical waste material in accordance with institutional ethical guidelines. LabVIEW 7.2 program (National Instruments, Austin, US) was used for the LLCT load cell and linear positioning for control and data acquisition. The LLCT was equipped with a 2.5 mm diameter probe, which applied a 20% compression deformation (0.2 stain) to the hydrogels within one second (strain rate, $\dot{\varepsilon} = 0.2\ s^{-1}$) and maintained compression for 100s. Stress (σ), defined as applied force (F) divided by probe area, was plotted as a function of strain and the slope of the stress-strain linear fitting was taken as the stiffness (Pa or N/m^2).Subsequently, during the 100s period of constant strain, the relaxing stiffness (*E(t)*) was represented as stress (σ(t)) divided by 0.2 strain. A Maxwell function (Eq. (1)) was fitted to *E(t)* curve to reveal how many Maxwell elements (MEs) and their corresponding relaxation time constant (τ_i) & relative importance (R_i, Eq. (2)) were involved in the stress relaxation process. The minimum number of MEs (n) was determined by monitoring the decrease in chi- square function expressed by Eq. (3) over N measurement points.

$$E(t) = E_1 e^{\frac{t}{\tau_1}} + E_2 e^{\frac{t}{\tau_2}} + E_3 e^{\frac{t}{\tau_3}} + \cdots + E_n e^{\frac{t}{\tau_n}} \quad (1)$$

$$R_i = \frac{E_i}{E_1+E_2+E_3+\cdots+E_n} \quad (2)$$

$$\chi^2 = \sum_{j=0}^{N}\left[\frac{E_j - E(t_j)}{\sigma_j}\right] \quad (3)$$

2.6.1 Volume normalization of stiffness & stress relaxation

During UC-MSC culture, hydrogel contraction occurred due to the contractility of UC-MSCs. To quantify the extent of contraction, hydrogel volume was measured both at the start and at specific time points during the culture period by multiplying the top-view projected area (A in mm^2) with the corresponding hydrogel thickness (H in mm, measured using LLCT): V (mm^3) = $A \times H$. The projected area of each hydrogel was obtained by imaging the culture plate using a flatbed scanner (HP ScanJet), followed by image analysis in Fiji [16] to calculate the area.

Hydrogel contraction increases matrix density, which enhances resistance to deformation (will cause an increase in stiffness) and restricts molecular chain mobility and water displacement (will cause a decrease in stress relaxation). To isolate the mechanical changes caused by intrinsic matrix remodeling from those arising solely from volume reduction, we normalized mechanical parameters to account for hydrogel contraction. Specifically, raw stiffness values were multiplied by the corresponding hydrogel volumes (geometric effects), while stress relaxation data were normalized by dividing the raw stress relaxation values by the corresponding hydrogel volume.

Volume-normalized stiffness (Enorm) was defined as:

$$E_{norm}(N \cdot mm) = E_{raw}\left(MPa{:}\frac{N}{mm^2}\right) \times V(mm^3) \quad (4)$$

Volume-normalized stress relaxation (SRnorm) was calculated as:

$$SR_{norm}(mm^{-3}) = SR_{raw}(\%) \div V(mm^3) \quad (5)$$

2.7. Cell viability staining

To evaluate the cytotoxicity of the hydrogels and the cell morphology of 3D embedded UC-MSCs, the cells cultured within the hydrogels were stained with calcein AM (5 μM; C1430, Thermo Fisher Scientific, US) for live cells, propidium iodide (PI; 3 μM; P4170, Sigma Aldrich, US) for dead cells and Hoechst (8 μM; Hoechst 33342, Thermo Fisher Scientific, US) for cell nuclei on day 1 and day 5. The stained cells were photographed using an EVOS inverted microscope (EVOS model M5000, Thermo Fisher) with GFP (λex 470/522 nm/λem 525/550 nm), Texas Red (λex 585/629 nm/λem 628/632 nm) and DAPI (λex 335/379 nm/λem 417/477 nm) filters.

CellProfiler 4.2.1 software was used to analyze cell viability on DAPI and PI-stained images, and to assess the cell aspect ratio and the average projected cell area on Calcein AM-stained images, as previously described [17]. For aspect ratio, the software measured each cell's major and minor axes (fitted ellipse method), and calculated the aspect ratio as the length of the major axis divided by the minor axis. A higher aspect ratio indicates a more elongated cell shape. Average projected cell area was calculated as the two-dimensional area of each segmented cell based on Calcein AM staining, reflecting the extent of cell spreading in the hydrogels. Data were obtained from two replicate hydrogel samples per culture condition per donor, for a total of five donors. For each hydrogel sample, one image was captured at 10x magnification from a randomly selected area within the central region of hydrogel to minimize edge effects. Cell viability, represented as the percentage of dead cells, was determined by dividing the number of dead cells (PI-positive cells that overlapped with DAPI-positive nuclei) by the total number of cells (DAPI-positive nuclei) in each image.

2.8. ECM histochemical staining

After 1d or 5d culturing and subsequent LLCT testing the cell embedded hydrogels were immediately fixed with 4% PFA in PBS at 37 °C for 30min. After 3 times PBS washing, the fixed hydrogels were pre-embedded with molten 2% agarose (Invitrogen, US) in PBS to prevent hydrogels from contracting during dehydration. The hydrogels were then stepwise dehydrated using a graded ethanol series and embedded in paraffin. 4μm thick sections were cut and mounted on glass coverslips (size 18 × 18 mm, Merk, Catalog #BR470045) and deparaffinized according to standard procedures.

After deparaffinization, 4µm sections were firstly stained with weigert's iron hematoxylin (Sigma Aldrich, St Louis, MO) for 10 min to visualize the cell nuclei. Sections were then washed under running tap water for 10 minutes before staining collagen fibers with 0.1% picrosirius red (PSR; Sigma-Aldrich) in 1.3 % aqueous solution of picric acid (Sigma-Aldrich) for 1h. Afterwards, sections were washed with 0.5% acetic acid, dehydrated with 100% ethanol and mounted in a resinous medium. Subsequently slides were scanned using 40x objective of the Hamamatsu NanoZoomer digital slides scanner (Hamamatsu Photonic K.K., Japan). Images were viewed digitally using Aperio ImageScope V 12.4.6 (Leica biosystem).

Quantification of collagen fibers was performed using CellProfiler 4.2.1 software. Data were obtained from one hydrogel section per donor, with a total of five donors. For each hydrogel section, three random regions of interest (ROI) (2,000 dpi × 2,000 dpi with 467 µm × 467 µm) were selected for analysis. The fractional area (FA) of PSR-stained collagen fibers was calculated by dividing the area of the positively stained pixels by the total area of the ROI. The mean intensity (MI) of collagen staining was determined by dividing the integrated density (i.e., the sum of pixel intensities within the PSR-positive pixels) by the total area (in pixels) of the ROI. To quantify the regions of non-stained holes surrounding cells within the ECM hydrogels - the area percentage of holes was determined using Fiji [16] by dividing the total area of blank holes by the total ROI area.

2.8.1. Volume-normalized collagen fiber analysis

To account for hydrogel contraction-induced densification, FA was normalized to initial hydrogel volume:

$$FA_{(norm)} = FA_{(raw)}(\%) \times V(mm^3) \quad (6)$$

where V represents the hydrogel volume measured after LLCT testing prior to hydrogel fixation (see Section 2.6.1). This correction aimed to eliminate the increase in FA caused by contraction-driven collagen compaction.

In contrast, MI did not require normalization because MI is an intensity-based measurement that is independent of hydrogel density.

2.9. Immunofluorescence staining

As described in Section 2.8, sections used for immunofluorescence staining were obtained following hydrogel embedding, sectioning, and deparaffinization. Afterwards, the rehydrated sections were heated in 10 mM citrate buffer pH 6 at 85 ℃ for 4 h for antigen retrieval. Following additional PBS washes the sections were blocked in 4% BSA in PBS for 15 min prior to being incubated with primary antibodies (See Table 1 for details) for 1 h at room temperature. The sections were then washed 3 times with PBS and incubated with a mixture of the appropriate secondary antibody (See Table 1 for details) and DAPI (4′,6-diamidino-2-phenylindole, Thermo fisher scientific, US, 1:7500), prepared in 2% BSA in PBS for 1 h at room temperature. The sections were thoroughly washed with PBS and then mounted using Citifluor mounting medium (Science Services, Munich, Germany) before being imaged using a Leica SP8 X white light laser confocal microscope (Leica, Wetzlar, Germany), λex 405 nm / λem 455 nm for DAPI and λex 630 nm / λem 665 nm for Piezo1/pFAK/MMP2/MMP14 at 40x magnification.

The mean fluorescent intensity of Piezo1, pFAK, MMP2, and MMP14 stainings was calculated using CellProfiler by dividing the total fluorescence intensity by the total area of the segmented fluorescent-positive regions. Data for each group were obtained from one hydrogel section per donor, with a total of two/three donors. For each hydrogel section, two non-overlapping 4×4 tile images (1160 µm × 1160 µm) were randomly captured. Within these tiles, five fields of view (290 µm × 290 µm) containing at least five visible nuclei per field — were selected for quantitative analysis.

Table 1. Details of the antibodies used for immunofluorescence detection in the study.

Antibody Type	Target / Specificity	Host	Fluorophore	Company	Catalog Number	Concentration
Primary	Piezo1	Mouse		Novus Biologicals	NBP2-75617	1:200
Primary	pFAK	Rabbit		Invitrogen	700255	1:300
Primary	MMP2	Rabbit		Abcam	ab37150	1:200
Primary	MMP14	Rabbit		Abcam	ab51074	1:200
Secondary	Goat Anti-Mouse	--	Alexa Fluor™ 647	Invitrogen	A21235	1:400
Secondary	Goat Anti-Rabbit	--	Alexa Fluor™ 647	Invitrogen	A21244	1:400

2.10 Statistical analyses

All statistical analyses were performed using GraphPad Prism v9.2.0 (GraphPad Company, San Diego, CA, US). All data are shown as mean ± standard deviation from the experiments that were performed with at least three independent experiments. The figure legends indicate the sample size associated with each experiment. Normality of the data was tested with a QQ plot and a ShapiroWilk test [44]. When normality was confirmed, statistical comparisons were performed using one-way analysis of variance (ANOVA) for experiments involving a single independent variable (e.g., hydrogel treatment), and two-way ANOVA for experiments involving two independent variables (e.g., hydrogel treatment and time). When data were not normally distributed, Mann-Whitney test and Kruskal-Wallis test were used for data analyses. Data populations were considered significantly different at $p < 0.05$.

3. Results

3.1 Culture and characterization of UC-MSCs

Primary UC-MSCs had a characteristic spindle-like morphology (Fig. S1A). Flow cytometry analysis confirmed their MSC phenotype, with cells positively expressing CD90, CD44, and CD105, and not expressing CD45, CD34, and CD31 (Fig. S1B). Under adipogenic induction, UC-MSCs transitioned from a spindle to an elliptical shape, with lipid droplets evident upon Oil Red O staining. Osteogenic differentiation was marked by the presence of calcium phosphate deposits (bright red after Alizarin Red S staining), and smooth muscle differentiation showed elevated αSMA expression compared to controls (Fig. S1C). These results collectively demonstrate the differentiation capacity of the isolated UC-MSCs.

3.2 The mechanics and shapes of ECM hydrogels are affected by UC-MSCs

3.2.1 The control, mechanically stable cell-free ECM hydrogels replicate skin and scar stiffness profiles

Cell-free skin-derived ECM hydrogels were engineered to replicate the stiffness range of normal human skin (Ru0, Ru3) and fibrotic scar tissue (Ru6). Human abdominal skin had a stiffness of 2.6 ± 2.2 kPa (Fig. S2). On Day 0, the hydrogels were different in stiffness, increasing with crosslinker concentration: Ru0 (1.1 ± 0.4 kPa), Ru3 (3.7 ± 2.0 kPa), and Ru6 (17.5 ± 10.7 kPa) ($P < 0.0001$ for Ru0 vs. Ru6 and Ru3 vs. Ru6; Fig. 1A). These results indicate that Ru3 closely resembles physiological skin stiffness, while Ru0 represents a softer baseline, and Ru6 mimics dermal scar stiffness. In addition to stiffness, the stress relaxation was assessed. Human abdominal skin demonstrated a stress relaxation of 75.2 ± 6.6% (Fig. S2). Hydrogels exhibited distinct and generally higher relaxation values: 95.6 ± 4.1% for Ru0, 80.9 ± 8.3% for Ru3, and 86.3 ± 7.4% for Ru6 ($P<0.0001$ for Ru0 vs Ru3, $P=0.0003$ for Ru0 vs Ru6) (Fig. S3A).

Over the five days culture period, the control and Ru3 cell-free hydrogels did not change in stiffness, resp. 0.7 ± 0.2 kPa and 3.0 ± 1.7 kPa at day 5 (Fig. 1A). In contrast, in the stiff hydrogels (Ru6) stiffness reduced from 17.5 ± 10.7 kPa to

12.1 ± 6.6 kPa (P=0.0128). After 5 days, stress relaxation values were: 94.4 ± 5.0% for Ru0, 91.2 ± 7.0% for Ru3, and 90.0 ± 5.5% for Ru6 (Fig. S3A).

3.2.2 UC-MSCs embedding preserves initial hydrogels stiffness and stress relaxation

Initial stiffness values (4 hours) of the cell-embedded hydrogels were comparable to the cell-free controls: 1.2 ± 0.5 kPa, 3.6 ± 2.3 kPa, and 17.7 ± 8.9 kPa for Ru0, Ru3, and Ru6 in the presence of cells respectively (P<0.0001 for Ru0/Ru3 vs Ru6) (Fig. 1A). All three groups demonstrated substantial stress relaxation (>83% reduction after 100 seconds) under a constant 0.2 strain, and no differences were observed between groups (Fig. S3A). These data indicate that embedding UC-MSCs into ECM hydrogels maintains the cell-free hydrogels' mechanical microenvironment for subsequent cell-driven processing.

3.2.3 Cells alter the ECM hydrogel stiffness in stiffness-dependent manner

Over five days culture, the presence of UC-MSCs altered the mechanical properties of the hydrogels in a stiffness-dependent manner. UC-MSCs in the control, Ru0 hydrogels increased the stiffness, rising from 1.1 ± 0.4 kPa on day 0 to 4.9 ± 3.6 kPa on day 5 (P=0.0253). The stiffness of Ru3 hydrogels did not significantly change over time (3.7 ± 2.0 kPa (day 0) to 1.5 ± 1.0 kPa (day 5)). In contrast, the cells in the stiff hydrogels (Ru6) reduced the stiffness from 17.5 ± 10.7 kPa to 3.4 ± 1.3 kPa (p<0.0001) (Fig. 1A). Notably, by day 5, the stiffness differences that had existed between the different hydrogels on day 0 had disappeared, with the cells modifying the stiffness values to around 1-5 kPa in each of the hydrogels. In summary, UC-MSCs actively remodeled their mechanical environment, ultimately converging all hydrogels toward a similar intermediate stiffness range.

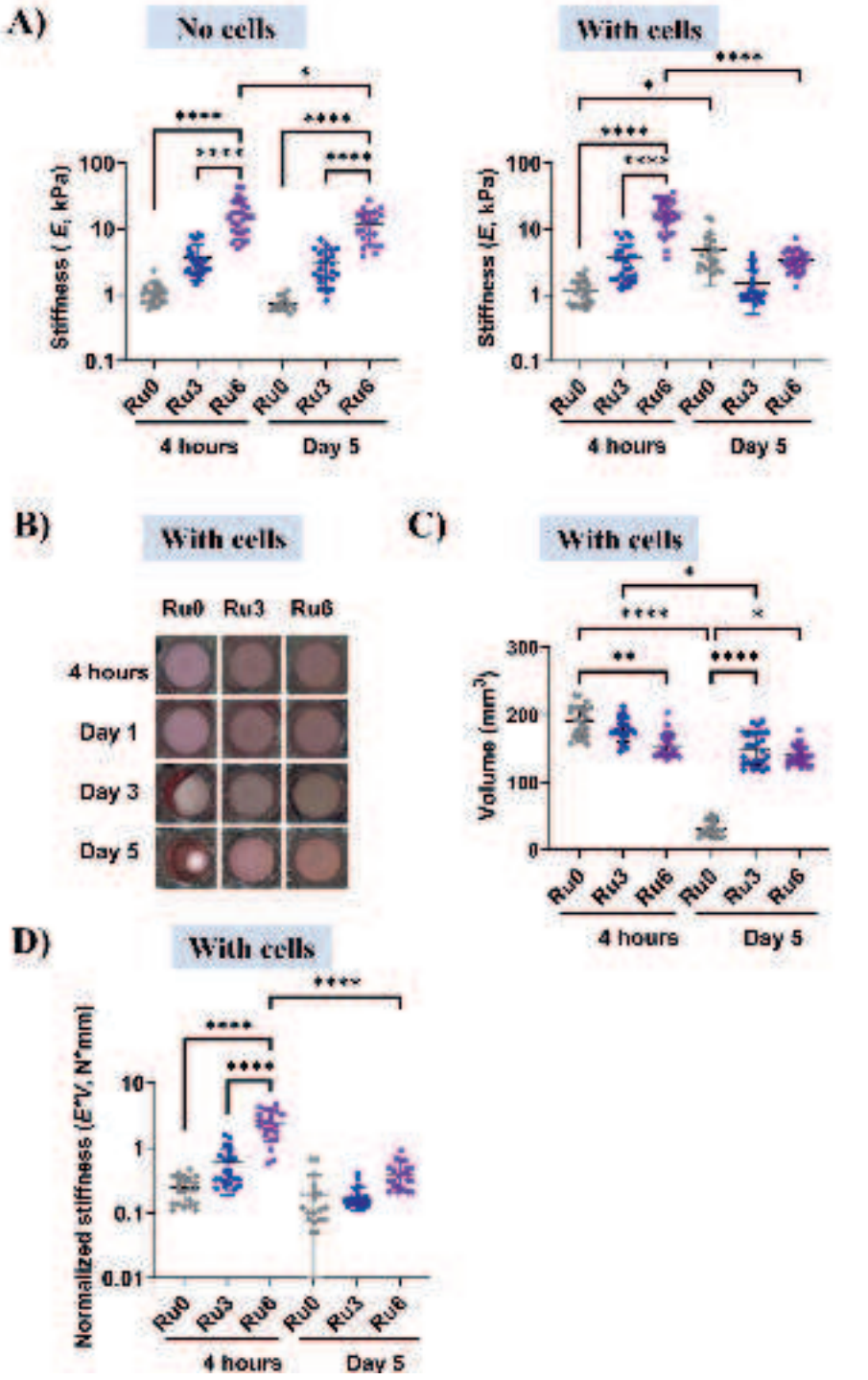

Figure 1. Hydrogel stiffness, volume, and volume-normalized stiffness of crosslinked

hydrogels with/without UC-MSCs. A) The stiffness (E) of ECM hydrogels (Ru0 (grey dots), Ru3 (blue dots), and Ru6 (purple dots)) at 4 hours and Day 5 in the absence (left) and presence (right) of UC-MSCs; B) Hydrogel shape changes (top view): Representative images of the same hydrogels at 4 hours, Day 1, Day 3, and Day 5, showing the degree of contraction over time in hydrogels with cells; C) Volume (V, mm3) of cell-embedded ECM hydrogels at 4 hours and day 5. D) Hydrogel volume-normalized stiffness (Enorm = Eraw×V in N.mm) of cell-embedded hydrogels at 4 hours and day 5, which decouple geometric effects (hydrogel contraction) from intrinsic matrix remodeling. Data are expressed as mean ± standard deviation (SD; n = 5 biological donors), with each dot representing individual measurements (two independent measurements per hydrogel) from two hydrogel replicates per condition per donor, resulting in a total of N = 10 hydrogel samples per condition. Statistical significance was analyzed by one way ANOVA (* $p < 0.05$, ** $p<0.01$, *** $p < 0.001$, **** $p<0.0001$).

3.2.4 Stiffness dependent volume contraction of UC-MSCs embedded hydrogels

The volume contraction of the cell-embedded ECM hydrogels was monitored over 5 days (Figure 1B &1C). 4 hours after crosslinking, the Ru6 hydrogel showed significant volume contraction compared to non-crosslinked Ru0 hydrogel (Ru0 vs Ru6: 190.9 ± 17.4 vs 154.5 ± 17.4 mm^3, P=0.0015), while Ru3 contracted less to 177.3 ± 16.8 mm^3 compared to Ru0 hydrogel. These differences in volumes are likely attributable to the crosslinking process with Ru, rather than an active cell driven process at 4 hours. After five-day culture, Ru0, Ru3 hydrogels had contracted to the volume of respectively 31.5 ± 11.3 and 150.1 ± 24.5 mm^3 ($P<0.0001$ for Ru0, day0 vs day5; P=0.02 for Ru3, day0 vs day 5) while the Ru6 hydrogel maintained the volume, 140.1 ± 14.3 mm^3, after 5 days. This highlights the differential influence of cell-driven contraction interacting with Ru derived covalent crosslinks on ECM remodeling.

3.2.5 Volume-normalized stiffness: Distinguishing stiffness changes driven by cell-mediated ECM intrinsic remodeling from hydrogel contraction

At 4 hours, the volume-normalized stiffness (Enorm) of the hydrogels followed the same trend as the raw stiffness across the three groups (i.e., stiffness increased with increasing Ru concentration), despite some contraction in Ru6 (Enorm_Ru0: 0.26 ± 0.11 N·mm; Enorm_Ru3: 0.59 ± 0.40 N·mm; Enorm_Ru6: 2.48 ± 1.19 N·mm. $P<0.0001$ for Ru0 vs Ru6 and Ru3 vs Ru6).

After 5 days of culture, stiffness changes for UC-MSC embedded hydrogels (Fig. 1A) can be attributed to two distinct, cell-mediated mechanisms: (1) ECM contraction, where cells physically contract and compact their surrounding ECM, leading to volume reduction and apparent stiffening; and (2) ECM intrinsic remodeling, a simultaneous processes of matrix degradation, deposition, fiber bundling, and architectural reorganization—any of which can alter material stiffness independently of volume change. Notably, even during remodeling, localized matrix contraction may still occur. To disentangle these effects, stiffness was normalized by hydrogel volume (Fig. 1D). If cells had not mediated intrinsic matrix remodeling (the process responsible for altering stiffness), the volume-normalized stiffness of Ru0, Ru3, and Ru6 hydrogels would have followed the same trend as observed at 4 hours, however, this trend was disrupted. The volume normalized stiffness of Ru0 and Ru3 did not significantly change after 5 days of culture (Fig. 1D). The volume normalized stiffness of Ru6, on the other hand, decreased after 5 days of culture as compared to 4 hours ($P < 0.0001$), suggesting a cell-induced ECM intrinsic remodeling and stiffness reduction. The normalized stiffness of Ru0 at day 5 remained unchanged compared to 4 hours, indicating that the observed increase in measured raw stiffness (Fig. 1A) of Ru0 was due to ECM contraction i.e. volume reduction of the hydrogels. Overall, this warrants the use of volume normalization to more accurately assess the cellular contribution to mechanical alterations in 3D cell cultures. In the skin-derived hydrogels cell-mediated ECM-intrinsic remodeling led to a reduction in stiffness in the high-stiffness (Ru6) gels, whereas cell-driven hydrogel contraction was the primary contributor to stiffness increases in the soft Ru0 gels.

3.2.6 Raw and volume-normalized stress relaxation of cell-embedded hydrogels

Supplementary Figure 2 presents data on the raw and volume-normalized stress relaxation of ECM hydrogels, with additional details provided in the supplementary materials following the figure. In summary, all hydrogels demonstrated rapid stress relaxation (>77%) at both 4 hours and 5 days. Ru0 and Ru6 hydrogels exhibited a significant reduction in stress relaxation over the five-day period, whereas Ru3 maintained stable values. By Day 5, all hydrogel groups showed comparable levels of stress relaxation. The volume-normalized data suggest that relaxation behavior is influenced by multiple factors beyond matrix

compaction, possibly including molecular chain mobility, water redistribution, and time-dependent viscoelastic responses.

3.3 UC-MSCs induced stiffness-dependent changes in collagen fiber distribution in ECM hydrogels

After cell embedding (4 hours), collagen fibers appeared to be arranged randomly and were non-homogeneously distributed with regions of denser and less dense fiber areas irrespective of stiffness (Fig. 2A). Collagen fiber density increased in a stiffness-dependent fashion as shown by increased FA and increased mean intensity (MI) (Fig. 2B). Specifically, the fractional area (FA) values for Ru0, Ru3, and Ru6 hydrogels were 57.4 ± 7.0%, 73.1 ± 6.6%, and 86.0 ± 3.5%, respectively ($P<0.0001$ for Ru0 vs Ru3 and Ru0 vs Ru6 and Ru3 vs Ru6), with corresponding collagen MI values of 0.70 ± 0.08, 0.85 ± 0.05, and 0.93 ± 0.01 ($P<0.0001$ for Ru0 vs Ru3 and Ru3 vs Ru6, $P=0.0084$ for Ru vs Ru6) (Fig. 2B).

After five days of culture, collagen fibers had been distinctly reorganized by UC-MSCs in all three hydrogel groups. In the soft control hydrogel (Ru0), collagen fiber bundles appeared more structured compared to day 0, as indicated by increases in FA and MI (FA: 57.4 ± 7.0% vs. 84.6 ± 8.2%, $p<0.0001$; MI: 0.70 ± 0.08 vs. 0.91 ± 0.02, $p<0.0001$) (Fig. 2A and 2B). In contrast, collagen fibers in the medium stiffness hydrogel (Ru3) had a reduced density after five days compared to 4 hours, accompanied by reduced FA and MI (FA: 73.1 ± 6.6% vs. 65.7 ± 9.2%, $p=0.0466$; MI: 0.85 ± 0.05 vs. 0.62 ± 0.10, $p<0.0001$) (Fig. 2A and 2B). Within the highest stiffness hydrogels (Ru6), ECM-free voids/holes surrounding the embedded cells became evident after 5 days; resulting in an unchanged FA (86.0 ± 3.5% vs. 82.9 ± 5.8%, $p>0.05$) and decreased MI (0.93 ± 0.01 vs. 0.84 ± 0.06, $p=0.0016$) (Fig. 2A and 2B).

To account for hydrogel contraction, FA was normalized by hydrogel volume (FA(norm)Fig. 2C). Immediately after cell embedding, FA(norm) still showed the stiffness-dependent trend, with Ru0, Ru3, and Ru6 exhibiting values of 109.3 ± 21.3, 129.3 ± 20.6, and 132.5 ± 15.4, respectively (Ru0 vs. Ru3, $P = 0.0091$; Ru0 vs. Ru6, $P = 0.0014$). Over five-days culture, FA(norm) significantly decreased across all groups, with final values of 26.5 ± 7.5 for Ru0, 98.9 ± 11.3 for Ru3, and 115.4 ± 12.4 for Ru6. Notably, Ru0 exhibited the most substantial decline in FA(norm) (Ru0 vs. Ru3/Ru6, $P < 0.0001$), indicating that the increased

FA(raw) observed in Ru0 were not solely due to hydrogel contraction but also involved intrinsic matrix remodeling by cells.

To further evaluate the influence of long-term culture medium exposure on viscoelastic ECM fiber arrangement, we examined bare ECM hydrogels (Ru0, Ru3, and Ru6) incubated for five days. After four hours, collagen fiber alignment in these acellular hydrogels was comparable to that observed in cell-embedded conditions (Fig. S4). However, after five days, all three hydrogels exhibited a noticeable decline in staining intensity (Fig. S4). This suggests that the viscoelastic properties of ECM hydrogels led to gradual relaxation over time even in the absence of cells altering fiber alignment. This effect may explain the significant reduction in MI(raw) observed in Ru3 at day 5. Overall, these findings highlight the distinct roles of matrix stiffness in cell regulated ECM remodeling: in soft Ru0 hydrogels, collagen fibers became denser and more stacked, indicating intrinsic remodeling by cells, while in stiff Ru6 hydrogels, cell-mediated ECM degradation was more prominent.

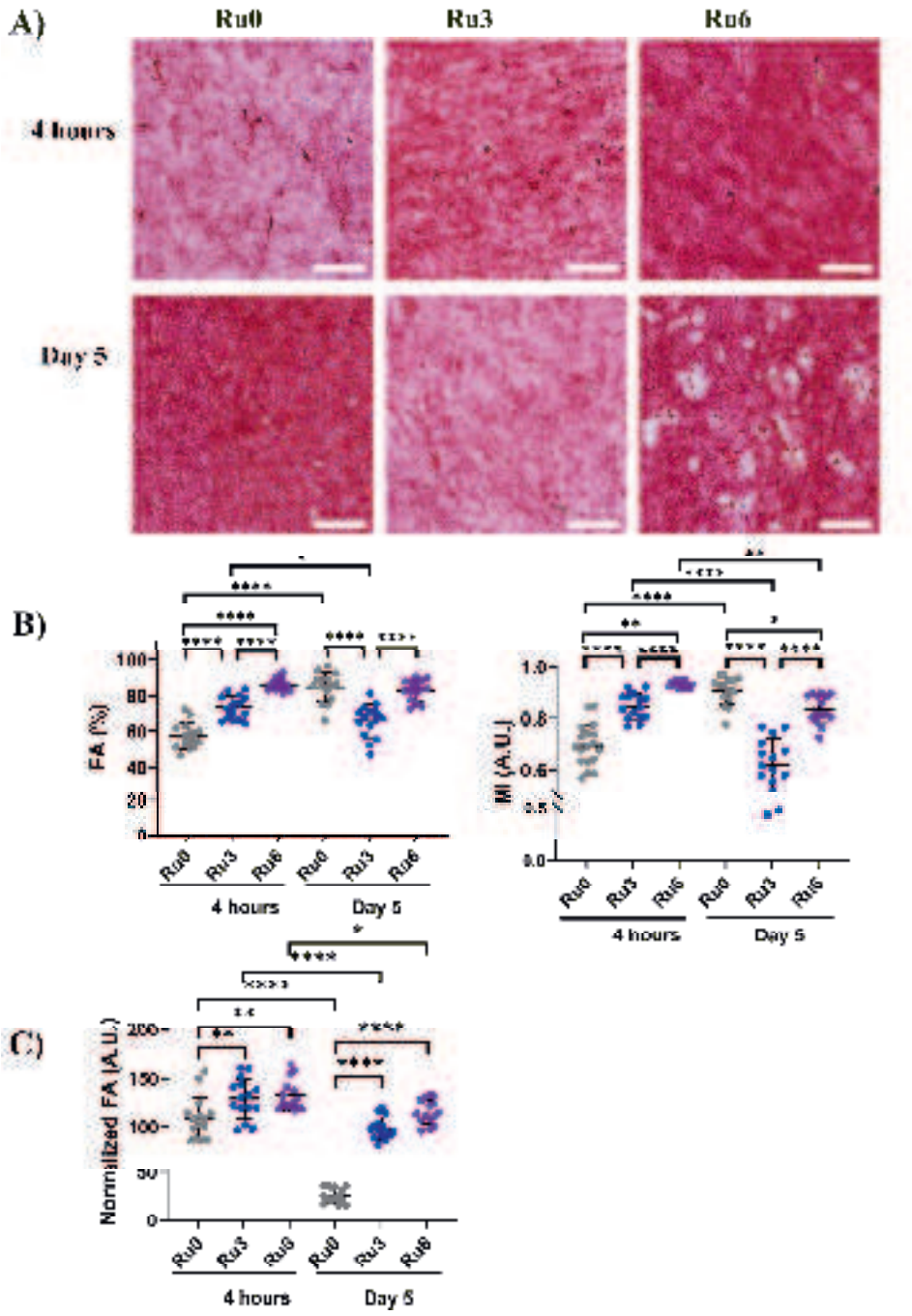

Figure 2. Characterization of ECM protein fiber structural changes induced by UC-MSCs embedded in ECM hydrogels with variable stiffness. A) Representative images

of PSR staining on skin-derived ECM hydrogels (Ru0, Ru3, Ru6) after 4 hours cell embedding and 5 days cell culturing (cell nuclei-blue black; collagen fiber-red). Scale bars:100 μm. B) Quantification for fiber fractional area (FA) and mean intensity (MI). C) Hydrogel volume-normalized FA (FA(norm) =FA(raw) (%) × V(mm^{-3})), accounting for contraction. PSR: Picrosirius red. FA was calculated by dividing the stained fiber area by the total image area. MI was determined by dividing integrated density (the sum of pixel intensities within the PSR-positive regions) by the total area (in pixels) of the positive pixels, representing the average PSR staining intensity of collagen fibers. Each dot represents data from three independent measurements per hydrogel for each cell donor (n = 5). Statistical significance was analyzed by one-way ANOVA (* $p < 0.05$, ** $p<0.01$, *** $p < 0.001$, **** $p<0.0001$).

3.4 UC-MSCs exhibited the greatest elongation and spreading in Ru3 ECM hydrogel

Irrespective of stiffness, all cells stayed alive during culturing within the hydrogels(Fig. 3A, B). To assess early cell morphology and adaptation to the matrix, imaging and quantification were performed on day 1. Across all stiffnesses, UC-MSCs elongated and spread over five days albeit in different fashions. At day 1, cells in medium stiffness hydrogels (Ru3) adopted a spindle-like morphology. In Ru0, cells exhibited a slightly elongated and spread morphology, whereas in Ru6, they appeared more rounded with limited spreading (Figure 3A). The aspect ratios of the cells in the different hydrogel environments at day 1 were as follows: 1.8 ± 0.1, 2.1 ± 0.3, and 1.4 ± 0.1 for Ru0, Ru3 and Ru6 respectively ($P=0.0134$ for Ru0 vs Ru6 and $P<0.0001$ for Ru3 vs Ru6) (Figure 3C). By day 5, cells in all three hydrogels showed clear signs of spreading. Among them, UC-MSCs in Ru3 hydrogels exhibited the most extensive spreading and highest surface area. The cell aspect ratios had increased across all groups, reaching 2.1 ± 0.2, 2.7 ± 0.6, and 2.2 ± 0.2 for Ru0, Ru3 and Ru6 respectively ($P<0.0001$ for Ru0 vs Ru3 and $P=0.0024$ for Ru3 vs Ru6).

Additionally, the average projected cell areas had increased during the five-day culture in Ru0 ($P=0.0021$), Ru3 ($P=0.0013$), and Ru6 ($P=0.0050$) hydrogels (Figure 3D), suggesting that the matrix environment influenced cellular growth and spreading across all conditions.

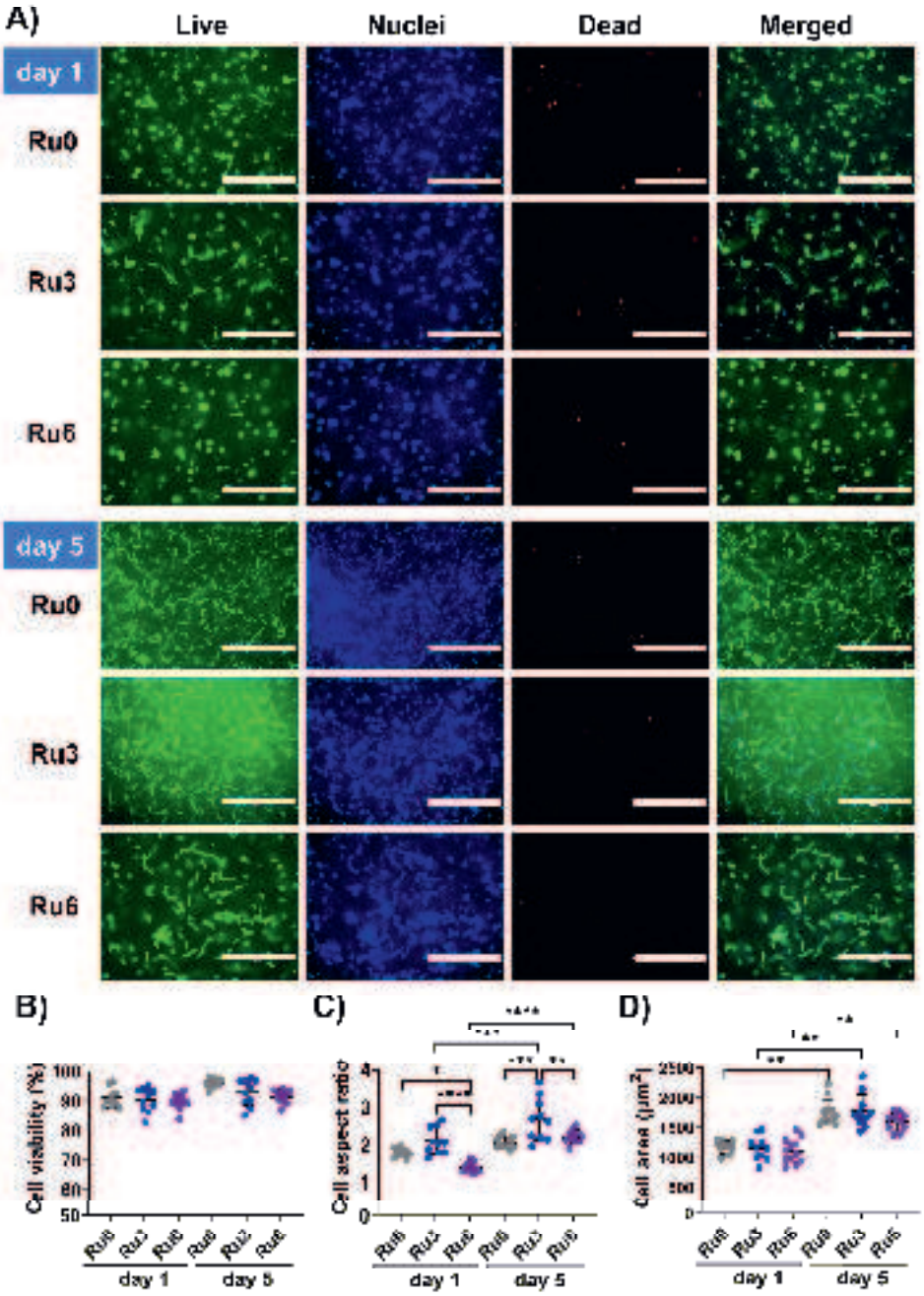

Figure 3. Morphology and viability of UC-MSCs embedded in ECM hydrogels with variable stiffness over 1 and 5 days. A) Representative fluorescence images of UC-MSCs embedded in Ru0, Ru3, and Ru6 hydrogels at day 1 and day 5. Live cells were

stained with Calcein AM (green), nuclei with Hoechst (blue), and dead cells with PI (red). Overlap images show merged channels. B) Quantification of cell viability, expressed as the percentage (%) of dead cells (PI-positive/DAPI-positive). C) Quantification of cell aspect ratio. D) Measurement of the average projected cell area. Viability was assessed on DAPI/PI-stained images and cell morphology was assessed on Calcein AM-stained images. Data were obtained from two replicate hydrogel samples per donor (n = 5 donors). One image per hydrogel was taken at 10x magnification. Scale bars: 400 μm. Statistical significance was analyzed by two-way ANOVA (* $p < 0.05$, ** $p<0.01$, *** $p < 0.001$, **** $p<0.0001$).

3.5 Piezo1 and pFAK are stiffness-dependent mechanosensors in UC-MSCs cultured in 3D ECM hydrogels

In general, in mesenchymal cell types like MSCs, mechanosensors and downstream transduction by e.g. Piezo1, YAP, and phosphorylated FAK, are involved in ECM remodeling. To investigate their roles in stiffness-dependent matrix remodeling, the activation of Piezo1, YAP, and pFAK was examined in UC-MSCs embedded within ECM hydrogels (Ru0, Ru3 and Ru6).

When UC-MSCs were cultured on (ultrastiff) tissue culture plastic (GPa range), Piezo1 (Fig. 4A), pFAK (Fig. 5A) and YAP (Fig. S5) were readily detectable. However, once embedded in the 3D environment of hydrogels, UC-MSCs constitutively downregulated Piezo1 and pFAK within 1d of culture, regardless of stiffness, yet remained detectable (Fig. 4B and 5B). On day 1, Piezo1 expression in UC-MSCs cultured within ECM hydrogels showed a positive association with hydrogel stiffness, with mean intensities of 0.086 ± 0.032, 0.102 ± 0.037, and 0.138 ± 0.052 in Ru0, Ru3, and Ru6, respectively ($P < 0.0001$ for Ru0 vs Ru6, $P = 0.0002$ for Ru3 vs Ru6) (Fig. 4B, 4C). Similarly, pFAK expression followed a stiffness-dependent trend, with values of 0.052 ± 0.014, 0.069 ± 0.029, and 0.098 ± 0.015 for Ru0, Ru3, and Ru6, respectively ($P = 0.0039$ for Ru0 vs Ru6) (Fig. 5B, 5C). By day 5, Piezo1 expression significantly declined across all groups, with mean intensities of 0.049 ± 0.017, 0.059 ± 0.026, and 0.077 ± 0.020 for Ru0, Ru3, and Ru6, respectively ($P = 0.0003$ for Ru0, day 1 vs. day 5; $P < 0.0001$ for Ru3/Ru6, day 1 vs. day 5). Notably, Piezo1 in Ru6 hydrogels maintained comparatively higher levels, compared to Ru0 and Ru3 hydrogels ($P = 0.0112$ for Ru0 vs. Ru6) (Fig. 4B, 4C). In contrast, pFAK levels in Ru6 hydrogels continued to decrease over the culture period, eventually

reaching similarly low levels as those observed in Ru0 and Ru3 hydrogels on day 5, with values of 0.031 ± 0.024, 0.029 ± 0.023, and 0.060 ± 0.030 for Ru0, Ru3, and Ru6, respectively (P = 0.0128 for Ru3, and P = 0.0302 for Ru6, day 1 vs. day 5) (Fig. 5B, 5C).

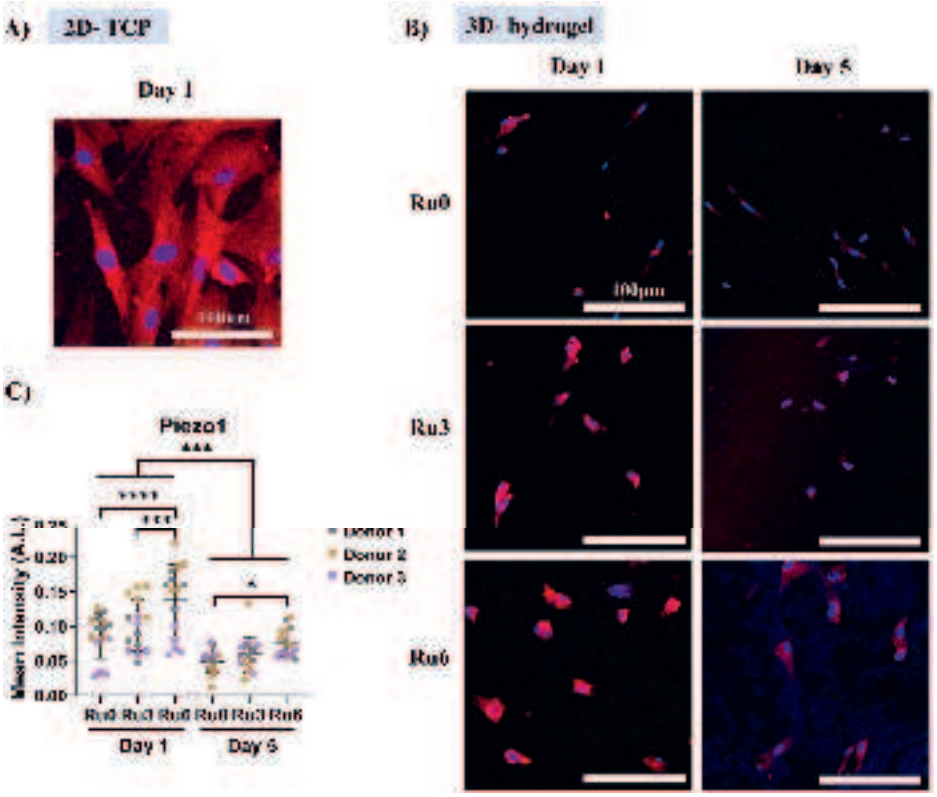

Figure 4. Stiffness-dependent regulation of Piezo1 in UC-MSCs embedded in ECM. A) Representative immunofluorescence images showing Piezo1 expression (red) in UC-MSCs cultured on TCP plastic (ultra-stiff substrate) and B) in ECM hydrogels (Ru0, Ru3, and Ru6) at day 1 and day 5. Cell nuclei are stained with DAPI (blue). C) Quantification of Piezo1 expression levels in UC-MSCs embedded in ECM hydrogels at day 1 and day 5, based on mean fluorescence intensity (MFI). The MFI of Piezo1 was calculated by dividing the total fluorescence intensity by the total area of the positive Piezo1 staining regions. The data are presented as mean ± SD (n = 3), with each dot representing technical measurements from five randomly selected regions within one hydrogel section per donor. Specifically, for each group, one hydrogel section per donor was used, and two 4×4 tile images (1160 μm × 1160 μm) were captured per section. Five random single-tile images (290 μm × 290 μm) with at least five visible nuclei per image were selected for

analysis. Statistical significance was determined by two-way ANOVA (* $p < 0.05$, ** $p < 0.01$, *** $p < 0.001$, **** $p < 0.0001$).

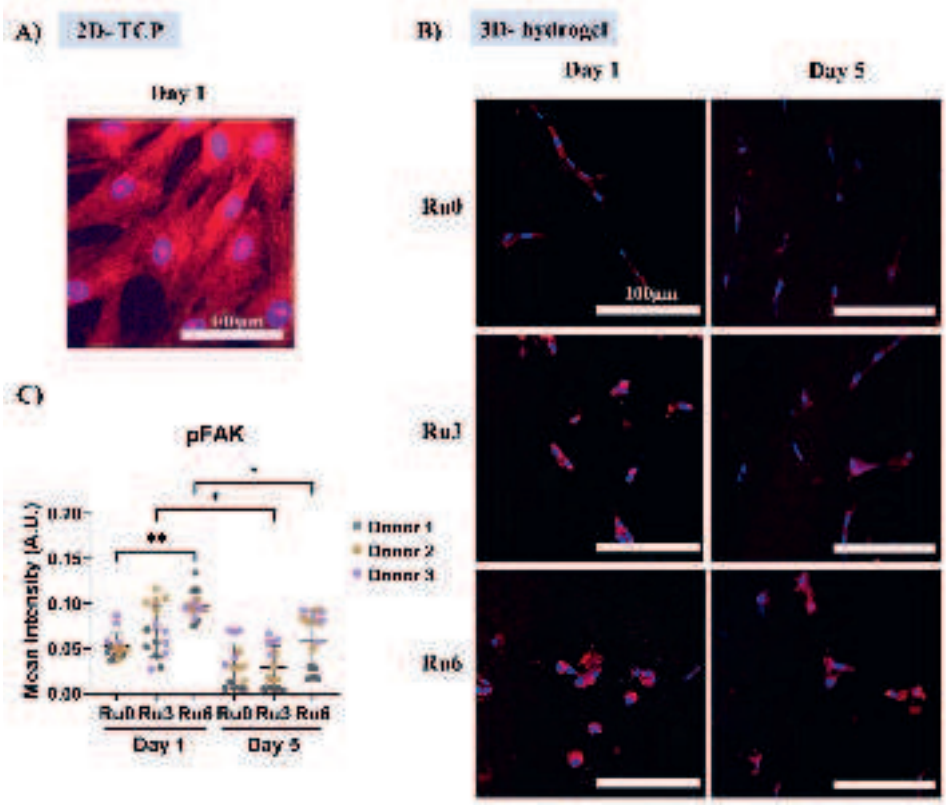

Figure 5. Stiffness-dependent regulation of pFAK in UC-MSCs embedded in ECM. A) Representative immunofluorescence images showing pFAK expression (red) in UC-MSCs cultured on TCP plastic (ultra-stiff substrate) and B) in ECM hydrogels (Ru0, Ru3, and Ru6) at day 1 and day 5. Cell nuclei are stained with DAPI (blue). C) Quantification of pFAK expression levels in UC-MSCs embedded in ECM hydrogels at day 1 and day 5, based on mean fluorescence intensity (MFI). The MFI of pFAK was calculated by dividing the total fluorescence intensity by the total area of the positive pFAK staining regions. The data are presented as mean ± SD (n = 3), with each dot representing technical measurements from five randomly selected regions within one hydrogel section per donor. Specifically, for each group, one hydrogel section per donor was used, and two 4×4 tile images (1160 μm × 1160 μm) were captured per section. Five random single-tile images (290 μm × 290 μm) with at least five visible nuclei per image were selected for analysis. Statistical significance was determined by two-way ANOVA (* $p < 0.05$, ** $p < 0.01$, *** $p < 0.001$, **** $p < 0.0001$).

YAP expression showed a rapid decline when UC-MSCs transitioned from 2D TCP cultures to 3D ECM hydrogels, regardless of hydrogel stiffness, which was similar to Piezo1 and pFAK (Fig. S5). However, unlike Piezo1 and pFAK, this downregulation was similar for all stiffnesses.

These findings underscore the mechanical sensitivity of Piezo1 and pFAKin 3D ECM embedded UC-MSCs, which dynamically respond to ECM stiffness.

3.6 Piezo1 modulation influences the stiffness and contraction of UC-MSC embedded ECM hydrogels

From this point forward, we aimed to determine whether modulating Piezo1 activity could directly influence cell-mediated ECM remodeling and stiffness changes in the hydrogels. To investigate this, UC-MSCs embedded in Ru0 and Ru6 ECM hydrogels were treated with a Piezo1 activator (Yoda1) or inhibitor (GsMTx4), and compared to their respective control groups (DMSO and Ctr), to assess the specific role of Piezo1 in these processes. Since we aimed to observe both the early and sustained effects of Piezo1 modulation on ECM remodeling, stiffness changes, and downstream signaling molecules, we included multiple time points--1, 2, and 5 days after treatment (initiated at 4 hours post-cell embedding) for monitoring.

For the Ru0 hydrogels group (Fig. 6A), stiffness remained relatively unchanged during the first two days (0.9 ± 0.2, 0.8 ± 0.3, and 0.9 ± 0.3 kPa on days 0, 1, and 2, respectively) and was consistent across all treatment groups. By day 5, stiffness increased in the control gel (2.7 ± 1.2 kPa), DMSO-treated cells (2.8 ± 1.8 kPa), and for Piezo1 activation (Yoda1+DMSO-treated) cells (2.0 ± 1.1 kPa). GsMTx4-treated cells (Piezo1 inhibition) showed minimal stiffness increase (1.2 ± 0.5 kPa). A significant effect of Piezo1 inhibition was observed in the high-stiffness Ru6 hydrogels by day 5. GsMTx4-treated cell embedded gels retained a higher stiffness (7.5 ± 5.0 kPa) compared to untreated Ctr (4.0 ± 1.2 kPa, $p = 0.0041$), suggesting that inhibiting Piezo1 can attenuate cell-mediated softening of the ECM in stiffer environments over time. No significant differences were found between the DMSO (4.3 ± 1.7 kPa) and Yoda1+DMSO (4.9 ± 3.3 kPa) groups, indicating that Piezo1 activation did not further accelerate stiffness decrease. Across the earlier time points (4 hours to 2 days), all Ru6 gels, regardless of cell treatment condition, followed a similar trend of progressive

stiffness reduction. These observations suggest that while Piezo1 modulation did not markedly alter short-term stiffness changes, a prolonged effect of Piezo1 inhibition becomes apparent under high-stiffness conditions.

Interestingly, Piezo1 inhibition also attenuated hydrogel contraction in the low-stiffness Ru0 group. By day 5, Ctr Ru0 gel contracted significantly, with volume reduced to 32.6 ± 16.8 mm^3, whereas GsMTx4-treated Ru0 gel retained a larger volume of 82.4 ± 13.5 mm^3, indicating reduced contraction (Figure 6C).

After normalizing day 5 stiffness values to hydrogel volume, the restricted stiffness increases in GsMTx4-treated Ru0 hydrogels compared to the Ctr was completely eliminated. The normalized stiffness values for Ctr, DMSO, Yoda1+DMSO, and GsMTx4 were 0.085 ± 0.029, 0.089 ± 0.048, 0.089 ± 0.028, and 0.095 ± 0.026, respectively, indicating that the raw stiffness differences in Ru0 groups were primarily due to hydrogel contraction rather than intrinsic mechanical changes. In contrast, within the Ru6 group, the restricted stiffness reduction observed with GsMTx4 treatment became even more pronounced after normalization, suggesting that GsMTx4 mitigated the loss of intrinsic mechanical properties in stiffer hydrogels. The normalized stiffness values for Ctr, DMSO, Yoda1+DMSO, and GsMTx4 were 0.429 ± 0.118, 0.469 ± 0.218, 0.515 ± 0.341, and 0.868 ± 0.519, respectively, with GsMTx4-treated hydrogels showing significantly higher stiffness compared to Ctr ($P = 0.0002$), DMSO ($P = 0.0008$), and Yoda1+DMSO ($P = 0.0049$).

Together, these findings revealed that Piezo1 modulated both key mechanisms of UC-MSCs-driven hydrogel remodeling: the softening of stiff matrix through intrinsic ECM remodeling, and the stiffening of soft matrix via contraction.

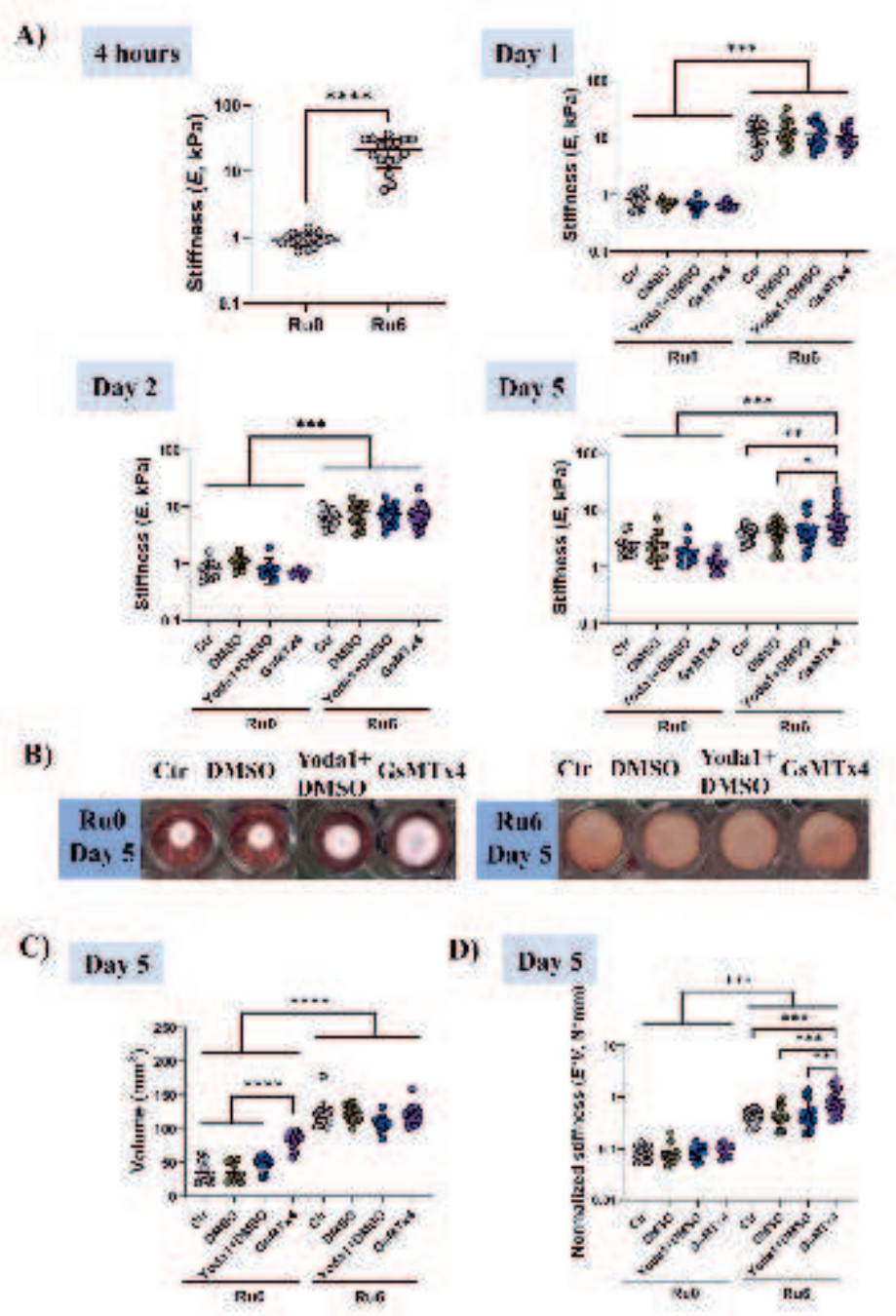

Figure 6. Effects of Piezo1 modulation on the stiffness and contraction of UC-MSC–embedded ECM hydrogels. A) Stiffness (*E*) of Ru0 and Ru6 hydrogels before (4 hours) and under Piezo1 inhibition (GsMTx4) and Piezo1 activation (Yoda1+DMSO)

conditions along with respective controls (Ctr, DMSO) over days 1, 2, and 5. B) Representative images of hydrogel shape at day 5 under different treatments. C) Hydrogel volume (mm^3) of hydrogels at day 5 under different treatments. D) Volume-normalized stiffness ($E \times V$, N·mm) at day 5, accounting for hydrogel contraction. Data are presented as mean ± SD (n = 3 biological donors), with each dot representing technical measurements (2 independent tests per hydrogel) from two hydrogel replicates per donor, totaling N = 6 hydrogel samples. Statistical significance was determined using one-way ANOVA (* $p < 0.05$, ** $p < 0.01$, *** $p < 0.001$, **** $p < 0.0001$).

3.7 Collagen matrix remodeling in UC-MSCs-embedded ECM hydrogels modulated by Piezo1

Based on the inhibition studies of Piezo1 where that remodeling of high stiffness hydrogels was Piezo1 regulated, we assessed its influence on collagen remodeling by UC-MSCs in all three stiffnesses over time. Piezo1 inhibition (GsMTx4) influenced UC-MSC-driven collagen remodeling, whereas Piezo1 activation (Yoda1) had no effect. In Ru0 group hydrogels, GsMTx4 treatment reduced dense collagen network formation, which progressively developed in the other groups (Fig. 7). No difference was observed between Yoda1+DMSO- and DMSO-treated hydrogels. Quantitative analysis before treatment initiation (at 4 hours) and after 5 days of culture are shown in Fig. 8. Additional early changes in FA, MI, and hole area (%) at days 1 and 2 are presented in Fig. S6. At day 5, GsMTx4-treated cell-embedded Ru0 hydrogels showed lower collagen FA compared to controls (65.0 ± 3.6 vs. 83.5 ± 2.4, $p < 0.0001$; Fig. 8A), along with a significant reduction in MI at all time points (day 1: 0.60 ± 0.07 vs. 0.67 ± 0.03, $p=0.0318$; day 2: 0.68 ± 0.03 vs. 0.75 ± 0.05, $p=0.0096$; day 5: 0.73 ± 0.02 vs. 0.87 ± 0.01, $p<0.0001$; Fig. 8A and Fig. S6). In contrast, all Ru6 hydrogels exhibited a gradual decline in FA and MI over time, with no treatment-related differences (Fig. 7, Fig. 8A and Fig. S6). Piezo1 modulation also affected hole formation in Ru6 hydrogels. At day 5, the hole area (%) in the control, DMSO, Yoda1+DMSO, and GsMTx4-treated Ru6 hydrogels was as follows: 2.1 ± 1.3%, 2.2 ± 1.4%, 3.3 ± 1.9%, and 1.7 ± 0.8%, respectively ($p=0.0295$ for Yoda1+DMSO-treated vs GsMTx4-treated hydrogel) (Fig. 8A).

At day 5, hydrogel volume-normalized FA (FA(norm)) was higher in GsMTx4-treated Ru0 hydrogels than in controls (Fig. 8B), suggesting that FA(raw) increases in control Ru0 hydrogels were mainly due to volume contraction. In

contrast, FA(norm) remained unchanged across all Ru6 hydrogels, indicating that Piezo1 modulation did not affect contraction or collagen density in stiffer hydrogels.

These findings show that Piezo1 inhibition (GsMTx4) inhibits ECM remodeling in alignment with its effects on stiffness and contraction. In Ru0 hydrogels, Piezo1 inhibition reduced collagen density, corresponding to decreased hydrogel contraction (Section 3.6). In Ru6 hydrogels, Piezo1 inhibition slowed down collagen hole formation while having little impact on collagen distribution, confirming with the relatively low reduction of stiffness.

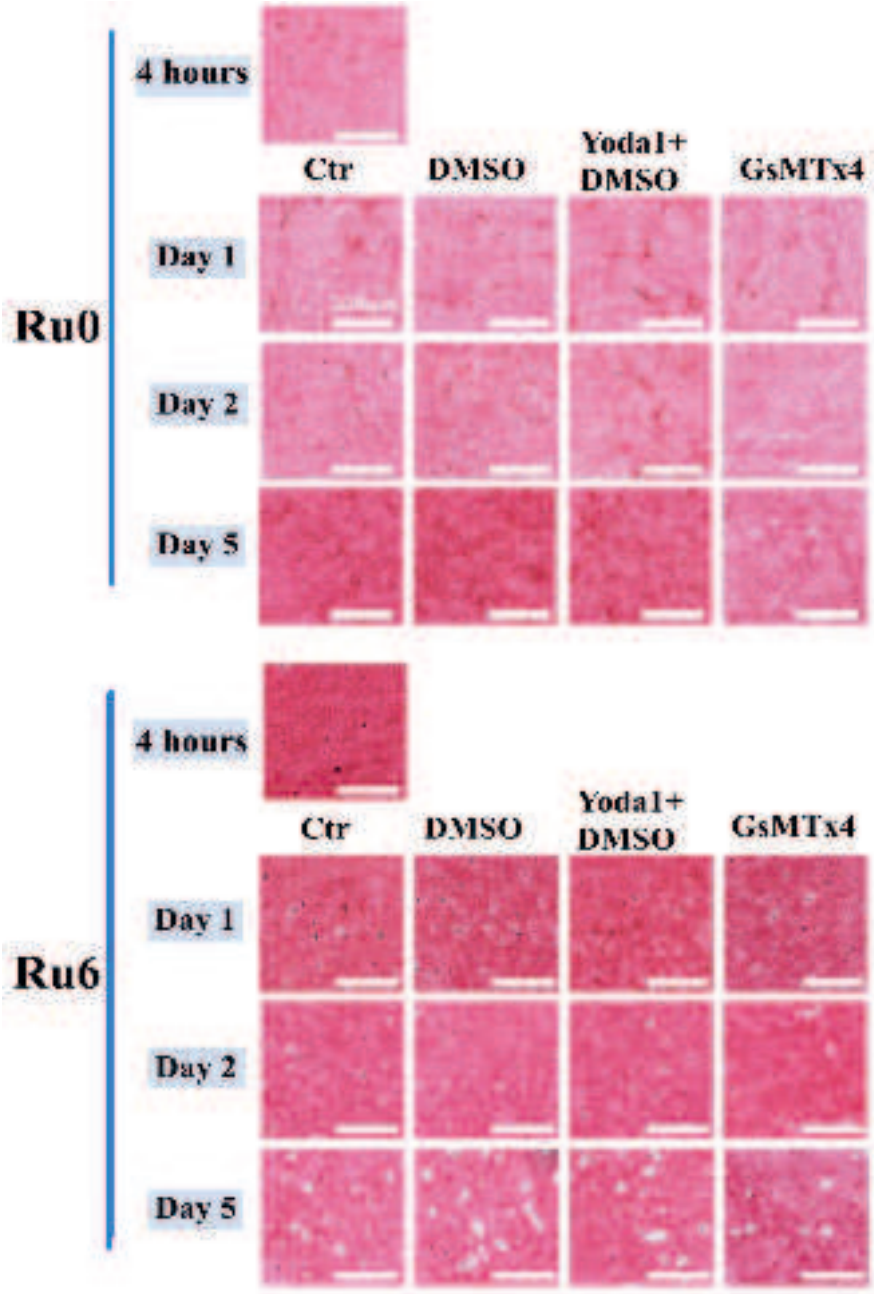

Figure 7. Collagen matrix remodeling in UC-MSCs-embedded ECM hydrogels after Piezo1 modulation. Representative PSR-stained collagen fibers images for Ru0 and Ru6 group hydrogels under different Piezo1 modulation treatments (Ctr, DMSO, Yoda1+DMSO (activation), and GsMTx4 (inhibition)) at 1, 2, and 5 days of culture (cell nuclei-blue black; collagen fiber-red). Scale bars:200 μm. PSR: Picrosirius red.

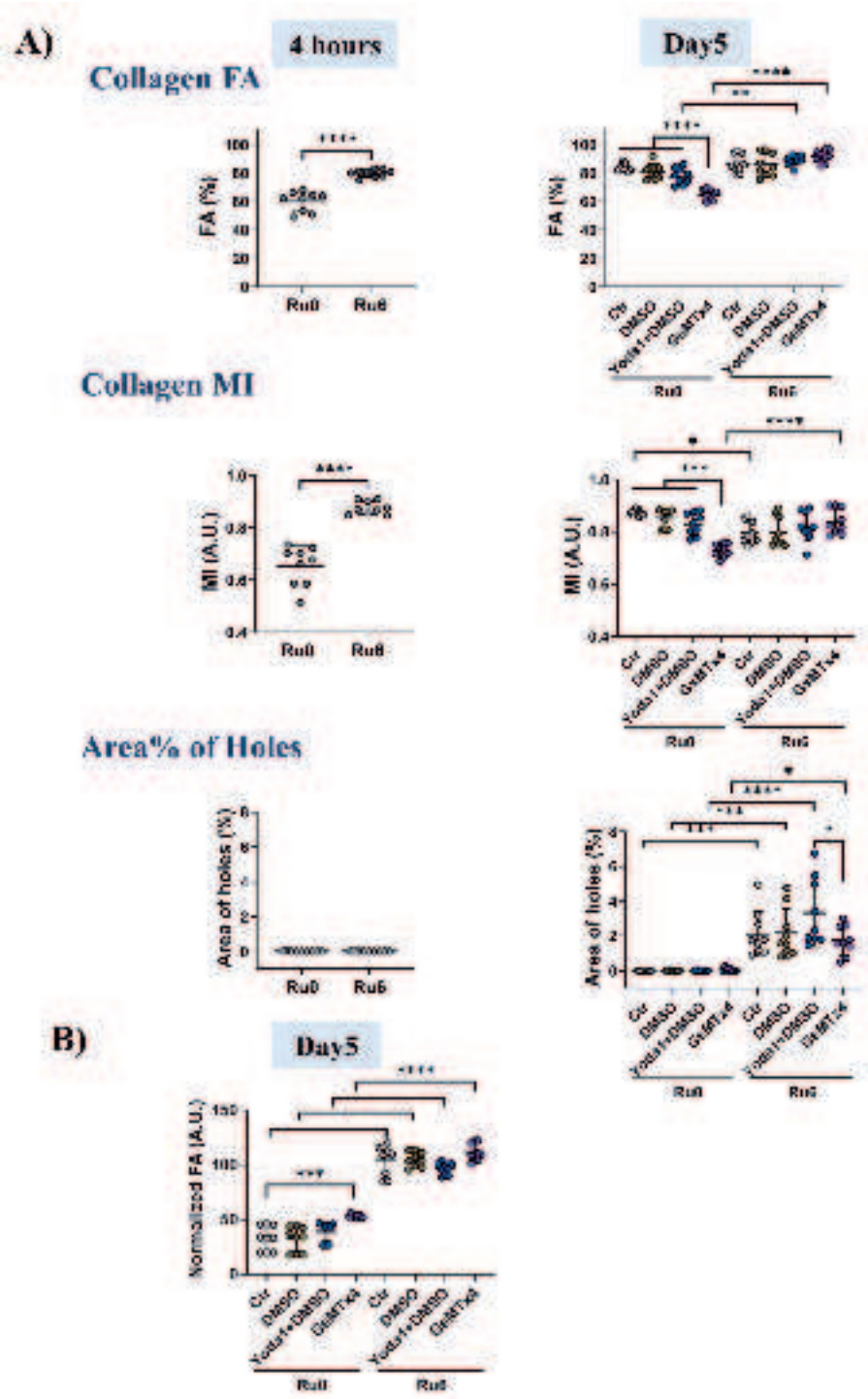

Figure 8. Quantitative analysis of collagen matrix remodeling in UC-MSCs-

embedded ECM hydrogels after Piezo1 modulation. A) Fractional area (FA), Mean intensity (MI) and Area percentage of collagen holes surrounding cells in Ru0 and Ru6 group hydrogels before treatment initiation (at 4 hours) and after 5 days of different Piezo1 modulation treatments B) Hydrogel volume-normalized FA(norm) =FA(raw) (%) $\times$V(mm^{-3}), accounting for contraction. FA was calculated by dividing the stained fiber area by the total image area. MI was determined by dividing the total color intensity by the total stained fiber area, representing the average PSR staining intensity of collagen fibers. Each dot represents data from three independent measurements of UC-MSC-embedded hydrogels for each cell donor (n = 3). Statistical significance was analyzed by one-way ANOVA (* $p < 0.05$, ** $p<0.01$, *** $p < 0.001$, **** $p<0.0001$).

3.8 Effect of Piezo1 modulation on cell viability, morphology, and protein expression in skin-derived hydrogels

After Piezo1 inhibition or activation, cell viability remained unaffected, with survival rates exceeding 90%. No changes in cell morphology were observed, except for cells from donor 1 in the Ru6 group, where Piezo1 inhibition caused the cells to transition from an elongated spindle shape to a small rounded morphology (Fig. S7). Additionally, at day 1, Piezo1 levels were higher in Ru6 hydrogels compared to Ru0 hydrogels, regardless of Piezo1 inhibition or activation. In the high-stiffness Ru6 group, Piezo1 activation increased Piezo1 protein levels compared to untreated cells, while Piezo1 inhibition had no effect. At days 2 and 5, Piezo1 expression in both Ru0 and Ru6 groups was similar across all four treatment conditions (Fig. S8).

These findings confirm that Piezo1 modulation does not affect cell viability or morphology, except in donor-specific cases under high-stiffness conditions. Given the minimal impact of Piezo1 activation on stiffness regulation and matrix remodeling, further investigations focused on Piezo1 inhibition (GsMTx4) and its effects on mechanotransduction signaling (pFAK, MMP2, and MMP14).

3.8.1 Piezo1 inhibition reduces pFAK expression

At day 1, Piezo1 levels were similar between the Ctr and GsMTx4-treated UC-MSCs in both the Ru0 and Ru6 hydrogels. However, by day 2, Piezo1 expression in GsMTx4-treated UC-MSCs was lower than in the Ctr cells in both Ru0 and Ru6 hydrogels (Ctr vs. GsMTx4 in Ru0 group: 0.28 ± 0.14 vs. 0.20 ± 0.08, $P = 0.0049$; Ctr vs. GsMTx4 in Ru6 group: 0.34 ± 0.04 vs. 0.27 ± 0.08, $P = 0.0154$).

Although pFAK levels decreased over time (Figure 9), pFAK expression in the GsMTx4-treated Ru6 group remained significantly lower than in the Ctr Ru6 group at day 5 (Ctr vs. GsMTx4 in Ru6 group: 0.29 ± 0.06 vs. 0.23 ± 0.07, P = 0.0006). Additionally, at days 1, 2, and 5, pFAK levels in the Ctr Ru6 hydrogels were consistently higher compared to Ru0 hydrogels. However, by day 5, the pFAK difference between the GsMTx4-treated Ru6 and Ru0 hydrogels at day 1 and day 2 was eliminated. These findings suggest that Piezo1 inhibition leads to a progressive reduction in pFAK expression, particularly in high-stiffness Ru6 hydrogels.

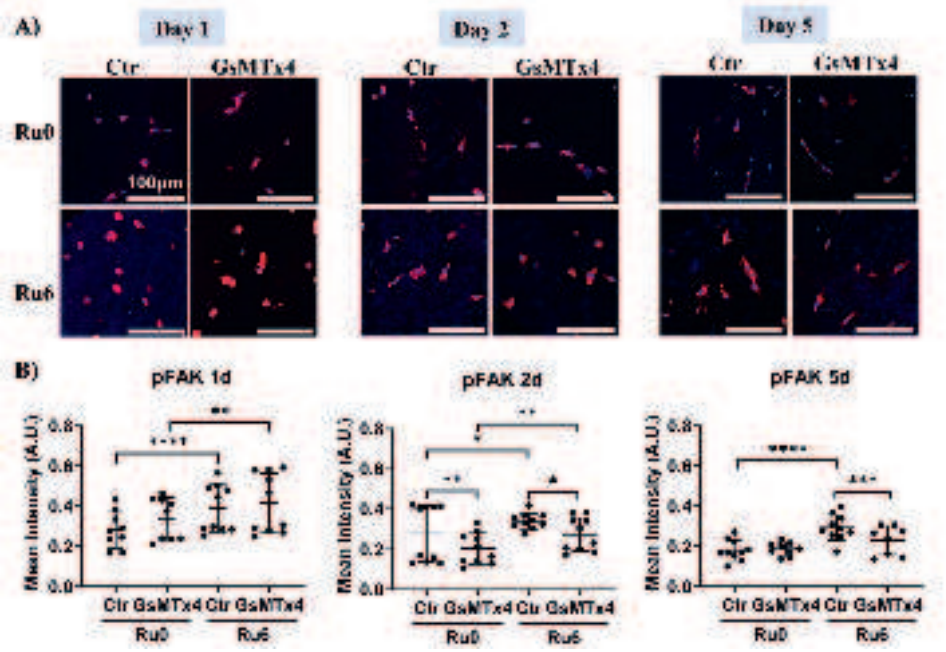

Figure 9. Expression of pFAK in UC-MSCs embedded within Ru0 and Ru6 ECM hydrogels following Piezo1 modulation at 1, 2, and 5 days. A) Representative immunofluorescence images of pFAK (red) in UC-MSCs cultured in ECM hydrogels under control (Ctr) and Piezo1 inhibition (GsMTx4) treatment. Cell nuclei are stained with DAPI (blue). **B)** Quantification of pFAK expression levels in UC-MSCs embedded in ECM hydrogels, based on mean fluorescence intensity (MFI). The MFI of pFAK was calculated by dividing the total fluorescence intensity by the total area of the positive pFAK staining regions. The data are presented as mean ± SD (n = 2), with each dot representing technical measurements from five independent tests, each performed on random regions within one hydrogel section per donor. Statistical significance was determined by two-way ANOVA (* $p < 0.05$, ** $p < 0.01$, *** $p < 0.001$, **** $p < 0.0001$).

3.9 Stiffness-dependent expression MMP2 and MMP14 is independent of piezo1 activity

At day 1, MMP2 expression was significantly higher in Ru6 hydrogels compared to Ru0 under both control and GsMTx4-treated conditions. (Ctr: Ru0 vs. Ru6: 0.15 ± 0.04 vs. 0.28 ± 0.04, P = 0.0296; GsMTx4-treated: Ru0 vs. Ru6: 0.09 ± 0.03 vs. 0.29 ± 0.03, P < 0.0001) (Figure10). By day 2, this difference disappeared under control conditions but reappeared by day 5. GsMTx4 treatment initially caused a difference in MMP14 expression between Ru0 and Ru6 at day 2, but this difference was eliminated by day 5.

Similar to MMP2, at day 1, MMP14 expression was significantly higher in Ru6 than in Ru0 hydrogels under control conditions (Ctr: Ru0 vs. Ru6: 0.21 ± 0.05 vs. 0.35 ± 0.05, P = 0.0051) (Figure11). By days 2 and 5, this difference disappeared. Under GsMTx4 treatment, the difference between Ru0 and Ru6 hydrogels at day 1 was eliminated, but by day 2, MMP14 expression in Ru6 was lower than in Ru0. By day 5, GsMTx4 treatment had no effect on MMP14 expression, with comparable MMP14 levels in both Ru0 and Ru6 hydrogels.

The results showed that both MMP2 and MMP14 expression increased with increasing hydrogel stiffness, consistent with their roles in stiffness-dependent matrix remodeling. However, there was no correlation between Piezo1 inhibition and the expression of MMP2 or MMP14 in UC-MSCs embedded in hydrogels, indicating that their stiffness-dependent regulation occurs independent of Piezo1 modulation.

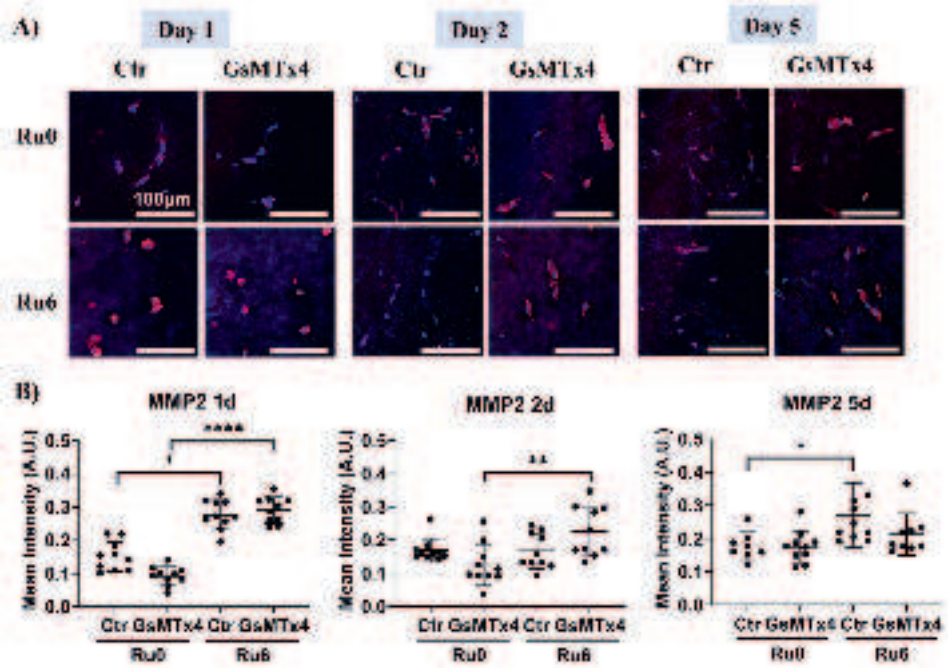

Figure 10. Expression of MMP2 in UC-MSCs embedded within Ru0 and Ru6 ECM hydrogels following Piezo1 modulation at 1, 2, and 5 days. A) Representative immunofluorescence images of MMP2 (red) in UC-MSCs cultured in ECM hydrogels under control (Ctr) and Piezo1 inhibition (GsMTx4) treatment. Cell nuclei are stained with DAPI (blue). **B)** Quantification of MMP2 expression levels in UC-MSCs embedded in ECM hydrogels, based on mean fluorescence intensity (MFI). The MFI of MMP2 was calculated by dividing the total fluorescence intensity by the total area of the positive MMP2 staining regions. The data are presented as mean ± SD (n = 2), with each dot representing technical measurements from five independent tests, each performed on random regions within one hydrogel section per donor. Statistical significance was determined by two-way ANOVA (* $p < 0.05$, ** $p < 0.01$, *** $p < 0.001$, **** $p < 0.0001$).

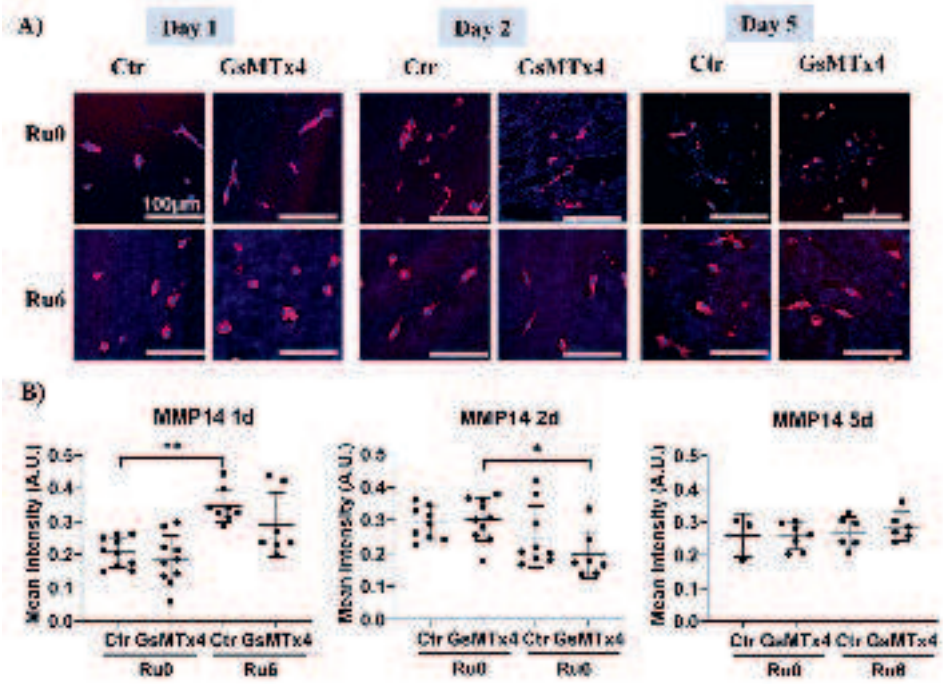

Figure 11. Expression of MMP14 in UC-MSCs embedded within Ru0 and Ru6 ECM hydrogels following Piezo1 modulation at 1, 2, and 5 days. A) Representative immunofluorescence images of MMP14 (red) in UC-MSCs cultured in ECM hydrogels under control (Ctr) and Piezo1 inhibition (GsMTx4) treatment. Cell nuclei are stained with DAPI (blue). **B)** Quantification of MMP14 expression levels in UC-MSCs embedded in ECM hydrogels, based on mean fluorescence intensity (MFI). The MFI of MMP14 was calculated by dividing the total fluorescence intensity by the total area of the positive MMP14 staining regions. The data are presented as mean ± SD (n = 2), with each dot representing technical measurements from five independent tests, each performed on random regions within one hydrogel section per donor. Statistical significance was determined by two-way ANOVA (* $p < 0.05$, ** $p < 0.01$, *** $p < 0.001$, **** $p < 0.0001$).

4. Discussion

Mechanotransduction, the process by which cells sense and respond to mechanical cues in their environment, is fundamental to cellular behavior and tissue remodeling. This study examined the stiffness-dependent behavior of UC-MSCs in 3D ECM hydrogels and revealed the mechanotransduction signaling

involved in mediating these processes. By employing ruthenium-catalyzed crosslinking to modulate skin-derived ECM hydrogels (Ru0, Ru3, and Ru6), we modulated the stiffness of skin-derived ECM hydrogels (Ru0, Ru3, and Ru6). This approach generated a stiffness range from 1.2 ± 0.5 kPa (Ru0) to 17.7 ± 8.9 kPa (Ru6), spanning values representative of normal skin to dermal scar tissue while they all exhibited rapid stress relaxation. After cell-embedding, by decoupling cell-mediated hydrogel contraction from ECM turnover, we demonstrate that UC-MSCs respond to matrix stiffness in a Piezo1-dependent fashion. Low stiffness drives contraction while high stiffness drives matrix remodeling both as part of the cells' mechanisms to reach an intermediate stiffness (1-5 kPa). Furthermore, we identified Piezo1 as a mechanosensor regulating these processes, with downstream effects on pFAK signaling but not MMP-mediated matrix degradation.

Cells generate traction forces exerting mechanical tension on their surrounding matrix. Softer ECMs offer minimal resistance, leading to pronounced contraction, while stiffer hydrogels provide more resistance, limiting contractabilty [12]. Beyond contraction, cellular activity also drives local ECM turnover i.e. ECM rearrangement, deposition and degradation, impacting hydrogel properties. To isolate and elucidate the effects of cell induced ECM remodeling and mechanotransduction across hydrogels of varying stiffness, we applied volume normalization of stiffness, stress relaxation, and fiber density. A linear model was assumed, where if a particular property would increase due to contraction, that property was multiplied with the hydrogel volume and vice versa a property which would decrease was divided by hydrogel volume.

UC-MSC morphology and ECM remodeling were significantly influenced by hydrogel stiffness, with cells adopting a more elongated and spindle-like shape in medium-stiffness hydrogels compared to soft and high-stiffness hydrogels. Volume-normalized data further elucidate the role of stiffness and hydrogel contraction in guiding these cellular behaviors and matrix remodeling patterns: In soft hydrogels, the compliance of the matrix results in relatively low resistance to cellular traction forces. While mechanosensing remains active, the mechanical feedback received by the cells is diminished compared to stiffer matrices. Consequently, cells contract the matrix predominantly through pulling ECM fibers closer together to form dense, compact networks and volume reduction, leading to increased stiffness. Medium-stiffness hydrogels appear to provide an

optimal mechanical balance between traction forces and matrix compliance, resembling the stiffness of human abdominal skin. In this environment, UC-MSCs experience sufficient counterforces to sustain traction without excessive dissipation or inhibition. This mechanical equilibrium appears to support a homeostatic cell–matrix interaction, allowing cells to maintain elongated morphologies while minimizing unnecessary remodeling activity. It suggests that medium-stiffness matrices offer the ideal mechanical environment for cellular mechanosensing and homeostatic ECM remodeling. In high-stiffness hydrogels, the matrix exhibits low compliance and resists deformation, thereby limiting cell elongation and spreading. Under these conditions, UC-MSCs experience elevated mechanical resistance upon generating traction forces, which may shift their mechanotransductive response toward matrix remodeling. Rather than relying solely on shape adaptation, cells may initiate ECM degradation and create localized porosity to reduce mechanical constraints. These stiffness-dependent behaviors demonstrate how UC-MSCs not only adapt their morphology in response to the surrounding matrix, but also actively remodel the ECM to create more favorable conditions.

Mechanosensitive ion channels and adhesion complex components have been proposed as primary mechanosensors for cells to sense and transduce mechanical cues [18-20]. Piezo1 is a mechanosensitive ion channel. Increasing evidence suggests that enhanced tissue mechanics stimulates Piezo1 expression across various cell types [10, 21, 22]. A study by Sun et al. [22] demonstrated that compared to substrates with a stiffness of 62–68 kPa, UC-MSCs cultured on softer matrices (13–16 kPa) exhibited lower Piezo1 levels. This finding aligns with our observations, where Piezo1 expression in UC-MSCs was stiffness-dependent.

Recent studies have described a synergistic relationship between Piezo1 and integrin-mediated focal adhesion signaling [23-25]. Piezo1 has been observed localized at focal adhesions, where it promotes their maturation in a force-dependent manner [26]. Following Piezo1 activation under frictional force (shear stress), Ca^{2+} influx activates calpain which directly impacts actin cytoskeletal organization and focal adhesion structure in endothelial cells, influencing their alignment [27, 28]. Our system similarly identified stiffness-dependent pFAK expression in UC-MSCs. Notably, Piezo1 inhibition reduced pFAK expression, positioning Piezo1 upstream of FAK activation. This FAK phosphorylation may,

in turn, contribute to downstream cytoskeletal remodeling processes such as RhoA/ROCK-dependent cellular contraction [29]. Similar Piezo1-FAK crosstalk occurs in invasive tumor cells, where stiffness-activated Piezo1 localized to focal adhesions to enable integrin-FAK signaling and ECM remodeling, creating a feedforward loop that amplifies tissue stiffening and aggression [30].

Importantly, Piezo1 inhibition attenuated UC-MSCs-driven hydrogel remodeling (the softening of stiff matrix through intrinsic ECM remodeling, and the stiffening of soft matrix via contraction), indicating that Piezo1-pFAK pathway acts as a regulator of MSC-ECM crosstalk. Besides, MMP2 and MMP14, enzymes involved in ECM degradation and remodeling, increased with ECM hydrogel stiffness (day 1), with their highest levels potentially contributing to ECM degradation in the stiff Ru6 hydrogels. Likewise, a study demonstrated that UC-MSC-conditioned medium significantly improved fibrosis pathology in animal models by enhancing MMP1 expression while reducing collagen content [6]. However, the insensitivity of MMP2/MMP14 to Piezo1 regulation suggests that UC-MSCs utilize some other, stiffness-dependent pathways for ECM remodeling. These observations underscore the complexity of UC-MSCs–matrix crosstalk and suggest that a coordinated network of mechanosensitive and stiffness-responsive mechanisms underlies the dynamic remodeling of the extracellular environment.

Conclusion:

In summary, our study identifies Piezo1 as a central mechanosensor guiding stiffness-dependent ECM remodeling by UC-MSCs in a 3D ECM hydrogel environment. Through the Piezo1-pFAK axis, cells contract soft matrices and degrade stiff ones, converging mechanical properties toward a common intermediate stiffness. Meanwhile, MMP2 and MMP14 respond to stiffness independently of Piezo1. These insights emphasize the dynamic interplay between cellular traction forces, ECM remodeling mechanisms, and mechanical microenvironments. Understanding this crosstalk may provide valuable guidance for designing engineered tissues and therapeutic strategies targeting fibrosis, wound healing, and regenerative medicine.

References:

1 Frantz, C., Stewart, K. M. & Weaver, V. M. The extracellular matrix at a glance. *J Cell Sci* 123, 4195-4200, doi:10.1242/jcs.023820 (2010).

2 Walma, D. A. C. & Yamada, K. M. The extracellular matrix in development. *Development* 147, doi:10.1242/dev.175596 (2020).

3 Martinez-Garcia, F. D., Valk, M. M., Sharma, P. K., Burgess, J. K. & Harmsen, M. C. Adipose Tissue-Derived Stromal Cells Alter the Mechanical Stability and Viscoelastic Properties of Gelatine Methacryloyl Hydrogels. *Int J Mol Sci* 22, doi:10.3390/ijms221810153 (2021).

4 Martinez-Garcia, F. D., van Dongen, J. A., Burgess, J. K. & Harmsen, M. C. Matrix Metalloproteases from Adipose Tissue-Derived Stromal Cells Are Spatiotemporally Regulated by Hydrogel Mechanics in a 3D Microenvironment. *Bioengineering (Basel)* 9, doi:10.3390/bioengineering9080340 (2022).

5 Zhang, M. *et al.* Fibroblasts alter the physical properties of dermal ECM-derived hydrogels to create a pro-angiogenic microenvironment. *Mater Today Bio* 23, 100842, doi:10.1016/j.mtbio.2023.100842 (2023).

6 Shi, X. *et al.* Human umbilical cord-derived mesenchymal stem cells attenuate hepatic stellate cells activation and liver fibrosis. *Mol Biol Rep* 51, 734, doi:10.1007/s11033-024-09664-6 (2024).

7 Migulina, N. *et al.* Mechanosensitive Channels in Lung Health and Disease. *Compr Physiol* 13, 5157-5178, doi:10.1002/cphy.c230006 (2023).

8 Fu, Y. *et al.* Targeting Mechanosensitive Piezo1 Alleviated Renal Fibrosis Through p38MAPK-YAP Pathway. *Front Cell Dev Biol* 9, 741060, doi:10.3389/fcell.2021.741060 (2021).

9 Zhao, X. *et al.* Mechanosensitive Piezo1 channels mediate renal fibrosis. *JCI Insight* 7, doi:10.1172/jci.insight.152330 (2022).

10 He, J., Cheng, X., Fang, B., Shan, S. & Li, Q. Mechanical stiffness promotes skin fibrosis via Piezo1-Wnt2/Wnt11-CCL24 positive feedback loop. *Cell Death Dis* 15, 84, doi:10.1038/s41419-024-06466-3 (2024).

11 Feng, X. *et al.* Piezo1 mediates the degradation of cartilage extracellular matrix in malocclusion-induced TMJOA. *Oral Dis* 30, 2425-2438, doi:10.1111/odi.14615 (2024).

12 Zhao, F. *et al.* Fibroblast alignment and matrix remodeling induced by a stiffness gradient in a skin-derived extracellular matrix hydrogel. *Acta Biomater* 182, 67-80, doi:10.1016/j.actbio.2024.05.018 (2024).

13 Wang, J. *et al.* Collagen-rich liver-derived extracellular matrix hydrogels augment survival and function of primary rat liver sinusoidal endothelial cells and hepatocytes. *Int J Biol Macromol* 278, 134717, doi:10.1016/j.ijbiomac.2024.134717 (2024).

14 Martinez-Garcia, F. D. *et al.* Architecture and Composition Dictate Viscoelastic Properties of Organ-Derived Extracellular Matrix Hydrogels. *Polymers (Basel)* 13, doi:10.3390/polym13183113 (2021).

15 Nizamoglu, M. *et al.* An in vitro model of fibrosis using crosslinked native extracellular matrix-derived hydrogels to modulate biomechanics without changing composition. *Acta Biomater* 147, 50-62, doi:10.1016/j.actbio.2022.05.031 (2022).

16 Schindelin, J. *et al.* Fiji: an open-source platform for biological-image analysis. *Nat*

Methods 9, 676-682, doi:10.1038/nmeth.2019 (2012).

17 McQuin, C. *et al.* CellProfiler 3.0: Next-generation image processing for biology. *PLoS Biol* 16, e2005970, doi:10.1371/journal.pbio.2005970 (2018).

18 Martinac, B. & Poole, K. Mechanically activated ion channels. *Int J Biochem Cell Biol* 97, 104-107, doi:10.1016/j.biocel.2018.02.011 (2018).

19 Sun, Z., Guo, S. S. & Fassler, R. Integrin-mediated mechanotransduction. *J Cell Biol* 215, 445-456, doi:10.1083/jcb.201609037 (2016).

20 Martino, F., Perestrelo, A. R., Vinarsky, V., Pagliari, S. & Forte, G. Cellular Mechanotransduction: From Tension to Function. *Front Physiol* 9, 824, doi:10.3389/fphys.2018.00824 (2018).

21 Gao, Q., Wang, M., Hou, X., Li, M. & Li, L. Substrate stiffness modulates osteogenic and adipogenic differentiation of osteosarcoma through PIEZO1 mediated signaling pathway. *Cell Signal* 127, 111601, doi:10.1016/j.cellsig.2025.111601 (2025).

22 Sun, Y. L., Jingwei Xu,Ziran Lin,Xiaoxuan Zhang,Xiaoling Li,Lisha Li,Yulin Matrix stiffness regulates myocardial differentiation of human umbilical cord mesenchymal stem cells. *Aging* 13, doi:10.18632/aging.202244 (2021).

23 Cheng, D., Wang, J., Yao, M. & Cox, C. D. Joining forces: crosstalk between mechanosensitive PIEZO1 ion channels and integrin-mediated focal adhesions. *Biochem Soc Trans* 51, 1897-1906, doi:10.1042/BST20230042 (2023).

24 Nourse, J. L. & Pathak, M. M. How cells channel their stress: Interplay between Piezo1 and the cytoskeleton. *Semin Cell Dev Biol* 71, 3-12, doi:10.1016/j.semcdb.2017.06.018 (2017).

25 Ellefsen, K. L. *et al.* Myosin-II mediated traction forces evoke localized Piezo1-dependent Ca(2+) flickers. *Commun Biol* 2, 298, doi:10.1038/s42003-019-0514-3 (2019).

26 Mingxi Yao *et al.* Force- and cell state–dependent recruitment of Piezo1 drives focal adhesion dynamics and calcium entry. *Science Advances* 8, doi:10.1126/sciadv.abo1461 (2022).

27 Li, J. *et al.* Piezo1 integration of vascular architecture with physiological force. *Nature* 515, 279-282, doi:10.1038/nature13701 (2014).

28 McHugh, B. J. *et al.* Integrin activation by Fam38A uses a novel mechanism of R-Ras targeting to the endoplasmic reticulum. *J Cell Sci* 123, 51-61, doi:10.1242/jcs.056424 (2010).

29 Pathak, M. M. *et al.* Stretch-activated ion channel Piezo1 directs lineage choice in human neural stem cells. *Proc Natl Acad Sci U S A* 111, 16148-16153, doi:10.1073/pnas.1409802111 (2014).

30 Chen, X. *et al.* A Feedforward Mechanism Mediated by Mechanosensitive Ion Channel PIEZO1 and Tissue Mechanics Promotes Glioma Aggression. *Neuron* 100, 799-815 e797, doi:10.1016/j.neuron.2018.09.046 (2018).

Supplementary Materials:

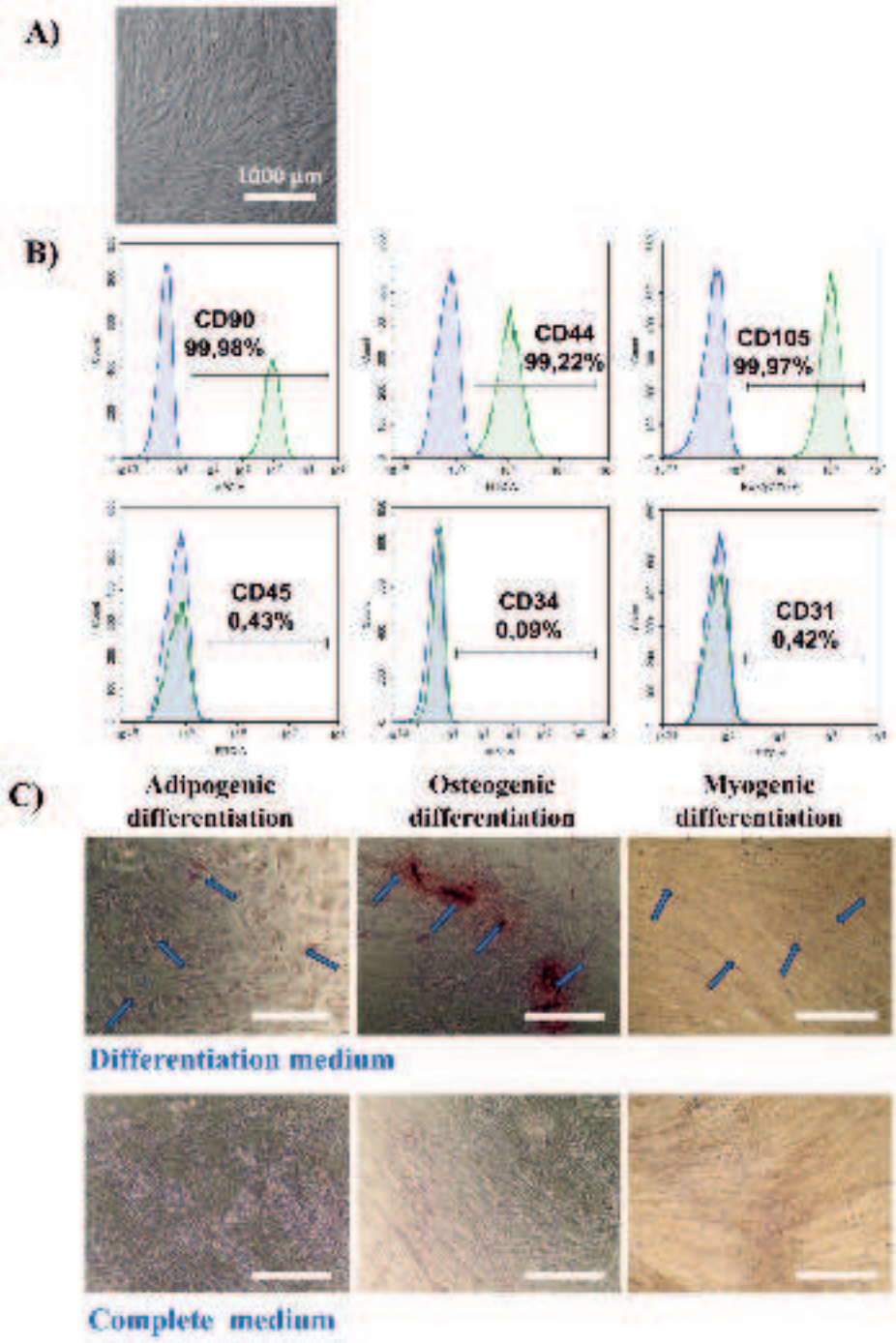

Fig. S1. Characterization of cultured UC-MSCs. A) Cell morphology of UC-MSCs on reaching 80% confluence. Scale bar = 1000 μm. B) FACS analysis of UC-MSCs for the surface markers CD31, CD34, CD45, CD44, CD90, and CD105. UC-MSCs were negative for hematopoietic/endothelial markers (CD31, CD34, CD45; <1% positivity) and positive for MSC markers (CD44, CD90, CD105; >99% positivity (n=5)). Histograms show isotype controls (purple) versus antigen-specific staining (green). C) Differentiation potential identification of UC-MSCs after 2 weeks treatment with complete medium and differentiation induction medias. Adipogenesis as detected by the formation of lipid vacuoles, stainable with Oil Red O. Osteogenesis as detected by the formation of calcium deposits, stainable with Alizarin Red S. Myogenic differentiation, specifically toward SMCs, was confirmed by α-SMA expression through immunohistochemistry staining. Blue arrows highlight positively stained regions. Scale bar = 1000 μm. Data show representative images from five independent donors.
Abbreviations: UC-MSC, umbilical cord mesenchymal stem cells; FACS, Fluorescence-Activated Cell Sorting (a specialized type of flow cytometry); SMCs, smooth muscle cells; α-SMA, α-smooth muscle actin.

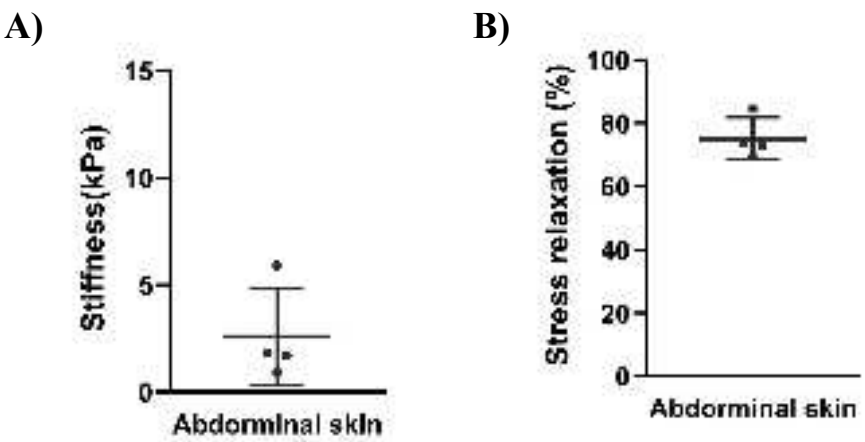

Fig. S2. The mechanical properties of the normal human abdominal skin tissue. A) Stiffness; B) Stress relaxation. The data represents the mean ± standard deviation generated from four independent experiments on one piece of skin from one donor.

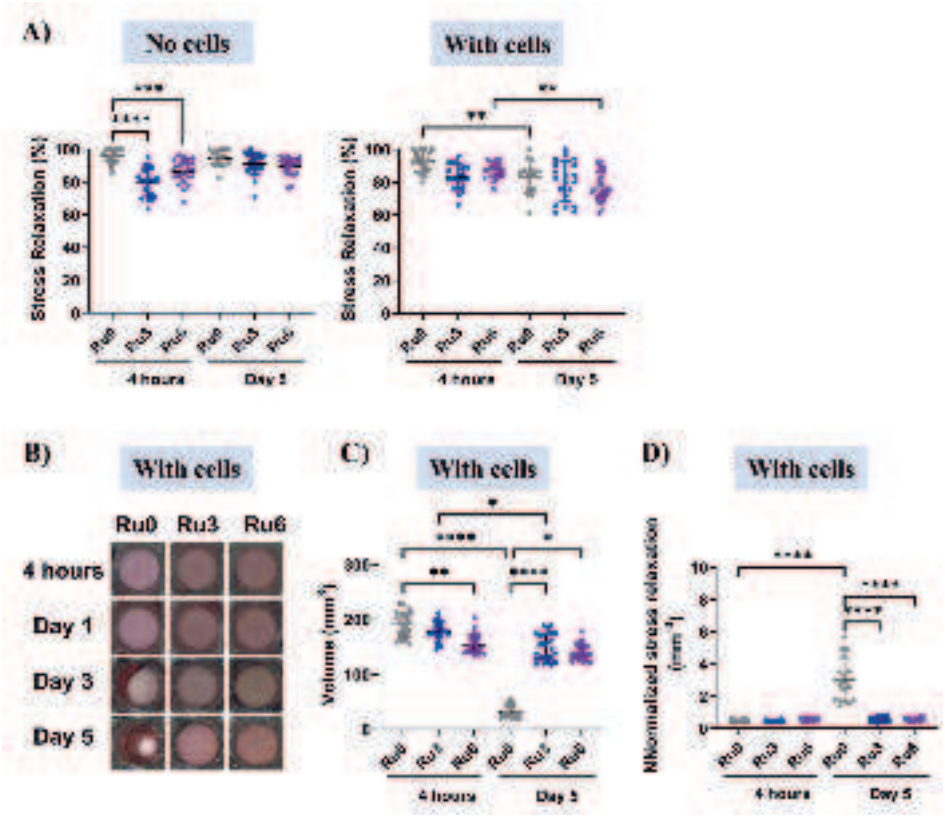

Fig. S3. The raw and volume-normalized stress relaxation of ECM hydrogels with/without UC-MSCs. A) Stress relaxation of ECM hydrogels (Ru0, Ru3, and Ru6) at 4 hours and Day 5 in the absence (left) and presence (right) of UC-MSCs; B) Hydrogel shape changes (top view): Representative images of the hydrogels at 4 hours, Day 1, Day 3, and Day 5, showing the degree of contraction over time in hydrogels with cells; C) Volume (V, mm^3) of cell-embedded ECM hydrogels at 4 hours and day 5. D) Hydrogel volume-normalized stress relaxation ($SRnorm = SRraw/V$) of cell-embedded hydrogels at 4 hours and day 5, which decouple geometric effects (hydrogel contraction) from intrinsic matrix remodeling. Data are expressed as mean ± standard deviation (SD; n = 5 biological donors), with each dot representing technical measurements (two independent tests per hydrogel) from two hydrogel replicates per donor, resulting in a total of N = 10 hydrogel samples. Statistical significance was analyzed by one way ANOVA (* $p < 0.05$, ** $p<0.01$, *** $p < 0.001$, **** $p<0.0001$).

Results: the raw and volume-normalized stress relaxation of ECM hydrogels

Although the embedded UC-MSCs influenced hydrogel stress relaxation, all three hydrogel groups exhibited stress relaxation values exceeding 77% at both the initial 4-hour time point and after five days of cell culture (Fig. S2). This indicates the rapid stress relaxation and significant viscoelasticity of the ECM hydrogel.

In Ru0 hydrogels, stress relaxation decreased from 92.5 ± 6.1% to 82.6 ± 9.6% (4h vs 5d, $P = 0.0056$), while Ru6 hydrogels showed a reduction from 87.1 ± 4.9% to 77.3 ± 8.9% (4h vs 5d, $P = 0.0033$). In contrast, Ru3 hydrogels, which had medium stiffness, exhibited no significant change in stress relaxation (83.1 ± 7.6% vs. 80.8 ± 12.2% for 4h vs 5d, $P > 0.05$). By Day 5, all three hydrogel groups had stress relaxation values within a comparable range (Fig. S2A).

At 4 hours, Ru0, Ru3, and Ru6 hydrogels displayed similar normalized stress relaxation values (Fig. S2D), consistent with trends observed in the raw stress relaxation data. However, after five days, the decrease in raw stress relaxation observed in Ru6 was no longer evident after normalization, whereas the decrease in Ru0's raw stress relaxation shifted to an increase in the normalized values. Since stress relaxation is influenced by multiple factors beyond hydrogel contraction-induced changes in matrix density—such as molecular chain mobility, water movement/redistribution, and time-dependent viscoelastic responses—the interpretation of the normalized data remains complex and challenging to fully elucidate.

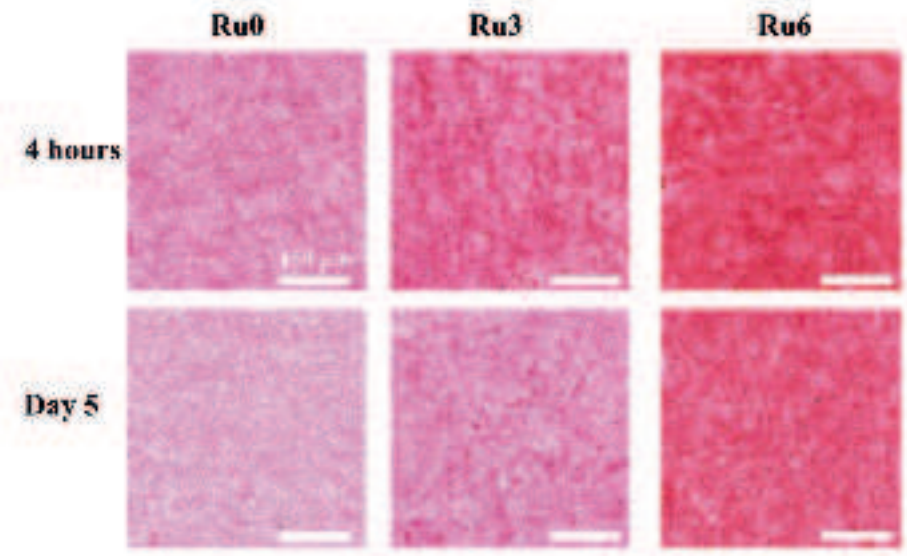

Fig. S4. Characterization of ECM protein fiber structure in non-cell embedded ECM hydrogels with variable stiffness. Representative images of PSR staining on 4μm section of non-cell embedded ECM hydrogels (Ru0, Ru3, Ru6) after 4 hours and 5days of soaking in cell culture medium (collagen fiber-red). Scale bars:150 μm.

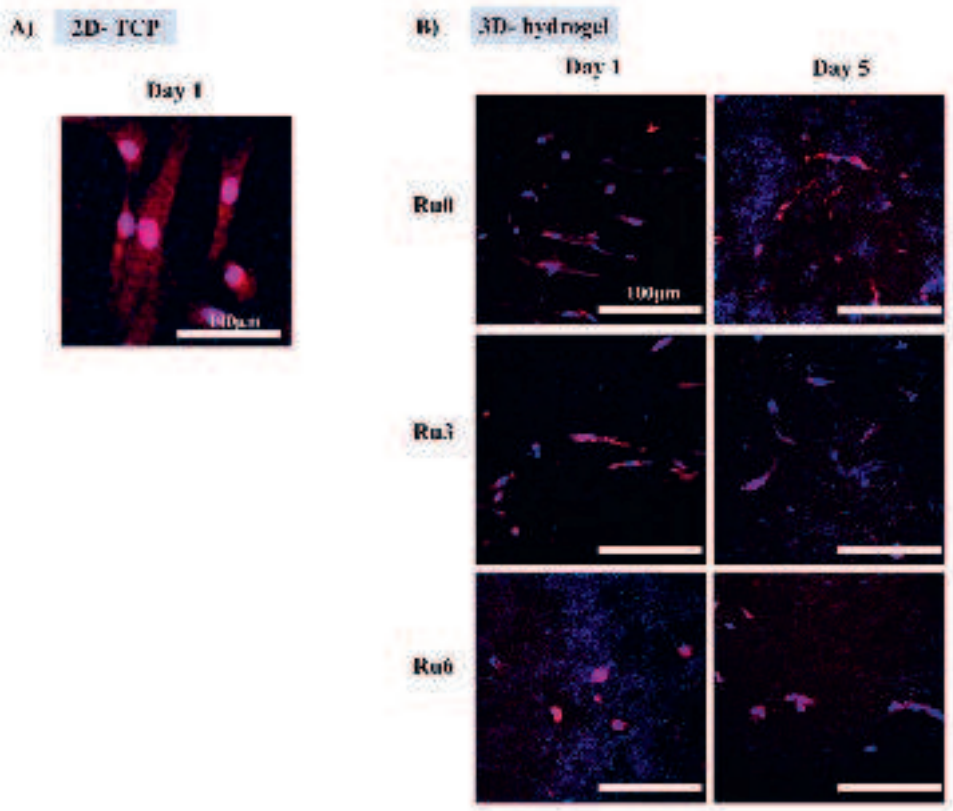

Fig. S5. YAP expression in 2D and 3D cultured UC-MSCs. A) Representative immunofluorescence images showing YAP expression (red) in UC-MSCs cultured on TCP plastic (ultra-stiff substrate) and B) in ECM hydrogels (Ru0, Ru3, and Ru6) at day 1 and day 5. Cell nuclei are stained with DAPI (blue).

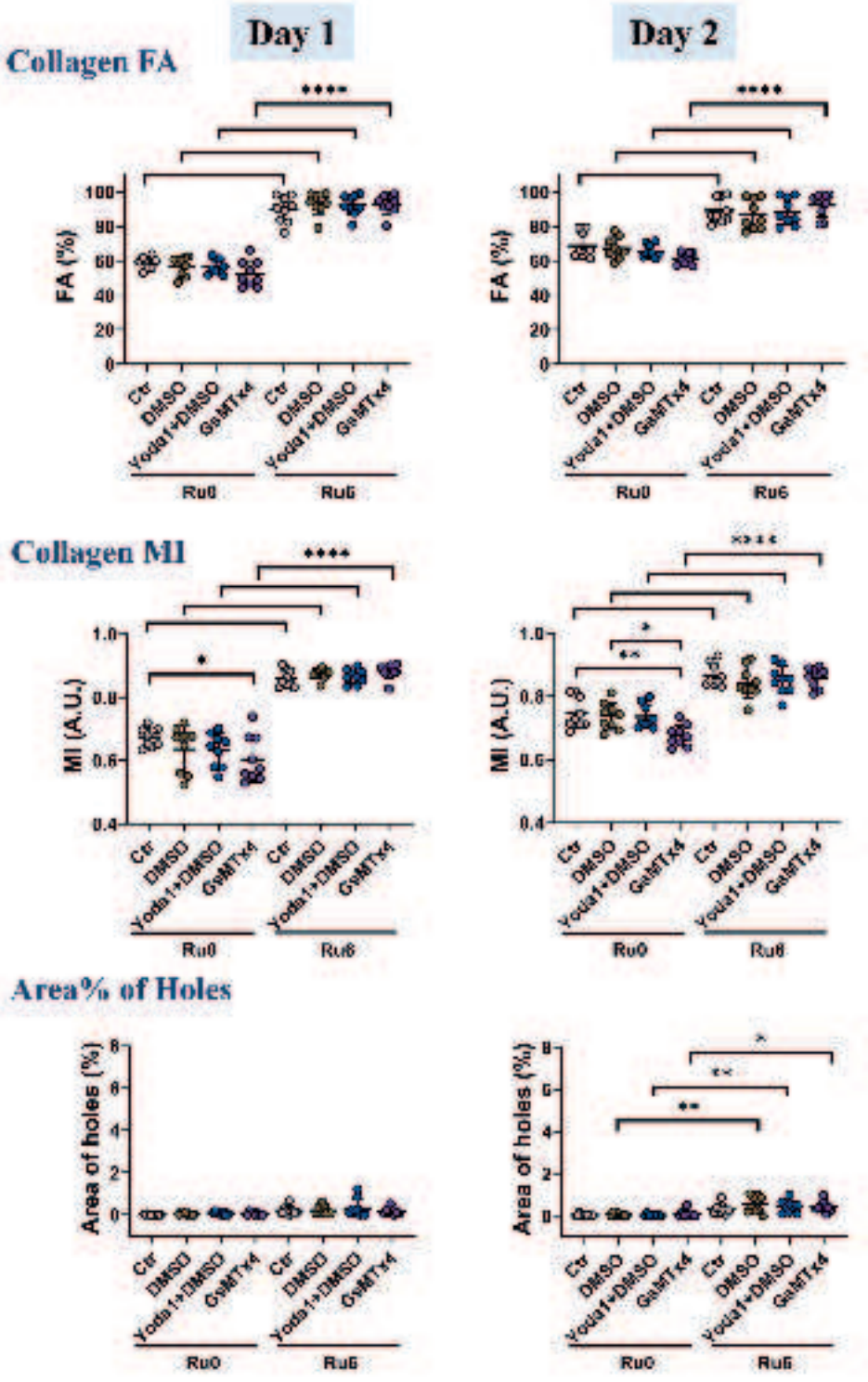
Day 1
Day 2
Collagen FA
FA (%)
Collagen MI
MI (A.U.)
Area% of Holes
Area of holes (%)
Ctr
DMSO
Yoda1+DMSO
GsMTx4
Ru0
Ru6

Fig. S6. Quantitative analysis of collagen matrix remodeling in UC-MSCs-embedded ECM hydrogels after Piezo1 modulation. Fractional area (FA), Mean intensity (MI) and Area percentage of collagen holes surrounding cells in Ru0 and Ru6 group hydrogels across different Piezo1 modulation treatments at day 1 and day 2. FA was calculated by dividing the stained fiber area by the total image area. MI was determined by dividing the total color intensity by the total stained fiber area, representing the average PSR staining intensity of collagen fibers. Each dot represents data from three independent measurements of UC-MSC-embedded hydrogels for each cell donor (n = 3). Statistical significance was analyzed by one-way ANOVA (* $p < 0.05$, ** $p<0.01$, *** $p < 0.001$, **** $p<0.0001$).

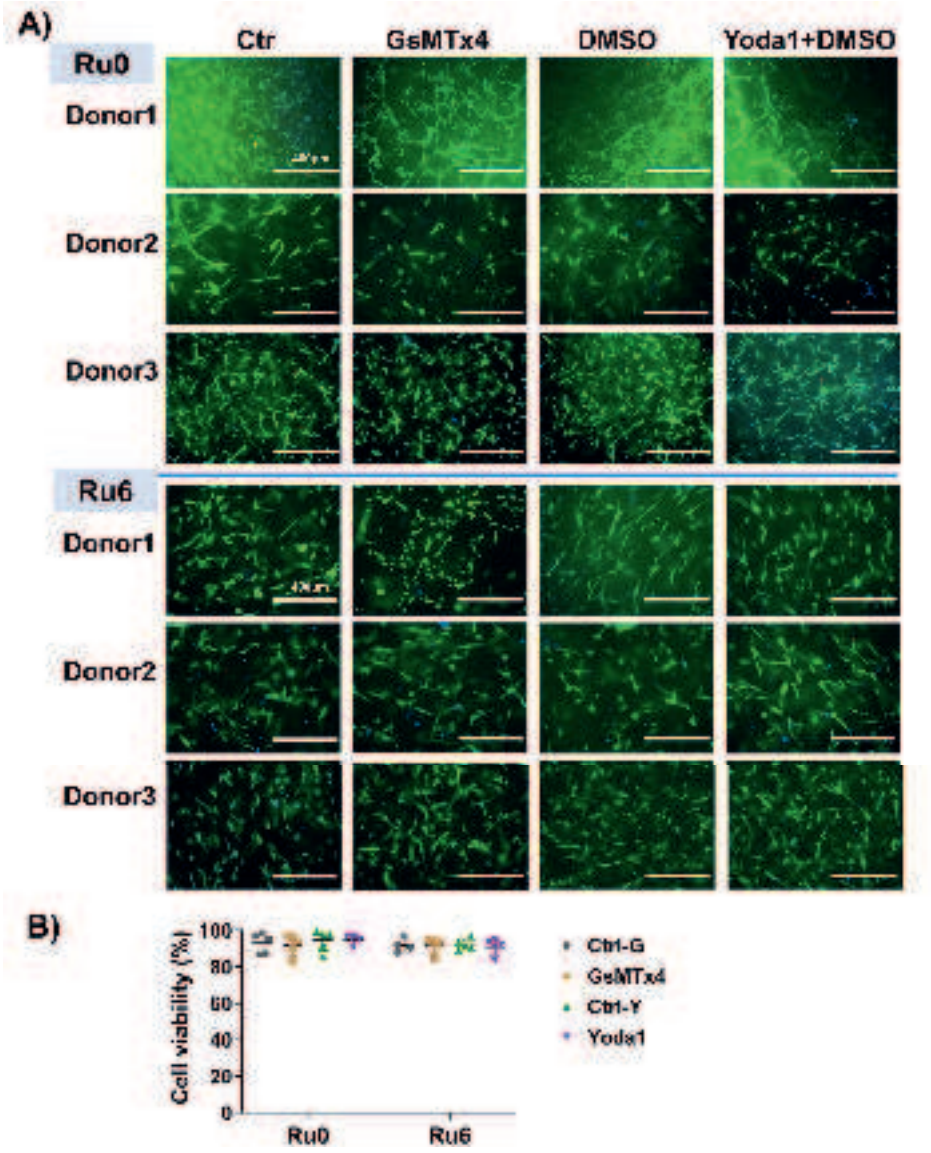

Fig. S7. The morphology and viability of embedded UC-MSCs in Ru0 and Ru6 ECM hydrogels over 5 days Piezo1 modulation. A) Representative images showing live-dead and nuclei staining of UC-MSCs in hydrogels. Live cells were stained with Calcein AM (green), nuclei with Hoechst (blue), and dead cells with PI (red). These overlap images show merged channels. B) Quantification of cell viability, expressed as the percentage (%) of dead cells (PI-positive/DAPI-positive). Data were obtained from two replicate hydrogel samples per donor (n = 3 donors). One image per hydrogel was taken at 10x magnification. Scale bars: 400 μm.

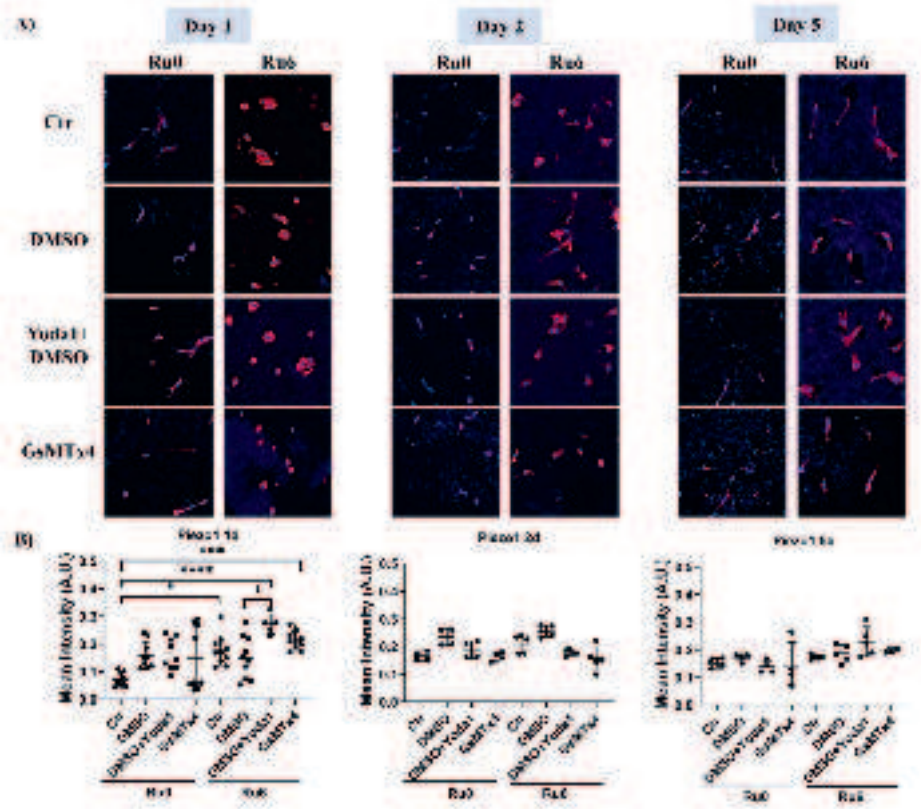

Fig. S8. **Expression of Piezo1 in UC-MSCs embedded within Ru0 and Ru6 ECM hydrogels following Piezo1 modulation at 1, 2, and 5 days. A)** Representative immunofluorescence images of Piezo1 (red) in UC-MSCs cultured in ECM hydrogels under different treatment conditions: Ctr, DMSO, Yoda1+DMSO, and GsMTx4. Cell nuclei are stained with DAPI (blue). **B)** Quantification of Piezo1 expression levels in UC-MSCs embedded in ECM hydrogels, based on mean fluorescence intensity (MFI). The MFI was calculated by dividing the total fluorescence intensity by the total area of the positive Piezo1 staining regions. The data are presented as mean ± SD (n = 2), with each dot representing technical measurements from five independent tests, each performed on random regions within one hydrogel section per donor. Statistical significance was determined by two-way ANOVA (* $p < 0.05$, ** $p < 0.01$, *** $p < 0.001$, **** $p < 0.0001$).

Discussion:

Volume normalization to compensate for hydrogel contraction (Continued.)

Despite the advantages of using linear volume normalization, it may have limitations. For example, Contracted hydrogels (e.g., Ru0, 48% volume loss) exhibit strain-hardening from pore collapse, violating $E \propto 1/V$. And, stress relaxation would also be influenced by molecular chain mobility and water redistribution introduce time-dependent effects beyond density. Whatsmore, for collagen fiber staining on 2D section, tight fiber packing in contracted matrices (e.g., Ru0 FA(raw) 84.6%) saturates pixel detection, masking true 3D remodeling. Therefore, while linear volume normalization provides useful insights, it should be regarded as a reference rather than definitive evidence of intrinsic ECM remodeling.

Chapter 8

General discussion

Disruptions in extracellular matrix (ECM) biochemical and biomechanical signals leads to tissue fibrosis or scarring characterized by excessive ECM deposition and tissue stiffening. Increasing evidence suggests that ECM stiffness directly regulates cell activation and sustains fibrotic cascades [1-3]. This thesis investigated two interconnected hallmarks of fibrosis: (1) ECM remodeling and (2) neovascularization and how these are regulated by stiffness. Using organ-derived ECM hydrogels with tunable mechanical properties, we investigated the dynamic interplay between ECM biomechanics and mesenchymal cells. Additionally, we explored the role of mesenchymal cells and ECM properties in modulating endothelial cell-driven neovascularization.

1. The value of 3D ECM hydrogel models

Proper physiological function of living tissues depends on their viscoelasticity, which is the time-dependent relaxation of mechanical stress [4]. Our 3D organ-derived ECM hydrogel model largely retains the biochemical and structural complexity of native ECM while partly preserving its viscoelastic properties. Thus, our ECM hydrogel model provides a physiologically relevant platform to study interactions between ECM and single or multiple cell types with tunable viscoelasticities which deepens insight into tissue-specific mechano-transduction dynamics.

Early studies primarily explored the regulation of cell behavior by ECM mechanical properties using two-dimensional (2D) culture models [5, 6]. However, cells naturally interact with ECM in 3D. Aashrith and coworkers systematically compared the differences in mechanotransduction mechanisms between 2D and 3D models, highlighting the irreplaceable value of 3D systems in mimicking pathological and physiological microenvironments [7]. To achieve precise ECM mechanical tuning, hydrogels based on alginate, silk, methacrylated gelatin (GelMA), and hyaluronic acid, have been developed [8-10]. Additionally, photocrosslinked GelMA and allylated gelatin (GelAGE) hydrogels, due to their tunable properties, have been shown to generate linear stiffness gradients through differential light attenuation using transparency gradient photomasks [11, 12]. Similarly, Pedron et al employed microfluidic technology to fabricate 3D hydrogels with graded stiffness by modulating the hyaluronic acid concentration gradient [13]. A key innovation of this thesis is the development of tunable stiffness hydrogels based on organ-derived ECM, including gradient-stiffness

hydrogels and separate hydrogels with distinct stiffness levels, which replicate the mechanical environments of both healthy and fibrotic tissues. Notably, our models not only preserve the biochemical signaling and structural complexity of native ECM but also offer a simple, equipment-free approach for generating tunable mechanical properties.

These two models serve different purposes. On the one hand, discrete stiffness hydrogels are ideal to investigate the influence of varying levels of stiffness on cell-ECM interactions in fibrotic and heathy tissues. On the other hand, gradient stiffness hydrogels allow us to explore dynamic cell behavior, such as migration and adaptation, across a spectrum of varying stiffnesses that e.g. mimics the progression from healthy to fibrotic tissue.

However, while gradient stiffness hydrogels provide a more physiologically relevant platform, they also present challenges. Firstly, cell-induced hydrogel contraction e.g. dermal fibroblasts (HDFn) showed very little contraction, and only in soft part of gradient dECM hydrogels (**Chapter 6**). However, different cells have different contractility characteristics. The UC-MSCs exhibited a higher contractility that contracted the soft non-crosslinked ECM hydrogel (**Chapter 7**) than HDFn (**Chapter 6**, soft hydrogel shape data not shown). This means that consideration of whether there is a need for minimal/no- hydrogel contraction is an element that needs to be taken along in research design consideration. Secondly, there are analytical limitations. The challenges involved in isolating cells from specific stiffness regions hinder mechano-transcriptomic profiling (e.g., qPCR), necessitating the engagement of new methodologies to enable spatially resolved molecular analysis.

Despite these limitations, in vitro encapsulated cells in 3D ECM-derived hydrogels remain valuable tools for unraveling the often complex cell-ECM interactions and have potential applications in fibrosis research, therapeutic development, and regenerative medicine.

2. ECM stiffness, both a stimulus to cells and a target for modulation

During progression of fibrotic disease, changes in ECM stiffness alter cellular mechanosensing, driving pathological remodeling. This raises the question of how stiffness influences the phenotype of mesenchymal cells within ECM

hydrogels of fixed composition.

2.1 ECM stiffness regulates cellular phenotype

The ECM and cells are in a continuous mutual and dynamic interaction. Our findings suggest mesenchymal cells (fibroblasts and UC-MSCs) respond dynamically to ECM stiffness, adjusting their behavior to adapt mechanical cues.

In our model, phenotypic changes in HDFn cells initially emerged in the soft and medium stiffness regions, characterized by a 45° alignment (day 1). Subsequently, cells within the stiffer hydrogel regions also exhibited a similar 45° alignment pattern by day 5, despite the stiffness gradient having already been adjusted due to cell-mediated ECM remodeling. This delayed response highlights a mechanical hysteresis effect, where cells retain memory of prior mechanical environments. Such memory aligns with report on cardiac fibroblasts isolated from a softer tissue of the volume overload heart failure model (aortocaval fistula). These fibroblasts exhibit a hypofibrotic phenotype compared to control fibroblasts from normal tissue when cultured on high stiffness polyacrylamide gels. This phenotype is characterized by suppressed ECM synthesis and lower YAP ((Yes-associated protein)) and MRTF-A (Myocardin-related transcription factor A) transcriptional activators nuclear translocation despite elevated TGF-β levels [14]. Similarly, fibroblasts cultured in stiff microenvironments maintain a profibrotic phenotype over several weeks when switched to a soft substrate [15]. Besides morphology, gradient stiffness is often found to guide cells to migrate in the direction of greater stiffness (durotactic migration). For example, Ektoras et al. observed durotactic migration of dermal fibroblast toward stiff ECM in 3D collagen matrices after 6 days [16]. However, our system showed 45° cell orientation along the direction of stiffness increasing but no durotactic migration across the stiffness gradient (**Chapter 6**). This alignment suggests that while fibroblasts exhibit some degree of collective organization, they may prioritize local stiffness sensing over directed migration. Rapid ECM degradation (formation of pores in the ECM matrix) and contraction (by day 5) possibly disrupted the gradient before sustained signaling that induced durotatic responses could occur, emphasizing the importance of autonomous ECM remodeling over paracrine signaling.

Like HDFn, other neonatal mesenchymal cell types such as UC-MSCs exhibit

stiffness-dependent mechanomemory. When UC-MSCs were cultured in medium-stiffness hydrogels—mimicking healthy dermis—they adopted elongated, spindle-shaped morphologies. Even after ECM remodeling reduced initial stiffness differences of the ECM microenvironments by day 5, UC-MSCs that started in medium-stiffness hydrogels retained higher aspect ratios than those that started in softer or stiffer hydrogels (**Chapter 7**), reinforcing the persistence of stiffness-induced mechanomemory.

2.2 Mesenchymal cells as ECM remodelers: sensing and changing the ECM stiffness to create a suitable environment

Decades of research have established that MSCs, including UC-MSCs, are widely used in experimental regenerative therapies for fibrosis and wound healing. To date, their effects are primarily attributed to paracrine signaling [17-20]. Our findings extend this understanding by demonstrating that UC-MSCs actively regulate ECM mechanics through stiffness-dependent remodeling.

In soft ECM hydrogels, UC-MSCs remodeled the ECM to form dense collagen bundles, driving hydrogel contraction, and increasing the stiffness. In high-stiffness regions on the other hand, the cells upregulated matrix metalloproteinase (MMP) activity that likely contributed to the increased number and size of pores (**Chapter 7**). The UC-MSCs mediated-ECM remodeling activity consistently shifted ECM mechanics toward a state more comparable to the stiffness of healthy dermal tissue. This phenomenon aligns with clinical and *in vivo* studies that report that MSCs mitigate fibrosis by normalizing ECM architecture in liver, lung, and dermal injury patients [21-24]. Likewise, HDFn fibroblasts remodeled ECM in hydrogels in a manner similar to UC-MSCs (**Chapter 6**), suggesting these mesenchymal cell types share mechanoregulatory capabilities.

A critical finding was the UC-MSCs' mechanomemory in UC-MSC-mediated ECM remodeling. This continuous remodeling, coupled with mechanomemory effects in cell morphology (**Section 2.1**), underscores the necessity for early biomechanical interventions to prevent pathological stiffness-regulated phenotypes. Obviously, this demands to recognize fibrotic disease in early stages too and thus requires improves (self)diagnostics tools too.

Targeting epigenetic regulators has emerged as a strategy to erase mechanical memory [25, 26]. For example, histone deacetylase (HDAC) inhibitors, such as

SAHA (suberoylanilide hydroxamic acid) and CG200745, were reported to prevent histone deacetylation, thereby altering gene transcription and resetting fibrosis-induced cell states [27]. SAHA has been shown to block TGF-β1-induced fibrotic differentiation of human lung fibroblasts. Similarly, evidence indicated that CG200745 mitigates cardiac hypertrophy and fibrosis in hypertensive rats by downregulating collagen I and III, connective tissue growth factor (CTGF), and fibronectin [28]. Given these findings, investigating whether HDAC inhibitors can reverse gradient stiffness-induced mechanical memory presents an exciting direction for future research.

2.3 Mechanosensing in 3D

The ECM–cell interactions require mechanosensing and inward mechano-signaling to adjust the cells' phenotype and to have the cells adjust the surrounding ECM too. Thus, mechanosensing and the subsequent molecular signaling pathways are relevant to dissect and understand.

In 2D culture on a stiff substrate, the transcriptional regulator YAP is a well-known mechanosensor that mediates stiffness-induced cell responses [29]. However, we observed that YAP signaling likely did not occur in cells embedded in 3D ECM hydrogels, regardless of stiffness (**Chapter 7**). We corroborate the results of a study on YAP-independent mechanotransduction in breast cancer patient samples and mechanically tunable 3D cultures. The authors show that MCF10A-human breast epithelial cells exhibited reduced nuclear size and decreased nuclear YAP intensity when cultured in the 3D hydrogel (a calcium alginate-Matrigel mix) compared to 2D hydrogel cultures and the lack of YAP activity in 3D culture was considered to be associated with the absence of perinuclear stress fibers [30].

We provide evidence that UC-MSCs embedded in skin ECM hydrogels, employ Piezo1 and focal adhesion kinase (FAK) as mechanosensors. Piezo1, a mechanosensitive ion channel, is found in numerous mechanosensitive tissues such as the kidneys, skin, lungs, and cartilage, where it regulates cellular responses to mechanical cues [31]. Increased matrix stiffness activates Piezo1 in bone marrow-derived macrophages, promoting proinflammatory polarization and suppressing wound healing [32]. Similarly, Chen et al. reported that Piezo1 gene expression was upregulated in endothelial cells of bleomycin-induced pulmonary

fibrosis mice, while endothelial-specific Piezo1 knockout alleviated fibrosis [33]. Our findings align with these observations, as UC-MSCs cultured in 3D ECM hydrogels exhibited a stiffness-dependent increase in Piezo1 expression (day 1, **Chapter 7**). We also observed increased phosphorylated FAK (pFAK) expression in UC-MSCs with ECM stiffening (**Chapter 7**), corroborating findings in induced pluripotent stem cell-derived MSCs (iMSCs), where pFAK levels increased with matrix stiffness [34]. However, this relationship is not universal—pancreatic ductal adenocarcinoma cells cultured in stiff 3D synthetic peptide gels exhibited downregulated FAK and unchanged levels of pFAK [35]. This suggests that the gel's unique composition, which supports cell adhesion through non-integrin-dependent mechanisms, may bypass FAK phosphorylation responses to stiffness.

Notably, Piezo1 inhibition reduced pFAK expression, positioning Piezo1 upstream of FAK activation. This hierarchy suggests Piezo1-mediated calcium signaling facilitates focal adhesion maturation, enabling mechanotransduction. Similar crosstalk occurs in invasive tumor cells, where stiffness-activated Piezo1 localized to focal adhesions to drive integrin-FAK signaling and ECM remodeling, creating a feedforward loop that amplifies tissue stiffening and glioma aggression [36]. Likewise, Piezo1 coordinated integrin recruitment at the leading edge of migrating T cells via calpain activation [37], further underscoring its role in adhesion complex dynamics.

Piezo1 inhibition treated by GsMTx4 did not reduce MMP2/MMP14 upregulation in UC-MSCs in stiff hydrogels, indicating MMP expression can be governed by FAK-independent pathways (**Chapter 7**). Integrin-ECM interactions are likely candidates, as integrins are major regulators of MMP expression [38]. For instance, collagen-binding integrins ($\alpha_1\beta_1$ and $\alpha_2\beta_1$) regulate MMP-13 expression in human dermal fibroblasts via p38 MAPK signaling in 3D collagen hydrogels [39]. The lack of direct Piezo1-pFAK control over MMP2/MMP14 regulation in our system suggest other mechano signaling pathways. These findings show the intricate interplay between Piezo1, pFAK, and MMP pathways in 3D ECM microenvironments. Unraveling their precise mechanistic relationships will deepen our understanding of how cells sense and respond to mechanical cues.

3. ECM Remodeling and Vascularization: A dynamic stromal

interplay

In *in vivo* wound healing, neo-vascularization and ECM remodeling are parallel processes. Previous work from our group showed that lipofilling of subdermal areas reduced symptomatic scars. This coincided with matrix remodeling, increased vascularization and immune cell infiltration. The originally thick, parallel-aligned collagenous fibers in dermal scars became thinner and more randomly organized, particularly in vascularized areas [21]. This raised a key question: Does ECM remodeling drive vascular niche formation, follow as a consequence of vascularization, or do both processes occur simultaneously in a mutually reinforcing manner? The ECM hydrogel platforms gave us the opportunity to dissect the bidirectional relationship between ECM remodeling and vascularization.

We observed that embedded endothelial cells initiated vascular network formation (VNF) within ECM hydrogels. During this process, endothelial cells actively remodeled the matrix, forming longer and thicker collagen fiber bundles with distinct intersecting gaps (**Chapter 4**). However, vascular maturation and stabilization depend on pericyte-like mesenchymal support [40, 41]. Pericytes are defined by their morphological integration into capillary basement membranes and direct endothelial contact [42]. They are recruited by primordial endothelium and differentiate from mesenchymal cells [40]. Previous work from our group demonstrated that adipose-derived stem cells co-cultured with endothelial cels act as pro-angiogenic pericytes, enhancing VNF [43, 44]. In this thesis, fibroblasts assumed a pericyte-like role, significantly enhancing VNF by further remodeling the ECM into a pro-angiogenic niche—characterized by increased stiffness, larger fiber diameters, and greater porosity. Notably, this effect was endothelial cell-dependent; fibroblasts alone, when embedded in ECM hydrogels, did not induce comparable matrix remodeling (**Chapter 4**). This suggests that endothelial cells actively prime fibroblasts for matrix remodeling, further reinforcing the dynamic interplay between vascularization and ECM adaptation.

While increased ECM stiffness is generally associated with enhanced vascularization, excessive stiffness disrupts vessel network formation. Fibroblasts played a dual role in this process—promoting vessel stabilization through ECM remodeling and stiffening but also posing a risk of pathological stiffening under excessive fibrotic responses.

A key advance of our work lies in resolving the "mechanical vs. biochemical influences on VNF" debate in vascularization. While many studies focus on individual ECM properties (e.g., stiffness, porosity), the ECM integrates multiple features that regulate vascularization. Our PCA-driven analysis of VNF in organ-specific hydrogels (skin, lung, and hybrid gels) revealed that mechanical properties—porosity, viscosity, stiffness, and fiber diameter—were the primary drivers of VNF (**Chapter3**). These findings build upon prior studies highlighting the influence of mechanical cues, particularly stiffness, in angiogenesis. However, our work advances this understanding by systematically disentangling the relative contributions of mechanical and biochemical factors of ECM to vascularization [45, 46].

In conclusion, we reveal that vascularization and ECM remodeling, though concurrent in healing tissues, are independently executable programs that are cross-regulated through biomechanical feedback.

4. Can ECM stiffness modulation reverse fibrosis?

This thesis demonstrates that mesenchymal cells dynamically remodel ECM in a stiffness-dependent manner and augment endothelial-driven angiogenesis (Chapters 4, 6, 7). These findings partly explain our previous clinical observations of fat grafting on dermal scars where scar remodeling coincides with vascular restoration, accompanied by an influx of M2 macrophages. This triad—ECM remodeling, neovascularization, and immune reprogramming—suggests that fibrosis reversal requires coordinated reinstatement of the multicomponent tissue niche, transcending ECM mechanics regulation alone.

Reframing the therapeutic challenge: beyond ECM softening

Current strategies targeting fibrosis reversal include MMP activation, TGF-β inhibition, and lysyl oxidase (LOX) inhibition (LOX: an enzyme that promotes collagen and elastin cross-linking and is elevated in many fibrotic diseases). These approaches rely on enzymatic ECM degradation but face a fundamental limitation: fibrotic tissues exhibit mechanical and biochemical memory. While these strategies can transiently soften ECM, they fail to establish a functional new ECM or alter the cells' memory phenotype. Resident fibroblasts in fibrosis may continue perpetuating profibrotic signaling even in softened environments (Section 2). Thus, durable resolution demands cellular reprogramming to erase

pathological memory.

Building on mesenchymal cells' mechanosensing and remodeling capabilities, we propose a synergistic approach that integrates biochemical and biomechanical signaling to drive fibrosis reversal. Firstly, targeted ECM degradation can be achieved through localized decoupling, involving the delivery of MMP-9/TIMP-1 regulators to dissolve excessive crosslinks while preserving physiologic ECM architecture. Another approach is mechano-priming, where Piezo1 activation amplifies mesenchymal cells' ECM-degrading capacity. Secondly, after ECM degrading, epigenetic resetting offers another strategy, including Piezo1 inhibition to halt mesenchymal cell degradation phenotypes and pause ECM degradation. Additionally, HDAC inhibitors (e.g., SAHA, CG200745) can reset fibrotic transcriptional programs and sensitize activated fibroblasts to mechanical normalization. Thirdly, multicomponent crosstalk further enhances therapeutic potential. Co-delivery of mesenchymal cells with M2-polarized macrophages and endothelial cells can reconstitute the pro-regenerative factors (IL-10, VEGF-A, HGF), enabling mesenchymal cells to remodel ECM into a functional state that achieves both biochemical and biomechanical balance.

While this framework advances beyond isolated ECM modulation, critical questions remain: Can biomechanical, biochemical, and immune parallel targeting effectively reconstruct functional new ECM? Can Piezo1 inhibitors and HDAC inhibitors achieve spatiotemporal specificity to avoid erasing cell memory in adjacent healthy tissues? Addressing these challenges will require advanced in vivo models for further exploration. Nevertheless, coupling mechanoadaptive strategies with epigenetic resetting offers a promising roadmap for fibrosis reversal.

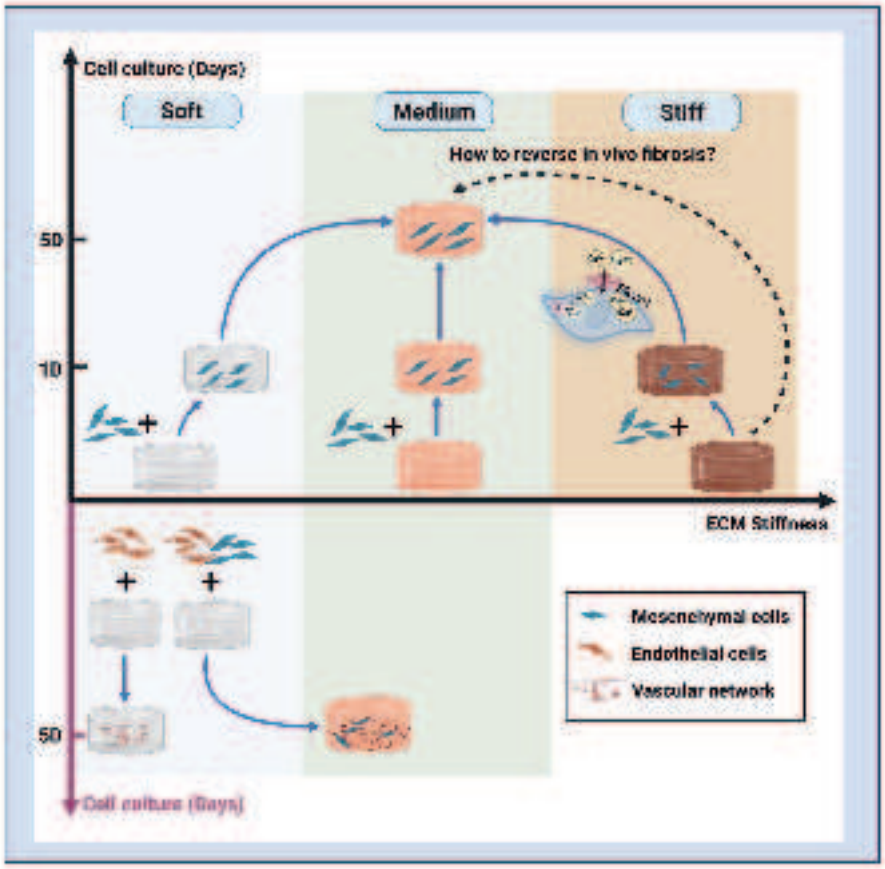

Figure 1. Illustration of mechanical regulation in stromal cell-ECM dynamic interactions. This figure highlights key findings regarding the dynamic interplay between ECM mechanics and stromal cells. To replicate normal and fibrotic tissue mechanics, organ-derived ECM hydrogels with variable stiffness were generated as a model to study fibrosis and tissue remodeling. The light blue background represents the soft hydrogel region, the green background indicates the medium-stiffness region, and the yellow background denotes the high-stiffness region. Top Panel: ECM stiffness acts as both a stimulus to mesenchymal cells and a target for modulation. Under different stiffness conditions in 3D ECM hydrogels, mesenchymal cells display stiffness-dependent phenotypes. Cells in both soft and stiff gels remodel the ECM to align with a medium stiffness zone. Mechanotransduction pathways, particularly Piezo1 and pFAK signaling (highly expressed in stiff gels), mediate these dynamic cell-ECM interactions. The dashed line highlights an open question raised in Part 4 of the general discussion:

How can *in vivo* fibrosis be reversed through ECM stiffness modulation? Bottom Panel: ECM remodeling and vascularization demonstrate a dynamic stromal interplay. Compared to endothelial cell-mediated vascularization alone, mesenchymal cells (as ECM remodelers) enhance vascular network formation when co-cultured with endothelial cells. This occurs by aligning with endothelial cells, remodeling the ECM, and increasing ECM stiffness, creating a pro-vascularization environment. Figure created with BioRender.

Future Perspectives:

Advancing our understanding of ECM mechanics and cellular responses holds significant potential for fibrosis treatment. Several key areas merit further exploration:

Dynamic tunable stiffness hydrogels to decipher mechanomemory mechanisms-- Existing hydrogels that can soften or stiffen on demand (e.g. light-responsive hydrogels) could provide a valuable tool for studying how cells adapt to dynamic mechanical environments. These systems may help determine whether oscillatory stiffness cues reset profibrotic memory or induce regenerative plasticity. Additionally, they may help identify molecular brakes, such as TIMPs, that prevent excessive ECM degradation and maintain the balance between tissue repair and fibrosis.

Cellular reprogramming: erasing mechanomemory-- While HDAC inhibitors have reported showing promise in resetting fibrotic transcriptional programs, their potential synergy with mechanical interventions in mesenchymal cells remains unexplored. Future studies could culture UC-MSCs in high-stiffness ECM hydrogels for several days, followed by HDAC inhibitor treatment, to assess epigenetic reprogramming. Similarly, genetic editing of mechanosensors (such as *PIEZO1* knockout) could clarify whether disrupting mechanosensing pathways erases stiffness-induced mechanomemory, offering a dual genetic-mechanical strategy for fibrosis reversal.

Immune-mesenchymal crosstalk-- Our clinical fat grafting study demonstrated neovascularization and M2 macrophage influx alongside scar softening [21]. However, the precise role of immune cells in scar remodeling remains unclear. Evidence suggests that modulating macrophage phenotypes, particularly shifting toward the M2 phenotype, could promote ECM remodeling and potentially aid in fibrosis reversal [47-49]. While this thesis explored endothelial-mesenchymal crosstalk, future work should investigate how immune-mesenchymal interactions contribute to breaking the fibrotic feedback loop and restoring tissue homeostasis.

Translational Considerations-- Bridging the gap between research and therapeutic applications requires addressing several factors. Developing ECM-based hydrogels that closely mimic the stiffness properties of healthy tissues could improve scaffolds for cell transplantation. Given that ECM stiffness varies across

tissues and disease stages, patient-specific stiffness profiling may be essential for precision-targeted anti-fibrotic treatments. Furthermore, while MSCs and fibroblasts have demonstrated ECM remodeling capacity, it remains unclear whether their effects are long-lasting or if repeated interventions are necessary for sustained therapeutic outcomes.

Collectively, these future directions could pave the way for novel regenerative therapies that integrate mechanical and biochemical cues to reverse fibrosis. By unraveling the complex interplay between ECM mechanics, cellular reprogramming, and immune-mesenchymal interactions, the development of personalized and durable anti-fibrotic strategies may become a reality, offering new hope for patients suffering from fibrotic diseases.

References:

1 He, J., Cheng, X., Fang, B., Shan, S. & Li, Q. Mechanical stiffness promotes skin fibrosis via Piezo1-Wnt2/Wnt11-CCL24 positive feedback loop. *Cell Death Dis* 15, 84, doi:10.1038/s41419-024-06466-3 (2024).

2 Han, X., Zhang, C., Lei, Q., Xu, J. & Zhou, Y. Stiffness regulates extracellular matrix synthesis in fibroblasts by DDR1-TGF-β/STAT3 mechanotransduction axis. *Biomaterials Advances* 172, doi:10.1016/j.bioadv.2025.214240 (2025).

3 Najafi, M., Farhood, B. & Mortezaee, K. Extracellular matrix (ECM) stiffness and degradation as cancer drivers. *J Cell Biochem* 120, 2782-2790, doi:10.1002/jcb.27681 (2019).

4 Chaudhuri, O., Cooper-White, J., Janmey, P. A., Mooney, D. J. & Shenoy, V. B. Effects of extracellular matrix viscoelasticity on cellular behaviour. *Nature* 584, 535-546, doi:10.1038/s41586-020-2612-2 (2020).

5 Sridharan, R., Cavanagh, B., Cameron, A. R., Kelly, D. J. & O'Brien, F. J. Material stiffness influences the polarization state, function and migration mode of macrophages. *Acta Biomater* 89, 47-59, doi:10.1016/j.actbio.2019.02.048 (2019).

6 Chester, D. *et al.* Elucidating the combinatorial effect of substrate stiffness and surface viscoelasticity on cellular phenotype. *J Biomed Mater Res A* 110, 1224-1237, doi:10.1002/jbm.a.37367 (2022).

7 Saraswathibhatla, A., Indana, D. & Chaudhuri, O. Cell-extracellular matrix mechanotransduction in 3D. *Nat Rev Mol Cell Biol* 24, 495-516, doi:10.1038/s41580-023-00583-1 (2023).

8 Ort, C., Chen, Y., Ghagre, A., Ehrlicher, A. & Moraes, C. Bioprintable, Stiffness-Tunable Collagen-Alginate Microgels for Increased Throughput 3D Cell Culture Studies. *ACS Biomater Sci Eng* 7, 2814-2822, doi:10.1021/acsbiomaterials.1c00129 (2021).

9 Baruffaldi, D., Palmara, G., Pirri, C. & Frascella, F. 3D Cell Culture: Recent Development in Materials with Tunable Stiffness. *ACS Appl Bio Mater* 4, 2233-2250, doi:10.1021/acsabm.0c01472 (2021).

10 Hasturk, O., Jordan, K. E., Choi, J. & Kaplan, D. L. Enzymatically crosslinked silk and silk-gelatin hydrogels with tunable gelation kinetics, mechanical properties and bioactivity for cell culture and encapsulation. *Biomaterials* 232, 119720, doi:10.1016/j.biomaterials.2019.119720 (2020).

11 Orsi, G., Fagnano, M., De Maria, C., Montemurro, F. & Vozzi, G. A new 3D concentration gradient maker and its application in building hydrogels with a 3D stiffness gradient. *J Tissue Eng Regen Med* 11, 256-264, doi:10.1002/term.1908 (2017).

12 Vahala, D. *et al.* 3D Volumetric Mechanosensation of MCF7 Breast Cancer Spheroids in a Linear Stiffness Gradient GelAGE. *Adv Healthc Mater* 12, e2301506, doi:10.1002/adhm.202301506 (2023).

13 Pedron, S., Becka, E. & Harley, B. A. Spatially gradated hydrogel platform as a 3D engineered tumor microenvironment. *Adv Mater* 27, 1567-1572, doi:10.1002/adma.201404896 (2015).

14 Kirk, T., Ahmed, A. & Rognoni, E. Fibroblast Memory in Development, Homeostasis and Disease. *Cells* 10, doi:10.3390/cells10112840 (2021).

15 Achterberg, V. F. *et al.* The Nano-Scale Mechanical Properties of the Extracellular Matrix Regulate Dermal Fibroblast Function. *Journal of Investigative Dermatology* 134, 1862-1872, doi:10.1038/jid.2014.90 (2014).

16 Hadjipanayi, E., Mudera, V. & Brown, R. A. Guiding cell migration in 3D: a collagen matrix with graded directional stiffness. *Cell Motil Cytoskeleton* 66, 121-128, doi:10.1002/cm.20331 (2009).

17 Guillamat-Prats, R. The Role of MSC in Wound Healing, Scarring and Regeneration. *Cells* 10, doi:10.3390/cells10071729 (2021).

18 El Agha, E. *et al.* Mesenchymal Stem Cells in Fibrotic Disease. *Cell Stem Cell* 21, 166-177, doi:10.1016/j.stem.2017.07.011 (2017).

19 Shi, M. *et al.* Mesenchymal stem cell therapy in decompensated liver cirrhosis: a long-term follow-up analysis of the randomized controlled clinical trial. *Hepatol Int* 15, 1431-1441, doi:10.1007/s12072-021-10199-2 (2021).

20 Caplan, A. I. Adult mesenchymal stem cells for tissue engineering versus regenerative medicine. *J Cell Physiol* 213, 341-347, doi:10.1002/jcp.21200 (2007).

21 Spiekman, M. *et al.* Autologous Lipofilling Improves Clinical Outcome in Patients With Symptomatic Dermal Scars Through Induction of a Pro-Regenerative Immune Response. *Aesthet Surg J* 42, NP244-NP256, doi:10.1093/asj/sjab280 (2022).

22 Zhang, Z. *et al.* Human umbilical cord mesenchymal stem cells improve liver function and ascites in decompensated liver cirrhosis patients. *J Gastroenterol Hepatol* 27 Suppl 2, 112-120, doi:10.1111/j.1440-1746.2011.07024.x (2012).

23 Lee, S. H. *et al.* The effect of adipose stem cell therapy on pulmonary fibrosis induced by repetitive intratracheal bleomycin in mice. *Exp Lung Res* 40, 117-125, doi:10.3109/01902148.2014.881930 (2014).

24 Chinnapaka, S. *et al.* Human adipose ECM alleviates radiation-induced skin fibrosis via endothelial cell-mediated M2 macrophage polarization. *iScience* 26, 107660, doi:10.1016/j.isci.2023.107660 (2023).

25 Yoon, S., Kang, G. & Eom, G. H. HDAC Inhibitors: Therapeutic Potential in Fibrosis-Associated Human Diseases. *Int J Mol Sci* 20, doi:10.3390/ijms20061329 (2019).

26 Lyu, X., Hu, M., Peng, J., Zhang, X. & Sanders, Y. Y. HDAC inhibitors as antifibrotic drugs in cardiac and pulmonary fibrosis. *Ther Adv Chronic Dis* 10, doi:10.1177/2040622319862697 (2019).

27 Wang, Z. *et al.* Suberoylanilide hydroxamic acid: a potential epigenetic therapeutic agent for lung fibrosis? *Eur Respir J* 34, 145-155, doi:10.1183/09031936.00084808 (2009).

28 Lee, E. *et al.* Histone deacetylase inhibitor, CG200745, attenuates cardiac hypertrophy and fibrosis in DOCA-induced hypertensive rats. *Korean J Physiol Pharmacol* 20, 477-485, doi:10.4196/kjpp.2016.20.5.477 (2016).

29 Dupont, S. *et al.* Role of YAP/TAZ in mechanotransduction. *Nature* 474, 179-

183, doi:10.1038/nature10137 (2011).

30 Lee, J. Y. *et al.* YAP-independent mechanotransduction drives breast cancer progression. *Nat Commun* 10, 1848, doi:10.1038/s41467-019-09755-0 (2019).

31 Tadge, T. *et al.* The role of Piezo1 and Piezo2 proteins in tissue engineering: A Comprehensive review. *Engineered Regeneration* 5, 170-185, doi:10.1016/j.engreg.2024.03.001 (2024).

32 Atcha, H. *et al.* Mechanically activated ion channel Piezo1 modulates macrophage polarization and stiffness sensing. *Nat Commun* 12, 3256, doi:10.1038/s41467-021-23482-5 (2021).

33 Chen, S. *et al.* Single-cell multiomics reveals endothelial mechanosensitive PIEZO1 coupling IL-33 regulates the development of pulmonary brosis. *Research squar*, doi:10.21203/rs.3.rs-4861689/v1 (2024).

34 Gultian, K. A. *et al.* Human induced mesenchymal stem cells display increased sensitivity to matrix stiffness. *Scientific Reports* 12, doi:10.1038/s41598-022-12143-2 (2022).

35 Betriu, N., Andreeva, A., Alonso, A. & Semino, C. E. Increased Stiffness Downregulates Focal Adhesion Kinase Expression in Pancreatic Cancer Cells Cultured in 3D Self-Assembling Peptide Scaffolds. *Biomedicines* 10, doi:10.3390/biomedicines10081835 (2022).

36 Chen, X. *et al.* A Feedforward Mechanism Mediated by Mechanosensitive Ion Channel PIEZO1 and Tissue Mechanics Promotes Glioma Aggression. *Neuron* 100, 799-815 e797, doi:10.1016/j.neuron.2018.09.046 (2018).

37 Liu, C. S. C. *et al.* Piezo1 mechanosensing regulates integrin-dependent chemotactic migration in human T cells. *eLife* 12, doi:10.7554/eLife.91903 (2024).

38 Yue, J., Zhang, K. & Chen, J. Role of integrins in regulating proteases to mediate extracellular matrix remodeling. *Cancer Microenviron* 5, 275-283, doi:10.1007/s12307-012-0101-3 (2012).

39 Ravanti, L., Heino, J., Lopez-Otin, C. & Kahari, V. M. Induction of collagenase-3 (MMP-13) expression in human skin fibroblasts by three-dimensional collagen is mediated by p38 mitogen-activated protein kinase. *J Biol Chem* 274, 2446-2455, doi:10.1074/jbc.274.4.2446 (1999).

40 Karen K. Hirschi, P. A. D. A. Pericytes in the microvasculature. *Cardiovascular Research 32* 32, 687-698, doi:10.1016/S0008-6363(96)00063-6 (1996).

41 Gerhardt, H. & Betsholtz, C. Endothelial-pericyte interactions in angiogenesis. *Cell Tissue Res* 314, 15-23, doi:10.1007/s00441-003-0745-x (2003).

42 Stapor, P. C., Sweat, R. S., Dashti, D. C., Betancourt, A. M. & Murfee, W. L. Pericyte dynamics during angiogenesis: new insights from new identities. *J Vasc Res* 51, 163-174, doi:10.1159/000362276 (2014).

43 Hajmousa, G. *et al.* Human adipose tissue-derived stromal cells act as functional pericytes in mice and suppress high-glucose-induced proinflammatory activation of bovine retinal endothelial cells. *Diabetologia* 61, 2371-2385, doi:10.1007/s00125-018-4713-0 (2018).

44 Terlizzi, V., Kolibabka, M., Burgess, J. K., Hammes, H. P. & Harmsen, M. C.

The Pericytic Phenotype of Adipose Tissue-Derived Stromal Cells Is Promoted by NOTCH2. *Stem Cells* 36, 240-251, doi:10.1002/stem.2726 (2018).

45 Califano, J. P. & Reinhart-King, C. A. in *Mechanical and Chemical Signaling in Angiogenesis* (ed Cynthia A. Reinhart-King) 143-160 (Springer Berlin Heidelberg, 2013).

46 Mason, B. N., Califano, J. P. & Reinhart-King, C. A. in *Engineering Biomaterials for Regenerative Medicine: Novel Technologies for Clinical Applications* (ed Sujata K. Bhatia) 19-37 (Springer New York, 2012).

47 Jiang, Y. *et al.* Macrophages in organ fibrosis: from pathogenesis to therapeutic targets. *Cell Death Discov* 10, 487, doi:10.1038/s41420-024-02247-1 (2024).

48 Tang, P. M., Nikolic-Paterson, D. J. & Lan, H. Y. Macrophages: versatile players in renal inflammation and fibrosis. *Nat Rev Nephrol* 15, 144-158, doi:10.1038/s41581-019-0110-2 (2019).

49 Wynn, T. A. & Vannella, K. M. Macrophages in tissue repair, regeneration, and fibrosis. *Immunity* 44, 450-462, doi:10.1016/j.immuni.2016.02.015 (2016).

Appendix:

English summary

Nederlandse samenvatting

Acknowledgements

List of publications

English summary

The extracellular matrix (ECM) plays a fundamental role in regulating cellular behavior, tissue structure, and disease progression through its biochemical and biomechanical properties. As a dynamic and tissue-specific scaffold, the ECM not only provides physical support but also influences critical processes such as cell differentiation, migration, and matrix remodeling. In fibrotic diseases and wound healing, changes in ECM mechanics are closely linked to pathological outcomes. This thesis focuses on the development and application of organ-derived ECM hydrogels as advanced 3D culture systems that closely mimic native tissue environments. By tailoring the mechanical properties and composition of ECM hydrogels, we investigated their impact on endothelial cells, fibroblasts, and mesenchymal stem cells in the context of vascularization, scar formation, and fibrosis. Through a series of experimental models, this work offers mechanistic insights into how ECM stiffness impacts cellular responses, especially ECM remodeling.

Chapter 2 introduced the development and application of organ-derived ECM hydrogels, emphasizing their biochemical and biomechanical possibilities for regulating cell behavior. Unlike 2D systems, these 3D hydrogels better replicate native tissue mechanics and support real-time monitoring of ECM dynamics regulated by cells embedded within them. The mechanical properties of ECM hydrogels can be tuned to mimic both healthy and fibrotic conditions, making them powerful tools for studying cell–ECM interactions.

In Chapter 3, we investigated the mechanical differences of ECM hydrogels derived from skin, lung, and a hybrid of these materials (1:1 mix) and their influence on vascular network formation (VNF) and ECM remodeling by endothelial cells. Physical property characterization revealed distinct differences among the hydrogels in terms of stiffness, viscosity, fiber diameter, pore size, and fiber density. After cell culturing, skin-derived ECM hydrogels most efficiently promoted VNF compared to both lung and hybrid hydrogels. Skin ECM hydrogels induced higher matrix metalloproteinase 1 (MMP1) secretion, while hybrid hydrogels were associated with increased MMP9 secretion and enhanced deposition of fibronectin and collagen IV. Principal component analysis further highlighted that the mechanical properties (like stiffness, stress relaxation) had a more pronounced effect on VNF than biochemical composition. Overall, the

study underscored that the specific properties of ECM from different organs influence its ability to support VNF.

Chapter 4 explored how fibroblasts modulate matrix to support angiogenesis in co-cultures of endothelial cells and fibroblasts within skin ECM hydrogels. Fibroblasts increased hydrogel stiffness, fiber diameter, and porosity while promoting fibronectin and fibulin-1 deposition near endothelial cells. These findings suggested that fibroblasts could dynamically interact with endothelial cells, modify the ECM microenvironment, promoting vascularization.

In Chapter 5, we aimed to modify the mechanical properties of lung-derived ECM hydrogels to model healthy and fibrotic environments. ECM hydrogels crosslinked with Ruthenium (Ru) exhibited enhanced stiffness and reduced stress relaxation without altering composition. Fiber analysis revealed that crosslinked hydrogels exhibited greater fiber density and shorter average fiber length. When fibroblasts were cultured on these hydrogels, they showed myofibroblastic differentiation, marked by elevated α-smooth muscle actin expression and morphological changes. This system provided an in vitro model for studying the mechanical effects of ECM during lung fibrosis progression.

In Chapter 6, we extended the Ru crosslinking strategy to skin-derived ECM hydrogels. By using a custom mold and diffusing ruthenium into skin-derived ECM hydrogels, we generated ECM hydrogels with a stiffness gradient that mimics the in vivo transition from normal skin to scar tissue. Along this gradient, regions with higher stiffness exhibited denser collagen and slower stress relaxation, which required an additional Maxwell element when stress relaxation curve fitting. Fibroblasts responded to this gradient by altering orientation, ECM remodeling behavior, and local stiffness. 3D embedded fibroblasts orientated at ~45 ° in regions below 120 kPa, while they decreased the stiffness prior to adjusting their orientation in areas above 120 kPa. Besides cell phenotype changes, fibroblasts also remodeled their surrounding ECM in a stiffness-dependent manner. For the ECM remodeling, fibroblasts rearranged ECM and made collagen-depleted holes surrounding cells in high-stiffness areas, and formatted interlaced collagen bundles in low-stiffness areas. Overall, these results showed that fibroblasts actively remodeled their surroundings to optimize their mechanical and topographical environment.

Chapter 7 explored how ECM stiffness shaped matrix remodeling by umbilical

cord-derived mesenchymal stem cells (UC-MSCs) within skin ECM hydrogels. The results showed that UC-MSCs exhibited stiffness-dependent behavior: in soft hydrogels (1.2 kPa, simulating a low-stiffness baseline), they caused contraction-driven stiffening; in medium stiffness (3.4kPa, mimicking normal skin), cells adopted a spindle-shaped morphology and maintained ECM integrity; while in stiff hydrogels (17.7 kPa, resembling scar tissue), cells remained more rounded and promoted ECM degradation, resulting in localized hole formation and a reduction in stiffness. Mechanistically, the mechanosensitive ion channel Piezo1 was identified as the regulator of these responses as Piezo1 inhibition altered remodeling outcomes-mitigating contraction in soft hydrogels and reducing ECM degradation in stiff hydrogels. Interestingly, while MMP2 and MMP14 expression was stiffness-dependent, it was unaffected by Piezo1 inhibition, suggesting the involvement of additional mechanotransduction pathways. Overall, this study underscored Piezo1's role in mediating stiffness-dependent ECM remodeling by UC-MSCs.

In conclusion, this thesis advances our understanding of how mechanics of ECM influence cellular behavior and remodeling. It introduces versatile in vitro models that replicate fibrotic microenvironments, highlights key mechanotransduction pathways like Piezo1, and provides a foundation for the future identification of potential targets for development of antifibrotic therapies and regenerative medicine strategies.

Nederlandse samenvatting

De extracellulaire matrix (ECM) speelt een fundamentele rol in het reguleren van cellulair gedrag, weefselstructuur en ziekteprogressie via haar biochemische en biomechanische eigenschappen. Als een dynamisch en weefselspecifiek scaffold biedt de ECM niet alleen fysieke ondersteuning, maar beïnvloedt deze ook relevante processen zoals celdifferentiatie, migratie en matrixremodellering. Bij fibrotische ziekten en wondgenezing zijn veranderingen in ECM mechanica nauw verbonden met pathologische uitkomsten.

Dit proefschrift richt zich op de ontwikkeling en toepassing van orgaan-specifieke ECM hydrogels als geavanceerde 3D-cultuursystemen die het natuurlijke weefselmilieu nauwkeurig nabootsen. Door de mechanische eigenschappen en samenstelling van ECM hydrogels aan te passen, onderzochten we hun effect op endotheelcellen, fibroblasten en mesenchymale stamcellen in de context van vaatvorming, littekenvorming en fibrose. Via een reeks experimentele modellen biedt dit werk mechanistische inzichten in hoe de stijfheid van ECM cellulaire responsen beïnvloedt, met name ECM remodellering.

Hoofdstuk 2 introduceert de ontwikkeling en toepassing van orgaan-specifieke ECM hydrogels, met nadruk op hun biochemische en biomechanische mogelijkheden voor het reguleren van celgedrag. In tegenstelling tot 2D systemen repliceren deze 3D hydrogels de mechanica van natuurlijk weefsel beter en ondersteunen ze het continue volgen van ECM dynamiek zoals deze wordt uitgevoerd door de ingekapselde cellen. De mechanische eigenschappen van ECM hydrogels kunnen worden afgestemd om zowel gezonde als fibrotische omstandigheden na te bootsen, waardoor het krachtige hulpmiddelen zijn voor het bestuderen van cel–ECM interacties.

In Hoofdstuk 3 onderzochten we de mechanische verschillen van ECM hydrogels afkomstig uit huid, long en een hybride mengsel (1:1 mix), en hun invloed op de vorming van vasculaire netwerken (VNF) en ECM remodellering door endotheelcellen. Fysische karakterisering toonde duidelijke verschillen tussen de hydrogels in stijfheid, viscositeit, vezeldiameter, poriegrootte en vezeldichtheid. Na celkweek bevorderden huid-afgeleide ECM hydrogels de VNF het meest efficiënt vergeleken met long- en hybride hydrogels. Huid ECM hydrogels induceerden hogere secretie van matrixmetalloproteïnase 1 (MMP1), terwijl

hybride hydrogels geassocieerd waren met verhoogde MMP9 secretie en meer afzetting van fibronectine en collageen IV. Principale componentenanalyse benadrukte dat mechanische eigenschappen (zoals stijfheid, spanningsrelaxatie) een grotere invloed hadden op VNF dan de biochemische samenstelling. Het onderzoek benadrukte dat de specifieke eigenschappen van ECM van verschillende organen van invloed zijn op hun vermogen om VNF te ondersteunen.

Hoofdstuk 4 onderzochten we hoe fibroblasten de matrix moduleren om angiogenese te ondersteunen in co-culturen van endotheelcellen en fibroblasten binnen huid-ECM hydrogels. Fibroblasten verhoogden de hydrogelstijfheid, vezeldiameter en porositeit terwijl ze de afzetting van fibronectine en fibuline-1 nabij endotheelcellen bevorderden. Deze bevindingen suggereren dat fibroblasten dynamisch kunnen samenwerken met endotheelcellen en het ECM-microklimaat kunnen veranderen om vascularisatie te bevorderen.

In Hoofdstuk 5 beoogden we de mechanische eigenschappen van long-specifieke ECM hydrogels te wijzigen om gezonde en fibrotische omgevingen na te bootsen. ECM hydrogels gecrosslinkt met ruthenium (Ru) vertoonden verhoogde stijfheid en verminderde spanningsrelaxatie zonder veranderingen in de samenstelling. Analyse van vezelstructuren liet zien dat gecrosslinkte hydrogels een hogere vezeldichtheid en kortere gemiddelde vezellengte vertoonden. Wanneer fibroblasten op deze hydrogels werden gekweekt, vertoonden ze myofibroblastdifferentiatie, gekenmerkt door verhoogde expressie van α-smooth muscle actine en morfologische veranderingen. Dit systeem bood een in vitro model om de mechanische effecten van ECM tijdens de progressie van longfibrose te bestuderen.

In Hoofdstuk 6 breidden we de Ru-crosslinkingstrategie uit naar huid-afgeleide ECM-hydrogels. Door gebruik van een op maat gemaakte mal en diffusie van ruthenium in huid-ECM-hydrogels genereerden we ECM-hydrogels met een stijfheidsgradiënt die de overgang van normale huid naar littekenweefsel in vivo nabootst. Langs deze gradiënt vertoonden regio's met hogere stijfheid dichter collageen en tragere spanningsrelaxatie, wat een extra Maxwell-element vereiste bij curve-fitting van de spanningsrelaxatie. Fibroblasten reageerden op deze gradiënt door oriëntatie, ECM-remodelleringsgedrag en lokale stijfheid aan te passen. 3D-ingekapselde fibroblasten oriënteerden zich rond de 45° in regio's

onder 120 kPa, terwijl ze eerst de stijfheid verminderden voordat ze zich heroriënteerden in gebieden boven 120 kPa. Naast veranderingen in fenotype, remodelleerden fibroblasten ook hun omringende ECM op een stijfheidsafhankelijke manier. In gebieden met hoge stijfheid maakten fibroblasten collageenarme holtes rond de cellen, terwijl ze in gebieden met lage stijfheid verstrengelde collageenbundels vormden. Deze resultaten tonen aan dat fibroblasten hun omgeving actief remodelleren om een optimale mechanische en topografische omgeving te creëren.

Hoofdstuk 7 onderzocht hoe ECM stijfheid matrixremodellering beïnvloedt door mesenchymale stamcellen afkomstig van de menselijke navelstreng (UC-MSCs) in huid ECM hydrogels. De resultaten toonden aan dat UC-MSCs stijfheidsafhankelijk gedrag vertoonden: in zachte hydrogels (1,2 kPa, een lage basisstijfheid) veroorzaakten ze contractie-gedreven verstijving; bij medium stijfheid (3,4 kPa, gelijkend aan normale huid) namen cellen een spoelvormige morfologie aan en behielden ECM integriteit; in stijve hydrogels (17,7 kPa, vergelijkbaar met littekenweefsel) bleven cellen ronder en bevorderden ECM afbraak, resulterend in lokale holtevorming en afname van stijfheid. Mechanistisch werd het mechanosensitieve ionkanaal Piezo1 geïdentificeerd als regulator van deze reacties, aangezien remming van Piezo1 de uitkomsten beïnvloedde – contractie werd verminderd in zachte hydrogels en ECM afbraak werd verminderd in stijve hydrogels. Interessant genoeg was de expressie van MMP2 en MMP14 weliswaar stijfheidsafhankelijk, maar werd deze niet beïnvloed door Piezo1-remming, wat wijst op aanvullende mechanotransductiepaden. Deze studie benadrukte de rol van Piezo1 in het mediëren van stijfheidsafhankelijke ECM remodellering door UC-MSCs.

Samenvattend bevordert dit proefschrift ons begrip van hoe ECM mechanica cellulair gedrag en remodellering beïnvloedt. Het introduceert veelzijdige in vitro modellen die fibrotische micro-omgevingen nabootsen, belicht sleutelmechanotransductieroutes zoals Piezo1, en biedt een basis voor de toekomstige identificatie van potentiële doelwitten voor de ontwikkeling van antifibrotische therapieën en strategieën in regeneratieve geneeskunde.

Acknowledgements

Pursuing a PhD has been one of the most unique and pivotal journeys in my life. The moment I received the invitation letter from my supervisors in the University of Groningen, I was overjoyed and eager to embark on what I knew would be a challenging, novel and enriching chapter. Over these 4.5 years, I gradually comprehended what scientific research is, cultivated the mind to propose research projects, appreciated the power of collaboration and communication, and experienced personal growth in many unexpected ways. Standing now at the threshold of my upcoming doctoral defense, countless memories from this journey resurface vividly. So many people have guided, helped, encouraged, supported, and accompanied me throughout this time, and I would not be here without them.

Firstly, I want to express my deepest gratitude to my **three supervisors**. It is your guidance that has helped me find direction whenever I felt lost. Being part of two departments and having three supervisors shared almost equal responsibility for my work was both a joy and, at times, a minor challenge. I remember Marco once asking if I ever felt stressed or overwhelmed, but the truth is, I have always felt deeply supported. The thoughtful insights, encouragement, and collaborative spirit you brought to our work made this journey not only productive but also genuinely rewarding. I have often felt incredibly fortunate to have had the three of you as my supervisors.

Dear Marco, from our very first video interview, I sensed your patience, kindness, and strong sense of responsibility. Meeting you in person for the first time in the BBT meeting room only confirmed those impressions. You were warm and open, asking about my ideas and plans for the PhD project. At that time, I could barely communicate in English, but you patiently wrote things down and helped me develop a research framework—the triangle of mechanics, ECM, and cells. During our Cavarem group meetings, you often encouraged me to share my thoughts, which helped me quickly integrate into the team. More importantly, you taught me a valuable lesson I had never considered before: that it's okay to say "no" to supervisors and colleagues. You recognized my strengths and weaknesses and guided me with both sensitivity and insight. In our one-on-one meetings, you taught me how to write academically and how to shape research ideas by continuously challenging me with thoughtful questions. Through this, you helped

me develop a clearer academic vision. I also deeply appreciated and enjoyed all of your presentations. Your talk on vascularization at the 3D meeting, in particular, remains the most engaging, insightful, and expressive presentation I've ever attended. Thank you for everything you've taught me and for all the support over the years.

Dear Prashant, to me, you have been not only a supervisor but also a friend. My formal affiliation was with BBT, even though much of my lab work took place in the MB department. You introduced me to every technician and colleague during coffee breaks and encouraged me to chat with them. You brought humor and warmth into every space you entered, creating a relaxed and fun atmosphere. You constantly encouraged me to present my work with confidence, to embrace unexpected results or failed experiments, and to speak up during conferences. Your support made me more self-assured and engaged. During work, you always offered valuable guidance in your areas of expertise. Sharing an engineering background meant you could quickly grasp my ideas—and sometimes even "battle" with the other two supervisors! I truly enjoyed those lively discussions and the intellectual sparks they created. Outside of work, you often brought our team together--organizing BBQs or celebrations for important festivals. I spent my first Christmas in the Netherlands at your home, which made me feel welcome and not alone. That kindness is something I will always remember and appreciate.

Dear Janette, from the time you helped me draft my PhD proposal before I officially started, I could already tell how rigorous and passionate you were about science. As we got to know each other better, I also came to admire your gentle wisdom, your patience and inclusive nature, and your extraordinary efficiency. You inspired me not only professionally, but also personally—I often thought about how I could grow to become a female scientist like you. You taught me the importance of staying focused on a main research line rather than being scattered across too many directions. You also showed me that sometimes, knowing when to stop is an efficient way to move forward. You often reminded me that I could reach out to you anytime for help. Even when I was frustrated by my limitations, you never lost faith in me. I was especially touched by the small but meaningful moments—whether it was at the WBC conference in South Korea when you introduced me to an old friend of yours, or in your office when you warmly introduced me to a professor I hadn't met before. Each time, you naturally introduced me as your student. Those gestures meant a great deal to me and

brought me a deep sense of joy. You are my female model, also giving me the future progress many motivations and goals.

I would like to express my gratitude to my thesis assessment committee members, **Prof. P. van Rijn**, **Prof. R. Gosens** and **Prof. L.F.P. Moreira**. I greatly appreciate the valuable time and effort you all dedicated to providing valuable suggestions and feedback on this thesis.

To my **paranymphs**, Rene and Jhon, First, I'm truly grateful that both of you accepted my invitation to be my paranymphs.

Rene, I feel so lucky to have you as both a colleague and my office mate. I still remember how quickly we connected the first time we met despite my initial nervousness. You spoke to me at length even though I was still stumbling over my words. We talked about not just academically, but also personally. Whenever I faced challenges in social situations, you were the one who offered kind, honest, and insightful advice. We could joke around without filters, show each other our flaws, and still feel completely accepted. Your words have always been full of encouragement and support. We even shared our cultures through food—I taught you how to make Chinese-style dumplings ("chao shou") and you taught me how to make beef burgers. Since we shared two supervisors and split our time between BBT and MB, our talks naturally include research. We often discussed experimental difficulties and brainstormed solutions together. You are a trusted collaborator. I'm so grateful to have had such a warm, thoughtful, optimistic, and uplifting friend by my side.

Jhon, we first got to know each other during an online meeting when you were still in Colombia. I remember how clear and engaging your presentation was. Shortly after, we met in person at UMCG, and I was amazed at how effortlessly you seemed to manage both work and life. I'll always cherish the memory of visiting you and Manu, and tasting delicious Colombian food—especially the arepas, which I can still remember vividly! Every conversation with you and Manu has been a delight. We spoke openly about politics, culture, and life. Your social skills are remarkable, and your presence at any gathering brings an extra dose of liveliness and relaxation. During moments of scientific frustration, we've vented to each other and offered words of encouragement. I know you will be supporting me when I need help. Besides, listening to you speak about your beloved homeland—its beauty, its climate—filled me with a strong desire to visit

someday. I hope I'll have the chance to attend your wedding in the future and learn to dance with Manu all over again.

I would like to express my heartfelt gratitude to the members of the **Cavarem group**. It has been a joy and privilege to work alongside each one of you: **Linda**, **Timara**, **Anita**, **Meng**, **Xue**, **Francisco**, **Elisabeth**, **Vasilena**, **Junyu**, **Qiqi**, **Jan Aart**, and **Mohammad**. The positive and collaborative atmosphere within our group has made every meeting something to look forward to. We shared our progress, brainstormed solutions to experimental challenges, and made each session both productive and engaging.

Linda, whenever I faced challenges in Z-Lab, I would come to you for help. You calmly and expertly solved the problems I encountered. All my staining skills were taught by you, and the clever method you proposed for preparing sections of hydrogels for SEM helped us overcome a long-standing issue. I also loved our casual chats during breaks—they made long days in the lab much more pleasant. I'll always remember our time at Kolff Day, where we tried archery, went sailing, enjoyed a fancy dinner, and had deep conversations that made the day so memorable and enjoyable. **Timara**, you're always kind and helpful. Thank you for your advice and support with endothelial cells and UC-MSCs. You patiently answered all my detailed questions about cell culture. I have learned a great deal from your organized project content classification and clear, concise experimental records. **Anita**, you were the first person who helped me when I joined Marco's team. You showed me how to properly culture cells. Your warm and friendly smile brightened every encounter, and I've enjoyed our conversations about how things were going. When I learned your daughter visited schools in China, I was thrilled. I truly hope you get to visit China someday—so we can meet again there! **Meng**, you were the only my Chinese "senior sister" in our group and someone who helped me tremendously during my PhD. You invited me to your home for meals and helped me quickly adapt to life in Groningen and into our work environment. I admire your calm, confident presentation skills and your clear, flexible thinking and critical ideas during academic discussions. Outside of work, we shared chats about the ups and downs of PhD life, shopping joys, and emotional support that helped both of us move forward. I wish you all the best now in China, and I look forward to our next face-to-face chat. **Xue**, I still remember picking you up from the train station on your first day in Groningen—and accidentally getting off at the wrong stop! Thankfully, you weren't too

worried and trusted me enough to continue the journey back with a smile. That was the beginning of our bond. We traveled together to Belgium, Germany, and Italy—each trip filled with laughter and unforgettable memories. Like **Meng**, your cooking is also amazing. I often found myself enjoying your delicious meals and homemade milk tea-those were such cozy and happy moments. Our time spent together in the Z-Lab made even the time-consuming and exhausting experiments more bearable. I hope you continue to embrace and enjoy life and that you graduate smoothly and soon. **Francisco,** you were undoubtedly the most popular guy in our office, even if you were the only guy at the time! haha! But truly, your outgoing and generous spirit brought joy to everyone. When I was struggling to define my research project in the first year, you shared your own experience and gave me great advice on how to seek help from our supervisors. Through you, I also discovered the world of salsa and bachata dancing--which I found to be incredibly fun and addictive. **Elisabeth**, you were always the earliest one in the office, working with admirable dedication. Your work ethic inspired me, and I'm grateful for all the talks with you and your willingness to answer my questions. **Vasilena**, your time management was impressive: you balanced clinical work at UMCG while completing your PhD research. I always enjoyed our walks to meetings, chatting along the way. Thank you for your company and all the pleasant conversations. **Junyu (Joey)**, you are one of the hardest-working people I know. You managed multiple projects at the same time and completed what seemed like impossible workloads. Since we started our PhD around the same time, I've always felt we were a team. Our collaboration only strengthened that bond, and I'm grateful for the friendship that grew from it. I'm thrilled to hear you're starting a postdoc--wishing you a successful and fulfilling research journey ahead! **Qiqi (Qi Zhou),** thank you for all the experimental support and especially for guiding me through UC-MSC characterization. We often encouraged each other through the uneasy PhD work. Our shared dinners and chats with mutual friends were always so relaxing. Your gentle personality and calm demeanor made every moment around you feel warm and pleasant. **Jan Aart,** it was fun learning how to isolate SVF together with you and Xue, and I will always remember the enjoyable times we spent together in the lab. You were also the first to introduce me to the Dutch stroopwafel--despite not having a sweet tooth, I found it delicious. This little treat has added something special to my memories of the Netherlands. **Mohammad,** I admire your dedication to learning and your humble attitude. Thank you for traveling all the way from Iran to share

your work—and for bringing those delightful traditional sweets from your home country.

Next, I would like to thank all my colleagues from the **3D Meeting** Group. **Yanzhe**, time truly flies. It feels like just yesterday we were writing our theses side by side, and now you've already defended yours, and mine is just around the corner. You've been more than a friend I could confide in—you've been a companion on this journey, a fellow warrior as we strived to improve ourselves. Yes, I did quite a few embarrassingly silly things during my PhD, but your warm words and unwavering support helped me laugh them off and stay positive. Whether I was presenting, revising a manuscript, or even learning to dive, every time you said "You can do it," you gave me real courage. Our trips and shopping are also some of my happiest memories. You always choose buying the comfiest shoes, so I hope that every path you take in the future is one that you truly love and suits you best. I hope the kindness and warmth you give are returned to you, and I look forward to all the reunions we'll have in the future. **Roderick** and **Mehmet**, you were among the first people who guided me into research when I joined the lab. Our collaboration on project of hydrogel mechanics regulation, in truth, more like a mentorship--thank you for teaching me how to prepare hydrogels, tune mechanical properties, and use various instruments. I deeply appreciate the time and care you invested in helping me get started. It was this project laid the foundation for my own PhD topic: the interaction between ECM mechanics and cells. It felt like a natural extension of the models we initially built together. Thank you for providing me with such a solid starting point. **Roderick**, you constantly reminded me that I was making progress--your words gave me confidence in myself. **Mehmet**, your precision in designing experiments, structuring research plans, and setting clear timelines made a lasting impression on me. **Taco**, I often came to you with questions or needing help, and yet you always welcomed me with patience and quickly offered solutions. Your careful guidance, especially in hydrogel preparation, made me very grateful to have someone with such rich experience on the team. **Mugdha**, every time I visited your office, you greeted me with such warmth. I enjoyed our chats in the office or over coffee. I still remember how well-organized and thoughtful you were when we planned Janette's birthday dinner. Your sense of detail and leadership truly stood out. I'm only sorry I couldn't attend your defense and celebration, but I heard from the supervisors that you did an amazing job. I wish you great success

in your postdoctoral work! **Lei**, your optimism, helpful nature, and ability to always consider others' perspectives made conversations with you feel comforting and supportive. **Brady**, thank you for your help improving my mold fabrication process and for sharing your ideas: it was very helpful. **Isidoria**, thank you for every talk in the office: from cultural exchanges to research questions, from daily life to weekend plans. Serbia is now officially on my travel list—and I'm especially looking forward to trying the ice cream you told me about.

I want to express my sincere gratitude to the technicians at MB. **Theo**, whenever your name comes up, people always speak with admiration for your incredible staining skills. Working with you was truly a pleasure as you seem capable of everything and always work with amazing efficiency. What I admire most is your emotional stability; it's something I really wish I could learn from, especially during those times I argued with my boyfriend. **Henk**, thank you for inviting me to your home to pick blueberries and for making delicious blueberry jam for us. I'm also especially grateful that even after your retirement, you still came back to help me prepare those tricky frozen sections. **Matthijs**, thank you for ordering experimental supplies and for helping us prepare various essential reagents. **Josee**, thank you for your warm greetings around the lab and for letting me borrow your special pipette.

Special thanks to **Klaas**, the amazing microscopy trainer at UMIC, who taught me to use many different microscopes. Every time a technical issue came up, you were able to solve it. The clear, beautiful cell images I captured were all thanks to your guidance.

To my colleagues at MB: **Yiwen**, being your office mate was joyful. We shared so many chats and snacks. Your desserts are the best! Making dumplings and zongzi together saved us from so many boring weekends. You're always full of energy, and being around you made me feel more livelier and more refreshed. **Taoyu**, I was always happy to run into you in the corridor. Thank you for sharing your daily stories and for listening to both my joys and worries. **Yutong**, my dear friend from Sichuan University, I'm so glad we became colleagues again here at MB. It's been such a wonderful reunion. **Han**, it was so much fun playing laser tag with you--what a thrilling experience. **Xin Tang**, catching oysters and having BBQ together were unforgettable summer memories in Groningen.

To the Regeneration & Biotribology group: **Hans**, **Ke**, **Yong**, **Yiwen**, **Victor**,

Jhon, **Rene**, **Natalia**, **Nikola**, and **Monize**. Our group has such a relaxed and harmonious vibe. I feel incredibly lucky to be part of this family. **Hans**, thank you for our frequent talks within BBT. You are open and approachable, and we could talk about anything. As our group's all-around technician, there's no instrument you can't handle. You helped me test the (μ)LLCT instrument so many times with incredible patience. Between tests, we talked about politics, family, work, fashion, shopping and so on. Those conversations were essential in helping me improve my spoken English. I'm especially grateful that you traveled all the way to China with everyone's blessings from our group to attend my wedding with Yilun. Our trip in Beijing together and your heartfelt speech at our wedding will remain cherished memories. I wish you continued good health and look forward to our next reunion in China. **Ke**, there are simply no words to express how thankful I am for you. When I first arrived at BBT, you helped me adapt to both our research group and to life in Groningen. As the only direct chinese junior ("师妹") in the group, I was very lucky to have you looking out for me. You introduced me to your circle of friends, helping me make Chinese friends and easing my homesickness. You always set high standards for yourself and were incredibly disciplined, yet you accepted my shortcomings during work and encouraged me to improve. I'll never forget that summer when you and Guang moved your fridge to my place on a bike! I truly miss those days when the three of us would hang out and chat. **Yong**, you are one of the most genuine and helpful people I've ever met. Everyone appreciates and admires you. You're always cheerful, and I've never heard you complain, whether in work or life. Being around you is simply uplifting. You've readily helped whenever I asked, and I'm deeply grateful that you coordinated the wedding wishes video from everyone. I hope you graduate smoothly and look forward to frequent meetups once you're back in China. **Yiwen**, I love your bright, outgoing energy. Thank you for inviting me to be your paranymph at your defense and for always bringing me gifts when you come from U.S. **Victor**, your relaxed attitude is inspiring, even when experiments weren't going well, you maintain a smile. **Natalia**, the banana cake and Greek cookies we made for the Christmas party were absolutely the best! A girl who smiles as much as you are bound to have great luck. **Nikola**, thank you for inviting me to your birthday celebration. The fried chicken schnitzels you and your boyfriend made were the best I've ever had. **Monize**, our talks were always enjoyable, and your presentations were also impressive.

I would also like to thank all the academic staff at BBT: **Hélder Santos, Henk J. Busscher, Henny van der Mei, Brandon Peterson, Inge Zuhorn, Patrick van Rijn, Romana Schirhagl, Theo van Kooten, Jelmer Sjollema, and Sarthak Misra**. I truly appreciated every conversation in the coffee room and in the elevator. Thank you for your helpful, constructive, and creative discussions during the lunch meetings. Your expertise, professionalism, and broad vision have deeply impressed and inspired me.

I also want to extend my sincere thanks to the BBT technicians: **Ed**, thanks for your help in solving any problems of my computers and email account. I was often amazed to see you wearing just a shirt even when I felt freezing, that made me truly admire your robust health. You're always smiling and open for a friendly chat, which I really appreciated. **Joop**, thank you for generously sharing your sandwich with me when you saw I didn't have time to grab lunch at the restaurant. You are such a kind-hearted person, always ready to lend a hand whenever I need help. **Marija**, you're always full of energy. Thank you for handling all the orders and for your greetings when we meet. **Willy**, our dear secretary, you are one of the kindest and warmest people I've met. Thank you for always being thoughtful and for helping me with the extension of my contract. **Wytse**, thank you for assisting with my reimbursements and the extension of my PhD contract. **Gesinda**, thank you for all your help with the OCT and freeze dryer training. **Willem**, thank you for teaching me how to use the confocal microscope. **Emma**, I'm grateful for your help with sectioning and microscopy work. **Reinier**, thank you for the enjoyable talks and for showing me how to use the scanner and centrifuge. **Willy and Jelly**, thank you both for all your help in the lab and during lab cleaning.

Next, to my colleagues in BBT department: **Qiaolan,** our meeting must have been fate! I was so surprised when you told me your former name was also Fenghua. We got to know each other through Sidi, and I later felt it was a case of "meeting too late in life." When I was not in a great state, I chose to move into your office thinking your cheerful energy would lift my mood—and it worked. That was the most happiness months during my PhD. We had plans to cook together, however you cooked far more often than I to give me more time to finish my final project. Our trip to Portugal deepened our understanding for each other, and I truly look forward to traveling with you again. Since returning to China, I often miss our evenings of dinners and watching series, your handmade noodles, and our times

working and shopping together. I wish you a smooth path to graduation and look forward to every reunion in the future. **Guang,** a true northeasterner (东北银)--generous, straightforward and warmhearted. Our trip to The Hague felt like a fresh "exploration" together. I really cherish the memories of deep talks and dinners with you and Ke. You supported me immensely in both research and life. When my husband visited the Netherlands, you welcomed him so warmly. He was truly touched and grateful. I regret not being able to attend your defense in person while I was in China, but I look forward to witnessing your coming big wedding day in China. **Jingjing (YanJing),** I honestly can't remember what exactly brought us closer, but now we've become such close companions. Our Iceland trip was filled with nonstop laughter and it remains my happiest journey. Traveling to Switzerland and Korea for conferences with you made everything more fun, thanks to all the food hunts and sightseeing we squeezed in. Thank you for coming to my hometown to attend my wedding. I'm looking forward to our future shopping sprees and travel dates post-graduation. **Tianqi,** your cheerful and infectious laughter lights up any room. At every department event, I'd naturally gravitate to you for a good chat. Despite the long distance, we eagerly went to every swimming class together. You were basically my freestyle coach. I also thoroughly enjoyed your cocktails and homemade Chinese dishes. Besides, thank you for saving me when I ran low on staining reagents. May all the kindness and help bring you good fortune. **Chen, Kaixuan and Zihan**, we started our PhD journeys around the same time, which made your presence especially comforting. **Chen,** thank you for your 3D printing help. It significantly accelerated my project. And thank you for introducing me to **Yiling,** the stylish sweetheart. Time spent with her always made me feel like we were two beautiful and joyful princesses. **Kaixuan,** our office chats were always relaxing and fun. **Zihan**, you were always full of encouraging words and generous support. Though we didn't become relatives, let's make sure our friendship lasts a lifetime. **Jie,** we clicked from the moment we met. Our conversations flowed endlessly. Even though we never hesitated to speak our minds when we disagreed, I believe that only strengthened our mutual respect. Celebrating the Mid-Autumn Festival and traveling to The Hague with you are among my fondest memories. **Sidi**, you were the best at encouraging me, making me feel confident in taking on and completing each challenge. Sitting next to you in the office meant constant fun chats. On trips, you were always like the team captain, looking out for everyone. I appreciate being

invited as your defense paranymph and am happy to be your friend. **Renfei**, I'm lucky we grew close during the final stage of your PhD. Spending time with you and Qiaolan helped me forget my worries about my graduation. You're the best fisherman among PhDs, the best bicycle repairman among fishermen, and the best barista among bicycle repairmen. **Fanfan** (**Fan Wu**), your grilled fish remains the best I've ever had. You're always polite and generously helpful. Thank you for everything. **Guimei**, I'm so glad we became friends. Your sincerity and kindness shine through. You were always the first to help me both in research and in daily life. **Cong**, time with you often meant delicious food. Thank you for sharing your cooking skills with me. Let's both graduates smoothly and successfully. **Tianrong**, our light-hearted office chats were always a pleasure. Thank you for the tomatoes you lovingly grew yourself. I hope you graduate smoothly and we can still meet when you return to China. **Siran**, watching the sunrise in Portimão on New Year's was breathtaking. Your gentle presence made the trip even warmer and more joyful. **Roujia**, I feel lucky to have you as my desk neighbor. Your diligence in research is sure to lead to great achievements. Your hand-drawn art is just like you: charming and full of character. **Meng** (**Meng Qiao**), I'm glad to have lived in the same apartment with you and Yakun. As Chinese northerners, we share a love for food made by wheat flour. Thanks for the handmade fried vegetable dumplings(炸菜角), and our chats over hot pot, which eased my homesickness. **Dayuan**, you not only excelled in chemical synthesis but were willing to share your knowledge. You're also a social butterfly and a master of poetry. Any gathering with you was lively and fun. **Lu**, we truly share a special bond. You were the first You're the first Sichuan University alumnus (and from the same department) that I met at BBT. Thank you for all the support you gave me. **Huijie**, the mud-hiking adventure was hilarious and unforgettable. I hope your current work is going smoothly.

I would also like to thank my other colleagues and friends: **Zhuoyue Wang, Dize Li, Han Gao, Yu He, Arturo El´ıas Llumbet, Ruichen Zhang, Yuewen Zhu, Jiachen Li, Yaran Wang, Yuanlong Cao, Torben van der Boon, Klaudia Jurczak, Devlina Ghosh, Liliana Agresti, Zhuoyi Cui, Runrun Li, Siyu Fan, Xixi Wu, Chuang Li, Lei Li, Yue Zhang, Yuanyuan Chai.** Thank you all for your company and support. Each conversation we shared at BBT brought me joy. I'm deeply grateful and hope I can say all this to you in person someday. Apologies if I missed anyone.

To the dear friends I am fortunate to have outside my departments: **Xinzi, Zhenhui, Keke (Yan Hu), Tingting, Xiaofang, Dongyi, Zhendong**, and **Lei Liu**:

Xinxin, we flew to the Netherlands together to begin our PhD journey. Having you by my side made those early, uncertain days far less lonely. I'm deeply grateful for your help during our time as housemates. I learned most of my cooking skills by watching you, and you've always taken such beautiful travel photos for me. You're efficient, decisive, and always thoughtful in how you treat others. I'm truly lucky to have you as a friend. We got to know **Huihui** shortly after arriving in the Netherlands. The three of us spent nearly every weekend together in those early days: cooking, hanging out, and shopping. Time flew by, and though our PhD work made us busier in the later years, we still made time to celebrate important festivals together. You two are not just close friends, you are my family in the Netherlands. **Huihui**, your passion for sports has always impressed me. We went skiing, swimming, and worked out together: those were some of my favorite and most fun activities. We've even had minor squabbles like kids during France trip, but those only helped us understand each other better and become even closer. I will always treasure the memories we three shared and look forward to reuniting after graduation.

Keke and **Tingting**, after we became friends in Groningen, you both left for Germany and Denmark respectively. I miss you so much. Thankfully, we made lots of beautiful memories before that. Ting's home was our go-to spot for gatherings and energy recharge. Our trip to Belgium was wonderful, though I still regret that Tingting didn't wear the green sweatshirt for our "sisters' outfit"! Even in different countries, we continued growing and becoming better versions of ourselves.

Xiaofang and **Dongyi**, you two are my ultimate joy-bringing travel buddies. Whether it was the group tour across five Nordic countries, our Iceland self-driving adventure, or shopping trips to the Roermond outlet village, every single moment was pure fun and relaxation. And let's not forget how our gossip sessions and deep conversations were essential emotional support that helped me push through my PhD. I hope the three of us will each find the perfect job and keep traveling together in the future.

Zhendong and **Lei**, you are both true gentlemen and incredibly kind-hearted. Every dinner with you was full of laughter and joy. And **Zhendong**: Without your

help, I probably wouldn't have passed the microscopy course! Wishing both of you great success in your academic careers and continued achievements ahead.

To **Hangyu, Yujie, Sunhuo, and Shiyi**, thank you for your help, your company, and the pleasant conversations throughout this journey.

最后，感谢我最重要的家人。你们的爱与守护，使我的这段求学旅程充满了光亮与力量。

感谢我的父母，感谢你们一直以来无条件的支持与信任，始终鼓励我追寻内心所愿。你们的坚韧与博爱、乐观与知足，塑造了我人生的底色，也教会我如何面对生活的风雨。你们深沉的爱，是我每一次跌宕时的精神支柱；能成为你们的女儿，是我最大的幸运。

感谢我的先生一轮，感谢你在我焦虑时始终给予的耐心与坚定支持，感谢你在我们彼此磨合中展现的包容与成长。感谢你在我博士期间无一日间断的视频陪伴，也谢谢你愿意听我每天的一万句闲话。你的乐观与豁达，是一种无声的力量，总能在我低落时带来信心与希望。期待与你携手走过每一个平凡却温暖的明天。

List of publications

1. **F. Zhao**, M. Zhang, M. Nizamoglu, H. J. Kaper, L.A. Brouwer, T. Borghuis, J.K. Burgess, M.C. Harmsen, P.K. Sharma, Fibroblast alignment and matrix remodeling induced by a stiffness gradient in a skin-derived extracellular matrix hydrogel, Acta Biomaterialia 182 (2024) 67-80.
2. J. Wang[#], **F. Zhao[#]**, L.A. Brouwer, M. Buist-Homan, J.C. Wolters, H. Moshage, M.C. Harmsen, Collagen-rich liver-derived extracellular matrix hydrogels augment survival and function of primary rat liver sinusoidal endothelial cells and hepatocytes, International Journal of Biological Macromolecules 278(Pt 2) (2024) 134717.
3. K. Ren[#], **F. Zhao[#]**, Natalia K. Tzaneti, Hans J. Kaper, Prashant K. Sharma, Glycosaminoglycan Depletion Lowers the Crack Resistance of Articular Cartilage Under Impact Loading, Journal of the Mechanical Behavior of Biomedical Materials 170 (2025) 107122.
4. **F. Zhao**, X. Zhang, T. Borghuisb, L.A. Brouwerb, J.K. Burgess, P.K. Sharma, M.C. Harmsen, Piezo1 regulates remodeling of skin-derived extracellular matrix by embedded umbilical cord mesenchymal stem cells in a stiffness-dependent fashion, Submitted.
5. M. Zhang, **F. Zhao**, Y. Zhu, L.A. Brouwer, H. Van der Veen, J.K. Burgess, M.C. Harmsen, Physical Properties and Biochemical Composition of Extracellular Matrix-Derived Hydrogels Dictate Vascularization Potential in an Organ-Dependent Fashion, ACS Applied Materials & Interfaces 16(23) (2024) 29930-29945.
6. M. Zhang, **F. Zhao**, X. Zhang, L.A. Brouwer, J.K. Burgess, M.C. Harmsen, Fibroblasts alter the physical properties of dermal ECM-derived hydrogels to create a pro-angiogenic microenvironment, Materials Today Bio 23 (2023) 100842.
7. X. Wu, **F. Zhao**, H. Wang, R. Schirhagl, M.K. Wlodarczyk-Biegun, Integrating melt electrowriting (MEW) PCL scaffolds with fibroblast-laden hydrogel toward vascularized skin tissue engineering, Mater Today Bio 31 (2025) 101593.
8. M. Nizamoglu[#], R.H.J. de Hilster[#], **F. Zhao**, P.K. Sharma, T. Borghuis, M.C. Harmsen, J.K. Burgess, An *in vitro* model of fibrosis using crosslinked native extracellular matrix-derived hydrogels to modulate biomechanics without changing composition, Acta Biomaterialia 147 (2022) 50-62.
9. M.C. Harmsen, V. Getova, M. Zhang, **F. Zhao**, J.V. Dongen, F.D. M. Garcia, M. Nizamoglu, J.K. Burgess, Organ-Derived Extracellular Matrix Hydrogels: Versatile Systems to Investigate the Impact of Biomechanics and Biochemistry on Cells in Disease Pathology, Handbook of the Extracellular Matrix. 2023, Springer Nature, pp. 1-27.